Anthony R.P. Janse

Sound absorption at the soil surface

Proefschrift ter verkrijging van de
graad van doctor in de landbouwwetenschappen
aan de Landbouwhogeschool te Wageningen,
op gezag van de Rector Magnificus,
Dr.Ir. F. Hellinga, hoogleraar in de cultuurtechniek,
in het openbaar te verdedigen
in de aula van de Landbouwhogeschool op
dinsdag 4 maart 1969 te 16.00 uur

1969 Centre for Agricultural Publishing and Documentation
Wageningen

This thesis is also published as Agricultural Research Reports 715

STELLINGEN

1. Het meten van akoestische impedanties aan bodemstrukturen biedt waardevolle perspektieven voor hun karakterisering.

2. Het meten van de mechanische impedantie van het bodemoppervlak om hieruit een stabiliteitsmaat van de bodemstruktuur te verkrijgen biedt geen perspektieven.

3. De buigstijfheid van bladeren van planten is een goede maat voor de beschikbaarheid van het bodemvocht.

4. Bij de klassifikatie van bodemfysische grootheden dient men rekening te houden met de amplituden van de praktisch voorkomende veranderingen.

5. Bij het laten verrichten van praktikumproeven verdienen de bepalingen, waarin processen worden gevolgd, de voorkeur boven het vaststellen van statische grootheden, zoals gehalten.

6. Bij het opstellen van een bemestingsadvies zal men de waarden van bodemfysische grootheden mede in rekening moeten brengen.

7. Het leren toepassen van schaalregels bevordert in hoge mate het inzicht in de werkwijze van een wetenschappelijke benadering.

8. Het gebruik van eerder gebrachte stellingen behoeft niet zonder meer te worden afgeraden.

9. Men dient geen steun toe te zeggen aan zg. personeelsverenigingen.

10. Bij de expertise van kunstvoortbrengselen, in het bijzonder van schilderijen wordt nog te weinig gebruik gemaakt van de resultaten van een grafologisch onderzoek.

Wageningen, 4 maart 1969. Proefschrift A.R.P.Janse

Voorwoord

Het werken aan een proefschrift gelijkt op het schrijven en regisseren van een toneelstuk. Men gaat uit van een min of meer toevallig ontdekt verband, dat verheldering behoeft. Met het aanvoeren van de benodigde argumenten groeit het inzicht in de probleemstelling. Telkens weer moet men op een weg, die aanvankelijk hoopvol was ingeslagen, terugkeren. De detailproblemen lijken moeilijk tot een eenheid te kunnen worden gebracht. Het hoofdprobleem schijnt zich minder duidelijk af te tekenen; een verwante behandeling van deelproblemen in andere wetenschappen maken een verantwoorde keuze van de begrippen en de toekenning van hun inhoud moeilijk. Soms verhogen gedachtenflitsen of aanvankelijk oppervlakkig gedane waarnemingen de spanning.

In tegenstelling met de bevrijdende katharsis raakt het probleem slechts scherper gesteld: de oplossing wordt naar een meer verwijd gebied verschoven. De katharsis is in feite een nieuwe uitdaging.

Het gekozen uitgangspunt was vreemd in het gegeven werkmilieu. De geboden kansen waren daardoor in het begin zeer ruim. De kans op een suksesvolle uitwerking was nogal klein. Zo werden bijvoorbeeld aanvankelijk veel trillingsmetingen aan de vaste bodemfase verricht. Tamelijk laat bleek dat zowel de meettechniek als de oplossing van de mathematische problemen weinig mogelijkheden bood.

Ook het zoeken naar begrijpende belangstellenden was moeilijk, in het bijzonder door het aanvankelijk onnauwkeurig afgestemd zijn van de ontvanger. Dat er thans een verdedigbare tekst openbaar wordt, is zeker ook te danken aan het mede peinzend zwoegen van Ir. D.W. van Wulfften Palthe, die vooral in de wiskundige problematiek de soms zwijgende souffleur was of de toneelknecht, welke achteraf terecht de deur gesloten hield.

Dat Professor Schuffelen, als een schouwburgdirekteur, na een oriënterende beoordeling het stuk koos, de regie voor een groot deel overliet aan Professor Kosten, stemde de vrijheidsminnende onderzoeker dankbaar. Ook de afdeling Wiskunde, van zowel de Landbouwhogeschool als de Technische Hogeschool te Delft, welke met de geboden hulp bij het programmeren voor schone requisieten zorgde, zij gaarne dank gebracht.

Contents

List of symbols

The symbols are defined or first used in or near the equations cited.
The numbers refer to the chapters, the characters refer to the appendices.

Symbol	Name and description	Ref.	Units
A	constant, integration constant	B-2	-
a	1) absorption coefficient of sample at normal incidence	1-38	-
	2) radius of calibration plate	2-13	m
b	dimensionless measure for tube radius	3-62	-
b_1, b_2	limits for b, calculated values	3-64	-
C	1) mechanical compliance	A-1	$N^{-1}m$
	2) electrical capacity	A-12	F
C_m^{-1}	effective compression modulus	3-2	$N\ m^{-2}$
c_{Vk}	specific heat per mol at constant volume for component k in gas mixture	1-28	$J^0K^{-1}\ kmol^{-1}$
c_{pk}	specific heat per mol at constant pressure for component k in gas mixture	1-41	$J^0K^{-1}\ kmol^{-1}$
c	velocity of sound for free, undamped wave	1-6	$m\ s^{-1}$
c_d, c_h	velocities of sound in dry and humid air respectively	1-48a	$m\ s^{-1}$
c_p	specific heat per unit mass at constant pressure	1-4	$Jkg^{-1}\ {}^0K^{-1}$
c_{pl}	velocity of longitudinal waves in a plate	2-13	$m\ s^{-1}$
c_v	specific heat per unit mass at constant volume	1-4	$Jkg^{-1}\ {}^0K^{-1}$
D	1) fissure width	B-1	m
	2) main slit width	3-126	m
D_a	average value for D	3-93	m
D_1, D_2, D_3	special values for D	3-94, 3-95, 3-96	m
d	crack width	3-126	m
F	acoustical quantity	3-117	-

$F(x)$	auxiliary function	3-71	-
$F_f(x)$	" "	3-97	-
f	1) mathematical function	1-13	-
	2) frequency	2-1	Hz
	3) force	A-1	N
f_k	mass fraction of gas component	1-41	-
$f(x)$	auxiliary arbitrary distribution function	3-25	-
$G(x)$	auxiliary function	3-81	-
G_m	specific acoustic parallel conductance per unit length	3-2	$m^2\ N^{-1}\ s^{-1}$
g	ratio of partial gaspressures	1-48a	-
g_1, g_2, g_3	weighting factors, calculated values	3-64a	-
$H(x)$	auxiliary function	3-70	-
$H_f(x)$	auxiliary function	3-102	-
h	1) volumetric fraction of pores	3-21	-
	2) thickness of calibration plate	2-13	m
	3) number of degrees of freedom	1-5,1-48a	-
	4) crack length	3-127	m
I	intensity of sound, sound power density transmitted	1-20	$W\ m^{-2}$
I_o	reference intensity of sound	1-49	$W\ m^{-2}$
K	compression modulus	1-2	$N\ m^{-2}$
k	wave number, free undamped wave	1-8	m^{-1}
k_B	Boltzmann's constant	1-51	$J\ {}^{0}K^{-1}$
k_m	structure factor	3-22	-
L	coefficient of self-induction	A-12	H
$L(x)$	auxiliary function	3-82	-
L_m	critical length, integration interval	3-46	m
L_I	sound intensity level	1-50	$dB(10^{-12} Wm^{-2})$
L_p	sound pressure level	1-50	$dB(2 \cdot 10^{-5} Nm^{-2})$
l	thickness of sample	1-56	m
l_h	thermal boundary layer thickness	B-14	m
l_{min}	(positive) distance between pressure minimum and sample surface	1-34	m
l_v	viscous boundary layer thickness	B-3	m
M	1) modulus of logarithmic spiral	1-65	-
	2) molecular mass	1-51	$kg\ kmol^{-1}$

$M(x)$	auxiliary function	3-72	-
M_k	molecular mass of component k	1-41	kg $kmol^{-1}$
m	1) dimensionless variable for layer thickness	3-47	-
	2) dimensionless variable for distribution functions	3-62	-
	3) mass	A-2	kg
N	number of channels per unit area normal to direction of propagation	3-25	m^{-2}
n	scale factor	3-118	-
p	1) sound pressure in free wave	1-1	N m^{-2}
	2) average sound pressure in pores	1-52	N m^{-2}
$\tilde{p}$	complex pressure amplitude	1-13	N m^{-2}
$\hat{p}_i, \hat{p}_r$	the peak values of p_i and p_r, resp.	1-11,1-8	N m^{-2}
p_k	partial pressure, component k	1-41	N m^{-2}
p_{max}, p_{min}	sound pressure maxima and minima,resp.	1-35	N m^{-2}
p_s	barometric pressure	1-3	N m^{-2}
Q	electrical charge	A-12	C
$\partial Q/\partial t$	net flow of heat per unit mass	B-10	W kg^{-1}
q	auxiliary variable	3-12a	-
q_a^2	fissure width ratio	3-96	-
R	1) gas constant per mol	1-41	$kmol^{-1}$ $^0K^{-1}$
	2) dimensionless radius of circle with constant reflection coefficient	1-60	-
	3) radius of equivalent tube	3-62	m
	4) radius of curvature of the impedance spiral	D-4	m
	5) electrical resistance	A-12	Ω
R_o	a prefixed value of R(4)	D-10	m
R_g	gas constant per unit mass	1-42	J kg^{-1} $^0K^{-1}$
r	1) pressure reflection coefficient	1-26	-
	2) relative partial gas pressure of water vapour	1-48a	N m^{-2}
	3) radius of reference sphere	3-62	m
	4) mechanical resistance	A-7	N s m^{-1}
S	1) cross-sectional area of channel	3-44	m^2
	2) total entropy of 1 kg gas mixture	1-42	J kg^{-1} $^0K^{-1}$
S_a	average value of S(1)	3-44	m^2

S_k	entropy of component k	1-42	$J\ kg^{-1}\ {}^0K^{-1}$
S	cross-sectional area	1-1	m^2
s	1) standing wave ratio in tube with negligible losses	1-37	-
	2) standing wave ratio, extrapolated to sample surface in tube with losses	1-37	-
ds	a line element of the impedance spiral	D-1	m
$\delta\hat{s}$	a maximum value of ds	D-1	m
s_n	ratio of specific maximum to specific minimum sound pressure	1-39	-
T	absolute temperature	1-41	^0K
T_s	static value of absolute temperature	B-7	^0K
t	time	1-1	s
U	volume velocity per channel	3-45	$m^3\ s^{-1}$
u	1) particle velocity in direction of propagation	3-51	$m\ s^{-1}$
	2) volume velocity per unit area normal to direction of propagation	3-3	$m\ s^{-1}$
	3) real part of reflection coefficient	1-62	-
$\hat{u}$	particle velocity (peak value)	1-49	$m\ s^{-1}$
$\tilde{u}$	complex particle velocity amplitude	1-19	$m\ s^{-1}$
V	1) volume	1-2	m^3
	2) volume of 1 kg gas mixture	1-41	$m^3\ kg^{-1}$
V_e	RMS value of the thermal velocity of molecules	1-51	$m\ s^{-1}$
v	imaginary part of reflection coefficient	1-62	-
W_m	specific acoustic wave impedance	1-55	$N\ s\ m^{-3}$
x	1) spatial co-ordinate in direction of propagation	1-1	m
	2) Cartesian co-ordinate	-	-
x	auxiliary variable	3-73,3-83,3-98,3-103	-
x_3, x_6	frequency dependent factors	3-75,2-84	-
x_1, x_2, x_4, x_5	auxiliary variables	3-76,3-77,3-84,3-85	-
x_1, x_2, x_3	special values for auxiliary variables	3-100	-
x_4, x_5, x_6	special values for auxiliary variables	3-105	-

Y_a	acoustical admittance per unit length	3-128	$N^{-1}\ m^{3}\ s^{-1}$
Y_m	specific acoustic parallel admittance per unit length	1-53	$m^{2}\ N^{-1}\ s^{-1}$
Y_s	acoustical admittance at the mouth of a slit	3-127	$m^{4}\ N^{-1}\ s^{-1}$
y	1) transverse co-ordinate	B-1	m
	2) Cartesian co-ordinate	-	m
Z	specific acoustic impedance (at the sample surface)	1-27	$N\ s\ m^{-3}$
Z_m	specific acoustic series impedance per unit length	1-52	$N\ s\ m^{-4}$
Z_M	mechanical impedance	A-15	$N\ s\ m^{-1}$
z	1) spatial co-ordinate in direction of channels	B-1	m
	2) Cartesian co-ordinate	-	m
α	attenuation constant, real part of γ	1-65	m^{-1}
α_o	attenuation constant in tube	1-23a	m^{-1}
β	phase constant, imaginary part of γ	1-65	m^{-1}
γ	propagation constant	1-18,1-54	m^{-1}
ϑ_p	relative error in sound pressure	2-8	-
Δ	1) tangent of loss angle	3-12a	-
	2) phase displacement	1-34	radian
ζ	normalized specific acoustic impedance	1-28	-
η	1) normalized specific acoustic reactance imaginary part of ζ	1-28	-
	2) dynamic coefficient of viscosity	1-47	$N\ s\ m^{-2}$
η_o	imaginary co-ordinate of the apex of impedance curl in the ζ-plane	3-15	-
η_m	thermal perturbation factor for inclined inhomogeneous channel	3-50	-
η_c	thermal perturbation factor for cylindrical tube	3-90	-
η_f	thermal perturbation factor for fissures	3-106	-
η'_m	thermal perturbation factor for homogeneous channels	3-46	-
η'_c	thermal perturbation factor for cylindrical tubes	3-84	-

r'_f	thermal perturbation factor for fissures	3-104,B-18	-
θ	1) incremental temperature, due to sound field	B-7	^0K
	2) angle of rotation of log. spiral	1-65	radian
	3) angle between direction of propagation and of channels	3-25	radian
κ	Poisson ratio	1-4	-
λ	1) thermal conductivity	1-48	$Wm^{-1}\,^0K^{-1}$
	2) wave length	1-34	m
λ	apparent thermal conductivity	B-22	$Wm^{-1}\,^0K^{-1}$
μ	1) mass of hydrogen atom	1-51	kg
	2) Poisson ratio	2-1	-
	3) dimensionless boundary layer thickness for viscous flow	3-32a	-
ξ	1) small displacement in x-direction	1-2	m
	2) real part of ζ	1-28	-
ξ_o	real co-ordinate of the apex of an impedance spiral in the ζ-plane	-	-
ξ_m	viscous perturbation factor for inhomogeneous channel	3-49	-
ξ_c	viscous perturbation factor for cylindrical tubes	3-80	-
ξ_f	viscous perturbation factor for fissure	3-101	-
ξ'_m	viscous perturbation factor for homogeneous channels	3-45	-
ξ'_c	viscous perturbation factor for cylindrical tubes	3-74	-
ξ'_f	thermal perturbation factor for fissures	3-79	-
ρ	incremental density due to sound fields	1-1	$kg\ m^{-3}$
ρ_s	static specific mass	1-1	$kg\ m^{-3}$
ρ_m	apparent specific mass	3-1	$kg\ m^{-3}$
Σ	auxiliary variable	3-32	-
σ_m	specific flow resistance	3-1	$N\ s\ m^{-4}$
σ_s	static value of σ_m	B-22	$N\ s\ m^{-4}$

τ	relaxation time	A-10	s
σ	specific flow resistance	3-22	N s m^{-4}
ϕ	1) phase angle	-	radian
	2) phase angle of reflection coefficient	1-30	radian
	3) angle between the tangents of the impedance spiral	3-38	radian
$\delta\hat{\phi}$	arbitrarily chosen maximum value of $\phi(3)$	D-10	radian
ψ	1) phase angle	1-10	radian
	2) phase angle of the sound pressure	1-22	radian
	3) argument of log. spiral	1-65	-
ω	angular frequency	1-8	s^{-1}

The following suscripts are used:

Symbol	Referring to
a	average value
c	cylindrical tube model
d	in a tube
e	electrical circuit
f	fissure tube model
h	thermal boundary layer
h	high frequency approximation
i	incident wave
k	serial number of component in gas mixture
l	local value
l	low frequency approximation
M	mechanical
m	in porous material
p	plane wave
p	constant pressure
r	reflected wave
s	static value
v	viscous boundary layer
v,V	constant volume
z	in channel
o	reference value
$R_g, q_a, \delta_p, \xi_o, \eta_o, Y_a,$ $Y_s, s_n, c_d, c_h, \alpha_o$	exceptions

same sample shortly after the first measurement or at a later date. Changes in structure with time can then be analysed and described in particular problems concerning the influences of climate, plant growth and tillage in the development of structure.

d. There should be an acceptable basis to examine existing structures in full. In other words, it should be possible to make a significant approach to the structural unit (Bolt, Schuffelen and Janse, 1958). If the soil surface cracks every 15 cm there is little value in examining a sample with 5 cm diameter.

e. At least in principle it should be possible to take measurements in the field.

For various reasons, such as study of the microclimate the complete ecological horizon must be identified. In this examination of the ecological horizon the pore system is of much importance.

Among the many workers, that have measured the distribution and behaviour of gases in the soil, are Lundegårdh, Free and Cannon. The physical aspects of gas exchange appear to be of particularly great importance. It was established that CO_2 percentages higher than 1% are often deleterious, and that 12 - 15% O_2 should be present in the soil for normal crop production. It was rightly stated that a study of transport processes is also of fundamental importance. The partly theoretical studies of Penman and later those of van Bavel helped especially to clarify how widely the magnitude and effect of the (mechanical) diffusion constant can vary and, for deep rooting plants in particular how much this constant can be affected by the structure of the soil profile.

The biological and microbiological activities, such as nitrification, are also influenced by the availability of O_2. Furthermore in an insufficiently aerated soil compounds of Fe and Mn can be locally reduced.

A separate problem which is difficult to analyse is answering the question of the required sensitivity and reproducibility of the measurements. Although this point will be discussed later in more detail, it can be stated here that:

a. the sensitivity and the required reproducibility in general is determined by the purpose for which the measurement is made. When studying for instance diffusion processes in the soil, the required level of sensitivity will usually be lower than that for investigations of heat transfer in soil.

b. the reproducibility will often vary widely in practice. A more or less homogeneous soil will show less scattering of data than a strongly inhomogeneous soil. Samples taken from different sections of a field will show a certain spread. The argument that the reproducibility of the experimental equipment

need not exceed that of the sampling may well be spurious in certain instances, e.g. if the progress of some process is being followed and the variation of some quantity under observation is of greater interest than its absolute value.

In-2 Total pore space

Soil is a three-phase system; the volume ratios of a multiphase system can easily be determined by drying and weighing after determination of the densities of the various components. Since the latter in the solid phase of the soil often show little variation, use can be made of an average density. The calculated air volume is usually given as a quantity without dimension; it varies linearly with moisture content. Separate weighings are necessary; from these the geometry of pore system cannot be evaluated.

Of more recent date are investigations on the occurrence of pore space based on the intrinsic properties of the material in which the air voids have been formed by tillage and fertilizer application etc. In this manner significant correlationships have been found with the clay fractions (Hooghoudt, 1948), with texture (Fraser, 1935) and with the nature of adsorbed ions (Aylmore, 1966).

A method more immediately directed to measure pore space is one based on connecting a sample with unknown pore space and known total volume with a sealed vessel of known volume, attached to a manometer.

This "gas expansion method" has been studied extensively in various countries. The "porosimeters", also called air pycnometers have been constructed in many forms and tested by Bourrier (1951), Loebell (1956), Misono (1961), Alten and Loofman (1962), and others. Comparable apparatus was constructed and used for routine measurements at our laboratory. In dry samples, the influence of the pressure range appears to be small. In moist samples, serious problems are caused by the release of adsorbed and dissolved gases. Changes in vapour pressure and slow attainment of equilibrium conditions are difficult to correct for in measurements and calculations.

In-3 The characterization of pore space

The study of the structure of porous materials is a fascinating one as is evident from the extensive literature. Many authors in the field of ceramics, filtering technology, geophysics and soil science are in fact interested in the charac-

terization or pore geometry. There are some handbooks in the almost endless array of publications as for instance those of Mc Dalla Valle (1943), Muskat (1946), Carman (1956), Scheidegger (1957), and Lykow (1958). Their approaches are predominantly directed towards selections of parameters which can represent the fluid flow resistance of the material.
The main object is often the reduction of the number of characteristic parameters or concepts determining the flow resistance. In this context, a homogeneous and isotropic configuration is often assumed. The introduction of but one parameter is much favoured and it is remarkable in this respect that so few publications deal with the effect of two or more parameters.

In 3.1 The Static specific flow resistance

Porous materials may be investigated by static or dynamic methods of measurement. For a static method, the variables, excess pressure and particle velocity, do not vary in time or vary so slowly that they can be considered constant. For a dynamic method the variables are functions of time and if these functions are periodic, the method is a steady state one. Static methods fall into the steady state class too as the limiting case of infinitely long period.
Swelling and often low mechanical stability of the soil samples still offer insurmountable difficulties for correct measurements of permeability, i.e. the reciprocal value of specific flow resistance for water. It is therefore not advisable to calculate intrinsic resistances for the soils and loosely packed materials from measurements with water.
Many simple devices are available for measuring air resistance. The value, obtained from the volume rate of flow at a certain induced, usually constant, pressure gradient. The volume rate of flow is measured for various pressure drops over the sample; the proportionality constant between the two quantities is a measure for the static flow resistance. In the flow resistance meter (see figure), used to measure the resistances of most of the samples investigated here, use is made of a sample holder encased in O-rings and connected with a pressure line in the laboratory. The pressure difference between the pressure gaskets is read from a Micro-Fuess manometer. The pressure difference across the sample can usually be limited to 0.04 cm water pressure. A calibrated Fisher and Porter microflowrator (type 130-13) is inserted into the circuit. The volume rates of flow are also kept low and lie between 0.1 and 0.3 cm^3/sec. The relationship between the volume velocity and the pressure drop usually proved to be linear, the slope varied slightly. The specific acoustic flow resistance was

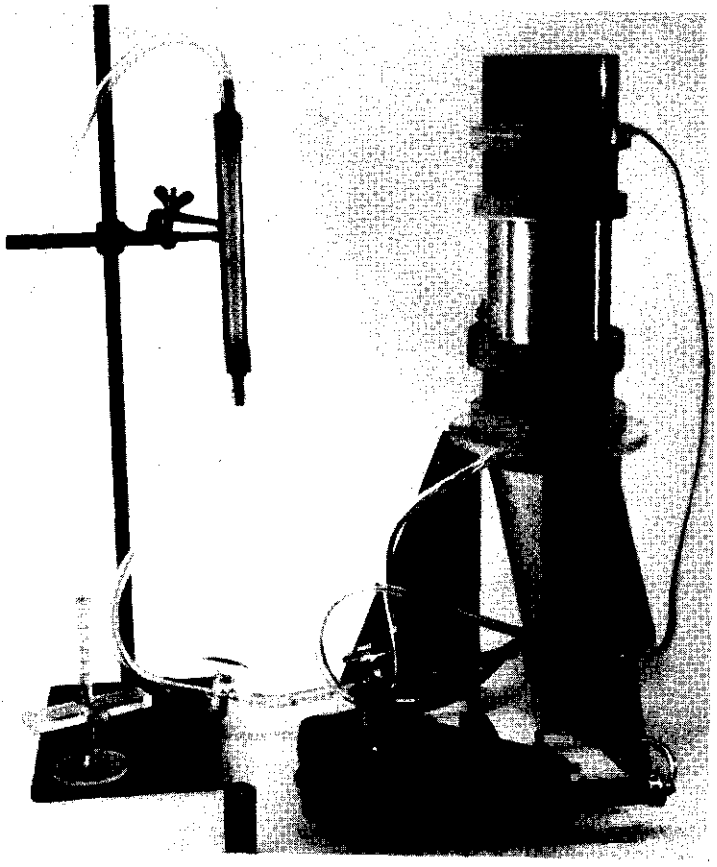

Figure
Apparatus for measuring air resistance of cylindrical soil samples. Description in the text.

obtained as the extrapolated value for vanishing pressure gradients. The concept of specific air flow resistance assumes a laminar flow. One of the reasons for measuring with low rates of flow is the avoidance of turbulence.
For measurements of air flow resistance, sample holders of various diameters were used. Wide holders were used primarily for coarse materials. It can easily calculated that only through use of the wide holders the effects due to the irregularities in the arrangements of the particles or aggregates near the walls of the sample-holder could be kept within experimental error.
Small pressure differences are to be preferred with moist samples, where moisture is easily displaced and where, at low moisture tensions, rupture of the menisci can occur.
It is remarkable that so little literature exists on experiments measuring both air resistance and water permeability of a porous material. Covey (1963) gives a brief summary and an interesting graph for the relative permeability for air and water in a soil sample.
The literature yields many references on the relationship between specific flow resistance and specific surface area of a sample material. An attempt was made to verify this relationship. For fine grained materials no linear relation exists between the total frictional area and flow resistance. For increasing fineness of the material the deviations from linearity became more important. The relationship between packing density and flow resistance was not linear. The results will be discussed in another publication.
Conversely the specific air flow resistance is no unambiguous measure for the frictional area per unit volume and as it fails to yield even this limited information this subject, will not be further pursued.

In 3.2 The acoustical approach

Soil as a porous system often with an extremely complicated structure cannot easily be described in simple terms. Two further remarks are necessary on this point.

1. Only part of the air is in free communication with the atmosphere contributing to the exchange of gases, such as CO_2, H_2O and O_2. This fraction of the total pore space fluctuates enormously with variations in moisture content. Measurements of total pore space or of mean pore diameter (whatever this may be) are therefore bound to be inadequate.
2. For various diverse reasons, the packing density of soil particles varies widely and usually increases with depth. This excludes the possibility to

obtain a true impression of the nature of spatial arrangements in a soil from flow resistances.

The question arises whether other methods can be used to supply information on this spatial arrangement. The problem parallels that confronting an acoustician, developing a sound absorbing material, even if the aims differ. Whereas the acoustician is interested principally in increasing sound absorption in the audible frequency range, here the sound-absorbing properties of a material, i.e. a soil sample, may be determined in order to gain insight into the spatial arrangement.

An advantage of this procedure is that the analytical and experimental methods, devised by acousticians for the investigation of sound-absorbing materials, may be employed.

The interesting question is therefore whether and, if so, to what extent a soil surface will absorb sound and whether this property can yield information on the spatial (in agriculture often "structural") arrangement of soil particles.

A comparison between porous materials developed for sound absorption and soil samples shows that it is certainly so. A practical tool for measuring the acoustical properties of soil samples seems to be the interferometer (arrangement), sometimes called the standing wave tube. The instrument will be discussed in detail in the following sections.

Acoustical investigation of soil samples presents several attractive features.

1. Sound pressures are so low (typically less than 10^{-5} atmosphere) that the sample is not disturbed; the method is non-destructive.
2. The effects of temperature and composition (e.g. humidity) of the gaseous medium in the pores of the material on its acoustical properties are slight; the results are thus governed principally by the spatial arrangement of the material.
3. Only those pores in open communication with the atmosphere contribute to acoustical behaviour.
4. Acoustical measurements yield more information on these pores than any other method, small pores especially having a relatively large effect on acoustical performance.

When a plane sound wave of a certain frequency impinges on the soil part of the incident energy will be reflected. The ratio of reflected to incident energy, the "energy reflection coefficient", can be measured. As a rule there is a phase

jump $|\phi|$ between the reflected and the incident wave at the surface of the sample. This phase jump can be determined too. Energy reflection coefficient and phase jump can be studied in a large frequency range, so that a large number of quantities can be measured.

1 Plane waves and interferometry

1.1 Introduction

The interferometer consists of a rigid cylindrical tube, fitted with a loudspeaker at one end and the sample (with its surface normal to the direction of the tube) at the other (see figure 1a). The loudspeaker generates harmonic plane waves in the tube. In the present context, plane waves are characterized by constant sound pressure in planes normal to the direction of the tube (an exception must be made for a slight perturbation near the walls of the tube). Thus only one spatial co-ordinate, to be designated x, directed along the tube, will be of predominant importance. The following conventions will apply: the positive x direction is from the loudspeaker towards the sample and the sample surface is situated at $x = 0$ (x thus takes on negative values inside the tube).
The sound field in the tube may be considered as the superposition of two waves, the incident wave, travelling from the loudspeaker towards the sample and impinging on the sample surface at normal incidence (p_1 in figure 1a) and the reflected wave returning from the sample (p_2 in figure 1a). These waves set up an interference pattern, determined by the acoustical properties of the sample, in the tube. This pattern may be explored with the aid of a movable microphone.
More detailed consideration requires the introduction of a number of physical concepts and quantities. As far as possible, nomenclature, symbols and units have been chosen in accordance with the recommendations given in "Ontwerp voor akoestische begrippen en grootheden (V 1029)" and in the draft "Electroakoestiek (V 1077)" and are conform to the recommendations given in the "ISONORM 31". A summary of general vibration theory, given in Appendix A, forms the basis for the definition of the concepts involved. Next, a discussion will be given of the method of employing the standing wave tube in the determination of acoustical quantities. Attention will also be paid in this first chapter to the manner in which the results obtained may be presented.

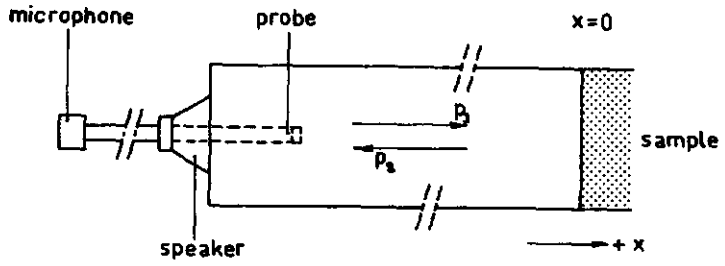

Figure 1a The interferometer tube

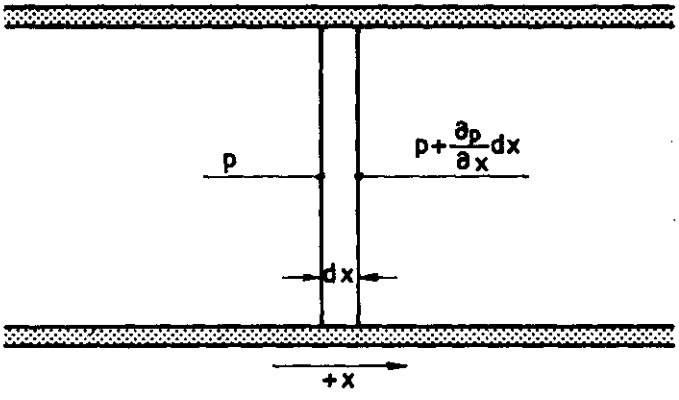

Figure 1b An infinitesimal slice of air

1.2 The wave equation

The wave equation will be derived and solved for plane waves. The sound field in the interferometer is characterized by two dependent variables (both of which are assumed to be constant over a normal cross-section of the tube):

1. The sound pressure p, i.e. the excess pressure over the barometric or static pressure p_s; the total pressure is thus given by $p_s + p$.
2. The particle velocity u, the drift velocity of the molecules of the medium caused by the sound; for plane waves the direction of the velocity vector coincides with that of propagation. The magnitude of the velocity, as that of the sound pressure, may assume both positive and negative values.

There are but two independent variables in the present case: the time t and the spacial co-ordinate x.

Consider an infinitesimal slice of the acoustic medium (see figure 1b), having a thickness dx. The resultant force exerted on this slice is due to p's depending on x; denoting the cross-sectional area of the tube by S, the resultant force in the + x direction is found to be: $-S\cdot(\partial p/\partial x)\cdot dx$. The mass of the slice is $S\cdot\rho_s\cdot dx$, where ρ_s is the (static) density of the medium. The particle velocity in the + x direction is u and therefore the equation of motion takes on the following form (in striking a factor $S\cdot dx$ from both members):

$$-\frac{\partial p}{\partial x} = \rho_s \frac{\partial u}{\partial t} . \qquad (1\text{-}1)$$

The infinitesimal slice will be compressed or expanded. On introducing the particle displacement, $\xi (u = \partial\xi/\partial t,\ \xi = \xi(t,x))$, the absolute increase in volume may be given as: $S\cdot(\partial\xi/\partial x)\cdot dx$ and the relative increase follows as: $\partial\xi/\partial x$. Owing to this expansion, the total pressure has dropped below the static value, the variation being the sound pressure p. In view of the fact that all variations are small, p is proportional to the relative expansion:

$$p = -K\cdot(\partial\xi/\partial x), \qquad (1\text{-}2a)$$

where the proportionality factor K is usually referred to as the compression modulus. Differentiating the latter equation with respect to time and using the fact that the differential operators $\partial/\partial t$ and $\partial/\partial x$ commute, $\partial^2/(\partial x\partial t) = \partial^2/(\partial t\partial x)$, it follows that:

$$-\frac{\partial u}{\partial x} = \frac{1}{K}\frac{\partial p}{\partial t} \cdot \qquad (1\text{-}2b)$$

Eq.(1-2b) is a specialized form of the "equation of continuity". A value for K may be derived on introducing certain assumptions. They are:

1. The medium is an ideal gas.
2. Its changes of state are adiabatic. Especially this latter assumption needs some justification. Heat exchange within the medium may be shown to introduce only negligible effects in air in the audible frequency range. Heat exchange between the medium and the walls of the tube does, however, affect wave propagation. This point will be discussed in a future section: for the moment it will be disregarded as being of secondary importance.

For an ideal gas and an adiabatic change of state:

$$(p_s + p)(V_s + \delta V)^{\kappa} = \text{constant} = p_s \cdot V_s^{\kappa} \ , \qquad (1\text{-}3)$$

where p_s and V_s are the barometric (static) pressure and the volume of the gas under consideration at pressure p_s, respectively, p and δV the sound pressure and the change in V_s due to p, respectively, and κ is the ratio of the specific heats at constant pressure (c_p) and at constant volume (c_v):

$$\kappa = c_p/c_v \ . \qquad (1\text{-}4)$$

(N.B.: In the following c_p and c_v should be conceived as specific heats per unit mass.)

In first order approximation, eq.(1-3) yields:

$$p = -\kappa p_s \cdot \delta V/V_s \ ,$$

and thus, from the definition of K, eq.(1-2a), it follows that:

$$K = \kappa p_s \ . \qquad (1\text{-}5)$$

Kinetic gas theory predicts values for κ for ideal gases. Let h_k represent the number of degrees of freedom of a molecule, then:

$$\kappa = 1 + 2/h_k \ ,$$

where, for diatomic molecules, $h_k = 5$ and for triatomic molecules $h_k = 6$. For air, a value of κ slightly below 1.4 would be expected; the experimental value

proved to be 1.403, in adequate agreement with theory.

Differentiating eq.(1-1) for x and eq.(1-2) for t and eliminating $\partial^2 u/(\partial x \partial t)$ (remembering that $\partial/\partial x$ and $\partial/\partial t$ commute), the wave equation for p is as follows

$$\frac{\partial^2 p}{\partial x^2} = \frac{1}{c^2} \frac{\partial^2 p}{\partial t^2} , \tag{1-6}$$

where

$$c = \sqrt{(\kappa p_s/\rho_s)} . \tag{1-7}$$

The meaning of the constant c will emerge later. If p is eliminated from eqs (1-1) and (1-2) instead of u, the wave equation for u results. This equation turns out to be identical with eq.(1-6) on replacing p by u.
Eq.(1-6) is a linear, homogeneous, partial differential equation of the second order and possesses as such a general solution composed of two independent functions, each incorporating two integration constants. The general solution may be represented in various ways, the following form being appropriate to harmonic waves:

$$p = \hat{p}_1 \cos(\omega t - kx + \phi_1) + \hat{p}_2 \cos(\omega t + kx + \phi_2) , \tag{1-8}$$

where
ω = the angular frequency (= 2π times frequency),
k = the wave number, $k = \omega/c$,
$\hat{p}_1$, $\hat{p}_2$ are integration constants having the character of peak values of sound pressures,
ϕ_1, ϕ_2 are integration constants having the character of phase angles.

Consider the first term on the right-hand side of eq.(1-8). For an observer moving with velocity $dx/dt = c$ in the + x direction, the argument of the cosine will remain constant, $t - x/c$ being constant. Thus the conclusion may be drawn that this term represents a wave travelling in the + x direction with a phase velocity c; in future c will be referred to as the velocity of sound. A similar consideration shows that the second term on the right-hand side of eq.(1-8) represents a wave travelling in the - x direction with the same velocity.
Using eq.(1-1), it follows that

$$u = \frac{\hat{p}_1}{\rho_s c} \cos(\omega t - kx + \phi_1) - \frac{\hat{p}_2}{\rho_s c} \cos(\omega t + kx + \phi_2) \ . \qquad (1\text{-}9)$$

A comparison of eqs (1-8) and (1-9) shows that, for waves travelling in the + x direction ,

$p/u = \rho_s c$,

and for waves, travelling in the - x direction,

$p/u = - \rho_s c$.

The ratio p/u is thus independent of time,position and, but for the change in sign, direction of travel.

The quantity $\rho_s c$, which is characteristic for the medium, is known as the specific acoustic wave impedance of the medium, its dimension being N s m^{-3} or, kg s^{-1} m^{-2}.

1.3 Complex representation

The complex representation of the dependent variables, customary in acoustics when harmonic phenomena are considered , is founded on de Moivre's theorem,

$$\exp(j\psi) = \cos(\psi) + j \sin(\psi) \ , \qquad (1\text{-}10)$$

where $j = \sqrt{-1}$ and ψ is an angle expressed in radians. The representation is introduced by an example; that of a plane, harmonic wave travelling in the + x direction. According to eq.(1-8), the sound pressure due to such a wave is represented by:

$$p = \hat{p} \cos(\omega t - kx + \phi), \qquad (1\text{-}11)$$

where $\hat{p}$ is the peak value of the sound pressure and ϕ is the phase angle.
On referring to eq.(1-10), the following equation,

$$p = \mathrm{Re}\left[\hat{p} \exp(j\omega t - jkx + j\phi)\right], \qquad (1\text{-}12)$$

is seen to be identical with eq.(1-11) since the symbol Re before a function indicates that the real part of that function should be taken. For the future, the symbol Im is introduced. This symbol implies that the imaginary part of the function must be taken. In this book, the convention will apply that the factor j

in the imaginary part of the function is stated explicitly, thus, for any function f,

$f = \mathrm{Re}(f) + j\ \mathrm{Im}(f)$,

and Im(f) itself is real.

The complex pressure amplitude, $\tilde{p}$, of the wave is introduced with the aid of the defining equation

$$\tilde{p} = \frac{1}{\sqrt{2}}\ \hat{p}\ \exp(j\phi), \tag{1-13}$$

and eq.(1-12) thus reduces to

$$p = \sqrt{2}\ \mathrm{Re}\left[\tilde{p}\ \exp(j\omega t - jkx)\right] . \tag{1-14}$$

Eq.(1-14) still represents the real sound pressure dependent on time and place and is identical with eq.(1-11). The complex representation, indicated by $\bar{p}$, is obtained by performing the following operations:

1. omit the factor $\exp(j\omega t)$,
2. omit the operator Re ,
3. omit the factor $\sqrt{2}$.

The result of these operations is:

$$\bar{p} = \tilde{p}\ \exp(-jkx) . \tag{1-15}$$

The first two of the above operations may be considered as short cuts: the real representation of p is obtained simply by re-instating $\exp(j\omega t)$ and Re. The last of the operations has further implications. Thus $|\tilde{p}|$ corresponds to the R M S value rather than to the peak value of p; the function of the modulus bars may be clarified by the following equation: $|a + jb| = \sqrt{(a^2 + b^2)}$. The introduction of the complex R M S quantity $\tilde{p}$ is a concession made to the widespread custom of giving R M S values for alternating quantities and of calibrating instruments in such values. A consequence is, for instance that sound powers, which are proportional to $\frac{1}{2}\hat{p}^2$ in the real representation, are proportional to $|\tilde{p}|^2$ in the complex representation. The problem of R M S against peak value is, however, of little importance for this text, since interest is centred on ratios of alternating quantities.

The derivation of the instantaneous, real value p from the complex representation $\bar{p}$, c.f. eq.(1-15), may be illustrated by a vector diagram in the complex

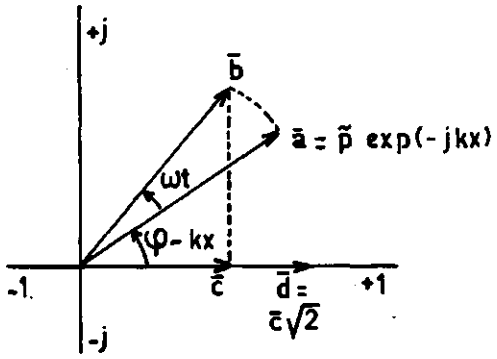

Figure 2 Vectors in the complex plane.

plane (see figure 2).
The complex quantity $\bar{p}$ is entered with the appropriate phase angle (vector $\bar{a}$ in the figure). This vector is rotated over the angle ωt (vector $\bar{b}$). The real part is obtained by projection onto the real axis (vector $\bar{c}$) and the instantaneous value is found by multiplication by a factor $\sqrt{2}$ (vector $\bar{d}$), the length of this latter vector corresponding to the value sought and receiving a negative sign if the vector lies along the - 1 axis.
The main advantage of the complex representation lies in brevity. E.g. differentiation with respect to x is equivalent to multiplication by a factor - jk according to eq.(1-15); for waves travelling in the - x direction the factor is + jk. $\bar{p}$ is formally independent of time; to differentiate with respect to time the factor exp jωt is temporarily re-instated and the differentiation is seen to correspond to multiplication by a factor jω. That these procedures lead to correct results is easily verified by inspection. Thus, in the complex representation:

$$\frac{\partial \bar{p}}{\partial t} = j\omega \tilde{p} \exp(-jkx).$$

Reversing the steps taken while introducing the complex representation, the real representation follows as:

$$\frac{\partial p}{\partial t} = \sqrt{2}\ \mathrm{Re}\ [j\omega \tilde{p} \exp(j\omega t - jkx)]$$

$$= \mathrm{Re}\ [j\omega \hat{p} \exp(j\omega t - jkx + j\phi)]$$

$$= -\ \omega \hat{p} \sin(\omega t - kx + \phi)\ ,$$

precisely the same result as found when differentiating eq.(1-11) with respect to time.
It is no cause for surprise that integration with respect to place and time corresponds to multiplication by factors $-1/jk$, $1/jk$ and $1/j\omega$, respectively, in the complex representation.

Ratios in the complex representation require interpretation. Consider, for instance, a sound pressure p and an associated particle velocity u, given by

$$p = \hat{p} \cos(\omega t + \phi) , \tag{1-16}$$

$$u = \hat{u} \cos(\omega t + \psi) , \tag{1-17}$$

in the real representation. Eqs(1-16) and (1-17) imply that p is advanced in time by a phase angle $\phi - \psi$ with respect to u. The ratio of the peak values of p and u is $\hat{p}/\hat{u}$. Now, in the complex representation:

$$\bar{p} = \tilde{p}, \tag{1-18}$$

$$\bar{u} = \tilde{u}, \tag{1-19}$$

where $\tilde{p} = \frac{1}{\sqrt{2}} \hat{p} \exp(j\phi)$; $\tilde{u} = \frac{1}{\sqrt{2}} \hat{u} \exp(j\psi)$. In this representation

$\bar{p}/\bar{u} = \tilde{p}/\tilde{u} = (\hat{p}/\hat{u})\exp(j\phi - j\psi)$.

One notes from the above equation that $|\tilde{p}/\tilde{u}|$ equals $\hat{p}/\hat{u}$ and that the phase angle of $\tilde{p}/\tilde{u}$, $\phi - \psi$, corresponds to the positive phase shift of p in relation to u.

A weak point in the complex representation is that products of quantities in this representation are meaningless. To obtain significant results, artifices have to be introduced, which detract from the elegance of the representation. This problem is illustrated by the concept of sound intensity.

In a plane wave, including the case of two waves travelling in opposite directions, the instantaneous value of the power transmitted in the selected positive direction per unit of cross-sectional area may be seen to be $p \cdot u$, in the real representation. As a rule, the sound intensity I, the time average of the sound power transmitted per unit area, is the quantity of major interest. For harmonic waves p and u may be introduced from eqs(1-16) and (1-17) and the time average is readily obtained:

$$I = \lim_{T \to \infty} \frac{1}{T} \int_0^T \hat{p}\hat{u} \cos(\omega t + \phi)\cos(\omega t + \psi)\,dt$$

$$= \lim_{T \to \infty} \frac{\hat{p}\hat{u}}{2T} \left[T \cos(\phi - \psi) + \frac{1}{2\omega} \sin(2\omega t + \phi + \psi)\right]_0^T$$

$$= \tfrac{1}{2}\, \hat{p}\hat{u} \cos(\phi - \psi). \qquad (1\text{-}20)$$

The validity of eq.(1-20) is confined to plane harmonic waves. In travelling waves, p and u are in phase and have a constant ratio for their peak values, as was discussed in section 1.2, c.f. eqs(1-8) and (1-9). Thus, for a wave travelling in the + x direction , the intensity is given by:

$$I_1 = \tfrac{1}{2}\, \hat{p}_1^2/(\rho_s c)\ , \qquad (1\text{-}21a)$$

and for one travelling in the - x direction by

$$I_2 = -\tfrac{1}{2}\, \hat{p}_2^2/(\rho_s c)\ , \qquad (1\text{-}21b)$$

the negative sign in eq.(1-21b) indicating that power is transmitted in the - x direction. The net power for two waves travelling in opposite directions, transmitted per unit area, the net intensity, is given by

$I = I_1 + I_2$,

the sum of the intensities of the two constituent travelling waves. That intensities may thus be added follows when p and u are introduced from eqs(1-8) and (1-9) and the time average of the product is determined. It should be noted however, that the summation of intensities leads to incorrect results for waves travelling in the same direction.

The hope that the quantity $\tilde{p}\cdot\tilde{u}$ (c.f. eqs(1-18) and (1-19))might be significant in determining the (net) intensity I is not realized.
The correct equation turns out to be either

$$I = \mathrm{Re}(\tilde{p}^{*}\cdot\tilde{u})\ , \qquad (1\text{-}22a)$$

$$\text{or } I = \mathrm{Re}(\tilde{p}\cdot\tilde{u}^{*})\ , \qquad (1\text{-}22b)$$

both of these equations proving to be identical with eq.(1-20) on introducing $\tilde{p}$ and $\tilde{u}$ from eqs(1-18) and (1-19) and taking into account that $\tilde{p}^{*}$ and $\tilde{u}^{*}$ are

the complex conjugates of $\tilde{p}$ and $\tilde{u}$, respectively, having the signs of their imaginary parts reversed. The introduction of the operator Re and the complex conjugate of one of the dependent variables in eqs(1-22a), (1-22b) are the artifices referred to earlier.

The concept of and the equations for sound intensity, discussed above, are limited to plane harmonic waves. Extension of the concept to other sound fields is beyond the scope of this book.

In future complex representation will be used almost exclusively. Departures from this representation will become clear from the context. Under these circumstances, the retention of the vector bars indicating complex representation of the dependent variables, as in $\bar{p}$ and $\bar{u}$, is unnecessary and these bars will thus be omitted.

1.4 Interferometry

The interferometer was introduced briefly in section 1.1. The present section will be devoted to the formal description of the sound field in the tube in its relation to the acoustical properties of the sample surface. Essentially, the sound field is represented by eqs(1-8) and (1-9). The notation will be altered slightly here, the incident wave being designated by p_i (travelling towards the sample) and the reflected wave by p_r. Moreover complex notation will be used. There are complications, however. In deriving the wave equation (c.f. section 1.2), perturbations in the sound field due to the proximity of the tube walls were alluded to. The principal effects are heat exchange between the medium and the tube walls and viscous friction of the medium along those walls. These effects are confined to the thermal and viscous boundary layers respectively and in a well designed interferometer the thicknesses of these layers are small in relation to the transverse dimensions of the tube. The influence on wave propagation is thus slight but, unfortunately not entirely negligible.

Sound power is dissipated in the boundary layers and this results in attenuation of travelling waves. In section 3.8 and 3.10 this attenuation is investigated in detail. For the present purpose it may be accounted for by the addition of an attenuation factor $\exp(-\alpha_0 x)$ for waves travelling in the +x-direction and a factor $\exp(+\alpha_0 x)$ for waves travelling in the reverse direction. The "attenuation constant", α_0, may be derived theoretically, assuming a smooth tube. In practice, tubes are not perfectly smooth and α_0 must be determined experimentally. The values thus obtained exceed the theoretical ones by factors typically of the order 1.5 to 2.

Following the same procedure as in the discussion of eqs(1-8) and (1-9), the sound field in the tube is considered to be composed of two travelling waves, an incident and a reflected wave, described by:
the sound pressure of the incident wave,

$$p_i = \tilde{p}_i \exp(-\alpha_0 x - jkx) \ , \tag{1-23a}$$

and its accompanying particle velocity,

$$u_i = \tilde{u}_i \exp(-\alpha_o x - jkx), \tag{1-23b}$$

their interrelation being given by:

$$p_i = \rho_s c \, u_i \ , \tag{1-23c}$$

the sound pressure of the reflected wave,

$$p_r = \tilde{p}_r \exp(+\alpha_0 x + jkx), \tag{1-24a}$$

and its accompanying particle velocity,

$$u_r = \tilde{u}_r \exp(+\alpha_0 x + jkx), \tag{1-24b}$$

their interrelation being given by:

$$p_r = - \rho_s c \, u_r . \tag{1-24c}$$

The total sound pressure now results as:

$$p = p_i + p_r, \tag{1-25a}$$

and the total particle velocity as:

$$u = u_i + u_r, \tag{1-25b}$$

and therefore (c.f. eqs(1-23c) and (1-24c)):

$$\rho_s c \, u = p_i - p_r . \tag{1-25c}$$

Properly speaking, these equations no longer satisfy eqs(1-1), (1-2) and (1-6). The quantities ρ_s and K, introduced in these latter equations for free waves, cannot be retained for plane waves constricted by tubes, a point discussed extensively in chapter 3. The error introduced by the retention of k in eqs (1-23a), (1-23b), (1-24a) and (1-24b) is quite negligible. The error in the factor $\rho_s c$, appearing in eqs(1-23c), (1-24c) is somewhat larger, but still insignificant when compared to the other errors to which interferometry is heir.

For an arbitrary (normal) cross-section of the interferometer tube, three additional quantities are defined. The first is the pressure reflection coefficient r:

$$r = p_r/p_i, \tag{1-26}$$

r is often referred to, briefly but ambiguously, as the reflection coefficient, and is essentially a complex quantity. Next, the specific acoustic impedance is defined as:

$$Z = p/u, \tag{1-27}$$

and finally the normalized specific acoustic impedance ζ is defined as:

$$\zeta = \xi + j\eta = Z/\rho_s c = p/\rho_s cu, \tag{1-28}$$

where ξ and η are the real and imaginary parts or the resistive and reactive parts of ζ respectively.
Referring to eqs(1-25a), (1-25c), it follows from eq.(1-28) that:
$\zeta = (p_i + p_r)/(p_i - p_r)$,
and thus that:

$$\zeta = (1+r)/(1-r), \tag{1-29a}$$

and conversely that

$$r = (\zeta-1)/(\zeta+1). \tag{1-29b}$$

Unless specifically stated otherwise, r, ζ and Z will in future apply to the plane x = 0, the sample surface. These quantities are interrelated and characteristic for the acoustical properties of the sample. Specifically, ζ is to be

considered as the most representative of these quantities and its determination is the aim of interferometry.

The sample surface imposes a boundary condition on the sound field in the tube at x = 0. A practical form for this condition is:

$$\tilde{p}_r = r \cdot \tilde{p}_i = |r| \exp(j\phi) \cdot \tilde{p}_i, \tag{1-30}$$

where $|r|$ and ϕ are the modulus and the phase angle of the reflection coefficient respectively . From eqs(1-23a), (1-25a) and (1-30) it now follows that

$$|p|^2 = |\tilde{p}_i|^2 \Big| \exp(-\alpha_o x)\cos(kx) + |r| \exp(\alpha_o x)\cos(kx+\phi)$$

$$- j \exp(-\alpha_o x)\sin(kx) + j|r|\exp(\alpha_o x)\sin(kx+\phi) \Big|^2$$

$$= |\tilde{p}_i|^2 \left[\exp(-2\alpha_o x) + |r|^2 \exp(2\alpha_o x) + 2|r|\cos(2kx+\phi)\right]. \tag{1-31}$$

Eq.(1-31) constitutes the foundation on which interferometry rests, as it opens the possibility of obtaining $|r|$ and ϕ from sound pressure measurements, and thus of determining the normalized specific acoustic impedance of the sample surface, using eq.(1-29a).
The first two terms of the right hand side of eq.(1-31) vary slowly and slightly with x, whereas the last term varies more rapidly between $-2|r|$ and $+2|r|$. It follows from this relationship between $|p|^2$ and x that there must be positions where the pressure amplitude $|p|$ will be minimum and maximum, respectively. Only the last term can become negative. Because the assumption $|\alpha_o x| \ll 1$ is justified under practical conditions, $\exp(\pm 2\alpha_o x)$ equals unity in zero-order approximation and $1 \pm 2\alpha_o x$ in first-order approximation. The position of the minima is derived from the zero-order approximation, the co-ordinate x_{min} following from

$$2 k x_{min} + \phi = \pi + 2 n \pi \quad (n = 0, +1, +2, \ldots\ldots). \tag{1-32}$$

Using eq.(1-32) ϕ follows from the positions of the minima but for an arbitrary angle of $2n\pi$ radians. The fact that ϕ is multi-valued is insignificant, as $\exp j\phi$ is not. The ambiguity in ϕ may thus be removed without loss of generality by requiring:

$$-\pi \leqslant \phi \leqslant \pi . \tag{1-33}$$

ϕ is determined from the measured position of the minima, in preference to those of the maxima, as the minima are the sharper of the two (see figure 3a). The movable microphone used in the measurement is one of the type having an acoustic centre or pressure-sensitive point, i.e. the output e.m.f. is proportional to the sound pressure at one point. The position of the acoustic centre in relation to the microphone often depends on frequency and must be determined by acoustic measurement. This calibration of the microphone is incorporated in the procedure described below.

Microphone position is measured on a scale having an increasing reading for displacement away from the sample towards the loudspeaker. Note that this is the - x direction. The reading for the first minimum, i.e. the minimum nearest the sample, is l_{min1} and thus

$$x_{min1} = - l_{min1} + l_{cor} ,$$

where x_{min1} is the value of x for the first minimum and l_{cor} is an unknown, possibly frequency-dependent, length incorporating such effects as displacement of the scale zero in relation to the sample surface and shift of the acoustic centre.

The sample is now replaced by a rigid plate, and the position of the first minimum is read from the scale: l'_{min1}. Now for such a plate $\phi = 0$ and the value for x for the first minimum is thus known from eq.(1-32):

$$x'_{min1} = - \frac{\pi}{2k} .$$

Now l_{cor} may be found:

$$l_{cor} = l'_{min1} - \frac{\pi}{2k} ;$$

and using this value it follows that

$$\phi = 4\pi (l_{min1} - l'_{min1})/\lambda, \qquad (1-34)$$

where λ is the wavelength and the range for ϕ is in accordance with requirement (1-33).

Although consideration of the first minimum suffices in principle, further minima have often to be evaluated as the sound field may be distorted near the sample surface through the inhomogeneity of the sample.

For the sound pressures in the minima and the maxima, respectively, it now follows from eq.(1-31) that

$$|p|_{min} = |\tilde{p}_i| \cdot [\exp(-\alpha_o x_{min}) - |r| \exp(+\alpha_o x_{min})],$$

and

$$|p|_{max} = |\tilde{p}_i| \cdot [\exp(-\alpha_o x_{max}) + |r| \exp(+\alpha_o x_{max})]. \qquad (1\text{-}35)$$

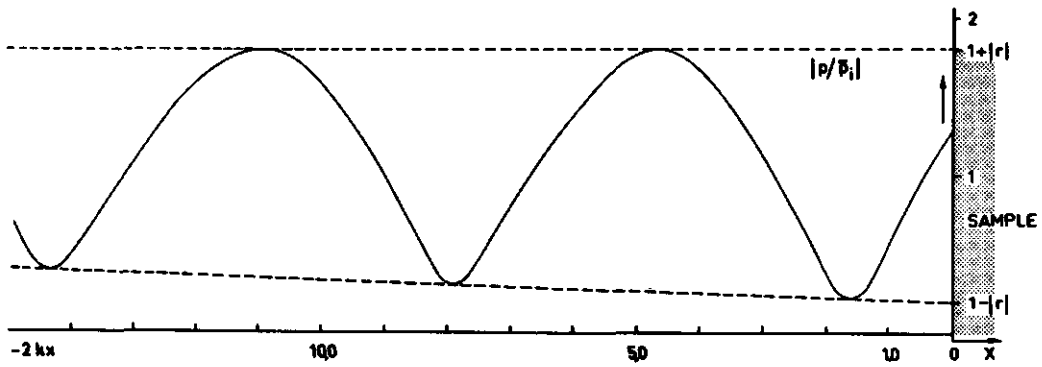

Figure 3a The "distribution" pattern of the sound pressure in an interferometer tube

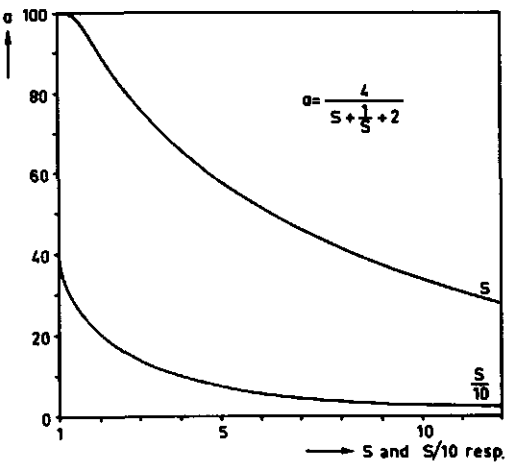

Figure 3b Relationship between standing wave ratio and absorption coefficient

Since in first-order approximation $|\alpha_o x| \ll 1$, it can now be written that

$$|p|_{min} = |\tilde{p}_i| . \left[1-|r|-(1+|r|)\alpha_o x_{min}\right]$$

and

$$|p|_{max} = |\tilde{p}_i| . \left[1+|r|-(1-|r|).\alpha_o x_{max}\right]. \qquad (1\text{-}36)$$

In figure 3a, $|p|$ is shown schematically as a function of x. Consider $|p|_{min}$ as a linear function of x (c.f. eq.(1-36). α_o may be eliminated by extrapolating $|p|_{min}$ to x = 0, the extrapolated value equalling $(1-|r|).|\tilde{p}_i|$. $|p|_{max}$ depends on x to a lesser degree; extrapolation is unnecessary, and $|p|_{max} = (1+|r|)\,|\tilde{p}_i|$ with sufficient accuracy.

The standing wave ratio s (dimensionless) is defined as the ratio of the maximum sound pressure and that of the minimum sound pressure. In a loss free tube, s is a fixed quantity. For a tube with attenuation, where the minima differ measurably in magnitude, one defines, unless specifically stated otherwise, the the standing-wave ratio as the ratio of the maximum pressure and the minimum pressure, both extrapolated to the sample surface:

$$s = \left[\frac{|p|_{max}}{|p|_{min}}\right]_{x=0} = \frac{1+|r|}{1-|r|} \qquad (1\text{-}37)$$

so that

$$|r| = \frac{s-1}{s+1} . \qquad (1\text{-}37a)$$

The absorption coefficient a of the sample surface (dimensionless) is defined as the ratio of the absorbed sound power to the incident power.
According to eqs(1-21a) and (1-21b) the incident and reflected powers are proportional to $|\tilde{p}_i|^2$ en $|\tilde{p}_r|^2$, respectively. The absorbed power is thus proportional to $|\tilde{p}_i|^2 - |\tilde{p}_r|^2$ and, using eq.(1-26) it follows that (see also V 1020-26)

$$a = 1-|r|^2 = \frac{4}{s+1/s+2} \qquad (1\text{-}38)$$

The number of maxima and minima that can be detected depends on the length of the interferometer tube. In an interferometer of a length of 1.5 meter, e.g., only one minimum is found below about 200 Hz. Extrapolation of $|p|_{min}$ to the site x = 0 is then no longer possible. Nevertheless $|r|$ at x = 0 can be determined in the following way. Instead of extrapolating s to x = 0 and converting s there into $|r|$ with eq.(1-37) one can convert s at the minimum into $|r|$ at the minimum with eq.(1-37) and extrapolate $|r|$ to x = 0 with the equation:

$$|r|_{min} = |r|_{x=0} \exp(2\alpha_0 x_{min}). \qquad (1\text{-}39)$$

One needs then to know, however, α_0. Since this is not the case one has to carry out an extra experiment, viz. after replacing the sample by a rigid, massive non-absorbing plate. In this case $|r|_{x=0} = 1$, so that

$$|r'|_{min} = \exp(2\alpha_0 x'_{min}). \qquad (1\text{-}40)$$

$|r'|$ and x' are measured and α_0 can be calculated.

At very low frequencies, no maximum is available within the finite length of the tube. However, in that case and for the sample used, sound pressure at the sample surface is practically maximum. Thus an approximate value for the standing-wave ratio may be found by introducing the sound pressure at the sample surface as the maximum value.

Under these conditions, - only one minimum available - the wavelength cannot be measured and accurate determination of the phase angle is impossible. A value for this latter quantity is then estimated by extrapolation from measurements at higher frequencies.
Summarizing one may state that the analysis of the standing wave pattern consists of determining the positions of the minima and the magnitudes of the sound pressures at maxima and minima.

Under these conditions - only one minimum available - the wavelength cannot be surface (which is usually the obvious plane of reference) as a function of frequency. From this function conclusions may be drawn about the acoustical properties of the sample material.

1.5 The velocity of sound in a mixture of ideal gases

Before a discussion of the velocity of sound in porous materials, some remarks will be made on the velocity of sound in air. In particular, attention will be paid to possible changes in velocity through changes in experimental conditions. The velocity can be calculated from the kinetic gas theory. Hardy, Telfair and Pielemeier (1941) made extensive investigations on the velocity of sound in gases of various composition and under various pressures. Starting from eq.(1-7) for the velocity of sound the question stated above can be formulated as follows. What are the values for κ and ρ_s for a mixture of gases with known partial pressures? To answer this question the following quantities are introduced

f_k = the mass fraction of component k	-
p_k = the partial pressure of component k	Nm^{-2}
R = the gas constant per kmol	$J^0K^{-1}kmol^{-1}$
M_k = the molar mass of component k	$kg\ kmol^{-1}$
T = the absolute temperature (identical for all components)	^0K
V = the total volume of 1 kg of the gas mixture (identical for all components)	m^3kg^{-1}
c_{Vk} = the molar specific heat of component k at constant volume	$J^0K^{-1}kmol^{-1}$
c_{pk} = the molar specific heat of component k at constant pressure	$J^0K^{-1}kmol^{-1}$
S_k = the entropy of component k	$J^0K^{-1}kg$
p_s = the total pressure of the gas mixture	Nm^{-2}
S = the total entropy of 1 kg of the gas mixture	$J^0K^{-1}kg^{-1}$

Assuming Dalton's law to hold the equation of state for component k in 1 kg of the mixture is:

$$p_k V = \frac{f_k}{M_k} RT. \tag{1-41}$$

For component k in 1 kg of the gas mixture the first law of thermodynamics yields

$$TdS_k = \frac{f_k}{M_k} c_{Vk} dT + p_k dV \ . \qquad (1\text{-}42)$$

Since

$$p_s = \Sigma_k p_k \text{ and } S = \Sigma_k S_k \ ,$$

$$TdS = dT\Sigma_k \frac{f_k}{M_k} c_{Vk} + p_s dV \ . \qquad (1\text{-}43)$$

Assuming isentropic change of state TdS is zero. Summation of eq.(1-41) over k and differentiation of the result obtained, yields

$$p_s dV + V dp = RdT\Sigma_k (f_k/M_k). \qquad (1\text{-}44)$$

Eliminating dT between (1-43) and (1-44) results in

$$\frac{dp}{p_s} + \left[1 + \frac{R\Sigma\ (f_k/M_k)}{\Sigma f_k c_{Vk}/M_k} \right] \frac{dV}{V} = 0 \ .$$

Integration of this equation gives $p_s V^{\kappa}$ = constant or

$$\kappa = 1 + \frac{R\Sigma f_k/M_k}{\Sigma f_k c_{Vk}/M_k}$$

$$= 1 + \frac{R\Sigma p_k}{\Sigma c_{Vk} p_k} = 1 + \frac{Rp_s}{\Sigma c_{Vk} p_k} \ .$$

When the number of degrees of freedom of a molecule of the component k is equal to h_k it follows from the kinetic gas theory that $c_{Vk} = \frac{1}{2} h_k R$, and so

$$\kappa = 1 + \frac{2}{\Sigma h_k p_k / p_s} \ . \qquad (1\text{-}45)$$

Since $\Sigma f_k = 1$ and $\frac{1}{V} = \rho_s$, summation of eq.(1-27) gives:

$$\rho_s = \frac{1}{RT} \Sigma p_k M_k \qquad (1\text{-}46)$$

Introduction of K and ρ_s from eqs(1-45) and (1-46) into the equation for the velocity of sound gives

$$c^2 = RT \left[1 + \frac{2}{\Sigma\, h_k p_k/p} \right] \cdot \left[\frac{1}{\Sigma\, M_k p_k/p} \right] . \qquad (1\text{-}47)$$

Some conclusions can be drawn from this equation. It appears that velocity is independent of barometric pressure, and that it varies with the square root of absolute temperature. The relevant physical constants for a number of gases are listed in table 1. To the quantities introduced previously, two new ones have been added: the dynamic coefficient of viscosity η and the thermal conductivity λ of the gases. It should be noted however that no allowance was made for either thermal or viscous losses in deriving eq.(1-47). The values given are valid for a pressure of 1 atmosphere.

Table 1. Some physical constants of a number of gases.

quantity	unit	O_2	N_2	H_2O	CO_2	dry air
eq.mass	kg kmol^{-1}	32	28	18	44	28.8
c_v	Jkg^{-1} ^{0}K^{-1}	661	740	-	639	715
c_p	Jkg^{-1} ^{0}K^{-1}	913	1038	2018(100°C)	833	1004(15°C)
c_p/c_v	-	1.401	1.404	-	1.304	1.403
c	m s^{-1}	316	334	401	259	331(0°C)
$\eta \cdot 10^5$	Nm^{-2}s	2.00	1.76	0.96	1.42	1.80
λ	Wm^{-1} ^{0}K^{-1}	0.0233	0.0228	-	0.0137	0.023
ρ_s	kg m^{-3}	1.43	1.25	0.81	1.98	1.29(0°C)

The most important practical conclusions to be drawn is that at wide variations in air composition, the velocity of sound hardly varies. Proof of this will be given in a calculation of the ratio of the velocity in dry air (= c_d) to that in moist air (= c_h). The partial pressures of the three gases are represented as p_{O_2}, p_{N_2} and p_{H_2O}; the molecular weights as M_{O_2}, M_{N_2} and M_{H_2O}, and the degrees of freedom as h_{O_2}, h_{N_2} and h_{H_2O}, respectively.

Introducing $h_{O_2} = h_{N_2} = h$, $p_{O_2}/p_{N_2} = g$ and $p_{H_2O}/p_s = r$, and using eq.(1-47) one finds:

$$\frac{c_d^2}{c_n^2} = \frac{1 + (h_{H_2O}/h - 1).r}{1 + (h_{H_2O} - h).r/(2+h)} \cdot \left[1 - \left(1 - \frac{(1+g)M_{H_2O}}{M_{N_2} + gM_{O_2}}\right).r \right] \qquad (1\text{-}48a)$$

As r is a small quantity at room temperature, eq.(1-48a) may be approximated as

$$\frac{c_d}{c_n} \approx 1 - \tfrac{1}{2}.r.\left[1 - \frac{(1+g)M_{H_2O}}{M_{N_2} + gM_{O_2}} - \frac{2.(h_{H_2O}-h)}{h.(2+h)} \right]. \qquad (1\text{-}48b)$$

For air, at a relative humidity of 100%, a temperature of 20°C and a pressure of 76 cm Hg,

$p_{H_2O}/p_s = 0.023$.

Substituting $g = 1/4$, $h_{N_2} = h_{O_2} = 5$, $h_{H_2O} = 6$, $M_{N_2} = 28$, $M_{O_2} = 32$ and $M_{H_2O} = 18$ into eq.(1-48b) yields : $c_d/c_h = 0.9963$.

Hence, the conclusion can be drawn that the velocity of sound is barely affected by the pressure of water vapour in air. This conclusion will also apply for changes in CO_2 pressure of the same order as those in pressure of water vapour. Furthermore, one may infer from eq.(1-47) that a 2° increase in temperature at room temperature affects the velocity of sound to the same extent as does saturating dry air with water vapour. The effect of variations in the composition of the gas on sound velocity is slightly greater than the effect of variations in the temperature of the gas under practical circumstances. However both have little influence. Thus, for the present purpose, conversions to normal pressure and/or temperature are unnecessary. It can also be inferred from the data of table 1 that the product $\rho_s c$ does depend on gas pressure and it might be argued that a correction for this effect should be introduced. This effect may cause variations of the order of 1%. As shown in Chapter 2 the accuracy of the measurements is of the same order so neither corrections will be made for variations in barometric pressure.

1.6 Intensity, decibel, damping in air

The concept of sound intensity was introduced in section 1-3. Intensities are often expressed on a logarithmic scale; the intensity level L_I is then defined by

$$L_I = 10 \log (I/I_o), \tag{1-49}$$

where I_o is the reference intensity, standardized at 10^{-12} W/m^2.
L_I is given in decibels, abbreviated to dB, and the reference quantity should always be given, e.g. in parenthesis, behind this unit; L_I is thus given in dB(10^{-12} W/m^2).
One of the advantages of the introduction of the decibel scale is that the numerically wide range of intensities encountered in acoustical practice, e.g. from 10^{-12} W/m^2 to 1 W/m^2, is considerably reduced on the intensity level scale, from 0 dB(10^{-12} W/m^2) to 120 dB(10^{-12} W/m^2).

The difference in intensity level ΔL_I for two intensities, I_1 and I_2, now follows as

$$\Delta L_I = 10 \log(I_1/I_2), \tag{1-50}$$

where ΔL_I is expressed in dB, the reference quantity being omitted as being arbitrary for level differences.
For sound pressures too, a logarithmic scale has been defined, the sound pressure level L_p. For a sound pressure having an RMS value p_e

$$L_p = 20 \log(p_e/p_o),$$

where p_o is the reference pressure, standardized at $2 \cdot 10^{-5}$ N/m^2. L_p is expressed in dB($2 \cdot 10^{-5}$ N/m^2). p_o has been so selected, that for a plane wave travelling in air, $L_I = L_p$ with an accuracy that is usually adequate. To gain some insight into the magnitudes of the quantities introduced it is noteworthy that the threshold of hearing at 1000 Hz is roughly 0 dB($2 \cdot 10^{-5}$ N/m^2) and that a sound pressure level of 130 dB ($2 \cdot 10^{-5}$ N/m^2) is experienced as painful. That sound pressures are relatively small may be concluded from the fact that $p_o \approx 2 \cdot 10^{-10}$ atmosphere. In section 1.5, it was shown that in air the velocity of sound is hardly affected by the composition of the gas mixture. Besides damping in the interferometer tube through losses along the walls, a slight damping occurs in the air itself. This damping can be ascribed to several causes:
1. A viscous damping of the free wave exists due to diffusion of impulse.

2. Thermal losses occur in the free wave due to diffusion of kinetic energy.
3. Over and above these above mentioned causes, which constitute portions of the "classical damping", a molecular damping occurs through the "long" relaxation time of a rotational level of the oxygen molecules.
This relaxation time is strongly dependent on the content of water vapour.
Reference is made to the work of Kneser (1931) and Harris (1963).
It appears from this investigation that for the present purpose this damping will be unimportant. No further attention will therefore be paid to it.

1.7 Velocities in air

To avoid possible confusion, the various velocities obtaining in gases will be commented on briefly. Air, considered as an ideal diatomic gas having a molecular mass M = 29, will serve as illustration, the approximation involved being acceptable for the present purpose.
The following velocities are distinguished.
1. The thermal velocity of the molecules, represented by its RMS value V_e. The average required may be taken in time for one molecule or over an ensemble of molecules, the results being identical as the system is ergodic.
2. The particle velocity u of the molecules. This is the drift velocity due to a sound field, the average velocity vector of the molecules in a domain that contains a large number of molecules, but is small in relation to wavelength. For such a domain the average thermal velocity vector approaches zero.
3. The velocity of propagation of a sound wave or the velocity of sound, c.

The kinetic theory of gases states that the average energy per degree of freedom and per molecule equals $\frac{1}{2}k_B T$, where k_B is Boltzmann's constant and T is the absolute temperature. The kinetic energy of translation of a molecule is thus given by $\frac{3}{2}k_B T$, as it corresponds to three degrees of freedom. This energy is also given by $\frac{1}{2}M \cdot \mu \cdot V_e^2$, where M is the molecular mass of the molecule and μ is the unit of atomic mass (roughly that of a hydrogen atom). Thus

$$V_e = \sqrt{(3k_B T/\mu M)}. \qquad (1\text{-}51)$$

Introduction of the numerical values $k_B = 1.38 \cdot 10^{-23}$ J^oK^{-1}, $T = 293$ ^oK, $M = 29$, $\mu = 1.66 \cdot 10^{-27}$ kg, into eq.(1-51) yields the numerical value for air at room temperature of $V_e = 502$ m s^{-1}. The particle velocity due to a sound field is essentially much smaller. For a plane wave having a sound pressure level

of 70 dB($2 \cdot 10^{-5}$ N m^{-2}), i.e. having an RMS sound pressure of $6.3 \cdot 10^{-2}$ N m^{-2}, the RMS particle velocity is found, making use of the numerical value of the specific acoustic wave impedance (see section 1.2), $\rho_s c$ = 420 Ns m^{-3}; $|\tilde{u}|$ = $1.5 \cdot 10^{-4}$ m s^{-1}.

The velocity of sound is closely related to the thermal velocity of the molecules. Appealing to simple kinetic gas theory once again and using eq.(1-7), it follows that

$$c = V_e \sqrt{(\kappa/3)}.$$

Introduction of V_e = 502 m/s and κ = 1.4 yields approximately c = 340 m/s, in agreement with experiment.

1.8 The heat generated

It is reasonable to think that heat dissipation as a result of absorption of sound energy will give rise to a measurable increase in temperature.

To take an example, a sound pressure level for the incident wave in the interferometer of 70 dB ($2 \cdot 10^{-5}$ N/m^2), thermal power developed in the sample per unit area will be less than 10^{-5} W m^{-2}.

For comparison, the radiation energy reaching the earth from the sun is approximately 1000 W m^{-2}. The resulting rise in temperature will be at the most a few tenths of degrees. Thus it will be clear that the heat developed in an absorbing material by a sound wave will not give rise to a measurable temperature increase. For this reason no evaporation or temperature gradient will occur in the sample when sound absorption is measured. Hence, water will not be displaced by convective currents.

1.9 Sound waves in porous media

For a free wave, the pressure gradient in the gaseous medium is governed by the inertia of that medium. In a porous material, however, consisting of interconnected, gas-filled pores enclosed in a rigid solid frame, sound waves propagating in the pores will encounter higher forces of inertia as the gas is accelerated through narrow vents and viscous friction will have to be overcome. Considered in time the viscous drag will give rise to a component in the pressure gradient in phase with the particle velocity while the forces of inertia correspond to a component at right angles to that gradient (this latter component performs no work on the medium). Thus the resultant complex pressure

gradient is no longer at right angles to the particle velocity, which may be accounted for by restating eq.(1-1) for harmonic waves:

$$-\frac{\partial p}{\partial x} = Z_m u, \tag{1-52}$$

where p is the actual sound pressure in the pores but u is the volume velocity of the gas per unit area (the actual particle velocity in the pores will be higher). The complex, frequency-dependent factor Z_m will be called the specific acoustic series impedance per unit length; its dimension is Nsm^{-4}.
The compressibility of the gas in the pores differs from that for a free wave, part of the available space being occupied by the solid frame and heat exchange taking place between the gas and the frame. As the exchange of thermal energy takes time, the relative compression of the medium and the sound pressure are no longer in phase. Indeed a small ellipse is traversed in the pV diagram. This results in a change in the difference of the phase between the complex velocity gradient and the complex sound pressure, now being less than $\pi/2$. In free air this last value will be found. The change may be accounted for by restating eq. (1-2) for harmonic waves

$$-\frac{\partial u}{\partial x} = Y_m p, \tag{1-53}$$

where the complex, frequency-dependent factor Y_m is called the specific acoustic parallel admittance per unit length ; its dimension is $N^{-1}s^{-1}m^2$.

Acoustically the material is characterized completely by the complex frequency-dependent factors Z_m and Y_m. The central problem of this text are the experimental determination of these factors and their relationship to the structure of the material, which will be discussed in detail in chapter 3.
For the time being, Z_m and Y_m are introduced formally and, as in section 1.2, u is here eliminated from eqs(1-52) and (1-53) yielding

$$\frac{\partial^2 p}{\partial x^2} = Z_m \cdot Y_m p,$$

an equation of the Helmholtz type, as explicit differentiation to time is absent.
Travelling waves in porous materials will undergo attenuation. Following a course suggested by eqs(1-23a) ... (1-25c), derived for waves, attenuated in

interferometers, a complex propagation constant is introduced,

$$\gamma_m = \alpha_m + j\beta_m,$$

and a solution of the form

$$p = \tilde{p}_i \exp(-\gamma_m x) + \tilde{p}_r \exp(\gamma_m x),$$

is essayed. It satisfies the Helmholtz equation if

$$\gamma_m = \sqrt{(Z_m \cdot Y_m)}. \qquad (1\text{-}54)$$

Using eqs(1-52) and (1-54), the solution for u follows

$$u = \frac{\tilde{p}_i}{W_m} \exp(-\gamma_m x) - \frac{\tilde{p}_r}{W_m} \exp(\gamma_m x),$$

where the specific acoustic wave impedance of the material, W_m, is given by

$$W_m = \sqrt{(Z_m / Y_m)}. \qquad (1\text{-}55)$$

It will be clear from eqs(1-54) and (1-55) that the material is also specified acoustically by the pair of complex quantities γ_m and W_m.

Now consider a sample of porous material fitted to the end of an interferometer tube in a sample holder. The interface between the air column in the tube and the sample material is at x = 0. Note that the quantities p and u in the material have been so defined that they are continuous with the quantities p and u in the tube at the interface.
Supposing the sample to have a rigid backing at x = 1, in practice a thick metal plate (see section 2.5), the boundary condition there is u = 0 and thus $\tilde{p}_r / \tilde{p}_i = \exp(-2\gamma_m 1)$. Introduction of this quantity and of x = 0 into the equations for p and u yields the values for these latter two at the sample surface

$$p = \tilde{p}_i \left[1 + \exp(-2\gamma_m 1)\right]$$

$$u = \tilde{p}_i \left[1 - \exp(-2\gamma_m 1)\right] / W_m \,.$$

The specific acoustic impedance at the sample surface now follows from its definition, eq.(1-27) as

$$Z = W_m \coth(\gamma_m l), \tag{1-56}$$

the fundamental relationship between the measurable quantity Z and the material constants W_m and γ_m.
In principle, this type of derivations may be extended to stratified samples, consisting of layers of porous materials with various acoustical properties (Kosten, 1953).
Before going into the problems raised by the transcendental nature of eq.(1-56), the derivation of Z, or rather of the closely related quantity ζ, c.f. eq.(1-28), from the quantities which follow more directly from measurement, as $|r|$ and ϕ, and forms of graphical representation for ζ will be discussed.

1.10 Presentation of the normalized specific acoustic impedance

The measurements in the interferometer tube lead directly to numerical values for l_{min} and s from which by simple computation ϕ and $|r|$ can be derived with the aid of eq.(1-32) and eq.(1-38) respectively. ϕ and $|r|$ determine the complex reflection coefficient r, from which the normalized specific acoustic impedance of the sample can be found by using the equation

$$\zeta = \frac{1+r}{1-r} = \frac{2s + j(s^2-1)\sin\phi}{s^2 + 1 - (s^2-1)\cos\phi}. \tag{1-29a}$$

This computation of ζ via s and ϕ is time consuming. To avoid this difficulty some handy tools have been developed. One can transform the complex r plane into a complex ζ plane or vice versa, which enables one to read the complex value ζ for a given complex value of r or in the reverse sense if desired. This transformation from r to ζ is a conformal transformation. In such a transformation a circle in one plane corresponds to a circle in the transformed plane; angles between lines in both planes remain unchanged. Two of these types of transformations, that are in practical use will be considered now.

A The impedance diagram
This diagram is the transformation of the complex r-plane into the complex ζ-plane (see figure 4). Any point in this diagram represents a value of the

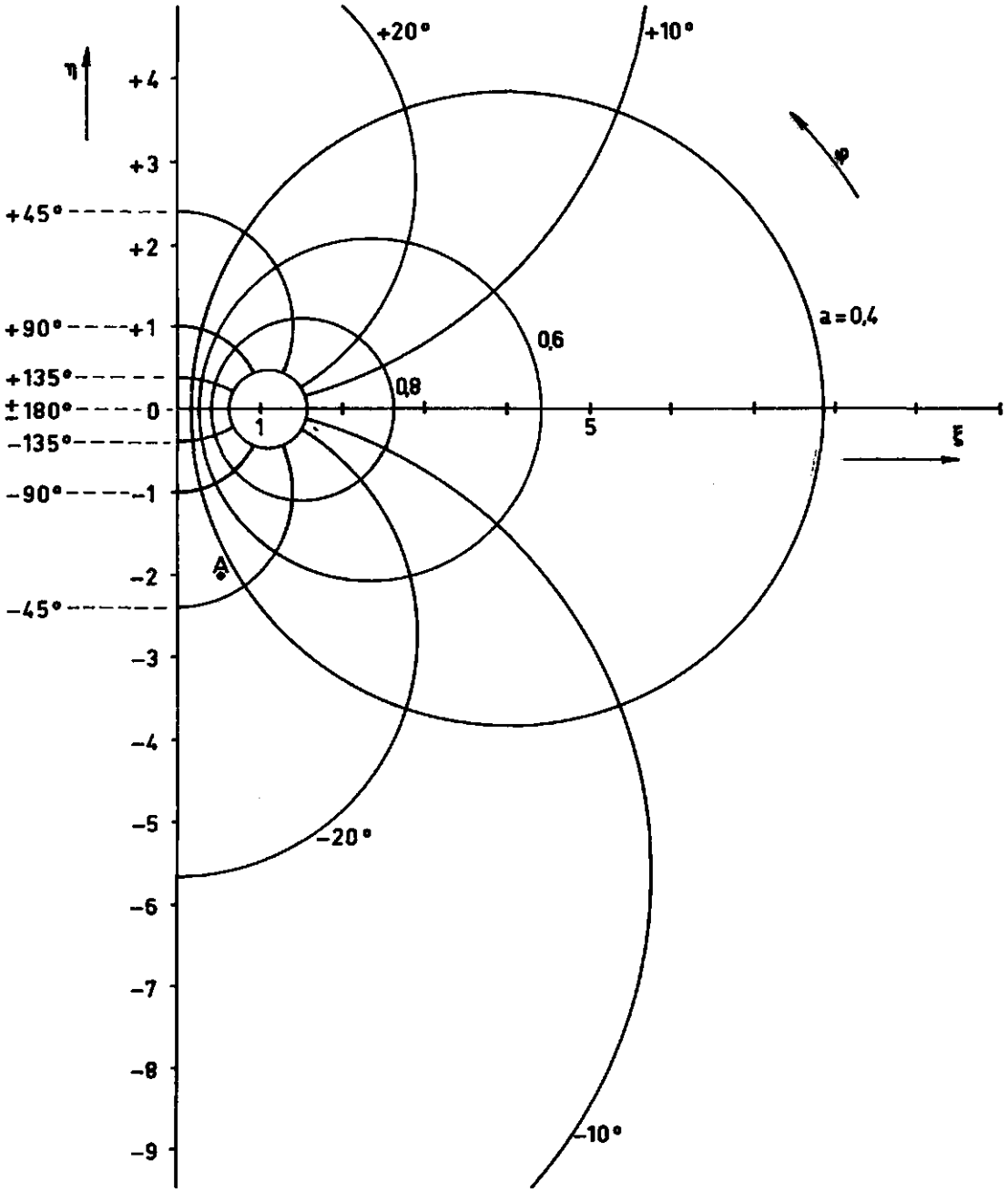

Figure 4 The impedance diagram.

complex quantity $\zeta = \xi + j\eta$.

The real part is the distance to the vertical (imaginary) axis; the imaginary part, the distance to the horizontal (real) axis. From eq.(1-29a) it follows that for each point in the ζ-plane, a corresponding value of $r = |r| \exp(j\phi)$ can be obtained. Therefore lines of constant $|r|$ and of constant ϕ can be drawn in this plane. Since $a = \sqrt{(1-|r|^2)}$ lines of constant $|r|$ are also lines of constant absorption coefficient.

From

$$\zeta = \frac{1+|r|\exp(j\phi)}{1-|r|\exp(j\phi)}, \tag{1-57}$$

it follows that

$$\xi = \frac{1-|r|^2}{1+|r|^2 - 2|r|\cos\phi}, \tag{1-58}$$

and

$$\eta = \frac{2|r|\sin\phi}{1+|r|^2 - 2|r|\cos\phi}. \tag{1-59}$$

The ϕ is eliminated from eqs(1-58) and (1-59) and $|r|$ is retained as a parameter. Thus a family of curves for constant $|r|$ is generated in the ζ plane, a member of the family being given by

$$\left[\xi - (1+|r|^2)/(1-|r|^2)\right]^2 + \eta^2 = \left[2|r|/(1-|r|^2)\right]^2. \tag{1-60}$$

The curves prove to be circles, having their centres at

$\xi = (1+|r|^2)/(1-|r|^2)$, $\eta = 0$,

and radii given by

$R = 2|r|/(1-|r|^2)$.

Similarly, $|r|$ may be eliminated and ϕ retained as parameter. A family of circles for constant ϕ is thus generated, which proves to intersect the ones for constant $|r|$ at right angles. A member of the family is given by

$$\left[\eta - \cot(\phi)\right]^2 + \xi^2 = \left[1/\sin(\phi)\right]^2, \tag{1-61}$$

these circles having their centres at

$\xi = 0$, $\eta = \cot(\phi)$,

and their radii are given by

$R = 1/\sin(\phi)$.

In figure 4, a number of circles from these families of circles is drawn. As was argued in section 1-4, an unambiguous value for ϕ may be obtained by imposing condition (1-33). Eq.(1-59) shows that, for $0<\phi<\pi \rightarrow \eta>0$ and conversely that, for $-\pi<\phi<0 \rightarrow \eta<0$.

Thus the circles for constant ϕ are given positive values above the real axis and negative values below this axis.

When, for instance, $|r|$ and ϕ are known from measurements, values of ξ and η can be read from the diagram. As an example, the position of one point A has been indicated in figure 4.

From the diagram it can be read that $|r| \approx 0.86$ and $\phi \approx 50^{o}$, $\xi = 0.5$ and $\eta = -2.0$.

B The Smith diagram

This diagram presents the reflection coefficient $r = |r|\exp(j\phi) = u + jv$ in the complex plane. In this case lines of constant ξ and η are circles. The loci of constant ξ and η can be calculated from the eq.(1-29b)

$$u + jv = \frac{(\xi+j\eta)-1}{(\xi+j\eta)+1}. \qquad (1\text{-}62)$$

When ξ is constant, η can be eliminated. This yields

$$(u - \frac{\xi}{\xi+1})^2 + v^2 = (\frac{1}{\xi+1})^2, \qquad (1\text{-}63)$$

and, concomitantly, when η is constant, it follows that

$$(u-1)^2 + (v - \frac{1}{\eta})^2 = (\frac{1}{\eta})^2. \qquad (1\text{-}64)$$

Some circle segments of these families of circles are shown.

When the position $|r|$, ϕ in polar co-ordinates is known from measurements, it can be plotted in the Smith diagram. The values of the corresponding ξ and η can now be read from the loci.

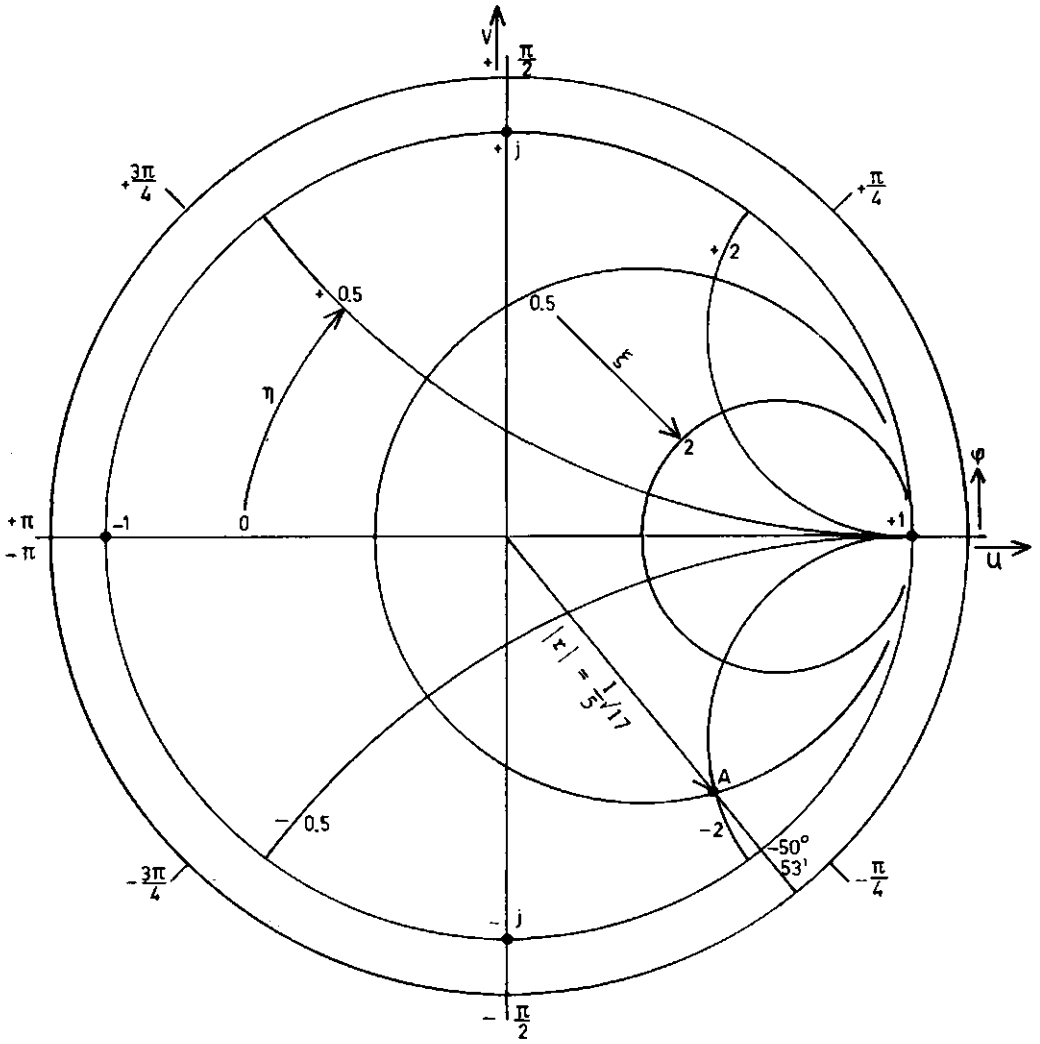

Figure 5 The Smith diagram.

In figure 5 one point A is the transformation of the point denoted by the same symbols in figure 4.
An advantage of the Smith diagram is that all values lie within one circle, whereas the impedance diagram is a semi-infinite plane and a finite part of it cannot show values for ξ and η beyond its limits.
The impedance diagram is not accurate for small values of ξ. In the Smith diagram, which is often used in electronics, the large values of ξ, which occur frequently in acoustics, cannot be read with any accuracy, which constitutes a major disadvantage for its adoption here. In the following chapters, the impedance diagram will be used exclusively.

1.11 The behaviour of the function $Z = W \coth(\gamma l)$ in the impedance plane

To gain at least a qualitative insight into the locus in the complex plane of the specific acoustic impedance at the sample surface, see eq.(1-56), the function $Z = W \coth(\gamma l)$ will be discussed, partly after Zwikker and Kosten (1949).
W and γ are complex constants of the sample material. They will depend upon the structure and the frequency. According to eqs(1-54) and (1-55) they are connected with Z_m and Y_m as follows: $\gamma_m = \sqrt{(Z_m Y_m)}$ and $W_m = \sqrt{(Z_m/Y_m)}$, where Z_m and Y_m are defined with the fundamental differential equations (1-52) and (1-53) respectively. Z_m and Y_m are also complex. In free air they are equal to $j\omega\rho$ and $j\omega/K$ respectively, so that in air $\gamma_m = j\omega\sqrt{(\rho/K)} = j\omega/c$ and $W_m = \sqrt{(K\rho)} = \rho c$ respectively. In free air, therefore, γ_m is proportional to frequency; W_m is independent of frequency.

In loose soil samples, therefore, W_m will probably vary slowly and slightly with frequency, where as γ_m will probably vary rather rapidly with frequency, increasing approximately proportionally with frequency. Introducing $\gamma_m = \alpha_m + j\beta_m$, β_m will probably be approximately proportional to frequency, but α_m - the attenuation coefficient of travelling waves in the material - will, again, be a weak function of frequency.
The denser the material is, the larger will be the difference from the behaviour of free air, but anyhow it seems reasonable to expect W_m "rather" constant and γ_m "more or less" proportional to frequency. The results of measurements corroborate these expectations.
Based on this consideration the behaviour of the function $Z = W \coth(\gamma l)$ can be studied in the complex plane.

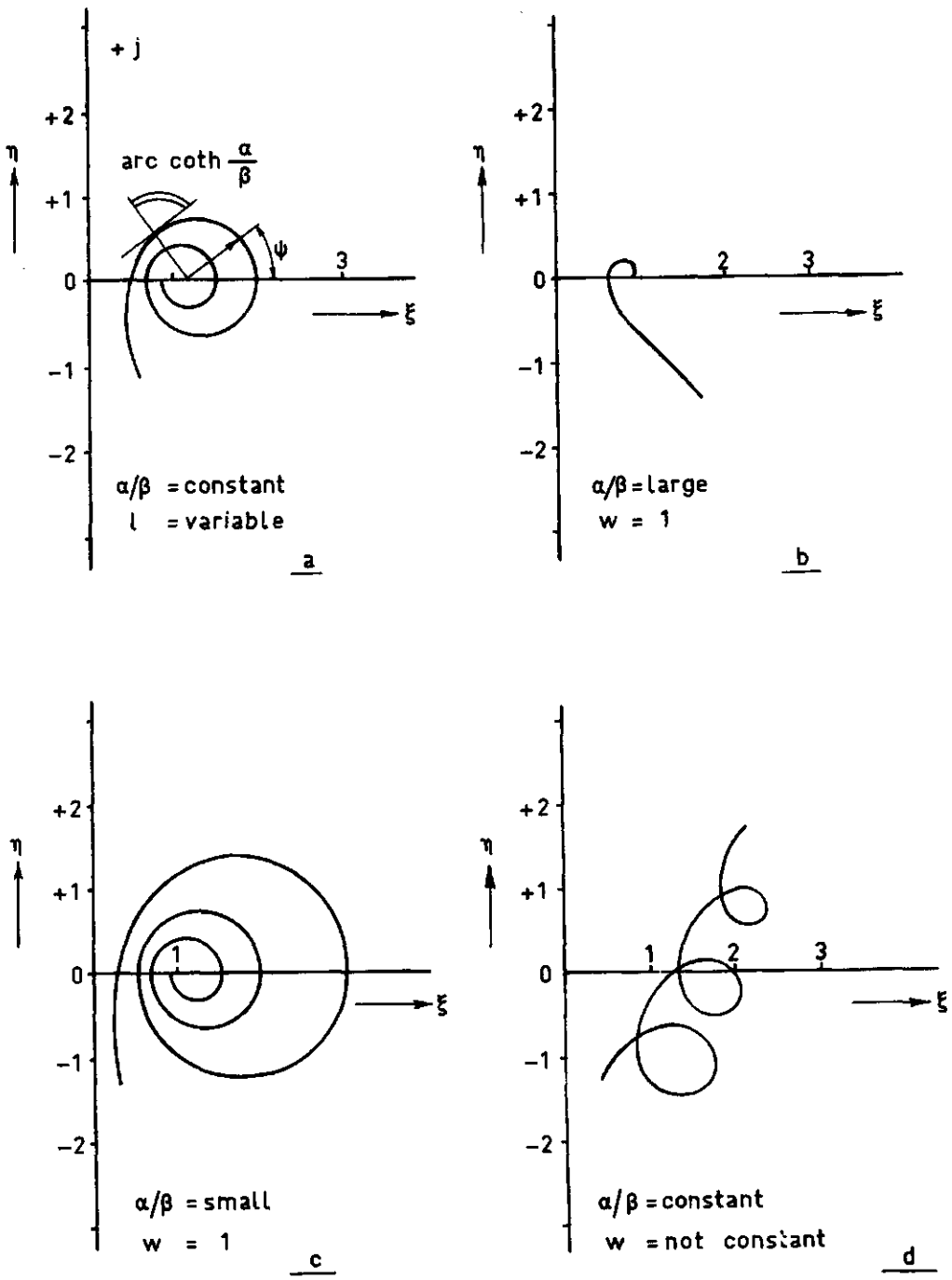

Figure 6 The behaviour of the function $W_m \coth \gamma_m l_m$ in the complex plane.

Assuming W = 1 one finds:

$$Z = \frac{\sinh(2\alpha l) - j \sin(2\beta l)}{\cosh(2\alpha l) - \cos(2\beta l)} . \qquad (1\text{-}65)$$

For very small values of $2\alpha l$ and $2\beta l$, a first-order approximation of eq.(1-65) is

$$Z = \frac{\alpha - j\beta}{(\alpha^2+\beta^2) l} .$$

Assuming ω being constant and l being variable, Z will vary with the argument of the hyperbolic tangent. In this case the locus for Z becomes a straight line in the lower right-hand corner of the impedance diagram, having a negative inclination to the real axis.
In the case, where the angular frequence ω varies and the sample thickness l rests constant, the locus of Z will be a straight only if the ratio α/β is independent of frequency.
The locus for Z in the complex plane approaches a logarithmic spiral for sufficiently large values of l, the condition $\alpha l > 1$ being adequate for all practical purposes. If so, $Z \simeq 1 + 2 \exp(-2\alpha l)\cdot\exp(-2j\beta l)$.
The modulus M of the spiral is given by $M = 2 \exp(-2\alpha l)$, and the argument Ψ is defined by $\Psi = -2\beta l$. The apex of the spiral is + 1, see figure 6a.

Now $M = 2 \exp(\alpha\Psi/\beta)$ and this implies that the shape of the spiral is completely determined by the ratio α/β, the slope of the spiral being given by arc $\coth(\alpha/\beta)$, see figure 6a.
These conclusions for the form of the locus can be retained for case I (variable ω, constant l), provided the ratio α/β is independent of frequency. Note that, whereas Ψ is proportional to l, its dependence on ω will generally be more complicated.

For materials having high damping, corresponding to comparatively large values of α/β, the spiral converges rapidly to the apex as in figure 6b. Conversely, for weakly dissipative materials, convergence is slow as in figure 6c.

In the general case, W equals $B\cdot\exp(j\theta)$; so being unequal to unity and a function of ω. For constant ω and variable l the apex of the spiral for Z is the complex vector W. Then the locus for Z may be obtained from that for W = 1 by magnifying that curve uniformly from the origin by a factor B and then rotating it around the origin over an angle θ in anti-clockwise direction.

If ω varies and l rests constant the locus of Z is complicated by the shift of the spiral's apex with frequency as the spiral is traversed. No general description of the resultant form of the locus can be given; an extreme example is illustrated by figure 6d.

Both these cases are amenable to experiment when soil samples are being examined acoustically. There are further possibilities for the investigation of porous materials, e.g. the consideration of the locus for Z for constant ω and l but variable backing impedance of the sample. Such methods for soil samples have insuperable experimental difficulties and will thus be ignored.

For weakly dissipative materials, W is almost real and the points of intersection of the Z locus for variable frequency and the real axis supply information on the propagation constant of the material. For real W these intersections occur when βl is a multiple of $\pi/2$, see eq.(1-65). For $\beta l = n\pi$, $n = 1, 2, 3, \ldots$, the prevailing condition will be termed resonance, for $\beta l = \pi/2 + n\pi$, $n = 0, 1, 2, \ldots$, anti-resonance. In resonance, $|Z|$ is larger than in anti-resonance. For strongly dissipative materials, W will always show appreciable phase angles and the points of intersection provide but little information.

2 The experimental equipment and its accuracy

2.1 Introduction

The customary type of acoustic interferometer, together with its auxiliary electronic equipment, consists of an oscillator which generates a harmonic electrical signal, and a loudspeaker which converts this signal into an acoustical one and feeds it into an interferometer tube. This tube ends with the sample in its holder. The sound field in the tube is explored with a movable microphone; the microphone signal is measured with a selective voltmeter.
Some practical considertions for the construction of an interferometer are the following

a. The tube should be rigid, i.e. it should not show mechanical vibrations in the instrument's frequency range. This is usually achieved by selecting a thick-walled tube.

b. The microphone should not perturb the sound field. If the microphone is placed in the sound field, i.e. within the tube, the microphone's cross-sectional area should not exceed 1% of that of the tube (Lippert, 1953). Another possibility is to place the microphone outside the tube and to connect the microphone with a kind of catheter, usually called a probe-tube, to the point where the sound pressure is to be measured. As a rule the probe-tube is placed along the axis of the interferometer or parallel to it, in which case the above mentioned 1% requirement should be applied to the cross-sectional area of the probe-tube and the interferometer tube, respectively.

c. Microphone position should be easily read from an accurate scale.

d. An air-tight seal is required between the sample holder and the tube. A leak tends to radiate sound power and might thus lead to incorrect results for the sound power absorbed by the sample.

e. The transmission of structure-borne sound from the loudspeaker to the microphone should be prevented. A common precaution is resilient mounting of the loudspeaker.

f. The major requirement for the electronic equipment is stability. Fluctuations should not exceed 0.1% in signal frequency or 1% in signal amplitude or voltmeter sensitivity. This accuracy is attainable.

A complication is the roughness of soil surfaces that is to say deviations of one or more millimetres from a reference plane occur. Although very coarse structures were not examined during the present experiments, a large cross-section for the interferometer tube is desirable to average out the roughness and inhomogeneity of the soil surface.
However, there is a limit to tube size for a given signal frequency; that is, there is a limiting frequency, the cut-off frequency, for a given tube. The cut-off constitutes an upper frequency limit, beyond which higher-order modes, corresponding to oblique incidence on the sample, will propagate in the tube. The quantity sought, however, is the specific acoustic impedance of the sample surface at normal incidence.
For tubes of circular cross-section the cut-off frequency may be determined from $k_c R = 1.84$, where k_c is the cut-off wave number and R is the tube radius. Wavelength is then 1.7 tube diameters (Rayleigh, 1910). It is inadvisable to measure at or even just below the cut-off frequency, as considerable distortion of the sound field may then occur, especially near the sample.
In the present case, three interferometer tubes of circular cross-section, distributed over two interferometers, were used, the larger for the lower frequencies and the smaller for the higher ones. Besides the large sample area, another advantage of using the large tubes at the lower frequencies is the smaller attenuation along the tube.

2.2 The interferometers

The larger interferometer has a flame-pipe of 155 cm length and inner- and outer diameters of 162 and 171 mm respectively. It is mounted vertically on the wall of the room. A loudspeaker 12 cm from the top is suspended elastically from three supports to prevent transmission of structure-borne sound from the loudspeaker to the tube (and the sample). The sample-holder can be attached to the lower end of the tube (figure 7a). The bottom plate of the sample-holder is a piston, that hermetically seals in the holder by means of an O-ring. In its lowest position samples with a layer thickness up to 16 cm can be studied (figure 7b).
The Ronette microphone, model MC 65, is approximately cylindrical and has a height of 12 mm and a diameter of 29 mm. With its axis normal to that of the tube, the microphone has a cross-sectional area of less than 0.5% of the tube. It is of the piezo-electric type and has a sensitivity of 1.7 mV/µbar at 1000 Hz. Frequency response is practically flat from 30 Hz to 1 kHz and then rises slowly. At 10 kHz the rise is 8 dB.

The microphone is attached to an endless belt running inside the tube 4 mm from the inner wall. Outside the tube the belt has been provided with a gauge. The displacement of the microphone can easily be read in fifths of a millimeter.
The Philips loudspeaker, model 9744, has a cone diameter of 130 mm, a voice coil impedance of 5 Ω at 1 kHz and a nominal power-handling capacity of 3 W.
The frequency range of the interferometer ranges from 50 - 1100 Hz.
For the measurement of the porosity of the sample a special lid that fits to the upper end of the sample-holder has been constructed. By a thick-walled plastic tube attached to an opening in this lid, the sample-holder can be connected with a porosimeter.
The porosimeter is founded on Boyle's law: $p \cdot V$ = constant. The porous material under test is enclosed in a container of known value. The actual volume available to the gas, however, is that of the container diminished by that of the solid matter in the sample.
The porosity of the material is easily calculated if the actual gas volume has been determined and this is done by introducing a known change in volume, measuring pressure both before and after the change. The initial value of the actual volume is now the only unknown and Boyle's law may be solved for it. As will have become apparent from the selection of a gas law, changes of state are assumed to be so slow that they are isothermal.
Porosimeters have been described, e.g. Loebell (1935), Bourrier (1951), Alten and Loofmann (1956). The instrument is satisfactory for samples composed of gases and impervious solid matter. But where liquids may evaporate during expansion or adsorbed gases may be freed, results will be unreliable. And as such conditions commonly prevail in soils, other methods must be sought for determining their porosity.

In principle measurements of resistance to air flow can also be made on the sample. With a reinforced "sieve plate" at the upper end of the sample-holder, the sample can be turned upside down. Next, the bottom plate can be removed. In this position, the sample-holder can be attached to the lower end of a gas container. In many cases the samples do not permit such a treatment without a disturbance of their geometrical arrangement. Therefore the required additional measurements were performed on separate samples in most instances. Measurements of air-flow resistance can also be made on samples contained in wide vessels. If so, the standing-wave tube is extended by a cylinder of the correct inner diameter, having a gasket at the top, sealing it to the main tube, and a cutting edge at the bottom. The cutting edge is driven into the sample.

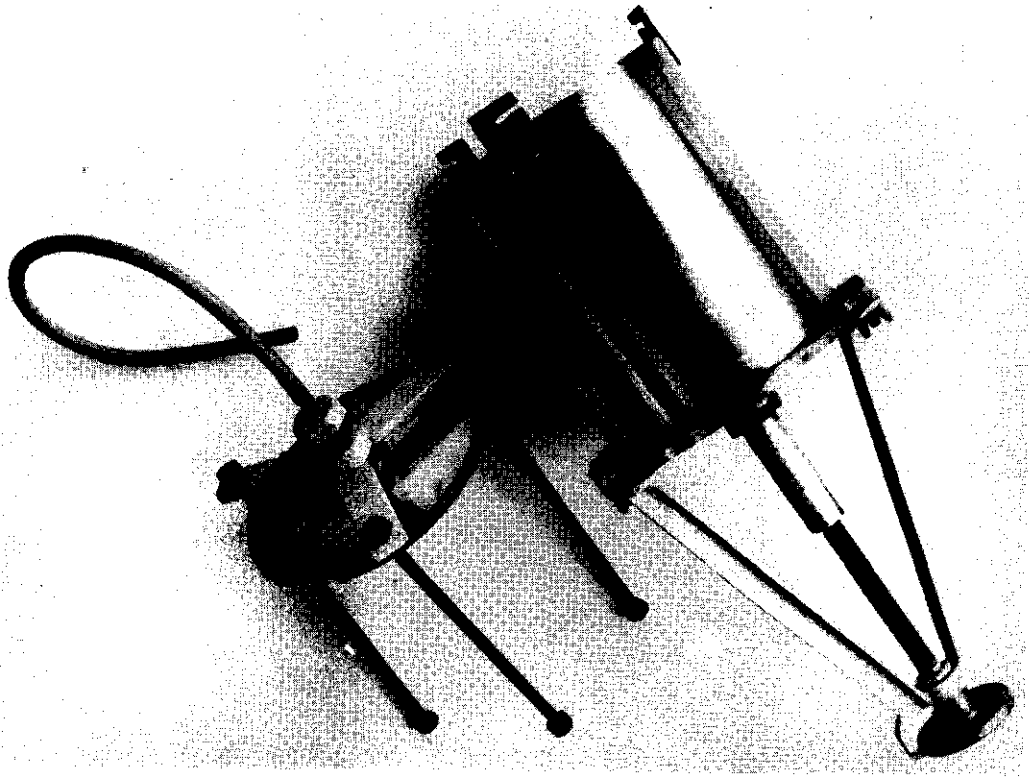

Figure 7a The sample-holder of the large interferometer; left the connecting tube to the porosimeter

The attenuation of travelling waves in the tube was measured and the proper functioning of the interferometer checked with a calibration plate 12 mm thick and 2.2 kg mass. This plate and the extension section mentioned in the previous paragraph can be sealed to the main tube with a gasket.

For measurements at higher frequencies, the Brüel and Kjaer interferometer, type 4002, is used. It contains measuring tubes with diameters of 9.9 cm and 2.9 cm, respectively, and a length of 100 cm and 26 cm, respectively, which make the instrument suited for measurements at frequencies ranging from 90 to 1800 Hz, and from 800 to 6500 Hz, respectively. The mobile microphone is of the probe type, the probe tube entering the measuring section through a simple wave trap, which pierces the loudspeaker axially.
This commercially available interferometer was built for horizontal use. For use with soil samples, it is necessary to place the measuring tube vertical. The tube was therefore fitted to a steel frame, under an angle of 5^{o} from verti-

cal. The steel frame was suspended from the wall. The microphone carriage was equipped with a counterweight, suspended by a steel tape. An engraved strip of perspex of 1 metre long was attached rigidly to the microphone housing by a bar. This arrangement permits rapid parallax-free reading of the microphone position. The interferometer is used with two sample-holders with fixed bottom plates and one sample holder with a movable, pistontype bottom plate. These plates are 16 mm thick.

In constructing the interferometer care has been taken to avoid transmission of structure-borne sound.

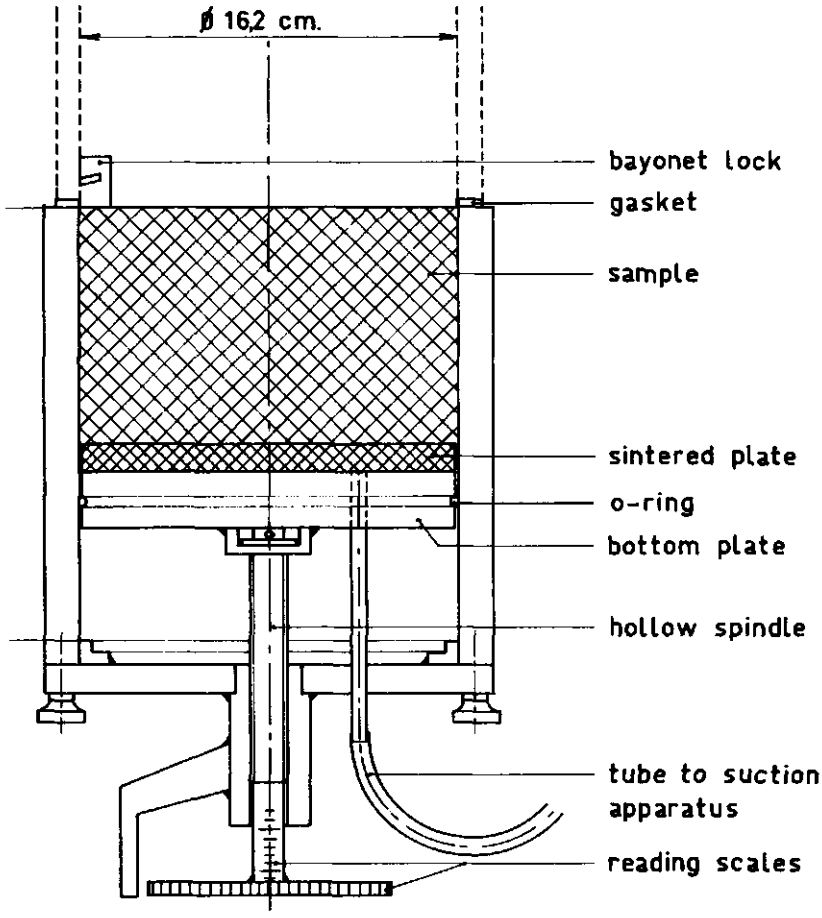

Figure 7b Cross section of the sample holder of the large interferometer

2.3 The electronic equipment

The selection of the electronic equipment was governed by the requirement that the apparatus have a wide range of applicability. The construction of equipment for use in the field was considered but will not be discussed here. The input impedance of the various appliances was always so high that loading effects on preceding circuits were negligible. The experimental system is illustrated in figure 8 and 9.

The signal source is an RC-type audio-oscillator, make Peekel, model 22A. After warming up, short-term frequency stability is of the order of 10^{-4}. Amplitude stability is given as 2%, but short-term stability is considerably better; the stability of the signal is more than sufficient for interferometry. Signal frequency may be read from the tuning dial with an accuracy of 1.5%, which is inadequate for the present purpose.

A power amplifier, make Philips, model HF-10, was interposed between the audio-oscillator and the loudspeaker. Oscillator loading is thus diminished and performance improved. The feedback loop of the amplifier, which was designed for use with record-players was modified to obtain a flat response. The nominal output is 10 W into a load of 7 Ω; the frequency range is from 10 Hz to 13 kHz and distortion and noise are low.

Loudspeaker current is monitored with an ammeter, calibrated in RMS values and having three ranges: 100, 200 and 300 mA f(ull) s(cale) d(eflection). The circuit diagram is given in figure 10. During the actual measurements the ammeter was always short-circuited.

The microphone signal is measured with a (selective voltmeter) frequency analyser to suppress spurious components such as: harmonics (of the signal frequency) generated in the audio-oscillator, the power-amplifier and, above all, the loudspeaker, hum and noise. The instrument used here, made by Brüel & Kjaer, model 2105, has a selective element consisting of an RC double-T network, introduced into the feedback loop of an amplifier stage. Selectivity is adjustable and was usually set for a 39 dB reduction in sensitivity at 1 octave from the signal frequency. Although selectivity is not very high, spurious-signal suppression meets the requirements for practical interferometry. The instrument has a pseudologarithmic scale permitting voltage measurement with an accuracy of 1%. The signal frequency may be read from the tuning dial with an accuracy of 1%, provided the instrument has been calibrated by tuning to the mains frequency and its harmonics. The signal fed to the meter is also available

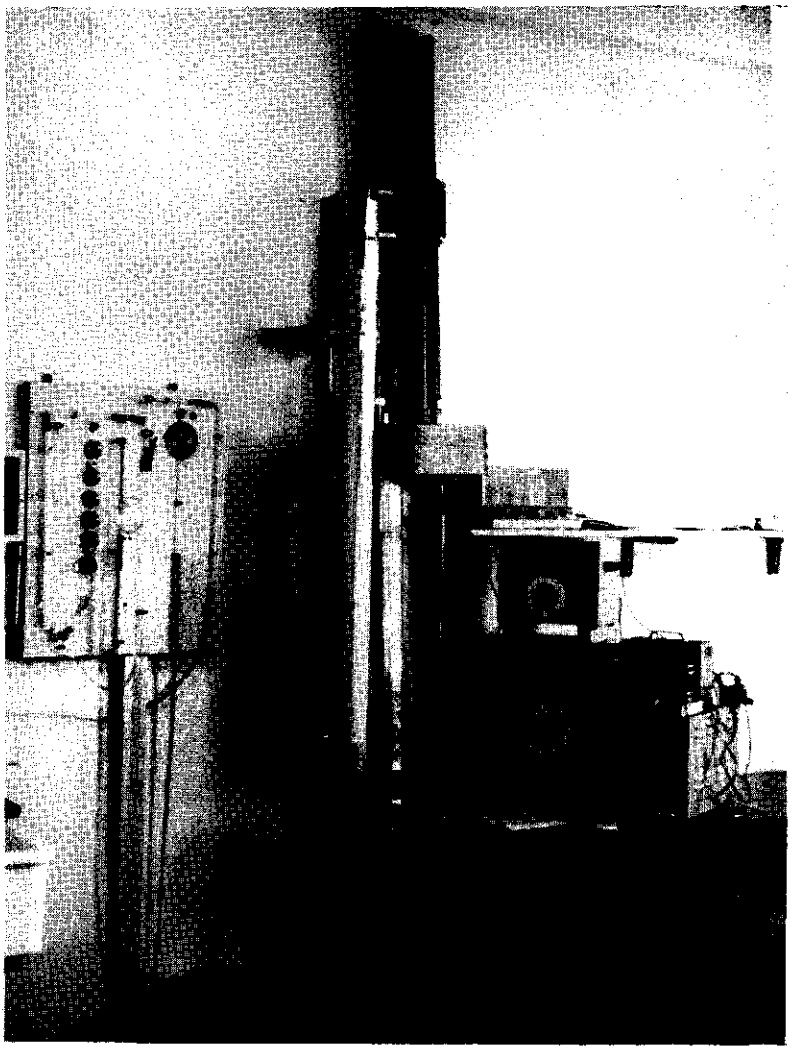

Figure 8 The measuring set-up

at the output terminals. Provision has been made for continuous adjustment of sensitivity if absolute calibration is not required.
The output signals from the audio oscillator and the selective voltmeter are monitored with the aid of an oscilloscope, make Philips, model GM 3156. To present both signals simultaneously, the oscilloscope is preceded by an electronic switch, make Heathkit, model S-3, having a switching rate adjustable to 150, 500, 1000 and 1500 Hz.

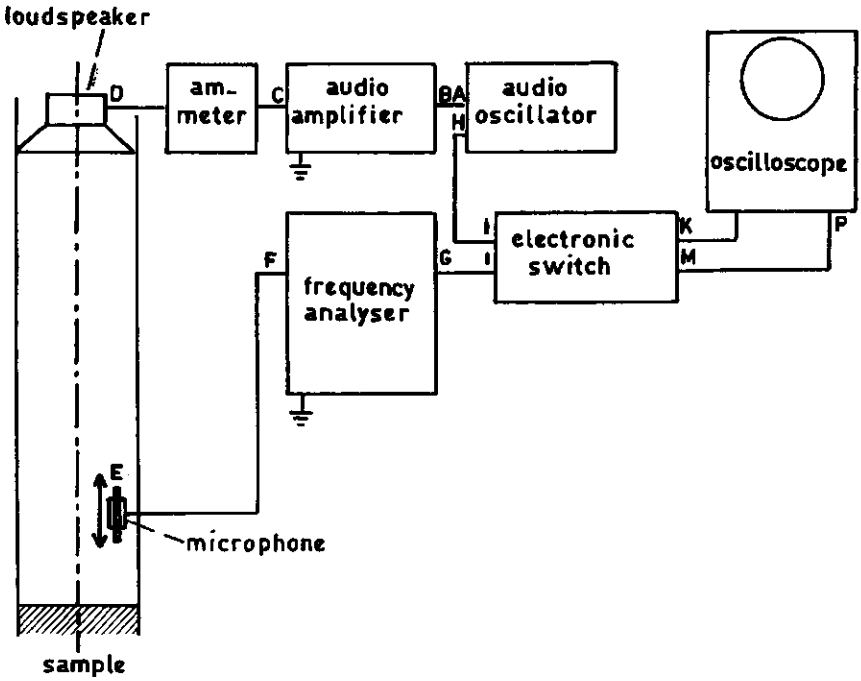

Figure 9 The arrangement of the measuring set-up

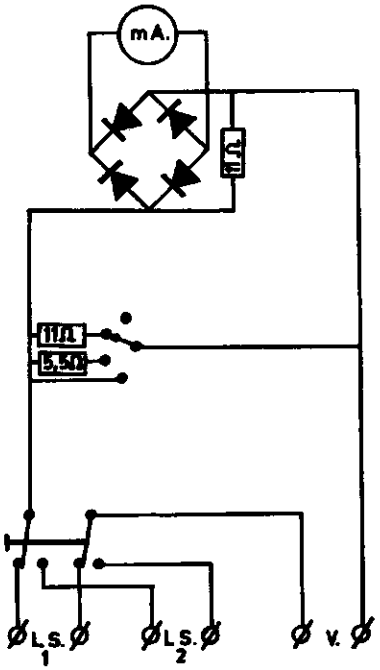

Figure 10 The Am-meter

2.4 The measurement

For rapid and complete tabulation the experimental data are entered on data sheets (see example). A sheet consists of a heading, giving general information, and a number of sections, each of which is devoted to a particular measuring frequency.

The heading gives the following information: type of material (Monster), grain size or texture, in mm (Monstermat.), sample thickness in the interferometer in cm (Laagdikte), porosity in % as derived for the dry sample from the amount of solid matter (Por. volume), moisture content in percentage weight of dry material (Vochtgehalte), total mass in g (Gewicht), density in kg/m^3. 10^{-3} (S.g.), specific acoustic static air flow resistance (σ), special remarks (Opm.), position of the sample surface in cm (meetniveau), sample number (No.), sample series (Serie), date of measurement (Datum), time of day (Tijd), ambient temperature in ^{o}C (Temp.).

Each of the sections has been divided into six columns. The upper half of the first column lists values for frequency in Hz, as read from the audio-oscillator (T), as read from the selective voltmeter (V) and as determined from wavelength, c.f. column 3, (G).

The upper figure in the second column is the position of the first minimum diminished by a quarter wavelength, in cm. The following figures are the readings for positions of the minima, in cm. In the third column, the upper figure is the average for the quarter wavelength, the following figures are values for the half wavelength in cm as derived from the second column and the average for the half wavelength is entered at the bottom of the column.

The second half of the first column gives the displacement of the first minimum in cm, in relation to that minimum with a hard termination at the sample surface. This requires the introduction of corrections for the position of the sample surface and the properties of the microphone (see section 2.5, point B 5) ( ), the wavelength in cm as obtained from the third column (λ) and the phase angle of the reflection coefficient in radians (ϕ).

The first figure of the fourth column is the value of the minimum sound pressure, extrapolated to the sample surface and in arbitrary units (voltmeter readings), entered under -. The following figures give the values for the various minima (in the same units). The same is done for the maxima in the fifth column, the extrapolated value being entered under +.

The sixth column gives the standing wave ratio at the sample surface (r), some

Meetstaat

Monster	: grond Koebongerd				Gewicht: 278,4 g				No. : 267		
Monstermat.	: 2-1 mm				S.g. : 2650 kg/m^3				Serie: N 4		
Laagdikte	: 4 cm				σ : ...				Datum: 25/2/65		
Por.volume	: 65.9				Opm. : 0.5% verdampt				Tijd : 11.30 VM		
Vochtgehalte:	7.28				meetniveau: 32.52				Temp.: 18.4° C.		
T 500			-1.27 +4.8	r35.277	T1005	29.87	8.53	-33.8 + 92		r2.717	
V	59.10		1.27 "	a2.028	V 998	38.40	17.15	34.0	"	a2.368	
G					G 996	55.55	17.05	34.2	"	5.085	
Δ				%10.72	Δ 2.65	72.60	17.00	34.4	"	%78.66	
λ					λ 34.12	89.60	17.06	34.9	"		
φ		$\lambda/2$			φ 0.077	=0.1315	$\lambda/2$			76.2	
T 425	29.75	20.24	-2,90 + 50	r17.241	T 1170	30.27	7.45	-31.8 + 61		r1.919	
V 422	49.99	40.49	2.99 "	a2.058	V 1141	37.72 52.80	15.08 14.68	31,8 32.0	" "	a2.521	
G 419	90.48		3.2	19.299	G 1141	67.48	15.07	32.0	"	4.440	
Δ 2.77				%20.72	Δ 2.25	82.55	14.75	32.0	"	%90.09	
λ 80.98		80.98			λ 29.80	97.30	14.90	32.0	"		
φ 0.034	=0.058	$\lambda/2$		22.0	φ 0.075	=0.128	$\lambda/2$			98.8	
T570	29.84	14.98	-3.99 +41	r10.275	T1250	32.05	6.90	-18.48 + 31		r1.678	
V568	44.82	29.96	4.0 "	a2.097	V 1240	38.95 51.79	13.84 13.63	18.5 18.5	" "	a2.596	
G567	74.78		4.02 "	22.372	G 1233	65.42	13.86	18.5	"	4.274	
Δ 2.68				%32.33	Δ 0.47	79.28	13.90	18.5	"	%93.60	
λ 59.92		59.92			λ 27.60	93.18	13.80	18.7	"		
φ 0.0122	=0.008	$\lambda/2$		31	φ 0.0017	=0.029	$\lambda/2$			94.0	
T790	31.35	11.63	-2.19 +14.1	r6.438	T1590	32.67	5.54	-6.76 + 13		r1.923	
V 734	42.98	23.22	2.20 "	a2.155	V 1556	38.21	11.10	6.8 6.9	" "	a2.520	
G 731	66.20	23.30	2.24 "	8.683	G1534	49.31	10.90			4.443	
Δ 1.17	90.50		2.24 "	%46.08	Δ 0.15	60.20 71.99	11.29 11.02	7.0 7.0	" "	%90.03	
λ 46.52		23.26			λ 22.16	82.51	11.08	7.0	"		
φ 0.025	=0.0427	$\lambda/2$		46.4	φ 0.007	=0.012	$\lambda/2$			38.1	
T860	29.95	9.95	-14.37 +59.9	r41.68	T 1790	32.79	4.90	-5.66 + 14		r2.474	
V 856	39.90	19.98	14.5 "	a2.239	V 1760	37.69 47.49	9.80 9.83	5.7 5.7	" "	a2404	
G 854	59.88	19.83	14.8 "	6.407	G 1734	57.22	9.58	5.75	"	4.878	
Δ 2.57	79.71		15.0 "	%62.43	Δ 0.27	76.80	9.95	5.9	"	%8200	
λ 39.80		19.90			λ 18.60	86.75	9.80	6.0	"		
φ 0.0645	=0.1102	$\lambda/2$		62.	φ 0.0145	=0.024	$\lambda/2$			84.0	

Figure 11 A data sheet.

auxiliary quantities (sub a) and the absorption coefficient in % (%). Usually the absorption coefficient, read directly from the selective voltmeter and thus ignoring tube attenuation, was entered at the bottom of the column. Its value can serve e.g. as a control during the measurements. Without any further calculation one can conclude at the end of a series of readings at different frequencies and after checking the readings at a few of those frequencies, that the sample was not disturbed during measurement. Noteworthy points are as follows.
The loudspeaker in the interferometer does not constitute an ideal piston even at low frequencies. The sound field near the loudspeaker may thus be distorted and no measurements should be taken close to it.
The measuring system has it own acoustical and mechanical resonance frequencies. The acoustical resonance frequencies can be heard easily; the detection of mechanical resonances in the measuring system is more difficult. They may originate from different sources and can sometimes not be traced. When these frequencies are suspected, measurements are made after a small shift in frequency. In the beginning the frequencies at which readings are made are chosen quite arbitrarily. All series of readings have been read for at least twelve frequencies. More readings were necessary with samples of high air resistance. The criterion chosen was determined by the accuracy with which the impedance curl could be drawn.
Through the imperfect homogeneity of the sample surface the readings of the sound pressure at some frequencies at the first minimum, nearest to the sample, were unreliable. If so the minima were extrapolated after starting from the following minimum. Then the value of the phase shift was derived from the readings of three-quarters of a wavelength, neglecting the position of the probe at the first minimum.
The value for the sound pressure at the maxima often do not show substantial variation for one frequency, eq.(1-36). Extrapolation is then not necessary.

2.5 Accuracy of the measurements

The specific acoustic impedance of a sample is determined in the standing wave tube in some reference plane and the worker is free in his choice of this plane as long as the impedance itself is the only quantity of interest.
But a different situation arises if material constants of the sample are to be derived from the specific acoustic impedance. If so, the interface between the air column and the sample material is selected as reference plane and the assumption is introduced that the properties of the medium change abruptly from those of air to those of the sample in this plane.

The concept of a plane of discontinuity is realistic enough for fine-grained materials, but for coarse-grained ones a transition may well exist where the properties of the medium change almost continuously. At present there appears to be no feasible procedure for incorporating the effect of such a transition into the calculations, e.g. for finding an optimum position for the reference plane somewhere in the range. Therefore the simple procedure of laying the reference plane through the highest peaks of the sample surface has been followed and no account was taken of any errors thus introduced. Thin layers are most severely affected by these errors.

Another problem presented by coarse-grained materials is that a specific sample may well be far from representative for the bulk of the material, the number of grains in the sample being limited. Here too the answer to the problem is far from obvious and was not further pursued. The problem was discussed in more detail for perforated panels by Mawardi (1956).

The following is confined to the errors inherent in the determination of the specific acoustic impedance, commencing with those in the modulus $|r|$ and the phase angle ϕ of the sample's pressure reflection coefficient r.

Now $|r|$ follows immediately from the standing wave ratios, c.f. eq.(1-38). Assuming an error $\delta|r|$ in $|r|$ and δs in s, one can derive from eq.(1-37) that

$$\delta|r| = \frac{2s}{(s+1)^2}\,\frac{\delta s}{s} = \tfrac{1}{2}(1-|r|^2)\frac{\delta s}{s} . \qquad (2\text{-}1)$$

Thus the absolute value of the error in $|r|$ is always less than half the absolute value of the relative error in s, vanishing for vanishing sample absorption.

The relative error $\delta a/a$ in the absorption coefficient a is also of interest, especially if sample absorption is low. From eqs(1-38) and (2-1) one concludes that

$$\delta a = -2|r|\,\delta|r| = -|r|\,(1-|r|^2)\,\frac{\delta s}{s}$$

or

$$\frac{\delta a}{a} = -\frac{s-1}{s+1}\cdot\frac{\delta s}{s} . \qquad (2\text{-}2)$$

The absolute value of the relative error in a is always smaller than in s, approaching this latter value for vanishing sample absorption.

Eqs (2-1) and (2-2) show that the errors in $|r|$ or a follow immediately from those in s, which will therefore be scrutinized.
In considering the errors in the determination of ϕ, errors in position are converted into errors in angle - expressed in radians - by multiplying the error in position by the wave number k.
One can now compile a list of sources of error, adding a short discussion and an estimate for the probable value of each error.

Table 3

Sources of error

A. In the determination of s:

1) The reading error of the wave analyzer
2) The error in probe position when adjusting for pressure minimum
3) The error in extrapolation of the minima
4) The error due to interfering signals.

B. In the determination of ϕ:

1) The reading error in probe microphone position
2) The error in probe position when adjusting for pressure minimum
3) The error in the wave number
4) The error in the position of the sample surface
5) The error in the correction for the probe's pressure-sensitive position.

Ad A 1. A relative error in the wave-analyser reading in an extreme will give rise to an equal relative error in s, when absolute values are considered. The wave-analyser having an approximately logarithmic scale, the relative reading error is approximately constant. The probable value, which represents the instrument's accuracy, may be 1%.

Ad A 2. The customary procedure for finding a minimum is the following. The probe microphone is swung to and fro past the minimum with reducing amplitude and keeping the wave-analyser readings at opposite ends of the swing equal. Finally the probe is brought to rest at the estimated midway position for the smallest swing, always coming from the same direction and it is then assumed to be at the minimum.
As a change in wave-analyser reading of 1% is clearly visible, the limiting process described above will presumably yield a relative error of less than 0.5% for the value of the minimum. Smaller errors will obtain for the maxima and also for the minima for highly absorbant samples because of the slow change in reading of the wave-analyser with probe position. However errors in minima will be rather large for samples with very low absorption.

Ad A 3. Assuming the attenuation constant α_o in the standing wave tube to be minutely small and approximating the righthand side of eq.(1-31) one finds

$$\left|\frac{\underset{\sim}{p}^2}{\underset{\sim}{p}_i}\right| = \exp(-2\alpha_o x) + |r|^2 \exp(2\alpha_o x) + 2|r| \cos(2kx + \phi) =$$

$$\approx 1 - 2\alpha_o x + |r|^2 (1 + 2\alpha_o x) + 2|r| \cos(2kx + \phi) =$$

$$= 1 + |r|^2 + 2|r| \cos(2kx + \phi) - (1 - |r|^2)\, 2\alpha_o x.$$

The positions of the pressure minima are given by eq.(1-32). Let the sound pressure equal p_1 and $x = -l_{min}$ for the first minimum. Eq.(1-31) now yields

$$\frac{|p_1|^2}{|\tilde{p}_i|^2} \approx (1 - |r|)^2 \left(1 + 2\alpha_o\, l_{min} \frac{1+|r|}{1-|r|}\right). \tag{2-3}$$

On introducing the extrapolated sound pressure in the minima

$$p_{min} = |\tilde{p}_i|(1 - |r|)$$

$$= |\tilde{p}_1|/\sqrt{(1 + 2\alpha_o s\, l_{min})}. \tag{2-4}$$

An error $\delta\alpha_o$ in α_o will result in an error δp_{min} in p_{min}.
Eq.(2-4) gives

$$p_{min} = |\tilde{p}_i|(1-|r|) = p_1/(1+2\alpha_o\, l_{min} s)^{\frac{1}{2}},$$

$$\delta p_{min} = -\tfrac{1}{2}|\tilde{p}_1|(1 + 2\alpha_o s\, l_{min})^{-3/2} \cdot 2\, s\, l_{min}\, \delta\alpha_o,$$

or

$$\frac{\delta p_{min}}{p_{min}} = -\frac{\alpha_o\, s l_{min}}{1+2\alpha_o s\, l_{min}} \cdot \frac{\delta\alpha_o}{\alpha_o}. \tag{2-5}$$

Note that the absolute value of the relative error in p_{min} is always less than half that for α_o. As a rule the error in p_{min} will be so small in relation to that in $\alpha_o - \alpha_o\, l_{min}$ being a small quantity - that it may be neglected. However, should $\alpha_o s\, l_{min}$ approach or even exceed unity, the relative errors in p_{min} and α_o will become comparable. This can only occur for large values of s and if so

$$\zeta = \frac{1+r}{1-r} = \frac{s+1 + (s-1)\cos\phi + j(s-1)\sin\phi}{s+1 - (s-1)\cos\phi - j(s-1)\sin\phi}, \qquad (2\text{-}6)$$

$$\approx \frac{2/s + j\sin\phi}{1-\cos\phi + (1+\cos\phi)/s^2}. \qquad (2\text{-}7)$$

ζ is thus rather insensitive to errors in s, unless ϕ approaches zero, when ζ approaches s.

Fortunately the combination of factors which make for large extrapolation errors is rare and mostly the probable relative error in s due to faulty extrapolation will remain below 0.5%

The errors due to interference have been discussed. Electrical cross-talk betrays itself by a regular fluctuation in the magnitudes of the minima and an inadequate signal-to-noise ratio may usually be avoided by a slight shift in frequency.

Taking the sources of error in s together, the probable value for the relative error in $|r|$ will usually remain below 2%, bringing the probable value of the relative error down to less than 1%.

Ad B 1. The reading error δx for the probe microphone position is of the order of 0.5 mm. On converting this error to radians by multiplication with k one finds an error that is proportional to frequency. For the highest frequency used, $\approx$ 2000 Hz, $k|\delta x| = 0.02$ radians.

Ad B 2. It was assumed in A 2 that the probe microphone was not adjusted correctly to the minimum, thus introducing a difference δ_p between the ratio p/p_{min} and δ_p as compared to unity.

$$\frac{p}{p_{min}} = 1 + \delta_p. \qquad (2\text{-}8)$$

The probe position deviates by δx from the correct position for a minimum. Thus, on referring to eq.(1-32), probe position is given by

$$2kx = \pi - \phi + 2k\delta x. \qquad (2\text{-}9)$$

On neglecting attenuation by introducing $\alpha_o = o$ into eq.(1-31), it follows that

$$|p/\tilde{p}_i|^2 = 1 + |r|^2 + 2|r|\cos(2kx + \phi). \qquad (2\text{-}10)$$

Elimination of 2kx from eq.(2-10) by means of eq.(2-9), and assuming kx is much less than unity, yields

$$|p/\tilde{p}_i|^2 = (1-|r|)^2 + |r|(2k\delta x)^2, \qquad (2\text{-}11)$$

and, on considering that $|p_{min}/\tilde{p}_i| = 1-|r|$,

comparison of eqs(1-8) and (1-11) yields

$$k|\delta x| = (1-|r|)\sqrt{(\tfrac{1}{2}\delta_p/|r|)}. \qquad (2\text{-}12)$$

To elucidate the magnitude of the error from faulty probe position in the minima, a short table is composed, introducing probable values for δ_p in accordance with A 2.

Table 4

Error due to faulty probe position

$\|r\|$	$\delta_p.10^3$	$k\|\delta x\|$ in radians
0.9	5	0.005
0.5	5	0.035
0.25	5	0.075
0.1	2.5	0.1

For values of $|r|$ as low as 0.1 the present approach is inappropriate. The rarity of such values justifies their exclusion from further discussion here.

Ad B 3. The wave number is derived from the measurement of the distance between two adjacent minima and, as such, is subject to the errors mentioned under B 1 and B 2. These errors are absolute errors, however, and as a rule there are a number of minima available over which the distance may be averaged. This reduces the relative error in k to such an extent that it may be omitted from further consideration, except for the lowest frequencies where errors of the order given under B 2 may prevail.

Ad B 4. The position of the sample surface is determined with a flat plate, fitted with a vertical bar consisting of plexiglass on which a calibrated scale has been engraved. The sample is introduced into its holder and the plate is placed on the smoothed surface. The scale is then sighted along the rim of the sample holder. The errors inherent in this procedure are so small compared to others that they may be neglected.

The sample-holder was usually filled completely, the material being levelled off to the rim of the holder.

Ad B 5. In interferometry, sound pressure is measured along the axis of the interferometer tube and the ideal instrument for this purpose would be an infinitely small microphone. Although the microphones used in interferometry are always small in relation to the wavelength, their dimensions are unfortunately finite and the e.m.f. at the electrical output terminals will be proportional to a weighted average of the various sound pressures prevailing at the microphone's surface. The e.m.f. is thus no longer a measure for the sound pressure at a given point.

Fortunately however there are microphones with 'pressure-sensitive points'. For such a microphone at a given frequency, the output e.m.f. is proportional to the sound pressure at the (pressure) sensitive point which is characterized by an invariant position in relation to the microphone, i.e. the proportionality factor referred to above is independent of the nature of the sound field in which the microphone is placed (thus for the interferometer, in a pressure maximum, in a minimum or between, for high or low standing wave ratio). The proportionality factor between the e.m.f. and the sound pressure in the sensitive point and the position of that point may vary with frequency. The position of the sensitive point should be determined experimentally as consideration of microphone construction may lead the unwary worker to fallacious conclusions, e.g. for the probe-tube microphone with a simple open-ended probe tube (a type popular in interferometry), the sensitive point might be imagined to lie in the centre of the orifice at the end of the tube. In fact it lies a fraction of a tube diameter ahead of that end.

In section 1-4 the procedure was described for eliminating the unknown position of the sensitive point experimentally, using a hard termination for the interferometer, a rigid plate to be referred to as the calibration plate. In the present context, the position of the sensitive point is being considered as a possible source of error and the question of the accuracy of determining its position thus arises.

In an interferometer terminated by a calibration plate the standing-wave ratio is high so wavelength may be determined with great accuracy and the first pressure minimum lies a quarter wavelength in front of the calibration plate. By adjusting the microphone to this minimum, the position of the sensitive point in relation to the microphone may be determined. Various authors, such as Scott (1946) and Lippert (1953) have investigated the positions of the sensitive points for various types of microphones. Figure 12 gives the distance between the sensitive point and the end of the probe tube as a function of frequency, for microphones with simple open-ended probe tubes. Lippert's (1953) values for

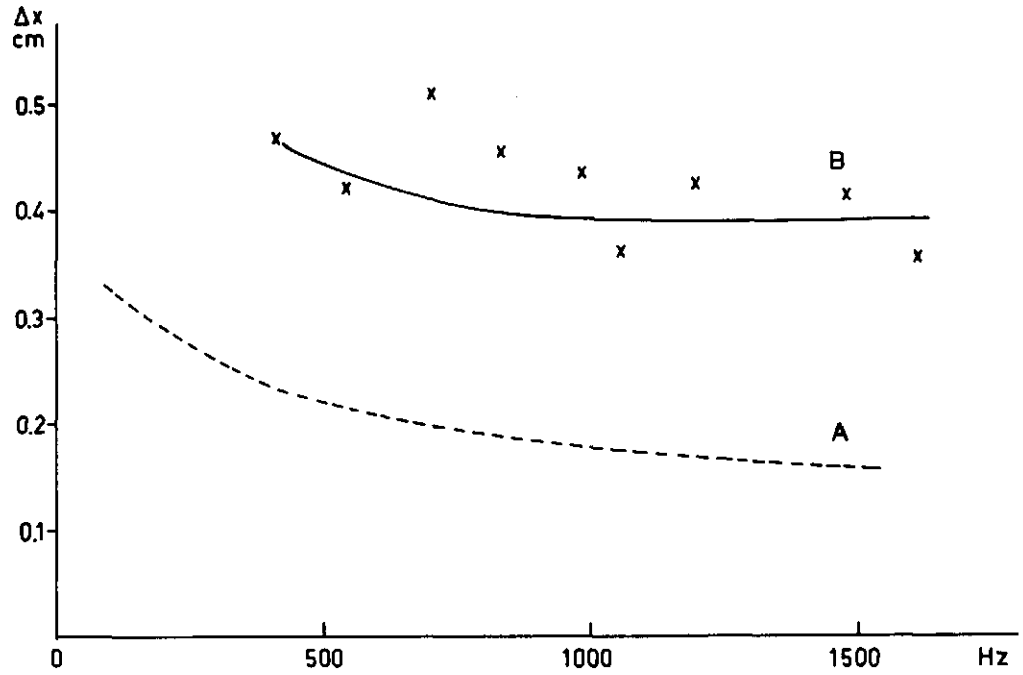

Figure 12 The deviation of the sensitive location from the end of the probe

a probe tube with inner and outer diameters of 2.8 and 4.7 mm, respectively, have been entered as curve A. The present author, using a probe tube with inner and outer diameters of 3.3 and 6.0 mm, respectively, found curve B. In order to show the accuracy attained, a number of the experimental points were entered into the graph. These points were specially selected as showing the largest deviations from the average curve, B.

Below 500 Hz, the accuracy of measurement is low. However, in view of the large wavelengths in this frequency range, comparatively large absolute errors in the position of the sensitive point can be tolerated. Thus, below 500 Hz, a uniform distance of 4 mm between the sensitive point and the tube end was assumed. Above that frequency, curve B was applied.

In the foregoing, the calibration plate was assumed to be rigid, i.e. immobile. Thick metal plates may be expected to meet this requirement, whether or not they are stiffness-controlled or mass-controlled (whether forces of elastic deformation or forces of inertia preponderate in the immobilisation of a plate). Signal departures from immobility are to be expected if a plate passes through mechanical resonance. Morse (1948) gives equations for the resonance frequencies of circular plates, clamped at their edges. One of his results may be

brought into the following form (his eq.(21.6))

$$f_{0.1} = 0.467\ h\ c_{pl}/a^2, \qquad (2\text{-}13)$$

where $f_{0.1}$ is the lowest resonance frequency, h is the thickness of the plate and a its radius and c_{pl} is the velocity of propagation of longitudinal waves in the plate.

The following numerical values for the steel calibration plate used with the large interferometer are introduced into eq.(2-13)

$h = 12$ mm, $a = 81$ mm, $c_{pl} = 5.3 \cdot 10^3$ m/s,

resulting in

$f_{0.1} = 4.5$ kHz.

This value for the lowest resonance frequency is probably rather higher than the value which would be found experimentally as the clamping of the plate at its edges is probably not completely rigid but somewhat compliant. Even so, the lowest resonance frequency is well beyond the operational frequency range of the interferometer and the calibration plate is thus stiffness-controlled in that range. Owing to its greater thickness, the resonance frequency of the piston under the sample is even higher and it is thus stiffness-controlled against deformation. As its weight is considerable, its position is mass-controlled.

The conclusion is, that the error B5 in establishing the microphone's sensitive point may be of the same order as the other errors in the position of the first minimum.

In summary the probable error in $k\delta x$ should not exceed 0.02 to 0.04 radians. Eq.(1-32) shows that the error in ϕ will be double these values.

The probable errors for $|r|$ (or a) and ϕ estimated above may be represented by error ellipses in the ζ plane. Size and shape of these ellipses vary considerably with their position in the plane, being smallest in the neighbourhood of + 1 (see figure 13). But the error ellipses prove to be of little practical importance.

In practice two samples prepared in an identical manner, as far as possible, show disparities in results far beyond the margins of error predicted by the ellipses. This leads to the usual conclusion for standing wave tube measurements, that the method of measurement is accurate enough, the main source of spread in the results being the lack of reproducibility in the preparation of the samples.

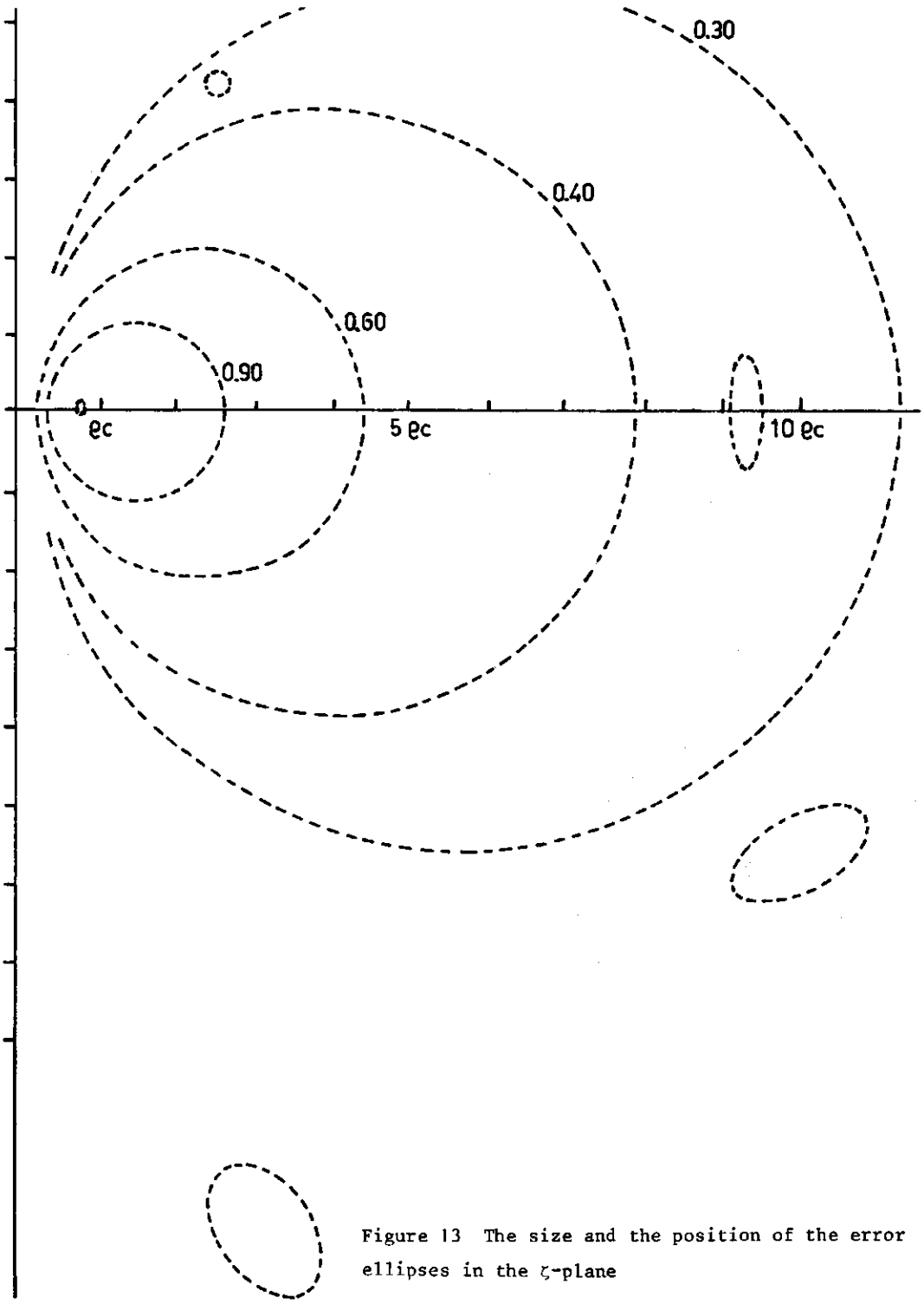

Figure 13 The size and the position of the error ellipses in the ζ-plane

3 The relation between the acoustical properties and the geometrical arrangement of pores in soils

3.1 Introduction

A soil sample is usually of a rather complicated composition, consisting of three phases: solid, liquid and gas. In the literature on soils the description of the sample is commonly approached from the build-up of the various aggregates in the solid phase and little attention is paid to the space surrounded by this phase: the pores. Sometimes attempts have been made to relate pore size and distribution with the processes of formation of the solid phase. Some studies on flocculation and sedimentation could be cited in this context, but literature on the subject is scarce and significant results can be found only in a few special cases.

The approach followed here is of a complementary nature, based on the arrangement of the pores rather than of the solid phase. Especially those pores in open communication with one another are of interest to the soil physicist, because gas-exchange or variation of moisture content play an important role in physical, chemical or biological processes in the soil.

Various methods of measurement have been developed to estimate characteristic quantities of the arrangement of the pores, total pore space often being the prime object. Ignoring transient methods, the stationary methods may be subdivided into a static group, discussed in the Introduction and to be discussed further in section 3.7, and a dynamic group. Various static methods have been developed for determining characteristic properties of the pore system and various authors have introduced various characteristic quantities. But the amount of information thus gathered is rather limited and dynamic methods of measurement extend the range of information available, at least in principle, as static methods restrict the frequency scale to the degenerate case of zero frequency.

Acoustic measurements fall into the dynamic group. Ernsthausen (1939) and Kaye-Evans (1949) were among the first to carry out such measurements, confining themselves to the determination of absorption coefficients. But no attempt was made to correlate the results with pore geometry.

Acoustical methods give rise to certain complications. A fairly obvious one is that the frame of solid matter, which is stationary in static methods of measurement, may be set into vibration in acoustical ones, thus complicating the inter-

pretation of the results. The vibrations will be especially pronounced for the resonance frequencies of the frame. Fortunately, for the majority of the samples considered here, frame damping was high enough to prevent significant frame vibration, even in resonance (see Appendix A).
Thus the assumption of a stationary frame is quite acceptable for most of the samples considered and departures from this assumption will be noted explicitly in future. It is customary to refer to stationary frames as 'rigid', although their immobility may well be due to inertia rather than to stiffness.
The interferometric method of measurement was selected for this book and here plane acoustic waves propagate in the sample. Now a second complication arises: the sample material must be homogeneous, at least in the direction of propagation, if significant quantitative results are to be obtained. Homogeneity, in the acoustic sense, implies that regions may be selected in the sample, large enough to be representative for the sample material, yet still small in relation to wavelength.
A related complication is caused by the assumption of a plane interface, where the properties of the medium change discontinuously from those of the gas (air) in the interferometer tube to those of the sample. For coarse, granular materials there is no clear plane of discontinuity but a transitional range and the scientist can only estimate a position for an equivalent interface somewhere in this range, thus introducing an element of uncertainty in his results.
A restriction, which is not fundamentally essential but does facilitate the interpretation of the results, is confinement to what amounts acoustically to a two-phase system: a solid frame enclosing pores which are completely filled with water and are thus immobilized for sound propagation, and interconnected gas-filled pores. In other words: all menisci are assumed to be immobilized. The samples selected for quantitative evaluation all belong to this group.
The variation of the moisture content of the pore system has a pronounced effect on the acoustic properties of the sample, but in the present stage of investigation the reduction of the observed effects to characteristic quantities of the sample material does not seem feasible.

Sample materials consisting of a rigid frame containing interconnected pores were formally introduced in section 1.9. Acoustically, such materials are completely defined by a pair of frequency-dependent complex quantities. As such, Z_m and Y_m are appropriate (eqs(1-52) and (1-53))but W_m and γ_m may serve just as well (eqs(1-54) and (1-55)). In view of the simplicity of the latter two equations, the two pairs of quantities may be considered equivalent.

A point of some significance may be read from the formulation of eqs(1-52) and (1-53). Z_m describes the flow of the gas through the pores and Y_m is determined by the compressibility of the gas in the pores. Both Z_m and Y_m are affected by the pore geometry and thus knowledge of Z_m as a function of frequency yields information on the configuration of the pores through which the gas flows; Y_m does the same thing for the pores in which the gas is compressed. The information thus obtained is too limited to permit anything approaching a comprehensive description of pore geometry. However, some characteristics of that geometry can be obtained and here acoustical methods do supply more information than static ones.

In section 1.9 the simple suggestion was introduced that two effects contribute to Z_m: the forces of inertia and those of viscous friction working on the gas, the corresponding quantities for Y_m being the compressibility of the gas, taking the presence of the frame into account, and heat-exchange between the gas and the frame. This simple picture is untenable for a number of porous materials, a case in point being materials containing side holes. A configuration of this kind is illustrated in figure 14: a side hole is connected to a channel by an

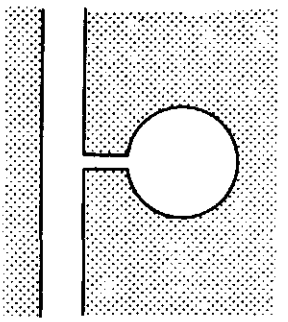

Figure 14 A side hole

orifice. The presence of the hole hardly affects the flow of the gas through the channel, but the presence of the extra volume of the hole does increase the acoustic compressibility of the gas in the channel, as long as frequency is not too high. For sufficiently high frequencies, the viscous resistance of the orifice will impede the gas exchange between the side hole and the channel and the acoustic compressibility will decrease to the value for the channel alone for very high frequencies. In this example, a viscous effect contributes to the frequency-dependence of Y_m.

Eq.(1-56) is the fundamental equation for deriving the properties of the sample material from the experimental values of the specific acoustic impedance of the sample surface Z. One measurement for one sample thickness and for a given

frequency yields only one complex quantity and if Y_m and Z_m are to be determined separately at least one further measurement at the same frequency is essential. Obvious solutions to this problem are: a change in sample thickness or the replacement of the rigid back-plate of the sample by another, known backing impedance (in the latter case, a modified version of eq.(1-56) must be used).
The method of variable sample thickness was followed in some cases but was inapplicable in others. Many materials, especially those of granular composition, are extremely sensitive in geometrical configuration and any mechanical interference with the sample tends to alter the acoustical properties of the material. For such materials, another solution must be sought.
The solution adopted here assumes a pore geometry, characterized by a limited number of parameters, not departing too far from reality but still simple enough to be amenable to calculation. Such a geometric arrangement can be conceived as a mathematical model and will yield a locus for Z in the complex impedance plane for variable frequency and constant sample thickness. By variation of the parameters a family of such loci may be generated. Measurements on the sample are also carried out for variable frequency and constant sample thickness and the resulting experimental locus for Z is compared to the family of theoretical ones. The numerical values of the parameters pertaining to the theoretical locus giving the best fit are accorded the status of characteristic quantities of the sample material.
As an example, a very simple model for pore geometry is considered, consisting of identical circularly cylindrical tubes drilled into the frame material in the direction of propagation of the acoustic waves. This model has only two parameters : the tube radius and the number of tubes per unit area. A more sophisticated version is obtained by drilling all the tubes at the same angle to the direction of propagation, thus introducing a third parameter. In fact, an infinite variety of arrangements may be postulated with any number of parameters. As will become clear in chapter 4 however, the introduction of more parameters beyond a fairly low limit does not increase information about the sample material.
A serious defect of the procedure considered is that Z_m and Y_m cannot be determined separately and thus that differentiation between effects due to gas flow and effects due to gas compression is impossible.
The principal aim of this chapter is the consideration of the various procedures for obtaining characteristic material constants from interferometric measurements. In this context, the following subjects will be discussed in more detail.

1. The method of Ferrero & Sacerdote (1960), which is founded on the use of very thin samples, permitting analytical approximation of the transcendental function appearing in eq.(1-56).

2. A method based on the use of two or more sample thicknesses, incorporating a graphical aid for the solution of eq.(1-56).

3. A simple mathematical model by Zwikker & Kosten (1941), which employs three parameters and does not require specification of the pore geometry.

4. The applicability of rules of proportionality for porous materials.

5. The formulation of two variants of the channel-type geometrical model, the channels consisting of circular cylindrical tubes in one case and of fissures in the other. The channels are inclined at a constant angle to the direction of propagation and have variable cross-sections. Besides the restrictions mentioned before (rigid frame, no liquid flow) a further assumption is added: the frame possesses sufficient thermal inertia to ensure that its temperature may be considered constant.

6. The formulation of a geometrical model for prismatic structures. These occur in heavy clay and slaked soils when dehydrated. This model allows for side holes.

7. The possibility of composing an analogous electrical circuit of the transmission-line type for the porous material. Essentially such a circuit would not contribute new information but might help in the understanding of wave propagation in porous materials.

3.2 Numerical examples of calculating Z_m and Y_m from measurements at layer thicknesses

Various authors have introduced different representations for Z_m and Y_m. Following Ferrero & Sacerdote (1960), modifying their notation slightly, the two quantities can be presented in the following general form:

$$Z_m = \sigma_m + j\omega\rho_m \tag{3-1}$$

$$Y_m = G_m + j\omega C_m \tag{3-2}$$

where the values of the real material constants σ_m, ρ_m, G_m and C_m may be frequency dependent. The material constants are the specific flow resistance of the material, the effective density, the conductance and the reciprocal of the effective compression modulus, respectively.

At low frequencies, air movement in the material will be hampered particularly

by viscous forces originating from friction along the walls of the capillary tubes in the porous material. In these cases a velocity distribution, as assumed in the Poiseuille flow, can be adopted and then σ_m stands for the static specific flow-resistance in the material. At higher frequencies, the air will oscillate more like a plug. Although it is customary to refer to high frequencies when the linear dimensions of the pore system under consideration are large in relation to wavelength, a modified criterion is intended here: the frequency is considered high when the linear dimensions are large relative to boundary-layer thickness. The viscous boundary layer thickness is given, for example, by Crandall (1927) and appears in this book as eq.(B-3).

In a cylindrical tube, σ_m decreases with frequency, as the boundary layer thickness decreases, and so does ρ_m, as air flow is less restricted to the centre of the tube.

In eq.(3-2), C_m represents the compliance of the gas in the pores, taking into account the reduction of the available space owing to the finite volume of the solid or liquid matter. If for example the porosity is 10%, the value of C_m becomes 10% of its value in free air. Sections 1-9 and 3-2 described dissipative mechanisms associated with compression; the results of such losses is represented by the term G_m. As far as the thermal losses are concerned, the situation is partly analogous to that of viscous losses. Provided that frequency is high, in the sense discussed above (see eq.B-14), the changes in state of the gas are nearly adiabatic.

For low frequencies those changes in state are nearly isothermal and in this case thermal losses are low. For such frequencies viscous losses are however high. Thermal effects are discussed by Kirchhoff (1927) and Zwikker & Kosten (1948).

Making use of eqs(1-54) and (1-55), eqs(3-1) and (3-2) may be written as:

$$\sigma_m + j\omega\rho_m = \gamma_m W_m \tag{3-3}$$

$$G_m + j\omega C_m = \gamma_m / W_m \tag{3-4}$$

Eqs(3-3) and (3-4) show that the four characteristic quantities, σ_m, ρ_m, G_m and C_m may be calculated from experimentally derived values of the complex quantities γ_m and W_m. These latter quantities require at least two measurements for a given frequency, as one measurement on one sample yields only two values.

The technique developed by Ferrero & Sacerdote (1960) attempts to circumvent this problem by performing measurements on very thin samples. One of the princi-

pal mathematical problems in reducing the experimental data is the transcendental function appearing in eq.(1-56),but for thin samples, the argument of the function is small and the latter may be developed into a series:

$$\coth(z) = (1 + z^2/3 + \ldots)/z. \tag{3-5}$$

Introducing ξ and η from eq.(1-28), using eq.(3-5) and assuming slight damping ($\sigma_m << \omega\rho_m$; $G_m << \omega C_m$), eqs(3-3) and (3-4) may be reduced:

$$\rho_s c\, \xi \approx \frac{G_m}{\omega^2 l C_m^2} + \frac{1}{3}\sigma_m l, \tag{3-6}$$

$$\rho_s c\eta \approx -\frac{1}{\omega l C_m} + \frac{1}{3}\omega l \rho_m. \tag{3-7}$$

It can be seen from the right sides of eqs(3-6) and (3-7) that the first two terms differ considerably in their frequency-dependence from the second two. Now, provided the characteristic quantities are slow functions of frequency, separation of the terms might be feasible, thus permitting the calculation of all four quantities. The equations

$$d(\rho_s c\eta/\omega)/d\omega \approx 2/(\omega^3 l C_m),$$

$$d(\rho_s c\xi)/d\omega \approx -2G_m/(\omega^3 l C_m^2),$$

yield G_m and C_m. A change of sample thickness l opens similar possibilities. This technique offers little possibilities in practice. In thin samples with a rigid backing there is only little gas flow and quantities such as σ_m and ρ_m, which represent the forces of viscous resistance and inertia, cannot be expected to affect the surface impedance substantially. The second terms in the right sides of eqs(3-6) and (3-7) are quite small in relation to the first. Owing to the accuracy of acoustic measurements, the separation of the terms cannot be achieved; a feasible approach is to neglect these small second terms, thus confining the use of eqs(3-6) and (3-7) to the calculation of G_m and C_m.

The accuracy of the results for the material constants for two different systems of interferometric measurement will be demonstrated with a numerical example. A fictitious porous material is considered having representative values for the characteristic material constants. For a given frequency, the standing wave ratio and the phase angle in the interferometer tube are calculated for various

thicknesses of the sample. The standing wave ratios and phase angles thus found are then approximated in accordance with the finite accuracy of interferometry (see section 2-6). The material constants are then calculated from these rough values, using the two systems, both of which require measurements at two sample thicknesses. Finally, the results for the constants are compared with initial values.

The fictitious porous material is acoustically determined by:

$\rho_m = 10\ kg/m^3$; $\sigma_m = 3 \cdot 10^4\ Ns/m^4$

$C_m = 3 \cdot 10^{-6} m^2/N$; $G_m = 1.5 \cdot 10^{-3}\ m^2/Ns$.

The measuring frequency is 250 Hz, the sample holder has a rigid back plate (see section 1-9 and 2-2), 7 sample thicknesses l, from 0.01 to 0.5 m, are considered and the air column in the interferometer is characterized by:

$\rho_s c = 410\ Ns/m^3$.

Table 3-1 gives the numerical results. The specific acoustic impedance at the sample surface Z_1 and its normalized version ζ_1 were calculated with the aid of eqs(1-56), (3-3) and (3-4). The modulus $|r_1|$ and the angle ϕ_1 of the reflection coefficient were obtained from eq.(1-57). The standing wave ratio s_1 and the absorption coefficient a_1 follow from eqs(1-37) and (1-38), respectively. The rough values for s_1 and ϕ_1, s_2 and ϕ_2, respectively, are presented in table 3-2. This table also lists the normalized specific acoustic impedance at the sample surface, ζ_2, the modulus $|r_2|$ of the reflection coefficient and the

Table 3-1

Standing wave ratio and phase angle, calculated from material constants

l (m)	Z_1 (10^3.Nsm^{-3})	ζ_1 (+)	$\lvert r_1 \rvert$ (+)	a_1 (+)	ϕ_1 (radians)	s_1 (+)
0.01	6.225 - 19.22 j	15.18 - 46.88 j	0.9874	0.026	0.0386	157.7
0.025	2.703 - 7.576 j	6.591 - 18.48 j	0.9665	0.0659	0.0966	58.70
0.05	1.701 - 1.647 j	4.148 - 8.896 j	0.9181	0.1571	0.1845	23.42
0.10	1.673 - 1.516 j	4.080 - 3.697 j	0.7658	0.4135	0.2472	7.540
0.15	2.033 - 0.9018 j	4.957 - 2.200 j	0.7130	0.4917	0.1485	5.968
0.25	2.467 - 0.9283 j	6.068 - 2.264 j	0.7466	0.4426	0.1117	6.893
0.50	2.420 - 0.995 j	5.903 - 2.427 j	0.7477	0.4410	0.1217	6.927

absorption coefficient a_2, as obtained from s_2 and ϕ_2 by the reverse process of calculation.

Table 3-2

Impedance calculated from standing wave ratio and phase shift, read in the impedance diagram

l (m)	s_2 (+)	$\lvert r_2 \rvert$ (+)	ϕ_2 (°)	ϕ_2 (radians)	a_2 (+)	ζ_2 (+)
0.01	157	0.987	- 2	- 0.0349	0.026	19. - 50 j
0.025	59	0.966	- 5.5	- 0.0960	0.067	6.7 - 18.5 j
0.05	23.4	0.918	- 10.5	- 0.1833	0.157	4.2 - 9.0 j
0.10	7.5	0.765	- 14	- 0.2443	0.415	4.1 - 3.7 j
0.15	6.0	0.714	- 8.5	- 0.1484	0.49	5.0 - 2.18 j
0.25	6.9	0.747	- 6.5	- 0.1135	0.44	6.0 - 2.29 j
0.50	6.9	0.747	- 7	- 0.1222	0.44	5.9 - 2.43 j

The first system of deriving the material constants from the supposedly measured results in table 3-2 uses the fact that for infinitely thick samples, the specific acoustic impedance at the sample surface equals the wave impedance of the sample material: $Z = W_m$. Consider the transcendental factor in eq.(1-56);

$$\coth\left[(\alpha_m + j\beta_m)l\right] = \left[1 + \exp(-2\alpha_m l - 2j\beta_m l)\right] / \left[1 - \exp(-2\alpha_m l - 2j\beta_m l)\right]. \qquad (3\text{-}8)$$

For large values of $\alpha_m l$, $\exp(-2\alpha_m l)$ is small and eq.(3-8) may be approximated to:

$$\coth\left[(\alpha_m + j\beta_m)l\right] \approx 1 + 2 \cdot \exp(-2\alpha_m l) \cdot \exp(-2j\beta_m l). \qquad (3\text{-}8a)$$

For variable l this function is a logarithmic spiral in the complex plane with its apex at +1. In the present sense, $\alpha_m l$ is large at numerically moderate values. Thus, for $\alpha_m l > 2.1$, the spiral is within an absolute distance of 0.03 from its apex, and in this range the sample behaves as though infinitely thick. In the present instance the difference in results for l = 0.25 m and l = 0.50 m is so small that no great error will results if the value found for l = 0.50 m is assumed to hold for an infinitely thick sample.

Replacing ζ_2 by $(\zeta_2)_\infty$ and selecting a second measurement for a sample thickness l, yielding $(\zeta_2)_l$, the derivation leads to

$$(\zeta_2)_1/(\zeta_2)_\infty = \coth\left[(\alpha_{m2} + j\beta_{m2})1\right]. \qquad (3\text{-}9)$$

Selecting 1 = 0.05 m for the finite value of 1 and assuming the value of ζ_2 for 1 = 0.5 m to be an adequate approximation of that for 1 = ∞, eq.(3-9) and table 3-2 yield the following numerical results:

$W_{m2} = (2.42 - 1.00\ j)\cdot 10^3\ Ns/m^3$,

$\coth\left[(\alpha_{m2} + j\beta_{m2})1\right] = 1.1535 - 1.054\ j$, 1 = 0.05 m.

The solution of the equation:

$\tanh(x + jy) = a + jb$,

derived from the nomograms in Rybners book (1947, p.27) prove to be rather inaccurate; the exact solutions are to be prefered:

$$\tanh(x) = \left[a^2 + b^2 + 1 - \sqrt{((a^2 + b^2)^2 - 2(a^2 - b^2) + 1)}\right]2a, \qquad (3\text{-}10)$$

$$\tan(y) = \left[a^2 + b^2 - 1 - \sqrt{((a^2 + b^2)^2 - 2(a^2 - b^2) + 1)}\right]2b, \qquad (3\text{-}11)$$

x and y following to the desired degree of accuracy from the relevant tables. The numerical result in the present case is:

$\alpha_{m2} + j\beta_{m2} = (8.1 + 9.9\ j)m^{-1}$.

The numerical values for the material constants now follow eqs(3-3) and (3-4):

$\rho_{m2} = 9.9\ kg/m^3$; $\sigma_{m2} = 2.9\cdot 10^4\ Ns/m^4$

$C_{m2} = 2.9\cdot 10^{-6}\ m^2/N$; $G_{m2} = 1.43\cdot 10^{-3}\ m^2/Ns$.

Agreement with the initial values is quite good, apparently the approximations introduced have had only a slight adverse effect. The method has disadvantages when applied to the measurements in this book, not only because of the disturbance of the sample when altering its thickness but also because soil samples are rarely homogeneous over the necessary thickness. The further disadvantage of the amount of material required for a sample which can be considered infinitely thick may be avoided by extrapolation from finite thicknesses. An appropriate graphical method will be described in section 3-4.

The second method to be investigated follows Ferrero & Sacerdote (1960). Two thin samples are considered, having 1 = 0.01 m and 1 = 0.025 m. Eqs(3-6) and (3-7) are used, neglecting the second terms in the right sides. The results for C_m and G_m are given under C_{m3} and G_{m3} in Table 3-3. This table also lists the quantity $\rho_s c\xi/1$, which should be inversely proportional to 1^2 if all the approxi-

Table 3-3

The material constants calculated according the method of Ferrero & Sacerdote

l	C_{m3}	$\rho_s c\xi/l$	G_{m3}
(m)	($N^{-1}m^2$)	(Nsm^{-4})	($N^{-1}s^{-1}m^2$)
0.01	$3.1 \cdot 10^{-6}$	$7.8 \cdot 10^{5}$	$2.0 \cdot 10^{-3}$
0.025	$3.4 \cdot 10^{-6}$	$1.1 \cdot 10^{5}$	$1.8 \cdot 10^{-3}$

mations introduced were justifiable. Thus the ratio of the two values appearing in Table 3-3 should be 6.25:1, in fact this ratio is practically 7:1.
The mean values taken from Table 3-3 are:

$C_{m3} = 3.25 \cdot 10^{-6}\ m^2/N$; $G_{m3} = 1.9 \cdot 10^{-3}\ m^2/Ns$.

They agree poorly with the initial values. The approximations are unsatisfactory. In particular the assumption of slight damping, which means neglecting G_{m2} relative to ωC_{m2}, is questionable. The method seems to need higher precision than is practically attainable. One of the principal limitations is the large error in measuring the very small phase angles for thin samples.

3.3 The logarithmic impedance plane as a tool for the numerical evaluation of W_m and γ_m

The complex $\ln(\zeta)$ plane may be of assistance if the normalized specific acoustic impedance ζ of the sample surface has been determined from measurement at a fixed frequency and for variable sample thickness l and the aim is the determination of the material constants, e.g. the complex constants W_m and γ_m. From eqs(1-28) and (1-56) it follows that:

$$\ln\zeta = \ln(W_m/\rho_s c) + \ln \coth(\gamma_m l). \qquad (3\text{-}12)$$

The first term on the right side of eq.(3-12) is independent of l; the second term determines the form of the locus in the $\ln\zeta = x + jy$ plane for variable l, and $\ln(W_m/\rho_s c)$ determines its position.
The quantities

$$\Delta = \alpha_m/\beta_m \text{ and } q = 2\beta_m l \qquad (3\text{-}12a)$$

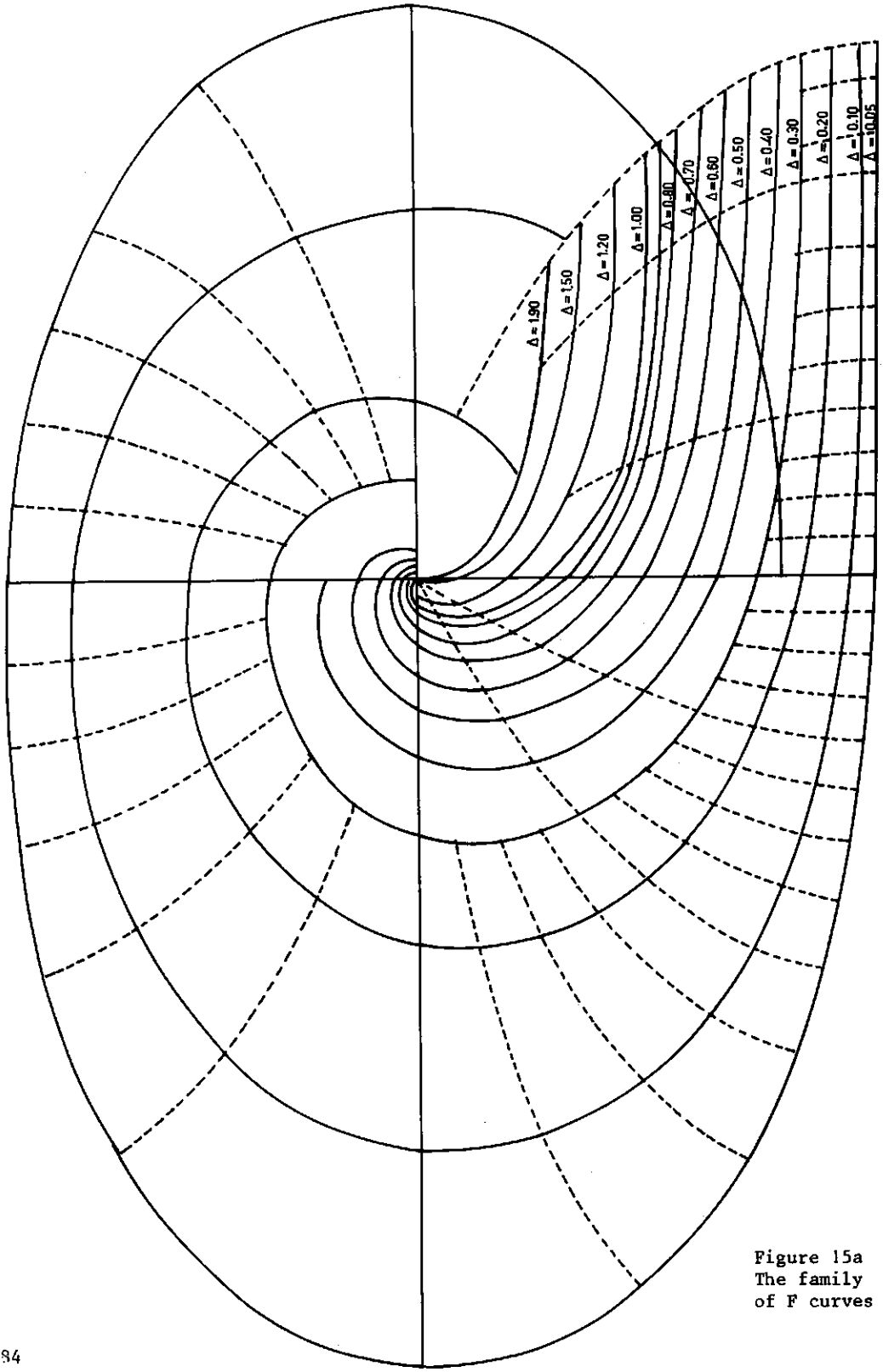

Figure 15a
The family
of F curves

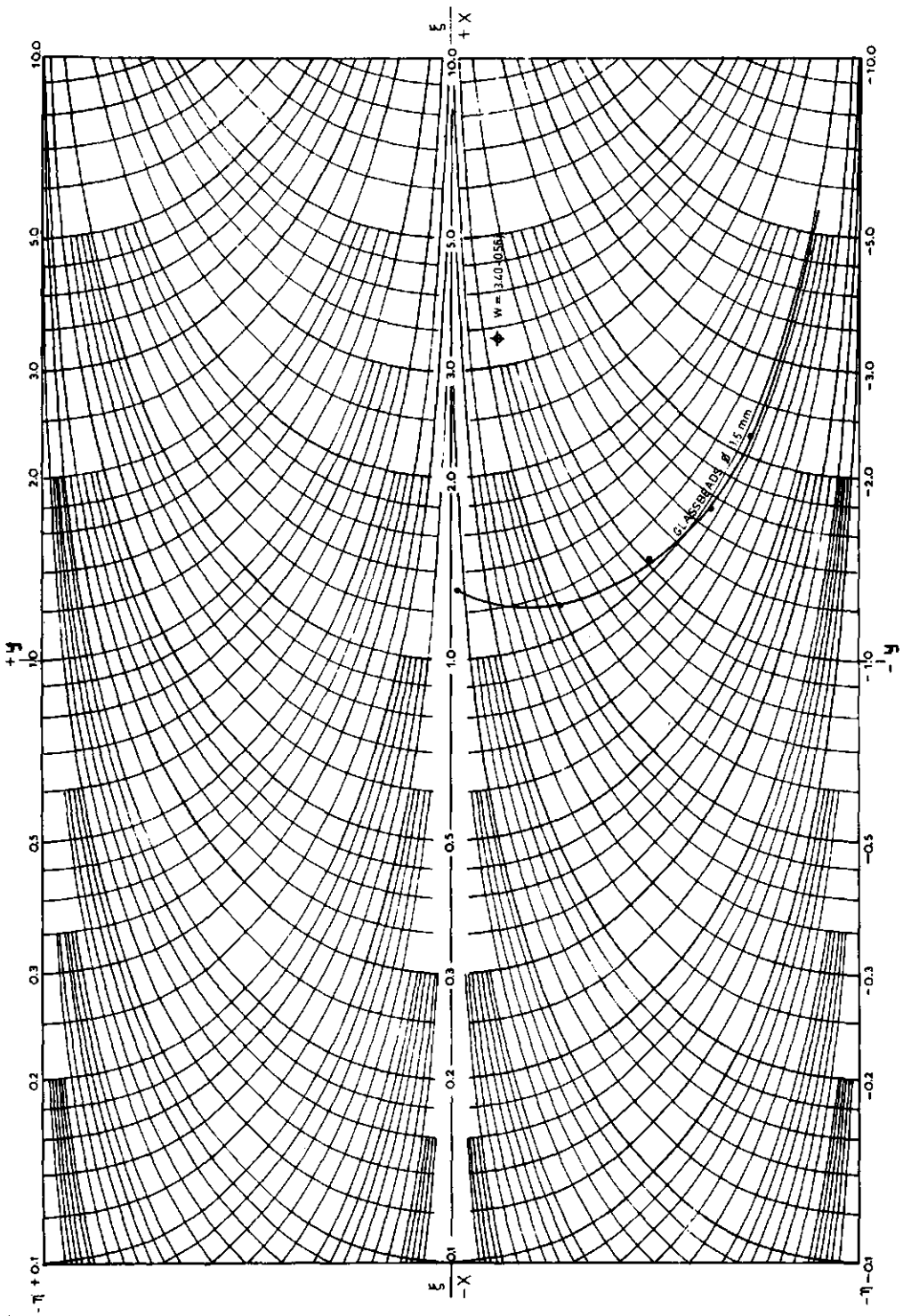

Figure 15b The complex ln ζ plane

are introduced and the locus of the function:

$$F = \ln \coth(\gamma_m l) = \ln \coth\left[\tfrac{1}{2}(\Delta + j)q\right], \tag{3-13}$$

in the complex x',y' plane is investigated for variable q and with Δ as parameter. As q approaches infinity, the argument of the natural logarithm in eq.(3-13) approaches unity and F approaches zero, the origin of the x',y' plane. A family of curves for F for a series of values of Δ now be constructed and plotted on transparent paper. The curves prove to have the form of a spiral (figure 15a). The experimental values for $\ln\zeta$ have been entered in the x,y plane. The x',y' plane, carrying the loci for F, is now placed on the x,y plane and shifted until the locus for F best fits the experimental points, keeping the x and x' axes (or y and y' axes, respectively) parallel. Under these conditions, the position of the origin of the x',y' plane lies at the point $\ln(W_m/\rho_s c)$ in the x,y plane; the use of the $\ln\zeta$ plane is essentially the extrapolation of the spiral for $\ln\zeta$ to its apex, the point for infinite layer thickness, which is determined by the specific acoustic wave impedance of the material, W_m. Once W_m is known, various paths are open for the determinaton of $\gamma_m = \alpha_m + j\beta_m$. The best fitting spiral for F yields some information on the value of α_m/β_m, if the associated value for Δ is known.

Let the apex of the spiral for $\ln\zeta$ be determined by $\zeta = \xi_0 + j\eta_0$, ξ_0 and η_0 being the quantities yielding the real and imaginary parts of W_m, after multiplication by $\rho_s c$ (see eq.(3-12)). A rapid estimate for ξ_o and η_o is facilitated if the loci ξ = constant and η = constant are entered in the x,y plane. From

$$x + jy = \ln(\xi + j\eta), \tag{3-14}$$

it follows that

$$x = \tfrac{1}{2}\ln(\xi^2 + \eta^2)\ ;\ y = \arctan(\eta/\xi). \tag{3-15}$$

In eq.(3-15), y has more than one value. It is the phase angle of the wave impedance of the sample. As passive samples only are considered, $\xi \geq 0$, and the imposition of the condition:

$$-\pi/2 \leqslant y \leqslant \pi/2, \tag{3-16}$$

does not entail a loss of generality. It may now be seen from eq.(3-15) that y

and η must be accorded the same sign.
Solving eq.(3-14) for ξ and η yields

$$\exp(x) \cdot \cos(y) = \xi, \tag{3-17}$$

$$\exp(x) \cdot \sin(y) = \eta. \tag{3-18}$$

Eqs(3-17) and (3-18) are useful for the calculation of the loci. Then these equations may be brought into the form:

$$\exp\left[x - \ln \xi\right] \cdot \cos(y) = 1,$$

$$\exp\left[x - \ln|\eta|\right] \cdot |\sin(y)| = 1,$$

and from this formulation it will be seen that a change in one of the parameters, either ξ or $|\eta|$, corresponds to a parallel shift of the locus in the x direction. It is thus sufficient to calculate the locus, for example, for constant ξ selecting a simple value for ξ (as such $\xi = 1$ springs to mind) and to obtain the other loci by shifting the curve along the x axis. The loci thus calculated may be applied to the construction of those for constant η by substituting $y = 2 + \pi/2$, allowing that negative values of y correspond to negative values of η. The family of curves for constant ξ and that for constant η intersect orthogonally, eq.(3-14) representing a conformal transformation (see figure 15b).

The construction of a family of curves for F in the x',y' plane (see eq.(3-13)) presents more difficulties. Reduction of equations given by Rybner (1947, p.25) yields

$$x' = \tfrac{1}{2} \ln \left[\frac{\cosh \Delta \cdot q + \cos q}{\cosh(\Delta \cdot q) - \cos q}\right], \tag{3-19}$$

$$y' = - \arctan \left[\frac{\sin q}{\sinh(\Delta \cdot q)}\right]. \tag{3-20}$$

These equations give the spirals in parametric form. As mentioned previously, the asymptotic point for large values of q is $x' = y' = 0$; for small values of q the spiral approaches an asymptote given by:

$$y' = - \operatorname{arccot}(\Delta).$$

With a Fortran programme, the co-ordinates x',y' for spirals corresponding to 14 values of Δ were generated.

The ln ξ plane was used to determine the normalized specific acoustic wave impedance of the sample material in a number of cases. As an example, a number of measured points for various sample thicknesses at one frequency have been entered in Figure 15b. In this cas., the best fit is obtained for a spiral having an estimated parameter $\Delta = 0.25$, and the result for the wave impedance is estimated at

$$W_m/\rho_s c = 3.40 - 0.56\ j$$

A Fortran programme was devised to calculate the other material constants.

The ln ξ plane, considered as a tool for estimating the wave impedance of the sample material, has several drawbacks. There are areas where the accuracy in reading ξ and η is small, especially near the asymptotes. This disadvantage can be avoided only by dropping the conformality of the transformation, eq.(3-14), and stretching the plane uniformly in the y direction.

3.4 The simple model of Zwikker & Kosten

As was discussed in Section 3.1, methods of interferometry requiring variation of the sample thickness are not feasible for soil samples, and so an alternative procedure will be followed here, based on variation of frequency and involving the introduction of a mathematically accessible model for the sample material. The first of such models to be considered is a simple model from Zwikker & Kosten (1941), which can be considered as a base for the other models. Subsequent extension of the simple model will be ignored here.

The principal task of the models is to predict the frequency-dependence of the material constants, and in the present context the specific acoustic series impedance per unit length Z_m and the specific parallel admittance per unit length Y_m (see Section 1-9, eqs(1-52) and (1-53)) are selected as such. The models are introduced to limit the number of parameters.

The first model allows for the fact that only a part h (the porosity) of the total volume is available for compression and expansion of the gas, but that the changes in state are adiabatic. These considerations yield

$$Y_m = j\omega h/\kappa p_s. \tag{3-21}$$

The viscous losses are accounted for in Z_m by the introduction of the specific flow-resistance σ_m. The forces of intertia are also incorporated in Z_m. The fact that the average particle velocity in the pores is a factor 1/h higher than the volume velocity per unit area of the material, suggests the introduction of that factor in the term corresponding to the effects of inertia. There are, however, further effects which tend to increase this term, one of the principal ones being the irregularity of the pores. These effects are accounted for by the introduction of the structure factor k_m in the term $j\omega\rho_m$. The above considerations yield

$$Z_m = \sigma_m + j\omega\rho_s k_m/h. \tag{3-22}$$

To start with, σ_m is considered frequency-dependent. In the simple model it is equated with its static value σ_s, which is defined by

$-\partial p/\partial x = \sigma_s u$, where p and u are time-independent.

Comparison of the present notation with that introduced in Section 3.2, eqs (3-3) and (3-4), shows:

$$\rho_m = k_m \rho_s / h \quad ; \quad \sigma_m = \sigma_s, \tag{3-23a,23b}$$

$$C_m = h/\kappa p_s \quad ; \quad G_m = 0. \tag{3-24a,24b}$$

To familiarize the reader with the concept of structure factor, two special cases will be discussed.

1. The porous material consists of uniform tubes, all at an angle θ to the direction of propagation. The particle velocity in the tubes can be presented as $u/h \cos\theta$, the pressure gradient along the tubes as $-\rho_s \frac{\partial}{\partial t} u/h \cos\theta$, and the pressure gradient in the direction of propagation (the x direction) in the equation:

$$\frac{\partial p}{\partial x} = - \frac{1}{\cos\theta} \cdot \rho_s \frac{\partial}{\partial t} \frac{u}{h \cos\theta},$$

so that now $k_m = 1/\cos^2\theta$.

2. The porous material consists of tubes parallel to the direction of propagation but with cross-sections $S = S(x)$ according to location. The average cross-section is given by

$$S_a = \frac{1}{l} \int_o^l S(x)\, dx.$$

It is assumed that, for sufficiently large values of l, S_a approaches a limit, which is the same for all tubes.

The function f is defined by

$$f(x) = S(x)/S_a. \tag{3-25}$$

With N tubes per unit surface area, the porosity follows as

$h = N S_a$,

and the particle velocity in a tube, u_d, follows from

$$u_d = \frac{u}{N S_a f(x)} = \frac{u}{h} \frac{1}{f(x)}$$

The pressure gradient can be presented as

$$\frac{\partial p}{\partial x} = - \rho_s \frac{\partial}{\partial t} \frac{u}{h f(x)},$$

and its average value is

$$\frac{\partial p}{\partial x} = -\frac{\rho_s}{h} \cdot \frac{\partial u}{\partial t} \cdot \frac{1}{l}\int_o^l \frac{1}{f(x)}\,dx,$$

so that, in this case

$$k_m = \frac{1}{l}\int_o^l \frac{1}{f(x)}\,dx, \qquad (3\text{-}26)$$

where l must be so large that its value no longer affects k_m, yet still small relative to wavelength (and in which f(x) must be in agreement with eq.(3-25)). The right side of eq.(3-26) is stationary for f(x) = 1 and has reached a minimum value. Thus k_m is larger than unity in the general case. This is made clear in the following derivation.

Substitute $f(x) = 1 + \delta(x)$, where $|\delta| \ll 1$ and where, in accordance with eq. (3-25)

$$\frac{1}{l}\int_o^l \delta(x)dx = 0.$$

Developing the integrand in eq.(3-26) yield

$$k_m = \frac{1}{l}\int_o^l \left[1-\delta(x)+\delta^2(x) - \delta^3(x) \ldots.\right]dx = 1+\frac{1}{l}\int_o^l \left[\delta^2(x)-\delta^3(x) \ldots.\right]dx$$

In the limiting case $|\delta| \to 0$, the first term of the integral, which is positive, is dominant. Hence: $k_m > 1$.

The literature (Kosten, 1941; Bies, 1964) shows that for many acoustical materials k_m is considerably larger than unity; values from 3 to 10 occur. Since similar combinations of parameters may correspond with very different arrangements, the experimental determination of the three independent quantities characteristic for the present model supplies only limited information on the pore distribution of the material.

In figure 16 cross-sections of porous materials are given. For every cross-section an estimate is made of the values for porosity, flow-resistance and structure factor. This drawing gives an idea of the complexity of the arrangement in the pore system.

The prediction of k_m from pore geometry is possible only for simple spatial arrangements. Soil samples do not belong to this class and give rise to a further complication as a change in moisture content of the sample introduces substantial changes in acoustical properties: not only the structure factor but

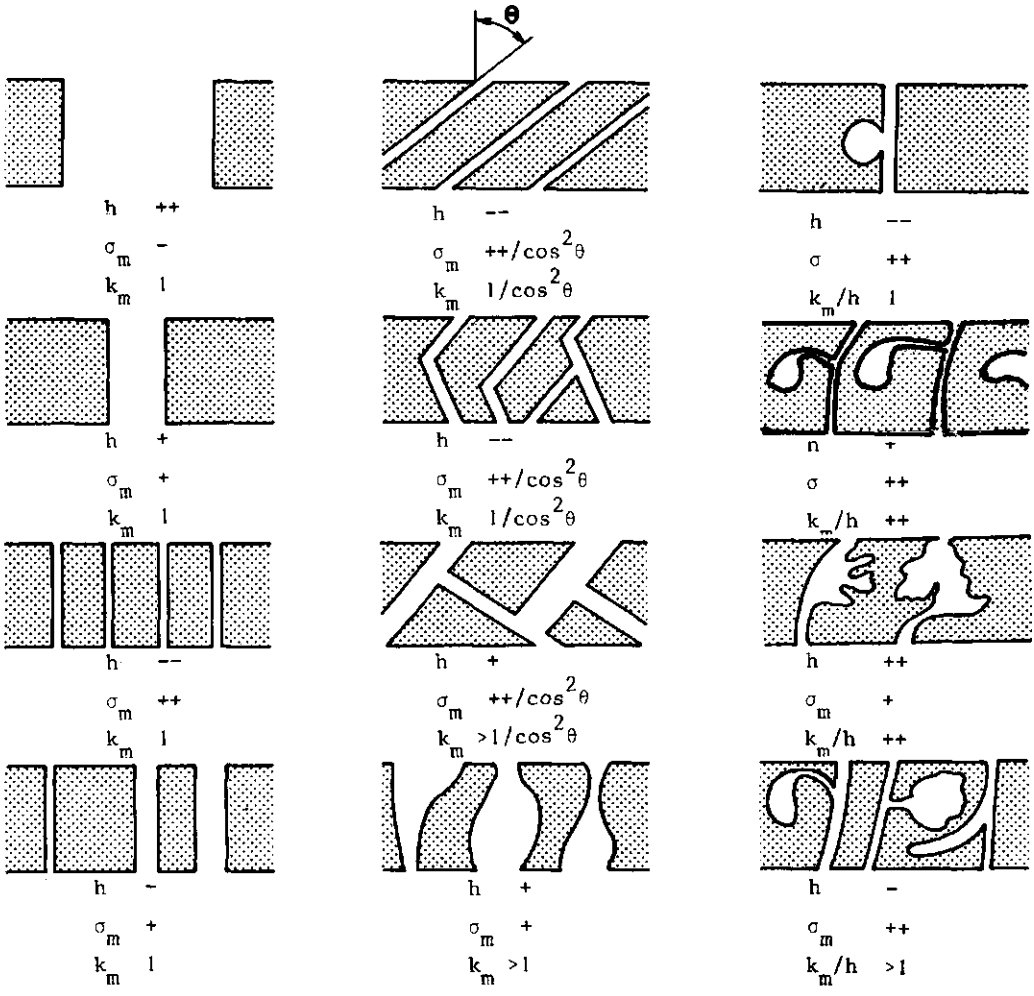

-- = very small

- = small

+ = large

++ = very large

Figure 16 Influence of the geometry of the pore system on the value of h, σ_m and k_m, respectively

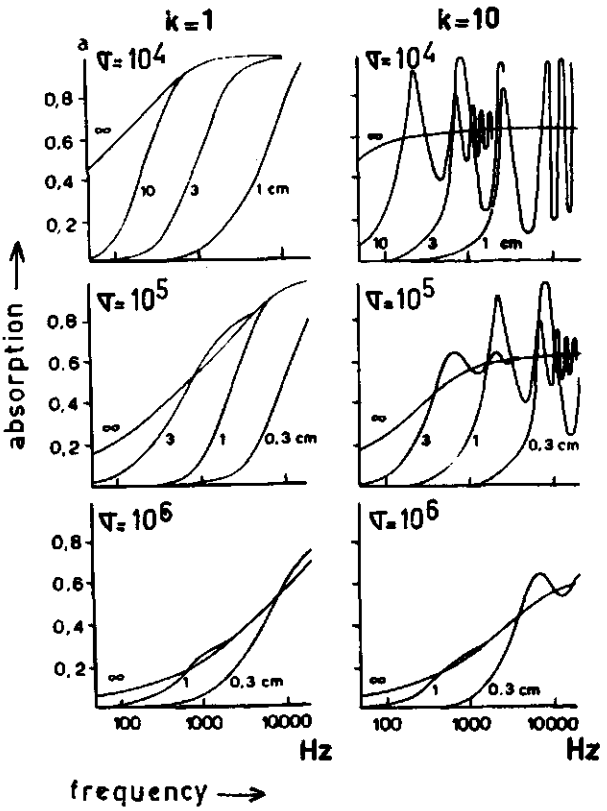

Figure 17 Calculated values of the absorption coefficient of rigid porous materials with rigid backing and presented as a function of layer thicknesses, flow resistance and structure factor; the porosity in all cases equals 0.80.

porosity and flow resistance are also affected. In the present context, the introduction of a separate factor for structure k_m was unavoidable. The tortuosity factor suggested by Carman (1956) or the ramification factor, introduced by some authors for flow-resistance (Visser, 1963), prove to be useless in acoustics. The specific flow-resistance σ_m should be considered as a separate material constant and to equate it with σ_s is rarely justifiable. Experiments show that σ_m tends to exceed σ_s. This is due to the dependence of flow profiles in the pores on frequency, an effect demonstrated in one of its simpler forms in a circular cylindrical tube of radius r. Following Crandall's (1927) considerations on the viscous boundary layer, a (dimensionless) characteristic number,

$$\mu = r\sqrt{(\omega\rho_s/\eta)}, \tag{3-27}$$

is introduced, where η is the dynamic coefficient of viscosity.
The magnitude of this number determines the nature of the flow profile in the tube. Thus, for $\mu<1$, Poiseuille flow is approached, with a parabolic distribution of particle velocity across the tube, and σ_m approaches σ_s where

$$\sigma_s = 8\eta/r^2. \tag{3-28}$$

For $\mu>10$, plug flow occurs: particle velocity is practically constant across the tube except for a sharp drop to zero at the tube walls. Now Helmholtz's approximation applies and

$$\sigma_m \approx \sqrt{(2\omega\eta\rho_s/r)}. \tag{3-29}$$

On determining the ratio of σ_m and σ_s from eqs(3-28) and (3-29) it follows that for $\mu>10$

$$\sigma_m/\sigma_s = \mu/4\sqrt{2}, \tag{3-30}$$

and so σ_m tends to exceed σ_s as frequency increases, see eq.(3-27).
In the transitional range, $1<\mu<10$, the flow profile is more complicated, and formal expressions may be found in appendix B. Note that eq.(3-30) does not hold in this range. Although the effect is not considered for the present simple model, it should be realized that the changes of state of the gas in the tube vary from isothermal to adiabatic in the same transitional range as defined for the flow profile in the tube, at least if the limits of the range are conceived as crude indications rather than as exact figures.
This apparent coincidence is due to the nearly equal thicknesses of the viscous and thermal boundary layers.
Using eqs(1-54), (1-55), (1-56), (3-21) and (3-22), it follows that

$$Z = (\rho_s c/h)\sqrt{(k_m(1+h\sigma_m/j\omega\rho_s k_m))}\coth jkl\sqrt{(k_m(1+h\sigma_m/j\omega\rho_s k_m))}, \tag{3-31}$$

which equation may be abbreviated by the introduction of the normalized specific acoustic impedance and of

$$\Sigma = h\sigma_m/\omega\rho_s, \tag{3-32}$$

thus reducing it to

$$\zeta h = \sqrt{(k_m(1-j\Sigma/k_m))}\coth\left[jkl\sqrt{(k_m(1-j\Sigma/k_m)}\right]. \qquad (3\text{-}33)$$

For the discussion, eq.(3-33) is brought into the form

$$\zeta h = \sqrt{(k_m(1-j\Sigma/k_m))}\coth \tfrac{1}{\sqrt{2}}jkl\sqrt{k_m}\left[\sqrt{(1+\Sigma^2/k_m^2)}+1\right]^{\frac{1}{2}} + \tfrac{1}{\sqrt{2}}kl\sqrt{k_m}\left[\sqrt{(1+\Sigma^2/k_m^2)}-1\right]^{\frac{1}{2}}. \qquad (3\text{-}33a)$$

Eq.(3-33a) is taken to represent the locus of ζ in the complex plane for a given frequency and variable sample thicknesses l, the locus having the general form of a spiral, converging to an apex for large values of l (see section 1.11). For a given value of Σ/k_m, an increase in k_m has the following results (excluding a limiting case, to be discussed later):

1. The velocity of propagation is reduced, being inversely proportional to $\sqrt{k_m}$.
2. The modulus of the apex is increased by a factor $\sqrt{k_m}$.
3. The spiral converges more swiftly to the apex (see the discussion on eq.(3-8a).

For a given value of k_m, an increase in Σ results in a shift of the apex, the reactive part becoming more negative and the resistive part increasing, although the latter effect is always the smaller. The swiftness of conversion of the spiral on the apex is increased (see eq.(3-8a)).

The apex corresponds to the normalized acoustic wave impedance of the sample material; thermal and equivalent losses increase the reactive component of this impedance but viscous losses decrease it, as may seen from eqs(3-3) and (3-4), which yield

$$W_m = \{(\rho_m - j\sigma_m/\omega)/(C_m - jG_m/\omega)\}^{\frac{1}{2}}.$$

Now in samples consisting of porous solid frames the viscous losses preponderate, driving the apex of the impedance curl below the real axis.

An increase in h, keeping Σ and k_m constant, results in a reduction in size of the spiral towards the origin, but does not affect its shape.

The effects of variations of k_m in the range $1<k_m<10$ and of σ_m in the range $10^4<\sigma_m<10^7$ Ns m^{-4} are well illustrated (although for the absorption coefficient a only) by Kosten (Richardson, 1953, Vol.I, chapter 4) (see figure 17).

In figures 18 and 19 a number of loci for h are presented in the complex plane. They were derived from eq.(3-33), but now for constant sample thickness and variable frequency, conditions corresponding to those under which most of the measurements were performed. These figures demonstrate the effects of vari-

ations in k_m and σ_m on the loci. The following values were selected:
for k_m: 2 and 8,
for σ_m: 10^3, 10^4 and 10^5 Ns m^{-4},
for l: 0.040 and 0.072 m.
The frequency scale is indicated by points on the loci, corresponding to multiples of 200 Hz. The points for 0.4, 1 and 1.6 kHz are marked by the numbers 4, 10 and 16, respectively.
In the limiting case of low damping is
$\Sigma/k_m << 1$,
a condition consistent with $\mu>10$, as discussed previously. If so eq.(3-33) may be approached by

$$\zeta h \approx (1-j\Sigma/2k_m)\sqrt{(k_m)}\coth\left[k1\Sigma/2\sqrt{(k_m)}+jk1\sqrt{(k_m)}\right]. \qquad (3\text{-}33b)$$

The locus for ζ in the complex plane, for constant frequency and variable sample thickness is now a wide spiral, converging slowly on an apex just below the real axis. In the present case, information may be obtained from the anti-resonances and resonances of ζ, where ζ is real (see Section 1-11). But, as Kosten (1947) has pointed out, preference should be accorded to the selection of minimum and maximum values for $|\zeta|$. Thus $|\zeta|$ achieves its minimum for

$$k1\sqrt{k_m} = \pi/2, \qquad (3\text{-}34)$$

and, in the prevailing order of approximation, this yields:

$$\zeta h \approx \tfrac{1}{4}\pi\Sigma/\sqrt{k_m}. \qquad (3\text{-}35)$$

Values for k_m and for $\Sigma/h = \sigma_m/\omega\rho_s$ may now be derived from eqs(3-34) and (3-35). These two equations hardly differ from those of the first anti-resonance (see section 1.11), especially if damping is very low. No great error will ensue in applying eqs(3-34) and (3-35) to the first anti-resonance.
In the general case of low damping, eqs(3-34) and (3-35) do not apply if sample thickness is kept constant and frequency varies, because h, Σ and k_m should then be considered as functions of frequency. In many cases, however, these quantities vary very slowly with frequency and the equations will yield approximations for k_m and σ_m.
The present considerations were not extended to anti-resonances of higher order or to resonances, as these occurred only sporadically in the frequency range and for the samples investigated in this book.

3.5 The choice of a model

For a better agreement between the structure of a geometric model and the soil structure, a number of supplementary assumptions should be made.
In the literature on porous media, Carman (1956), Scheidegger (1957) and Dallavalle (1943) particularly commented on many views and hypotheses in this field. Also, in the literature on soil physics pertaining directly to the orientation of pores, many models can be found (de Vries, 1952; van Bavel, 1952). Some points of consideration are listed here. Research on diffusion of gases was said to show that except for the effect of path length (Penman, 1940; Call, 1947), only the total pore space is of importance. The very short free path lengths of the diffusing molecules as a result of mutual collisions cause this effect. The contributions of large and small pores are in proportion. The arrangement of pore spaces is therefore of no importance. Variation, for instance, in the density of packing does not cause systematic rearrangement of pores.
Total porosity should be estimated by the expansion method (see section 4-2). Starting from data on weight and specific weight of the sample material erroneous results will be found because isolated pores are included.
Many measurements and considerations are partially based directly on mass flow of gases or liquids through porous media (Poiseuille). The largest pores and capillary tubes contribute most, leading to a small sensitivity for the detection of pores of small diameter. Even less information was available on the occurrence of pores in a certain fluctuating regularity and to the effect of a changing pore diameter. This lack of information is partly due to the fact that often only two independent variables, namely pressure gradient and flow, can be correlated.

The simple model introduced by Zwikker & Kosten (1941) (see section 3-5), had the advantage that no assumptions are introduced a priori about pore geometry; the major disadvantage is that the frequency-dependent effects due to viscous and thermal boundary layers are ignored.
The introduction of a mean radius or any related quantity, as found in literature on flow, turns out to be inadequate, as can be seen from eq.(3-27), which suggests that any averaging process will require some type of weighting factor. Therefore it seems logical to start with a model, based on channels with a variable cross-section. Soils can be very often considered as a packing of soil aggregates. Each aggregate consists of soil particles cemented together. The volume-weight corresponds roughly to a value equal to that of a dense packing of spheres.

The investigation of a model incorporating such a spatial arrangement thus appears to be attractive; the objections will be clarified in a later paragraph. Nonetheless a channel type model may be brought more or less into line with closely packed spheres by according the cross-section of the channels the same distribution function as the cross-sections of the interstices between the spheres.

So the basic model consists of channels of variable cross-section enclosed in the solid material of the frame. The channels are inclined at a constant angle to the direction of propagation. In one of the variations, each channel consists of a cylindrical tube of varying radius. It is called the capillary model. In the other variation the channels consist of fissures between parallel planes, varying in spacing. It will be referred to as the fissure model. Figure 20 represents a section of either material, the channels may be taken to represent the fissures or capillaries as the case may be. A fundamental limitation of this approach is that the distribution of the channel cross-section is the same for the flow and for the compression of the gas. Numerous examples may be adduced where this limitation is not justifiable, (c.f. the discussion on figure 14 in section 3-2) but simplification was allowed to override such considerations.

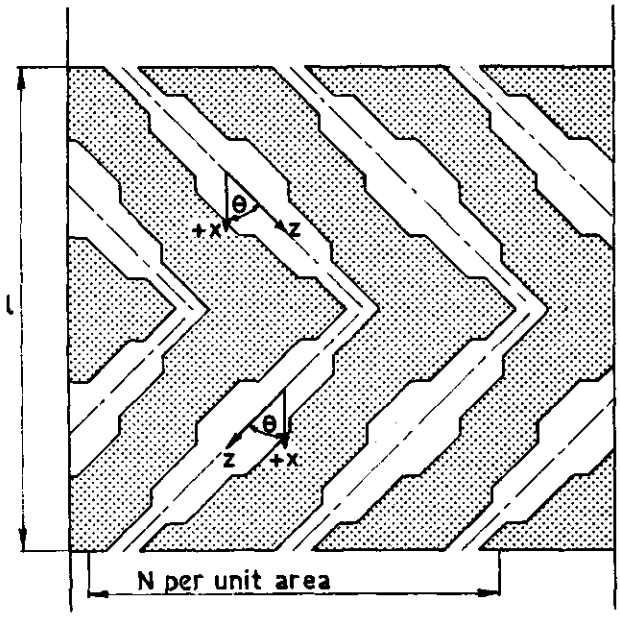

Figure 20 Model of a channel with different cross-sections

Zwikker & Kosten (1949, p.25) did consider the effects of boundary layer thickness, in later papers, departing from the case of the homogeneous, circular cylindrical pore. In this case homogeneous means having constant cross-section. For the purpose of this book, their work was extended to inhomogeneous channels. An alternative approach was followed by Korringa, Kronig and Smit (1945). They selected a model with a cubic packing of spheres and succeeded in calculating the characteristic quantities. An attractive feature of this model is that it has two geometrical parameters for fitting theory to experiment:

1. Sphere radius
2. Lattice constant.

The porosity of cubic packing is unfortunately far higher than anything encountered in experimental samples. The results were therefore rejected from consideration. This model yields values for specific acoustic impedance at the sample surface which do not agree with experimental results.

I did not, however, work out the extension of the Korringa, Kronig and Smit model for a hexagonal packing, which yields a porosity in better agreement with those encountered in soil samples. The principal reasons are: the mathematical difficulties involved and the fact that such a model is still only an idealization of the structures prevailing in practice.

For the general description of the channel type model the following symbols will apply:

x = direction of propagation

z = direction of channel

θ = angle between z and x axis, $x = z\cos\theta$

N = number of channels per unit area normal to x

U = volume velocity per channel, $u = NU$

S = cross-sectional area of a channel, normal to z, $S = S(z)$

S_a = average of S over z.

A number of these definitions are significant for fine-grained materials only. From the definitions one has for the porosity

$$h = N S_a/\cos\theta. \tag{3-44}$$

Now a short section of a channel is considered, S being assumed constant over this section. Equations of motion and continuity for the section may be given in the form

$$-(\partial p_a/\partial z)_1 = \frac{j\omega\rho_s}{S_a}\,\xi'_m\,\frac{S_a}{S}\,U, \tag{3-45}$$

$$-(\partial U/\partial z)_1 = \frac{j\omega S_a}{\kappa p_s}\,\eta'_m\,\frac{S}{S_a}\,p_a, \tag{3-46}$$

where p_a is average sound pressure in a cross-section of the channel, U is the volume velocity and ξ'_m and η'_m are referred to as the perturbation factors for homogeneous channels, i.e. having a constant cross-section. The subscript 1 indicates that the local values of the pressure gradient and the volume velocity-divergence are intended. Values for ξ'_m and η'_m will be derived in appendix B, replacement of subscript m bv subscript c denoting cylindrical capillaries and f that of the fissures.

Referring once again to the assumption of a fine-grained material, an interval L_m in z is selected, large enough to encompass a representative range of values for ξ'_m, η'_m and S, yet small relative to wavelength. Thus U in eq. (3-45) and p_a in eq. (3-46) may be considered constant over L_m.

Now eqs(3-45) and (3-46) are averaged over the interval L_m in z and the following quantities are defined:

$$\xi_m = \frac{1}{L_m} \int_0^{L_m} \frac{S_a \xi'_m}{S} \, dz,$$

$$\eta_m = \frac{1}{L_m} \int_0^{L_m} \frac{S \eta'_m}{S_a} \, dz,$$

where, from the definition

$$S_a = \frac{1}{L_m} \int_0^{L_m} S \, dz.$$

Elegance is enhanced by the introduction of a dimensionless variable m,

$$m = z/L_m \, , \quad 0 \leq m \leq 1, \tag{3-47}$$

and considering S, ξ'_m, η'_m as a function of m. Thus

$$S_a = \int_0^1 S(m) \, dm, \tag{3-48}$$

$$\xi_m = \int_0^1 \frac{S_a}{S(m)} \, \xi'_m(m) \, dm, \tag{3-49}$$

$$\eta_m = \int_0^1 \frac{S(m)}{S_a} \, \eta'_m(m) \, dm, \tag{3-50}$$

ξ_m and η_m will be referred to as perturbation factors, the subscript m being replaced by c or f for capillaries and fissures, respectively. In the absence of heat conduction, viscosity and variations in channel cross-section, ξ_m and η_m both equal unity.

The average values of the pressure gradient and the volume-velocity divergence along the channel, follow from eqs(3-45), (3-46), (3-47), (3-49) and (3-50):

$$-\frac{\partial p}{\partial z} = \frac{j\omega\rho_s}{S_a}\,\xi_m\,U, \tag{3-51}$$

$$-\frac{\partial U}{\partial z} = \frac{j\omega S_a}{\kappa p_s}\,\eta_m\,p, \tag{3-52}$$

On referring to the definition of u, it follows that eqs(3-51) and (3-52) may be restated in the following form:

$$-\frac{\partial p}{\partial x} = \frac{j\omega\rho_s\xi_m}{N\,S_a\cos\theta}\,u, \tag{3-53}$$

$$-\frac{\partial u}{\partial x} = \frac{j\omega N S_a\eta_m}{\kappa p_s\cos\theta}\,p \tag{3-54}$$

and, a comparison of these eqs to eqs(1-52) and (1-53) and making use of eqs (1-54), (1-55) and (3-44) shows that:

$$\gamma_m = \frac{jk}{\cos\theta}\sqrt{(\xi_m\eta_m)}, \tag{3-55}$$

$$W_m = \frac{\rho_s c}{h\cos\theta}\sqrt{(\xi_m/\eta_m)}. \tag{3-56}$$

No allowance is made for edge effects in deriving these results. Such edge effects occur at discontinuities in the cross-sections of the channels and are essentially due to local distortions of the sound field. Their exclusion is clear from eqs (3-49) and (3-50), where the quantities ξ'_m and η'_m are valid for homogeneous channels only . The correlation between ξ'_m and η'_m was not taken into account. This may be seen from the separate averaging processes introduced in the equations mentioned. In other words: no attempt was made to solve the equations for the sound field on the inhomogeneous transmission line.

Various arguments may be cited to justify the crudity of the above procedure, the principal one being that the edge effects and the parameters chosen to obtain the model are arbitrary and there is little reason to suppose that they correspond to anything in a real material. It is thus doubtful whether their inclusion would constitute an improvement.

As was stated previously the adoption of the same channel profiles for the determination of both ξ_m and η_m is incorrect for certain structures, e.g. those having dead end side pores, which may exercise considerable influence on η_m while hardly affecting ξ_m. However adherence to the simple assumption avoids an unmanageable number of parameters. Eqs (3-55) and (3-56), in conjunction with eq.(1-56), solve the problem of calculating sample impedance, as long as the perturbation factors are known. These factors may be considered as a further addition to the ways of representing Z_m and Y_m, as introduced in eqs (1-52) and (1-53). It is thus desirable to connect the present representation with the previous ones, the general notation following Ferrero & Sacerdote (1960) being the first choice (see eqs(3-1) and (3-2)). Eqs(3-55) and (3-56) in conjunction with eqs(3-3) and (3-4) show that

$$G_m = - \frac{\omega h}{\kappa p_s} \operatorname{Im} \eta_m \,, \tag{3-57}$$

$$C_m = \frac{h}{\kappa p_s} \operatorname{Re} \eta_m \,, \tag{3-58}$$

$$\sigma_m = - \frac{\omega \rho_s}{h \cos^2 \theta} \operatorname{Im} \xi_m \,, \tag{3-59}$$

$$\rho_m = \frac{\rho_s}{h \cos^2 \theta} \operatorname{Re} \xi_m \,, \tag{3-60}$$

where C_m and ρ_m are, in first order approximation, independent of frequency. A comparison of the simple model of Zwikker & Kosten (1941) with the present results shows that the former is equivalent to the assumption $\eta_m = 1$ (compare eqs(3-24a) and (3-24b)) and that (see eqs(3-23a) and (3-23b))

$$k_m = \frac{1}{\cos^2 \theta} \operatorname{Re} \xi_m \,, \tag{3-61}$$

σ_m according with eq(3-59). These latter equations are presented principally

to clarify the relationships between the various parameters only: the frequency dependence for σ_m and k_m (following from eqs(3-59) and (3-61)) being incompatible with the postulates for the simple model.

3.6 The capillary model

First a suitable distribution function must be selected for the capillary diameters. This function will be founded on the distribution of pore areas in a hexagonal close packing of spheres.
Figure 21 presents a pattern of spheres of equal diameter, each sphere resting in the hollow formed by three spheres immediately below. In this manner, a so-called hexagonal array is formed. In the next figure, figure 22, a vertical section of the array is drawn and a number of significant planes are indicated. After closer examination it appears that a study of the pores lying between the spheres can be limited to two layers. Through such a packing of spheres a model capillary can be laid. In figure 21 this capillary is shown by means of an prism having the cross-section of a parallelogram. The free area S of such a prism varies as a function of height. The model capillary tube may be seen as two adjacent prisms each having an equilateral triangle as cross-section. The equivalent radius R for the free cross-section can now be defined as $R = \sqrt{(S/\pi)}$, where S is the free area within the triangular standard pore. Figure 23 shows a number of cross-sections for two such prisms for various values of the height a above a reference plane through the centres of a layer of spheres in the range $0<a<2r\sqrt{(2/3)}$. It is clear from the figure that the free cross-sections in the two adjacent prisms are far from identical. This height a can be referred to the radius r of the sphere. A simple check leads to the conclusion that the range in size of S is symmetrical in relation to $a = 2r\sqrt{(2/3)}$ when the third layer in top view is above the first layer.
This means that the search for the distribution function can be confined to the variation in the interval $0<a<r\ 2\sqrt{(2/3)}$.
Subdivision of this range is necessary however. Thus it is apparent from the figure 22 that in the interval $0<a<r(2\sqrt{(2/3)}-1)$ the free area is determined by the lower layer of spheres only but that in the interval $r(2\sqrt{(2/3)}-1)<a<r\sqrt{(2/3)}$ the void is affected by the next higher layer too.
The average free area in each of the two adjacent triangular prisms in figure 23 is taken as representative for the pore. To facilitate calculation, dimensionless quantities are introduced for the equivalent pore radius R and the vertical displacement a: $\longrightarrow$ $b = R\sqrt{\pi}/r$ and $m = a/r\sqrt{(2/3)}$ respectively. For the two intervals referred to above, it now follows that:

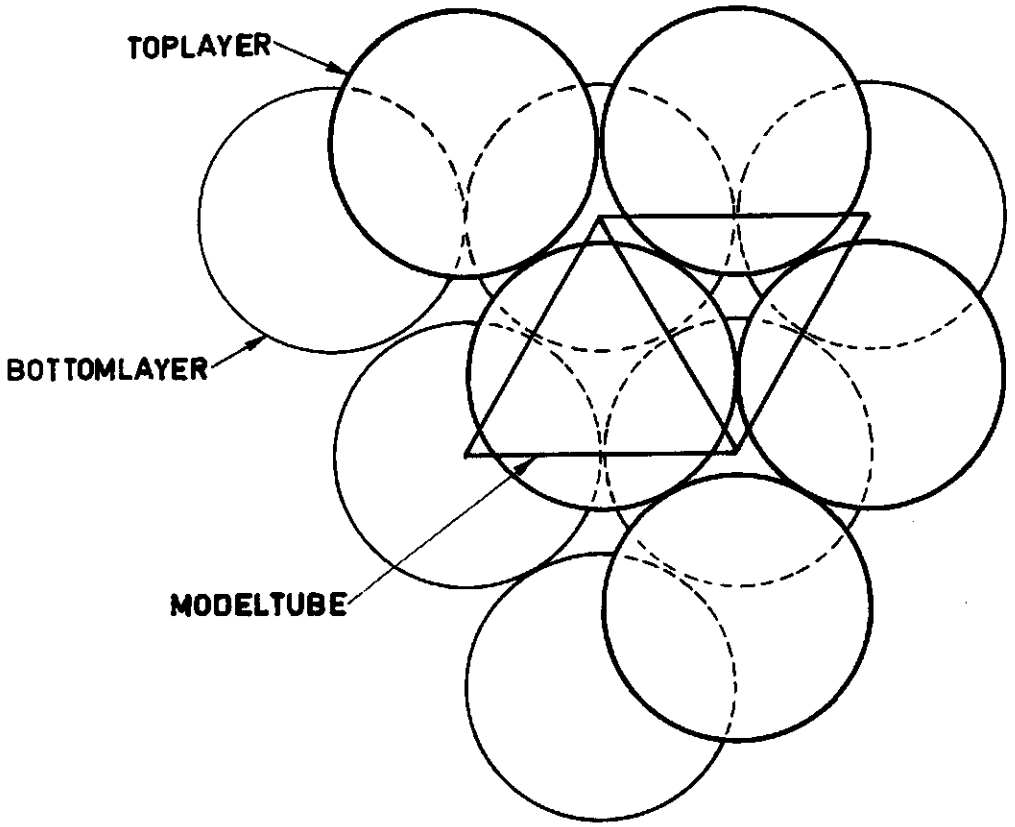

Figure 21 Top view at two layers of a hexagonal packing of spheres

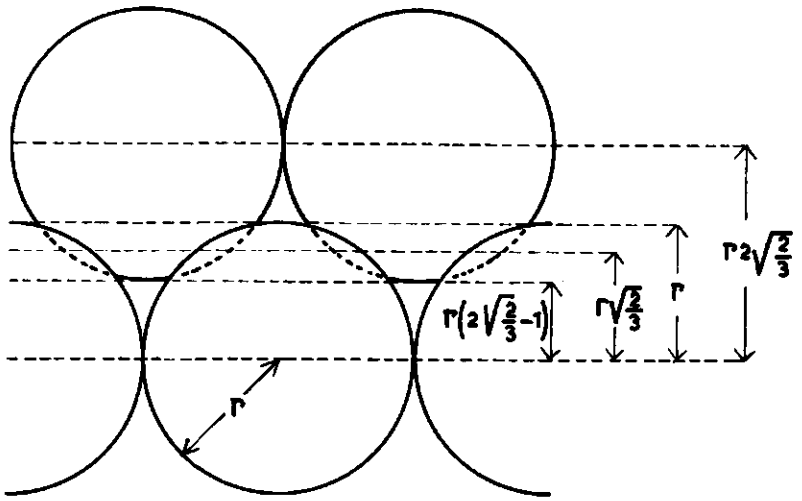

Figure 22 Side view at two layers of a hexagonal packing of spheres

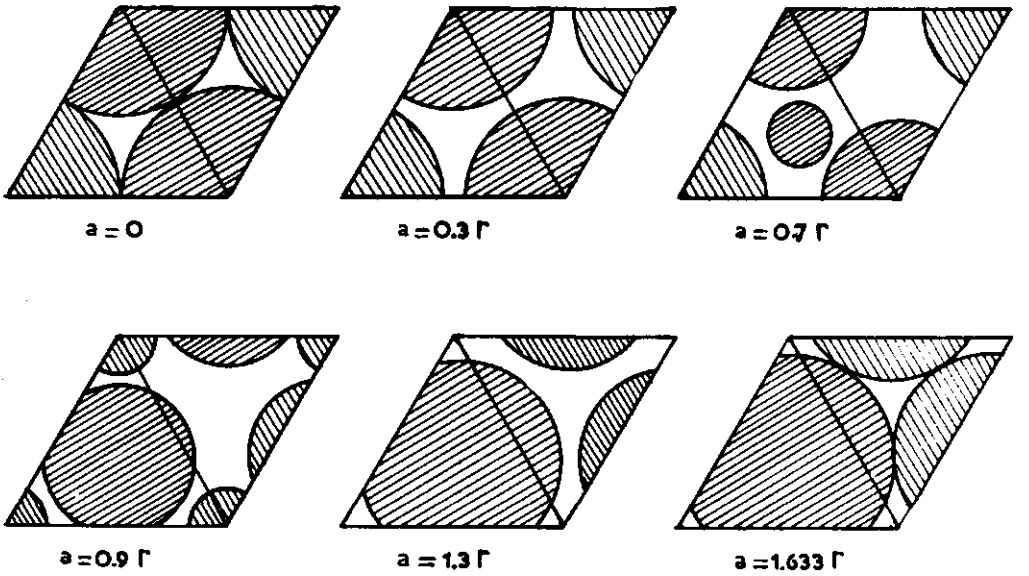

Figure 23 Horizontal cross-sections through a hexagonal packing at different heights

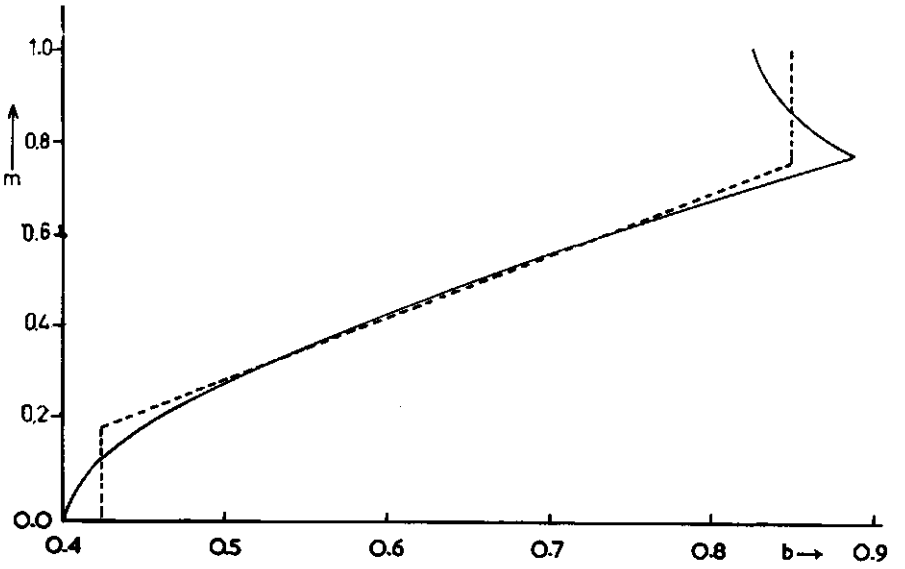

Figure 24 The distribution function of pore areas in a packing of spheres

respectively. For the two intervals referred to above, it now follows that:

$$\left.\begin{array}{l} 0 \leqslant a \leqslant r(2\sqrt{(2/3)}-1) \\ 0 \leqslant m \leqslant 0.7753 \end{array}\right] b = \sqrt{(\sqrt{3} - \pi/2 + m^2\,\pi/3)} \qquad (3\text{-}62)$$

$$\left.\begin{array}{l} r(2\sqrt{(2/3)} - 1) \leqslant a \leqslant r\sqrt{(2/3)} \\ 0.7753 \leqslant m \leqslant 1 \end{array}\right] b = \sqrt{(\sqrt{3} - \pi/3 + 2\pi(1-m)^2/3)}. \qquad (3\text{-}63)$$

The relationship between m and b can be visualized in a graph. This is shown in figure 24. The calculated data from Table 3-6 are represented by the solid line. The figure shows that this curve is rather complicated and does not lend itself to mathematical evaluation. But this is not necessary, however, since the model is a rough approximation, particularly by the introduction of an equivalent diameter. The most practical solution lies in the use of an approximate distribution function of a mathematical simple form. The dotted line in figure 24 represents the approximate function, chosen from the wide range of possibilities. The simultaneous presence of large and small diameters imposes upon the sample an acoustic behaviour differing from an arrangement of capillaries with constant radius along their entire length.

The approximated function may be described as follows: a volume fraction g_1 of the total pore space has a dimensionless diameter $b = b_1$ and a volume fraction

Table 3-6

The distribution function for a hexagonal packing

m	b
0	0.4016
0.1382	0.4257
0.2764	0.4912
0.4146	0.5842
0.5528	0.6937
0.6910	0.8132
0.7753	0.8892
0.8292	0.8637
0.8983	0.8405
1.00	0.8276

g_2 has a diameter $b = b_2$, $b_1 < b_2$. The remaining pores possess a dimensionless radius b given by

$$b = b_1 + (m - g_1)(b_2 - b_1) / g_3;\ b_1 \leq b \leq b_2, \tag{3-64}$$

where $g_3 = 1 - g_1 - g_2$.
The numerical values selected are:

$$g_1 = 0.20;\ g_2 = 0.25;\ g_3 = 0.55;\ b_1 = 0.425;\ b_2 = 0.850, \tag{3-64a}$$

and eq.(3-64) is brought into the form:

$$m = -0.35 + 1.294\ b;\ 0.20<m<0.75.$$

Summarizing, it can be said that in the total pore space 20% is occupied by pores with a radius $R = \frac{0.425}{\sqrt{\pi}}\ r = 0.2398\ r$, and 25% is occupied by pores with a radius $R = \frac{0.850}{\sqrt{\pi}}\ r = 0.4796\ r$, while the remaining pores have radii with equal statistical weight, between the two above radii. These occupy 55% of the total pore space.

Applying eq.(3-48) one finds

$$S_a = (g_1 \pi R^2)_{b_1} + (g_2 \pi R^2)_{b_2} + \int_{g_1}^{1-g_2} \pi R^2\, dm. \tag{3-65}$$

On replacing R by b, and using eq.(3-64) in the form

$$dm = \frac{g_3}{b_2 - b_1}\, db, \tag{3-66}$$

the formula may be integrated; it follows that

$$S_a = r^2 \left\{ g_1 b_1^2 + g_2 b_2^2 + \tfrac{1}{3} g_3 (b_1^2 + b_1 b_2 + b_2^2) \right\}. \tag{3-67}$$

Introduction of the numerical values from eq.(3-64a) yields

$$S_a = 0.4485\ r^2. \tag{3-68}$$

Assuming in this way that the porous material is characterized by inhomogeneous pores with a given distribution function and inclined with an angle θ to the direction of propagation, the porosity can, making use of eqs(3-44) and (3-68), be calculated. One finds

$$h = 0.4485\ r^2\ N/\cos\theta\ . \tag{3-69}$$

The following auxiliary functions for the calculation of ξ_c can be defined:

$$H(x) = \frac{2}{x\sqrt{-j}} \cdot \frac{J_1}{J_0}(x\sqrt{-j}), \tag{3-70}$$

with the abbreviated notation:

$$\frac{J_1}{J_0}(x) = \frac{J_1(x)}{J_0(x)},$$

$$F(x) = 1-H(x), \text{ and} \tag{3-71}$$

$$M(x) = \int \frac{1}{x^2 F(x)}\,dx, \tag{3-72}$$

$$\text{where } x = R\sqrt{(\omega\rho_s/\eta)}. \tag{3-73}$$

Comparing eq.(3-71), in conjunction with eqs(3-70) and (3-73), with eq.(B-2) in appendix B, one sees that

$$\xi'_c = 1/F(x). \tag{3-74}$$

As special value for x is introduced

$$x_3 = r\sqrt{(\omega\rho_s/\pi\eta)}, \tag{3-75}$$

and it is noted that

$$\text{for } b = b_1 \rightarrow x = x_1 = b_1 x_3, \tag{3-76}$$

$$\text{for } b = b_2 \rightarrow x = x_2 = b_2 x_3, \tag{3-77}$$

$$S = \pi R^2 = b^2 r^2 = x^2 r^2 / x_3^2, \tag{3-78}$$

and, by using eqs(3-66), (3-73) and (3-75), that

$$dm = \frac{g_3}{b_2 - b_1} \cdot \frac{1}{x_3}\,dx. \tag{3-79}$$

Eq.(3-49) can be used now for the calculation of ξ_c, the integration in the right side presents hardly any problem for the intervals in m where b is constant. In the interval where such is not the case, x is introduced as the integration variable, S being eliminated with the aid of eq.(3-78) and m with the aid of eq.(3-79). Referring to the definition eq.(3-72) one finds

$$\xi_c = \frac{S_a}{r^2}\left\{ \frac{g_1}{b_1^2 F(x_1)} + \frac{g_2}{b_2^2 F(x_2)} + \frac{g_3 x_3}{b_2 - b_1} M(x) \,\middle|\, \begin{matrix} x_2 \\ x_1 \end{matrix} \right\} \tag{3-80}$$

where S_a/r^2 may be obtained from eq.(3-68) and the other numerical values for factors and arguments from eqs(3-64), (3-76) and (3-77).

The following additional auxiliary functions are defined for the calculations of

η_c

$$G(x) = 1 + 0.4\ H(x), \tag{3-81}$$

$$L(x) = \int x^2\ G(x)\ dx, \tag{3-82}$$

where, in this instance

$$x = R\sqrt{(\omega \rho_s c_p/\lambda)} \tag{3-83}$$

and a comparison of eq.(3-81) in conjunction with eqs(3-83) and (3-70) with eq.B-22) as cited in appendix B, shows that

$$\eta'_c = G(x), \tag{3-84}$$

with adequate accuracy for bi-atomic gases.

A special value for x is introduced

$$x_6 = r\sqrt{(\omega \rho_s c_p/\pi\lambda)}, \tag{3-85}$$

and it is noted that:

$$\text{for } b = b_1 \rightarrow x = x_4 = b_1 x_6, \tag{3-86}$$

$$\text{for } b = b_2 \rightarrow x = x_5 = b_2 x_6, \tag{3-87}$$

$$S = x^2 r^2/x_6^2, \text{ (see eq.(3-78))}, \tag{3-88}$$

and eqs(3-66), (3-83) and (3-85) show that

$$dm = \frac{g_3}{b_2 - b_1} \cdot \frac{1}{x_6}\ dx. \tag{3-89}$$

Eq.(3-50) is now used for the calculations of η_c, the integration in the right side presenting few problems for the intervals in m where b is constant. In the interval where such is not the case x is introduced as the integration variable, S being eliminated with the aid of eq.(3-88) and m with the aid of eq.(3-89). On referring to the definition, eq.(3-82), one finds

$$\eta_c = \frac{r^2}{S_a} \left\{ g_1 b_1^2\ G(x_4) + g_2 b_2^2\ G(x_5) + \frac{g_3}{(b_2 - b_1)} \cdot \frac{1}{x_6^3} L(x) \Big|_{x_4}^{x_5} \right\}, \tag{3-90}$$

where r^2/S_a may be obtained from eq.(3-68) and the other numerical values for the factors and arguments from eqs(3-64a), (3-86) and (3-87). Note that the various definitions given for x in eqs(3-73) and (3-83) no longer affect the results, eqs(3-80) and (3-90). The model has been idealized to such an extent that r and θ are formal parameters and cannot be derived from the geometrical parameters of a sample material considered.

In the special case of static flow, the specific resistance σ_s may be obtained from eqs(3-59) and (3-80), permitting ω to approach zero. In that case, the arguments of the function F(x) (see eqs(3-75), (3-76) and (3-77)) are small and the function approaches

$F(x) \quad jx^2/8.$

This approximation yields

$$\sigma_s = \frac{8\,\pi\eta}{h\,r^2\cos^2\theta}\,\frac{S_a}{r^2}\left\{\frac{g_1}{b_1^4}+\frac{g_2}{b_2^4}+\frac{1}{3}\,g_3\,\frac{b_2^2+b_1b_2+b_1^2}{b_1^3\cdot b_2^3}\right\}, \tag{3-91}$$

and, on introducing the numerical values from eqs(3-64a) and (3-68) the result is

$$\sigma_s = \frac{129.92}{h\,r^2\cos^2\theta}\,. \tag{3-92}$$

Eq.(3-92) is in accordance with the model rule for static-flow resistances, eq.(3-121).

3.7 The fissure model

The study of the fissure model will run along the same lines as that of the capillary model. Where possible similar symbols will be used. The cross-sectional area of a channel is obtained by considering a slab of material of unit thickness in the direction normal to the plane of drawing figure 20. Thus for a fissure of width D the cross-sectional area is D times unit length.
In future, the unit length as factor will be omitted from the equations.

A rather simple distribution function for the fissure widths D will be introduced, which, while showing some resemblance to the distribution function for the capillary radii, avoids the necessity of solving the integrals appearing on the right side of the defining eqs(3-49) and (3-50).
For the inhomogeneous fissure the following assumptions are made with respect to the distribution function for the fissure widths.

a fraction 0.25 has a width $D_1 = 4\,D_a/(1+q_a)^2$, (3-94)

a fraction 0.50 has a width $D_2 = 4\,D_a q_a/(1+q_a)^2$, (3-95)

a fraction 0.25 has a width $D_3 = 4\,D_a q_a^2/(1+q_a)^2$. (3-96)

where D_a is the average fissure width, independent from the value selected for q_a. The ratio of the widths of the widest and the narrowest parts of the inhomogeneous fissure, the fissure width ratio equals q_a^2.

For the calculation of ξ_f the following auxiliary function is defined now:

$$F_f(x) = 1 - \frac{\tan(x\sqrt{-j})}{x\sqrt{-j}}, \tag{3-97}$$

where

$$x = (D/2)\sqrt{(\omega \rho_s/\eta)} \tag{3-98}$$

A comparison of eq.(3-97) in conjunction with eq.(3-98) and (B-6), shows that

$$\xi'_f = 1/F_f(x) . \tag{3-99}$$

On introducing the special values:

$$x_1 = \frac{2\,D_a}{(1+q_a)^2} \cdot \sqrt{\frac{\omega \rho_s}{\eta}} \quad ; \; x_2 = q_a\, x_1 \; ; \; x_3 = q_a^2\, x_1, \tag{3-100}$$

the right-hand side of eq.(3-49) is readily integrated resulting in

$$\xi_f = \frac{(1+q_a)^2}{16}\left\{ \frac{1}{F_f(x_1)} + \frac{2}{q_a F_f(x_2)} + \frac{1}{q_a^2 F_f(x_3)} \right\} . \tag{3-101}$$

The following auxiliary function for the calculation of η_f is defined as

$$H_f(x) = \frac{\tan(x\sqrt{-j})}{x\sqrt{-j}} \tag{3-102}$$

where

$$x = \frac{D}{2}\sqrt{(\omega \rho_s c_p/\lambda)}. \tag{3-103}$$

Comparison of eq.(3-102) in conjunction with eq.(3-103) with eq.(B-18), as derived in appendix B, yields

$$\eta'_f = 1 + 0.4\, H_f(x) \tag{3-104}$$

with adequate accuracy for bi-atomic gases.
On introducing the special values:

$$x_4 = \frac{2\,D_a}{(1+q_a)^2}\sqrt{\left(\frac{\omega\rho_s c_p}{\lambda}\right)};\quad x_5 = q_a\,x_4\;;\quad x_6 = q_a^2\,x_4, \qquad (3\text{-}105a,b,c)$$

the right side of eq.(3-50) is readily integrated and yields:

$$\eta_f = 1 + \frac{0.4}{(1+q_a)^2}\{\,H_f(x_4) + 2\,q_a H_f(x_5) + q_a^2\,H_f(x_6)\,\} \qquad (3\text{-}106)$$

As in the case of the capillary model D_a,q_a and θ should the considered as formal parameters, not related directly to the sample geometry. Eqs(3-59) and (3-106) yield the static specific flow resistance for the fissure model by permitting ω to vanish. In that case the arguments of $F_f(x)$ are small(compare eq.(3-105, a,b and c)) and hence

$$1/F_f(x) \approx -3j/x^2$$

The result is

$$\sigma_s \approx \frac{3}{64}\cdot\frac{\eta}{h\cos^2\theta}\cdot\frac{(1+1/q_a)^6\cdot(1+q_a^3)^2}{D_a^2} \qquad (3\text{-}107)$$

in accordance with the scale rule (eq.(3-121)).

3.8 Comparison of the behaviour of the capillary and the fissure model

As stated prevously, eqs(3-56) and (3-55) furnish the solution for the specific acoustic impedance Z of the sample surface, where ξ_c and η_c may be introduced from eqs(3-80) and (3-90) or alternatively ξ_f and η_f from eqs(3-102) and (3-106) for the capillary and fissure models, respectively. Computers were used for the numerical calculations, and the locus of Z was determined for constant absolute steps in frequency. A consequence is that the steps in Z vary considerably in the complex plane. However it was not felt worthwhile to correct for this tendency as that would involve extremely complicated programmes and excessive computation times. The problem is reconsidered in appendix D.

The auxiliary functions $F_f(x)$ and $H_f(x)$, see eqs(3-97) and (3-102), for the fissure model present no difficulties. Greater problems are encountered in the calculation of the auxiliary functions for the capillary model, H(x), F(x), M(x) and L(x) (see eqs(3-70), (3-72), (3-71) and (3-82)) and appendix C has been devoted to this subject.

For the cylindrical capillary model, two geometrical parameters are available for fitting the theoretical curves to the experimental ones: (1) the sphere radius r and (2) the angle θ. For the fissure model, in addition to the average fissure width D_a and the angle θ, a third parameter is available: the fissure width ratio q_a^2. The introduction of this parameter in the fissure model only appeared to be the wisest course, as this model is more sensitive to changes in the distribution function of the channel cross-sectional areas than is the capillary model. This may be seen from the following argument.

The locus of Z may be shifted by variation in the phase angles of Z_m and Y_m and here ξ_c and ξ_f are far more effective than η_c and η_f, the latter two quantities departing but little from the real axis. The attention is thus focused on the two former quantities and restricted to the high-frequency range, where $|R/l_v|$, $|\frac{1}{2}D/l_v| >> 1$ (see appendix B). One can thus find the approximations for large values of the argument:

$$1/F(x) \approx 1 - \frac{j}{R}\sqrt{\left(\frac{2\eta}{\omega\rho_s}\right)}, \tag{3-108}$$

$$1/F_f(x) \approx 1 - \frac{j}{D}\sqrt{\left(\frac{2\eta}{\omega\rho_s}\right)}. \tag{3-109}$$

In these two cases, the approximations eqs(3-108) and (3-109) reduce eq.(3-49) to

$$\xi_c \approx \frac{S_a}{\pi}\int_0^1 \left\{\frac{1}{R^2} - \frac{j}{R^3}\sqrt{\left(\frac{2\eta}{\omega\rho_s}\right)}\right\} dm, \tag{3-110}$$

$$\xi_f \approx D_a\int_0^1 \left\{\frac{1}{D} - \frac{j}{D^2}\sqrt{\left(\frac{2\eta}{\omega\rho_s}\right)}\right\} dm. \tag{3-111}$$

Eqs(3-110) and (3-111) are now compared under the special conditions:

$$R^2(m) = D_a^2 f(m), \tag{3-112}$$

$$D(m) = D_a f(m), \tag{3-113}$$

the definition of D_a (see eqs(3-48) and (3-93)) requiring

$$\int_0^1 f(m)\, dm = 1, \tag{3-114}$$

where f(m) may be any function of m. However monotonic functions are applied in the present models exclusively.
By eqs(3-112) and (3-113), eqs(3-110) and (3-111) may be reduced to

$$\xi_c = \int_0^1 \left\{ \frac{1}{f(m)} - \frac{j}{D_a f^{3/2}(m)} \sqrt{\left(\frac{2\eta}{\omega \rho_s}\right)} \right\} dm, \tag{3-115}$$

$$\xi_f = \int_0^1 \left\{ \frac{1}{f(m)} - \frac{j}{D_a f^{2}(m)} \sqrt{\left(\frac{2\eta}{\omega \rho_s}\right)} \right\} dm. \tag{3-116}$$

It should be noted that the real parts of ξ_c and ξ_f are identical. A variation in f(m), of such a nature that eq.(3-114) is still satisfied, will however tend to introduce a larger change in the imaginary part of ξ_c than in ξ_f as f(m) appears to a higher absolute power in the former case. The change in phase angle for ξ_f will thus exceed that in ξ_c. This suggests that the fissure model may be appropriate in those cases, where substantial variations in phase angle of the propagation constant especially are required to match theoretical and experimental data. Physically it is significant that the capillary of circular cross-section has the minimum possible wall area for a given cross-sectional area.

3.9 Discussion on the possibilities of scale-rules

Before selecting simple spatial arrangements as models for porous materials it is worthwhile noting that the results for such models, culminating in the impedance at the sample surface, will depend on absolute geometrical dimensions and the frequency as separate quantities: in other words scale rules do not apply in cases of this kind. What a scale rule implies may be clarified by an example: an acoustical system is characterized by the spatial dimensions a, b,..., and some acoustical quantity F is calculated for a given wave number, k. The result is of the general form

$$F = F(k,a,b,\ldots). \tag{3-117}$$

If this result may be brought into the form

$F = F\,(k \cdot a,\ k \cdot b, \ldots)$,

then a scale rule applies for the system. If so, increasing all linear dimensions by an arbitrary factor and decreasing the frequency and thus the wave number by the reciprocal of that factor, will yield the same solution F, the quantities $k \cdot a$, $k \cdot b$,... remaining the same.

That solutions of this type do not obtain for porous materials may be concluded on considering two samples of such materials, A and B, where all geometrical dimensions of sample B have been scaled down by a factor $n (n > 1)$ in relation to sample A.

So B has the same shape as A, but is smaller in size. If a scale rule is to apply, the sound field in sample B must have the same form as in A, only reduced in dimension by the factor $1/n$. This imposes, e.g., the thicknesses of the viscous and thermal boundary layers must be reduced by $1/n$ and the free wave-length must be reduced by $1/n$.

On assuming the same ideal gas to be the acoustic medium in both samples, the boundary layer thicknesses are universely proportional to the square root of frequency (see appendix B), thus requiring an increase in frequency by a factor n^2 for sample B in relation to sample A, whereas the free wavelength is inversely proportional to frequency, thus requiring an increase in frequency by a factor n. Excepting trivial cases, both conditions cannot be met simultaneously, and no frequency can be indicated for sample B, yielding a sound field of the same form as for sample A.

The problem may be illustrated by deriving a scale rule for the static value of the specific acoustic flow resistance and investigating its consequences for the sound fields in the two samples. In the case of static flow, the forces exerted by the frames of the samples on the medium are viscous ones and the compressibility of the medium is irrelevant; generality is not impaired by assuming an incompressible medium. These considerations are expressed in three-dimensional notation in general form:

$$\partial p/\partial x_i = \eta \, \Sigma_j \partial^2 u_i/\partial x_j^2 \quad ; \quad i,j = x,y,z \tag{3-118}$$

The incompressibility can be expressed by

$$\Sigma_i \partial u_i/\partial x_i = 0, \tag{3-119}$$

where x_i is the generalized spatial co-ordinate and u_i is the generalized component of particle velocity. Note that eq.(3-118) in fact represents three equations.

One solution for sample A is assumed to be known:

$$u_i = \Psi_i(x,y,z),$$

and a second assumption is that a solution of the same form holds for sample B. The generalized spatial co-ordinate for sample A is indicated by x_i, that for B by ξ_i:

$$n\xi_i = x_i. \tag{3-120a}$$

Requiring equal particle velocities in corresponding points in the two samples implies that for sample B:

$$u_i = \Psi_i(n\xi_i,\ n\xi_j,\ n\xi_k),$$

a solution which satisfies the boundary conditions automatically and, after some consideration, is seen to satisfy eq.(3-119) too.
Sound pressure is indicated by q for sample B and eq.(3-118) yields

$$\partial q/\partial \xi_i = n \Sigma_j \partial^2 u_i/\partial \xi_j^2 = n\partial q/\partial x_i = nn^2 \Sigma_j \partial^2 \Psi_i (x_i, x_j, x_k) /\partial x_j^2 .$$

This equation is identical with that for case A, if

$$q = np. \tag{3-120b}$$

The flow-resistance for flow in the direction k follows from

$$-\partial \bar{p}/\partial x_k = \sigma \bar{u}_k. \tag{3-120c}$$

where $\bar{p}$ the average sound pressure in the pores and $\bar{u}$ is the volume velocity per unit area.
In the present instance, an averaging process is required over an area large enough to be representative for the sample and thus the flow resistance now follows as:
for sample A

$$\sigma_A = \lim_{X_i, X_i \longrightarrow \infty} \frac{\frac{-1}{hX_i X_j} \int_{-X_i/2}^{X_i/2} dx_i \int_{-X_j/2}^{X_j/2} dx_j \frac{\partial p}{\partial x_k}}{\frac{1}{X_i X_j} \int_{-X_i/2}^{X_i/2} dx_i \int_{-X_j/2}^{X_j/2} dx_j\ u_k}, \tag{3-121a}$$

for sample B

$$\sigma_B = \lim_{X_i, X_j \to \infty} \frac{h \frac{-n^2}{X_i X_j} \int_{-X_i/2n}^{X_i/2n} d\xi \int_{-X_j/2n}^{X_j/2n} d\xi_j \frac{\partial q}{\partial \xi_k}}{\frac{n^2}{X_i X_j} \int_{-X_i/2n}^{X_i/2n} d\xi \int_{-X_j/2n}^{X_j/2n} d\xi_j \, u_k} . \qquad (3\text{-}121b)$$

The limits introduced above are assumed to exist. Taking into account that:

$$\partial q/\partial \xi_k = \partial np/\partial (x_k/n) = n^2 \partial p/\partial x_k, \qquad (3\text{-}122)$$

and reducing the integration variables in eq.(3-121b) to x_i and x_j, it follows from eqs(3-121a) and (3-121b) that

$$\sigma_B = n^2 \sigma_A. \qquad (3\text{-}123)$$

Eq.(3-123) is a scale rule but not in the general sense required in acoustics as its validity has been proven only for static flow.

Now eq.(1-1) is adduced; the limitation to one spatial dimension does not affect the principles involved. Air, as medium, is permitted to retain its density but its motion is assumed to be hampered by a flow resistance, σ_A or σ_B respectively for the two samples under consideration. The sound fields generated in these samples are harmonic, having circular frequencies ω_A and ω_B, respectively. Thus

for sample A

$$-\partial p/\partial x = (j\omega_A \rho_s + \sigma_A) u, \qquad (3\text{-}124a)$$

for sample B

$$-\partial q/\partial \xi = (j\omega_B \rho_s + \sigma_B) u . \qquad (3\text{-}124b)$$

Using eqs(3-122) and (3-123), eq.(3-124b) is seen to be identical with eq. (3-124a), if:

$$\omega_B = n^2 \omega_A . \qquad (3\text{-}124c)$$

This result was to be expected on the grounds of the frequency dependence of the boundary layers. That it clashes with the requirement imposed on the free wavelength will become apparent from eq.(1-2), which yields:

for sample A $-\partial u/\partial x = j\omega_A\, p/K,$ (3-125a)

for sample B $-\partial u/\partial \xi = j\omega_B\, q/K.$ (3-125b)

Eqs(3-120a), (3-120b) and (3-120c) reduce eq.(3-125b) to:

$$-\partial u/\partial x = j\, n^2\omega_A\, p/K,$$

which is not in accordance with eq.(3-125a), thus showing that the scale rules eqs(3-120a), (3-120b) and (3-120c) lead to an inconsistency, although essential for eqs(3-118) and (1-1). Hence a scale rule for porous materials proves impossible.

3.10 The model of the prismatic soil structures

The models that were worked out are based on the principle of a homogeneous layer. Heavy clay soils and slaked soils after a dry period often show prismatic structures. The larger cracks and fissures in such soil structures perpendicular to the surface of the soil are often combined with smaller horizontal slits at almost regular intervals.
As in homogeneous, isotropic porous materials, an idealized geometrical arrangement is introduced, see figure 25. The problem is reduced to two dimensions, the cross-section in figure 25 is assumed to be constant in the direction normal to its plane.
The vertical principal fissures or main slits have a width D, a depth l and their number per unit length is M. The smaller horizontal cracks or side slits are accorded a width d, a depth h (not to be confused with porosity) and there are N of them per unit length. Wave propagation in the main slits is assumed to be governed by inertia and adiabatic compressibility of the medium (air) only, which is quite reasonable as these slits are usually rather wide and viscous and thermal boundary layers have little effect. Viscous and thermal losses are thus confined to the side slits. No end corrections for the slits were introduced, as the geometry has been idealized to such an extent that it was felt that this additional straw was unlikely to break the camel's back. The basic unit to be considered is half a main slit, its associated side slits and the accorded unit depth in the direction normal to the plane of figure 25. This implies that all volume velocities and acoustic admittances are to be considered per unit depth, a fact that will be tacitly assumed in the following.

Wave propagation in homogeneous slits is discussed in appendix B: eqs (B-6) and (B-18) give the perturbation factors ξ_f' and η_f' for such slits, in conjunction with the equations for the boundary layer thicknesses, eqs (B-3) and (B-14), respectively. Here, the side slits are homogeneous and the perturbation factors for the homogeneous slits apply in the general case. Thus

$$\xi_f = \xi_f' \; ; \quad \eta_f = \eta_f' \quad , \tag{3-126}$$

and $S_a = d$

may be introduced into eqs(3-51) and (3-52). The equations of motion and continuity in channels may be solved on the boundary condition U = o at the bottom of these side slits. The method of solving is the same as that applied in 1-9

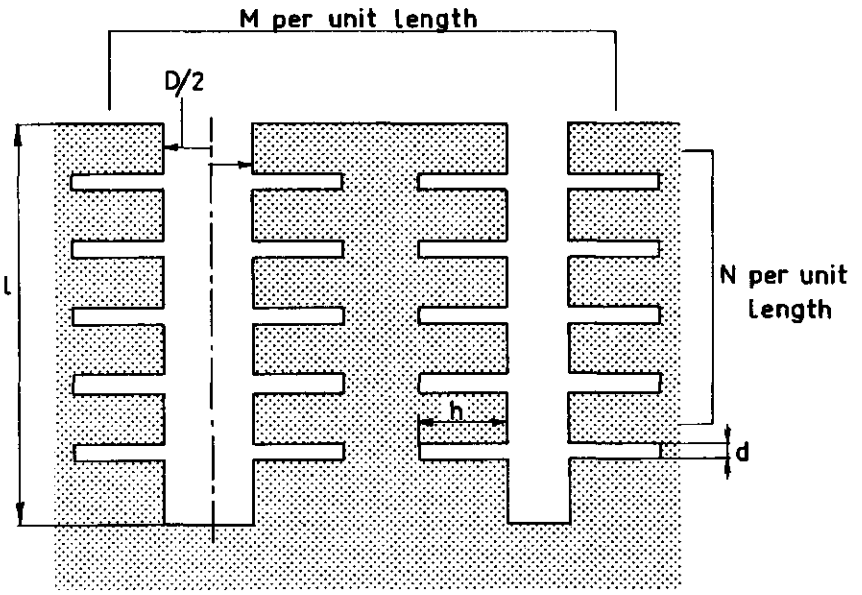

Figure 25 Idealized geometry for a prismatic structure

(note the similarity between eqs(I-52), (I-53) and (3-51), (3-52); the result sought now is the acoustical admittance at the mouth of the side slit, Y_s, where

$$Y_s = \frac{jd}{\rho_s c} \sqrt{(\eta_f'/\xi_f')} \tan\ kh \sqrt{\xi_f' \cdot \eta_f'} \quad , \tag{3-127}$$

(see eqs(B-6) and B-18) for ξ_f' and η_f').
The acoustic admittance of the wall of the section of the main slit under consideration, per unit length, is N Y_s, and the acoustic admittance due to the compressibility of the air is given by

$j\omega D/2\kappa p_s$.

Thus the total acoustic admittance per unit length is given by

$$Y_a = \frac{j\omega D}{2\kappa p_s}\left[1 + \frac{2h_s}{kD}\sqrt{(\eta_f'/\xi_f')}\tan\left[kh\sqrt{(\xi_f' \cdot \eta_f')}\right]\right] , \tag{3-128}$$

where the surface porosity for the side slits h_s is given by

$$h_s = N \cdot d. \tag{3-129}$$

The acoustic impedance per unit length for the section of the main slit under consideration is given by

$$Z_a = 2j\omega\rho_s/D, \tag{3-130}$$

and the equations of motion and continuity for this slit thus take on the forms

$$-\partial p/\partial x = Z_A U, \tag{3-131}$$

$$-\partial U/\partial x = Y_A p. \tag{3-132}$$

Following the procedure adumbrated in section I-9, with U = 0 at the bottom of the main slit as boundary condition, the acoustic admittance Y_p at the mouth of a complete main slit is derived:

$$Y_p = \frac{jD}{\rho_s c}\sqrt{\left[1+\frac{2h_s}{kD}\sqrt{\left(\frac{\eta_f'}{\xi_f'}\right)}\tan\{kh\sqrt{(\xi_f'\cdot\eta_f')}\}\right]}\tan\left(kl\sqrt{\left[1+\frac{2h}{kD}\sqrt{\left(\frac{\eta_f'}{\xi_f'}\right)}\tan\{kh\sqrt{(\xi_f'\cdot\eta_f')}\}\right]}\right). \tag{3-133}$$

The acoustic admittance per unit length at the sample surface is $M\cdot Y_p$ in the present nomenclature. Note, however, that this value is actually the acoustic admittance per unit area, i.e. the specific acoustic admittance. Thus, on introducing the surface porosity

$$h_m = M\cdot\Sigma \tag{3-134}$$

eq.(3-124) yields, for the normalized specific acoustic impedance at the sample surface

$$\zeta = \frac{1}{h_m}\,\frac{-jcot\left(kl\sqrt{\left[1+\frac{2h_s}{kD}\sqrt{(\eta_f'/\xi_f')}\tan\{kh\sqrt{(\xi_f'\cdot\eta_f')}\}\right]}\right)}{\sqrt{\left[1+\frac{2h_s}{kD}\sqrt{(\eta_f'/\xi_f')}\tan\{kh\sqrt{(\xi_f'\cdot\eta_f')}\}\right]}}. \tag{3-135}$$

A Fortran program was devised for the calculation of ζ from eq.(3-124). Some results, for constant sample thickness and variable frequency are presented in table 3-7.

In the low frequency range, where the boundary layer thicknesses exceed the slit width of the side slits, eq.(3-135) may be approximated, provided h is not too small. This latter condition is unlikely to be violated, as satisfaction of the inequality, $k/d\sqrt{(6\omega\eta/p_s)} > 2$, will hold. In that case

Table 3-7

Specific acoustic impedance for a prismatic soil structure $(\xi + j\eta)h$; crack width (D) = 0.001 m, slit width (d) = 0.008 m.

	h	0.050		0.100	
Hz	1(m)	0.040	0.072	0.040	0.072
200		0.08 - 72.11j	1.01 + 1.00j	0.06 - 14.14j	1.04 + 1.00j
400		0.10 - 33.58j	1.02 + 1.00j	0.05 - 4.90j	1.03 + 1.00j
600		0.10 - 19.59j	1.02 + 1.00j	0.53 - 0.50j	1.47 + 1.07j
800		0.01 - 11.52j	1.00 + 1.00j	1.40 - 3.72j	14.23 + 7.15j
1000		0.34 - 5.51j	1.06 + 1.00j	2.06 - 11.60j	4.27 + 2.25j
1200		2.09 - 0.34j	1.46 + 1.07j	2.36 - 14.29j	1.86 + 1.19j
1400		7.26 - 2.57j	6.25 + 3.20j	1.34 - 5.71j	1.43 + 1.06j
1600		7.70 - 12.00j	7.74 + 3.93j	1.26 - 1.62j	1.40 + 1.05j

In that case one may write:

$\xi_f' \approx \frac{-12\ j\eta}{\omega\rho_s d^2}$ and $\eta_f' = \kappa$. This gives

$$kh\sqrt{(\xi_f'\ \eta_f')} \approx \frac{kh}{d}(1-j)\sqrt{\left(\frac{6\kappa\eta}{\omega\rho_s}\right)} = (1-j)\frac{h}{d}\sqrt{\left(\frac{6\omega\eta}{p_s}\right)}. \qquad (3\text{-}136)$$

From $\tan\{(1-j)x\} = -j\frac{1-\exp(-2x(1+j))}{1+\exp(-2x(1+j))}$ it now follows, that with $x>2$, $\tan(kh\sqrt{(\xi_f'\ \eta_f')}) \approx \tan(1-j)x \approx -j$. In this case

$$\zeta \cdot h_m = -j\frac{\cot\left(kl\sqrt{\left[1+(1-j)\,h_s\frac{\kappa d}{D}\sqrt{(p_s/6\omega\eta)}\right]}\right)}{\sqrt{\left[1+(1-j)\,h_s\frac{\kappa}{D}\sqrt{(p_s/6\omega\eta)}\right]}} \qquad (3\text{-}137)$$

Note that the width of the side slits has a predominant influence on ζ, affecting both the side surface porosity h_s and the ratio of the slit widths d/D.

3.11 Electro-acoustical equivalent networks

Sometimes the behaviour of an acoustical system may be classified by examining its electrical analogous circuit. In the present instance, a porous material is such a system and eqs (1-52) and (1-53) indicate the procedure for transition from acoustical to electrical symbolism. If p is conceived as the voltage on an electrical transmission line, u as the current, and Z_m and Y_m are taken to represent the series impedance and parallel admittance per unit length of that line, respectively, the equations named become identical with the telegraph equations.

In electrical analogous circuits of the sort intended here, masses are replaced by self-inductances, flow resistances by resistors and compliances with damping by combinations of capacitors and resistors. In the present section, the possibility of composing reasonably simple electrical equivalent circuits for Z_m and Y_m is examined; complicated circuitry may be ignored as it does not contribute to clarity

A simple porous material will be considered, consisting of cylindrical pores of constant, circular cross-section of radius R. The pores are inclined from the direction of propagation, the angle of inclination does not need to be constant if the material remains homogeneous in the acoustical sense. For frequencies so low that boundary layer thickness exceed tube radius, Zwikker & Kosten's (1949, p. 38) results may be applied and after some reduction it follows that

$$Z_{m\ell} = \frac{4}{3} \cdot \frac{j\omega k_m \rho_s}{h} + \frac{8\, k_m \eta}{hR^2}\,, \tag{3-138}$$

$$Y_{m\ell} = \left[\frac{p_s}{j\omega h} + (\kappa-1)\,\frac{\rho_s c_v p_s R^2}{8h\lambda}\right]^{-1}, \tag{3-139}$$

where the added subscript ℓ indicates the low-frequency approximation and h stands for porosity.
For comparison an electrical transmission line is considered, a unit length of which is represented in Figure 26.

From this circuit diagram it follows that:

$$Z_{me} = j\omega L + R_l, \tag{3-140}$$

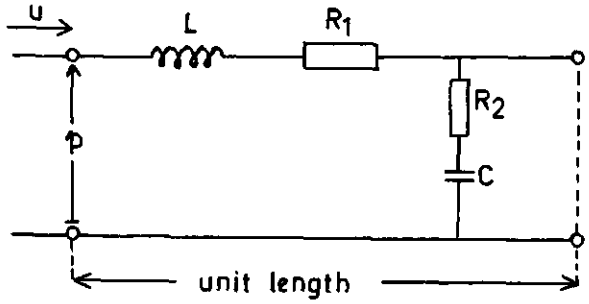

Figure 26 An element of an analogous electrical transmission line

$$Y_{me} = 1/\left[\, 1/j\omega C + R_2 \right] \quad , \tag{3-141}$$

where the added subscript e indicates the electrical circuit. On comparing eqs (3-138) with (3-140) and (3-139) with (3-141) it will be seen that these equations become identical, pair by pair, and thus that Figure 26 is representative for the porous material, if

$$L = \frac{4}{3}\,\frac{k_m \rho_s}{h} \quad ; \quad R_1 = \frac{8 k_m \eta}{h R^2} \; ; \tag{3-142, 143}$$

$$C = \frac{h}{p_s} \quad ; \quad R_2 = (\kappa - 1)\,\frac{\rho_s c_v p_s R^2}{8 h \lambda} \; . \tag{3-144, 145}$$

It should be noted, however, that the analogous circuit in Figure 26 is valid only as a representation of the porous material under consideration for low frequencies. Use of Zwikker & Kosten's (1949, p.38) results for frequencies so high that pore radius is large in relation to boundary-layer thickness yields:

$$Z_{mh} = \frac{j\omega \rho_s k_m}{h} + \frac{2 k_m}{hR}\sqrt{(j\omega \rho_s \eta)} \quad , \tag{3-146}$$

$$Y_{mh} = \frac{j\omega h}{\kappa p_s} + \frac{2h(\kappa - 1)}{\kappa p_s R}\sqrt{\left(\frac{j\omega \lambda}{\kappa \rho_s c_v}\right)} \quad , \tag{3-147}$$

where the added subscript h indicates the higher frequencies and λ refers to the heat conductivity of free air.

It is impossible to devise a simple electrical circuit, of the same order of complexity as that in Figure 26, yielding circuit equations of the form of eqs (3-140) and (3-147). This is due to the nature of the frequency dependence of boundary-layer thickness. Thus a unit length of a transmission line representing eqs(3-146) and (3-147) would have to contain infinite transmission lines as

circuit elements and even if these latter can be approximated by a finite number of elements, discernability is lost.

It seems impossible to compose a satisfactory equivalent electrical circuit for the geometrically simple porous material considered, covering the entire frequency range. Thus no further efforts were made to search for equivalent circuits for more complex materials.

4 Some experiments discussed

4.1 Introduction

The principal aim of this chapter is the examination of the applicability of the three mathematical models discussed in the previous chapter to the description of soil-like materials. The examination is carried out by comparing measured and calculated curves for the quantity $\zeta \cdot h$, the product of normalized sample surface impedance and porosity, for samples of given thickness and for variable frequency. In assessing a mathematical model, two questions are posed: does the model, with its parameters adjusted to optimum fit, describe the sample and do these parameters yield information on the geometrical arrangement of the sample material?

The quantity $\zeta \cdot h$ is appropriate in the present instance as all three models happen to yield expressions for it which are independent of h. The calculated curves are determined by the values of $\zeta \cdot h$ for a series of frequencies with spacings of 100 Hz in most cases. Measurements were made from about 150 to 1750 Hz, but could not be carried out systematically at the spot frequencies. This is due to the exigencies of the interferometer (e.g. resonances in the tube) and the following procedure was introduced to find interpolated values for $\zeta \cdot h$ at the spot frequencies. The measured points for ζ are entered in the complex plane and the absorption coefficient a is plotted against the frequency f. In both cases smooth curves are drawn through the points. From the a-f diagram values of a for the spot frequencies are found and these values are used to find the complex value of $\zeta \cdot h$ in the complex plane.

ζ was measured with the equipment described in chapter 2 and h was found by a static method (cf. Introduction). In addition, the specific static flow resistance σ_s was determined (cf. Introduction).

The measured curves were matched with those obtained from the models, the latter being constructed for various values of the parameters. A number of provisional fits were obtained by comparing tables of measured and calculated values for $\zeta \cdot h$. However the calculated curve giving the best fit was selected graphically, by visual examination, taking into account the local accuracy in the $\zeta \cdot h$ plane (cf. figure 14) and the sensitivity of the calculated curves for variations in the parameter. Special attention was paid to those sections of the curve where

the absorption coefficient is high, as accuracy is high there too. These sections are commonly found near the first anti-resonance.

In a small number of cases the value of a parameter was interpolated after matching one measured curve with two or more calculated ones. Thus broken values for k_m have been found notwithstanding the fact that the calculations were carried out with integer values.

With the imperfection of the models in view, no effort was made to develop a numerical method of comparison. Such a method would be feasible after transformation of the locus from the ζ-h plane to another plane having e.g. an invariant error circle. The derivation of an appropriate transformation presents considerable difficulties however. Better fitting curls could undoubtedly have been calculated in some instances. This was not done, as the selected models were in need of further refinement anyway.

4.2 Materials studied

For the purpose of matching measured and calculated curves three types of sample materials were used: isodiametrical spheres, gravel and crushed bricks. The first series of measurements were made on isodiametrical spheres. The balls were made of steel, glass or polystyrene. The steel balls, obtained from a ball bearing factory, were perfectly round, and did not lend themselves to loose packing. The glass spheres served their purpose, the very thin layer of water, always covering them in the conditions of the experiment, made it possible to obtain packings of varying densities. The polystyrene spheres had the same disadvantage as the steel ones. Gravel and crushed bricks were also used, since they allowed not only a study of the effects of variable porosity, but also permitted variation of the pore size distribution function. The gravel used consisted of both rounded particles and particles that had been crushed to create sharp edges. Two sample thicknesses were used practically exclusively: 40 and 72 mm. The spheres and the gravels hardly absorb any water (in the order of 0.15 - 0.30 weight percent), so crushed bricks are a better simulation of soil than the other materials. The material sometimes possesses many small pores which may or may not be filled with water. It was chosen as it does not show any rearrangement or desintegration (of particles) upon changes in moisture content resulting from variations in moisture tension. This might have occurred in soil aggregates as these are subject to structural changes through swelling and air explosions. No attempt was made to explain the effect of moisture content with the aid of a model as adequate models incorporating the effect of water content at a given suction on accessible pores

are unavailable.

Measurements were also made on soil aggregates which had been stabilized with soil conditioners, such as Krilium, Aerotil or carboxymethylcellulose. The use of these aggregates was not very attractive because of the difficulty in wetting them completely. They can only be made to absorb moisture by repeated evacuation and moistening under vacuum.

Many measurements were made on core samples obtained from field plots under different methods of tillage. But none of the geometrical models selected allows interpretation of the results obtained. These results will therefore not be discussed. Although many measurements were made at other layer thicknesses than given above, the results of these measurements will not be listed later in the tables nor will they be discussed. Discussion of results obtained with layered systems in arrangements of coarse particles stacked on fine ones and the reverse will also be omitted. But very interesting acoustical results come from a layer of fine particles on a layer of coarse ones and they certainly justify extension of the geometrical models in the future.

4.3 Comments on the calculation of the impedance curls

The calculated values for $\zeta \cdot h$ were obtained from the mathematical models with computers. Each calculated curl was determined by calculating $\zeta \cdot h$ for at least eight spot frequencies: 200, 400 ... 1600 Hz. Sometimes smaller steps in frequency were chosen. In a few cases the frequency range was increased. The layer thicknesses for calculation corresponded to those that were measured. Two sample thicknesses, 40 mm and 72 mm, were used almost exclusively, both for measurement and calculation.

It is clear that the sensitivity for a variation in one of the parameters on $\zeta \cdot h$ cannot be predicted in a simple way from the mathematical models, which do not lend always themselves to differentiation to the principal parameters. Thus the most promising approach is the examination of the position, form and course of the calculated impedance curl for various values of the parameters. Sometimes the apex is of special interest.

Initially the values of cos θ were varied between 0.50 and 1.00. A comparison of the results obtained by measurement and calculation showed that the lower values of cos θ were seldom required. These were thereupon excluded from further calculations.

It can be concluded from figures 21 and 22 that a vertical displacement along a model capillary of 0.816 r corresponds to a lateral displacement of $r/\sqrt{3} = 0.5773$ r, thus a nominal value of 0.7303 might be introduced for cos θ. After a

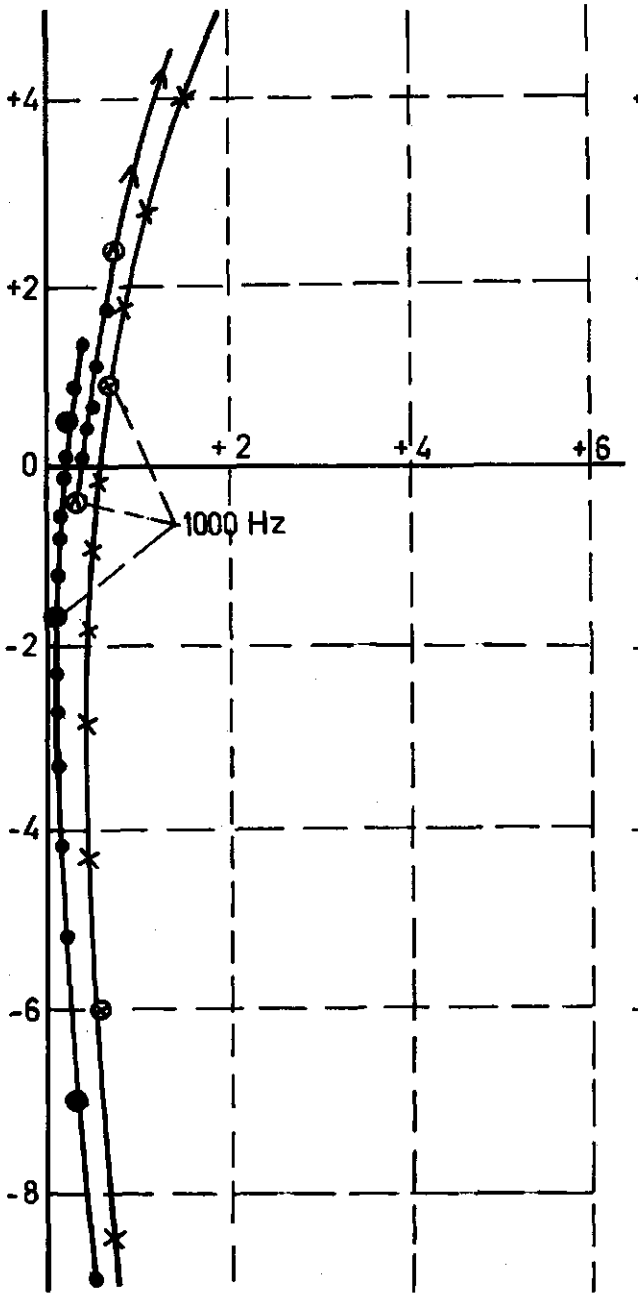

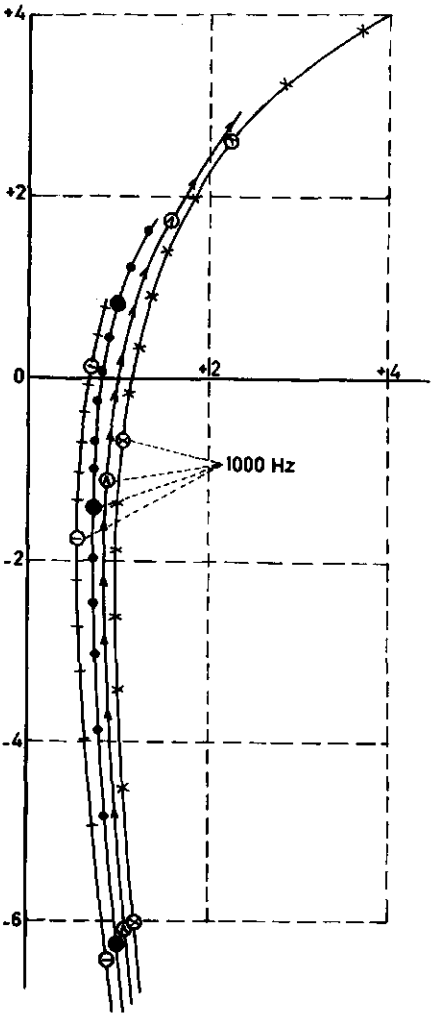

Figure 27 (left) Calculated values of $\zeta \cdot h$ for the fissure model (D_a = 0.00068 m; l = 0.040 m; q_a = 2.0; cos θ = 0.645; 0.700; 0.780 resp.)

Figure 28 (right) Calculated values of $\zeta \cdot h$ for the fissure model (D_a = 0.00033 m; l = 0.040 m; q_a = 2.0; cos θ = 0.645; 0.700; 0.780; 0.866 resp.)

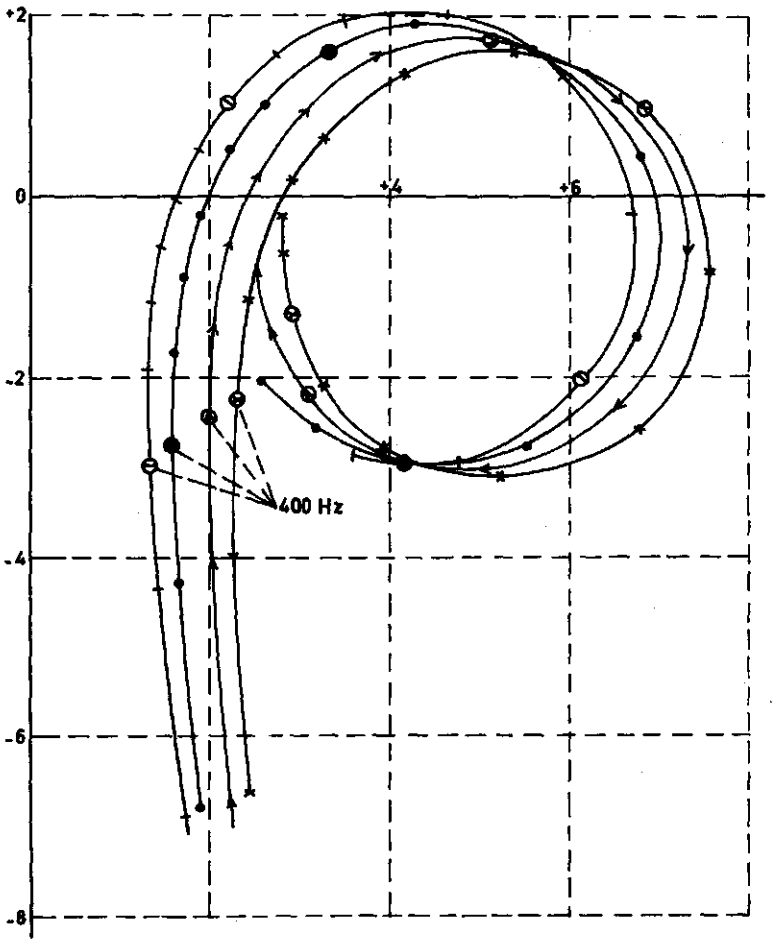

Figure 29 Calculated values of $\zeta \cdot h$ for the fissure model (D_a = 0.00039 m; l = 0.040 m; q_a = 2.0; cos θ = 0.645; 0.700; 0.780; 0.866 resp.)

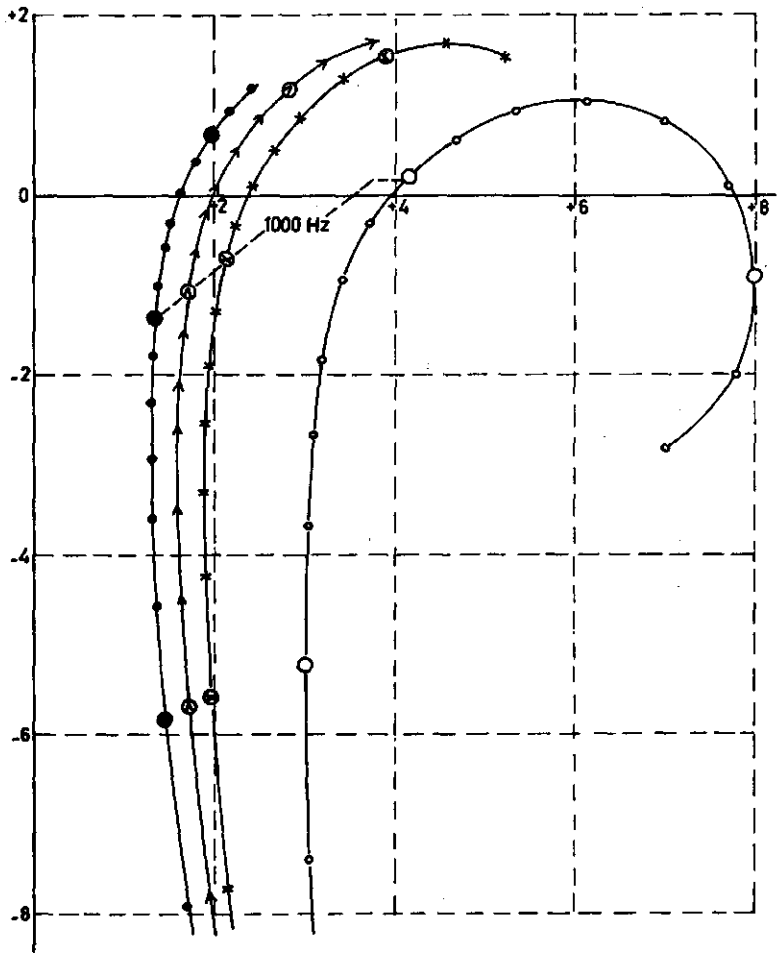

Figure 30 Calculated values of $\zeta \cdot h$ for the fissure model (D_a = 0.00022 m; l = 0.072 m; q_a = 2.0; cos θ = 0.500; 0.645; 0.700; 0.780 resp.)

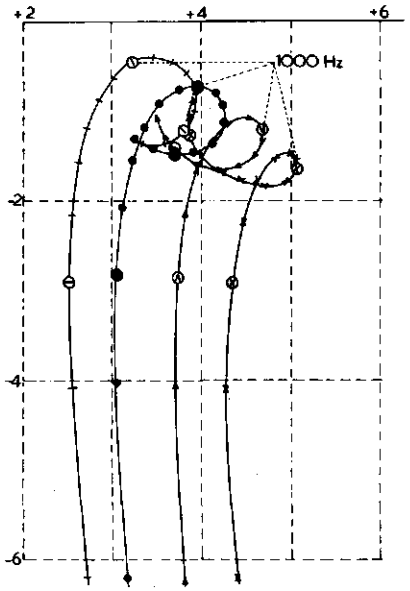

Figure 31 Calculated values of $\zeta \cdot h$ for the fissure model (D_a = 0.00018 m; l = 0.072 m; q_a = 2.0; cos θ = 0.645; 0.700; 0.780; 0.860 resp.)

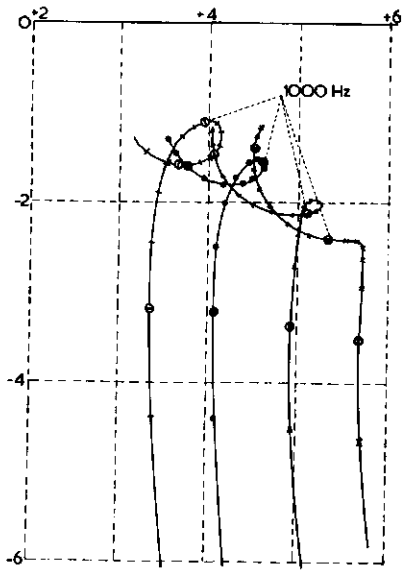

Figure 32 Calculated values of $\zeta \cdot h$ for the fissure model (D_a = 0.00022 m; l = 0.072 m; q_a = 2.45; cos θ = 0.645; 0.700; 0.780; 0.866 resp.)

few trials, the following values were selected for q_a: 1.6; 1.8; 2.0; 2.2; 2.3; 2.4 and 2.6. D_a was varied with 12 steps per decade. In total a few thousand curls were generated.

In the graphs representing the calculated impedance curls the points for integer multiples of 100 Hz have been marked; those for 400, 1000 and 1600 Hz receiving an enlarged symbol. The upper frequency in figures 27 to 39 is 1800 Hz. The symbols used to mark the spot frequencies indicate the value of cos θ and the following markings were applied.

cos θ	0.500	0.645	0.700	0.780	0.866
symbol	O	X	Λ	●	–

In the complex planes where the calculated curves are represented, a rectangular grid for integer values of $\xi \cdot h$ and $\eta \cdot h$, with a spacing of two units, has been entered. The lines of the grid corresponding to the axes of the complex plane are drawn in full, the others are dotted. The transparency in the flap of this book may be placed on the graphs thus permitting an estimate of the absorption coefficient and the phase shift for the values of $\zeta \cdot h$ plotted.

When considering the calculated curls it should be borne in mind that the precise position of the curve in those regions of the complex plane, where measuring accuracy is low, is comparatively unimportant (see figure 13). Thus the effects of variation in the parameters is of only secondary interest for such regions.

Figure 27 shows the results for a relatively wide fissure (D_a = 6.8 mm) and small layer thickness. The real component of $\zeta \cdot h$ possesses a low and practically constant value for increasing frequency; the imaginary component of $\zeta \cdot h$ decreases gradually. After crossing the real axis an increase in frequency leads to higher absolute values for both the real and imaginary components of $\zeta \cdot h$. An increase in cos θ shifts the curve towards the imaginary axis and the real axis is crossed at higher frequencies if so, the influence of cos θ is quite small. Figures 27 and 28 permit comparison of the effects of D_a. For equal values of cos θ, the smaller value for D_a leads to higher values for the real part of $\zeta \cdot h$ and the real axis is crossed at a far higher frequency. The increase in the real component exceeds inverse proportionality in relation to fissure width. The anti-resonance frequency can be determined accurately in the present case, which is of considerable assistance when making comparisons with measured curves.

Comparison of figures 28 and 29 shows the effect of sample layer thickness. The curves for the thicker sample incorporating the first resonance show larger and more evenly distributed intervals between the points for the spot frequencies. An increase in cos θ, corresponding to a decrease in k_m in the Zwikker Kosten model, leads to an increase in the propagation velocity in the sample material

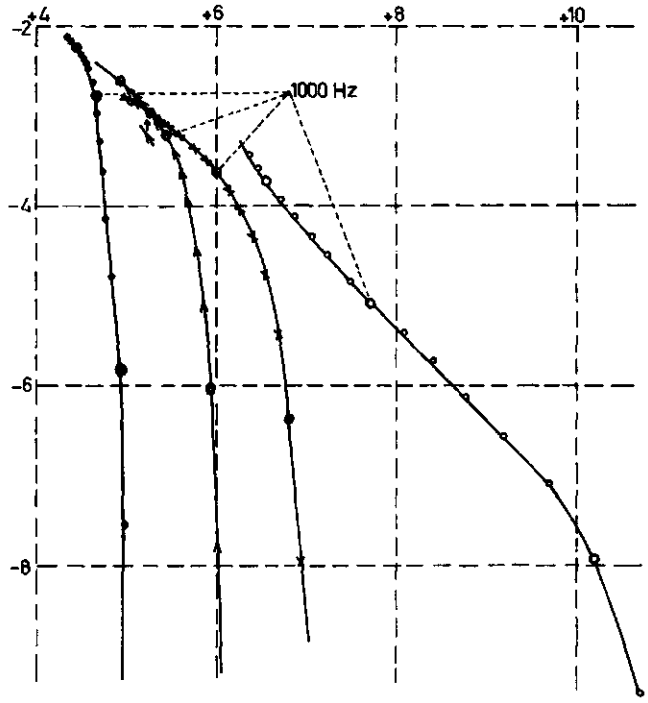

Figure 33 Calculated values of $\zeta \cdot h$ for the fissure model (D_a = 0.000100 m; l = 0.040 m; q_a = 2.0; cos θ = 0.500; 0.645; 0.700; 0.780 resp.)

as may be seen from, for instance the points for 1000 Hz in the figures 28 and 29, respectively. This result was to be expected (cf. eq.3-55) as the direction of propagation in the pores now coincides more closely with that of the sound wave in the material.

The apexes of the curls in figure 29 lie below the real axis (cf. eq.3-56). This is due to the preponderance of the viscous losses over the thermal ones, as may be proved mathematically.

Figure 30 gives curls for a very small fissure width but with the same values of the other parameters as those for figure 29. An interesting feature can be detected: as values of cos θ increase the apex of the curl shifts towards the real axis and the propagation velocity in the material obviously decreases.

Figure 31 shows the effect of cos θ on the position of the curl. At the higher frequencies the curl approaches its apex fairly closely and the effect of cos θ on the propagation constant is rather small at the lower frequencies. Note that the apexes corresponding to the wave impedances should be considered slow functions of frequency. The figure demonstrates that the wave impedances are very nearly real and not very large. All this means that in this sort of case accurate comparison with measured curls is feasible.

Another phenomenon appearing in figure 31 is that some of the curls intersect themselves. This implies that at least one point is bi-valued for frequency.

In figure 32 q_a has been increased in relation to figure 31, and D_a increased slightly. It shows the transition from impedance curls with a loop to those that are characterized by more simple forms. For very fine slits and a large variation in pore size (q_a = 2.45) high absorption coefficient will be attained at moderate frequencies. The distribution of the frequency markers along the curls is regular above 1000 Hz. Thus interpolation between the spot frequencies is facilitated and assists in the comparison with measured curls.

For this small figure width, the air flow resistance is high. The coth converges towards unity for high frequency, so the upper part of the impedance curl should approach the form of a rectangular hyperbola (Zwikker & Kosten, 1948, p.47).

As in figure 31, the curves approach their wave impedances for higher frequencies. These impedances are nearly real and determined to a large extent by specific flow resistance. The figure shows that for larger values of cos θ and thus for lower resistances the real part of $\zeta \cdot h$ decreases almost in inverse proportion to $\cos^2 \theta$.

At low frequencies the same trend for all curls is characteristic; the absorption coefficient is proportional to the real part of $\zeta \cdot h$. Here the result is a family

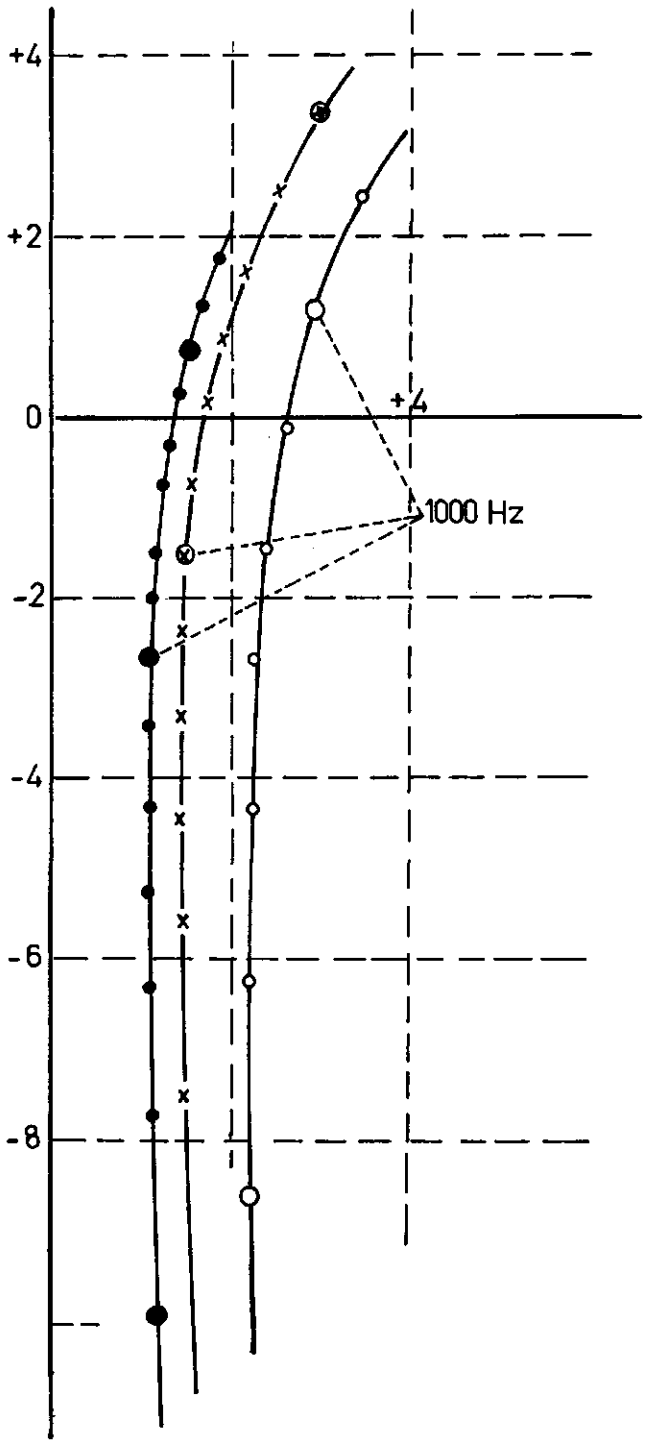

Figure 34 Calculated values of $\zeta \cdot h$ for the capillary model
(r = 0.00160 m; l = 0.040 m; cos θ = 0.500; 0.645; 0.700; 0.780 resp.)

of straight lines parallel to the imaginary axis, at a larger distance from this axis when the air resistance is higher.

Another effect appears in the figure: for the lower values of the flow resistance, damping is still low enough to yield spiral-like contours. For high air flow resistance these spiral-like forms vanish.

In figure 33 the fissure width has been diminished still further to 0.1 mm and the spiral-like curves no longer appear. This small fissure width corresponds to very high air flow resistances and leads to almost straight lines in the direction +1 with an apex just below the point. For high frequencies the different curls show small shifts due to variations of cos θ. Their course corresponds to that of wood fibre plate as shown in Zwikker Kosten (1949, figure 18c). This means at the same time that the effects of a variation in pore size distribution, leading to a different value of q_a together with a different value of cos θ gives practically identical impedance values. So the limits of the curves for high frequencies are practically determined by fissure width, the effects of cos θ and q_a are small. The absolute values of the impedances are quite high.

Sometimes the curves for $\zeta \cdot h$ approach lines parallel to the imaginary axis. This behaviour may be understood as follows. Necessary conditions are: low frequency, small layer thickness and high air flow resistance. The sample may now be consider as a system of distributed acoustical resistance and compliances. If the modulus of the product of the propagation constant and the sample thickness is comparatively small, the resistance and the compliances may be lumped and the complex impedance shows the behaviour typical of an R-C series circuit: a constant resistive part and a negative reactance diminishing in inverse proportion to increasing frequency. At higher frequencies the mass reactance becomes more important and the system starts to behave as a long transmission line.

In figure 34 some curls are drawn, obtained from the capillary model. The sphere radius was 1.6 mm. The curls can be compared to those in figure 28. The sensitivity to variations of cos θ is practically the same. No position of the apex can be found within the frequency range studied.

Figure 35 surveys the capillary model for variations of the sphere radius, with a fixed layer thickness (here 80 mm) and a fixed value for cos θ. As R is diminished the average radius of the impedance curls decreases practically proportionally with R and for the highest frequency the progress towards resonance increases. Some of curls have been calculated up to 3000 Hz and so an indication of the apex is found. Due to the small scale of presentation a large of frequency markers were omitted. For one of the curls a layer thickness of 32 cm was chosen which demonstrates a different form of the curl analogous to those

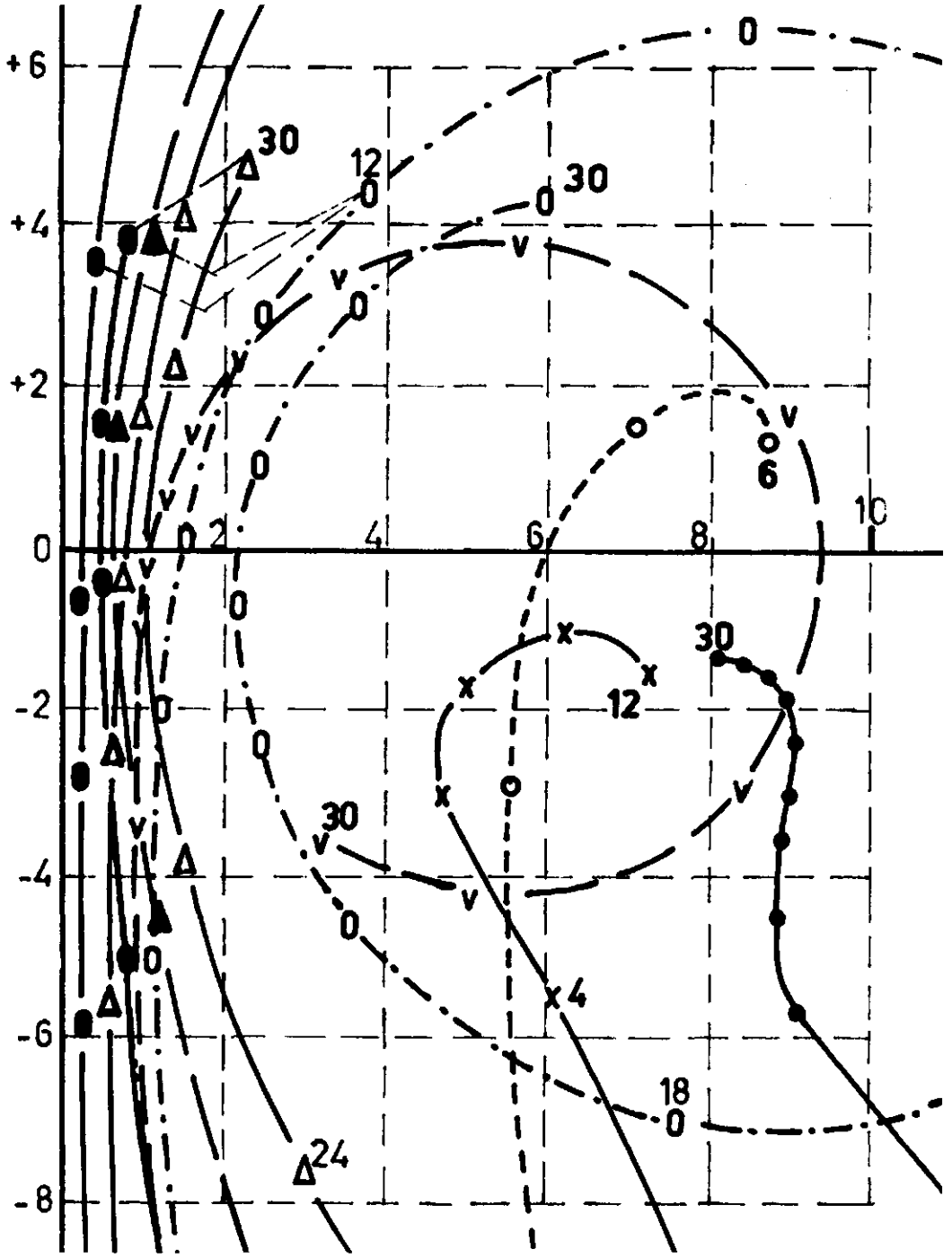

Figure 35 Calculated values of $\zeta \cdot h$ for the capillary model (influence of sphere radius ranging from 0.050 to 1.00 mm; l = 0.080 m)

	R in mm	l in m
■	1.000	(.08)
▲	0.800	"
Δ	0.400	"
0	0.200	"
v	0.150	"
o	0.075	"
x	0.050	(.08)
•	0.050	(.32)

(legend to figure 35)

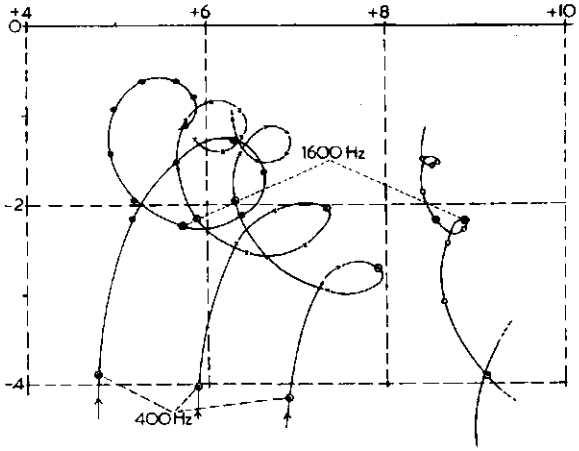

Figure 36 Calculated values of $\zeta \cdot h$ for the capillary model (r = 0.00070 m; l = 0.072 m; cos θ = 0.500; 0.645 m; 0.700; 0.780 resp.)

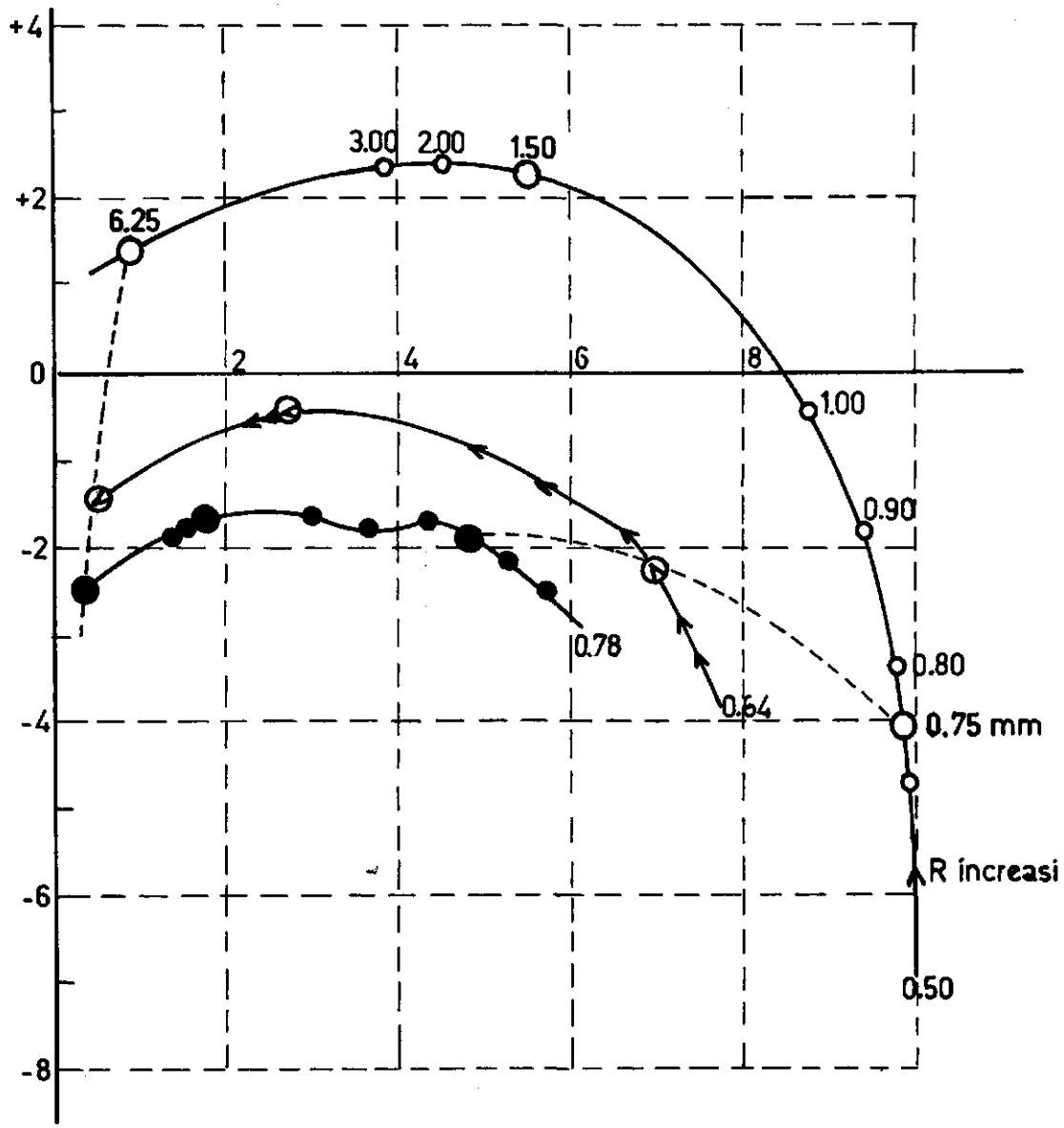

Figure 37 Calculated values of $\zeta \cdot h$ for the capillary model (influence of sphere radius, ranging from 0.75 to 6.25 mm; cos θ = 0.500; 0.645; 0.780 resp., frequency 600 Hz.)

in figure 33. For small values of R and as resonance is approached, $|\zeta \cdot h|$ becomes large and comparison to measured curves is very difficult as measuring accuracy is low.

In figure 36 some curls for fine-grained materials are given in more detail. The interesting shift of the apex with frequency is very clear and resembles that in figure 31. The loops in the curls are smaller at lower values of cos θ. With those complicated contours interpolation between various curls is impossible as is obvious from the figure, certainly this will be the case at the higher frequencies.

Figure 37 presents the results for $\zeta \cdot h$ for the capillary model in a different manner. For one frequency, 600 Hz, loci for varying sphere radius have been entered, with cos θ as parameter. For this low frequency the comparatively straight-forward course of the curves permits interpolation. For higher frequencies this is no longer possible.

Calculations for the Zwikker Kosten model were carried out on the IBM 1620 computer and took about 2 minutes per curve (eight spot frequencies). From a preliminary comparison with the results of the measurements it soon appeared that the structure factor for the materials discussed seldom exceeds 4. In total more than 600 curls were generated with this model. From the results of these calculations selection for steps and ranges for σ_d and k_m could be determined. It turned out that large ranges for σ_d were required. Although the effect of k_m is quite large at high frequencies, its influence at low frequencies is only slight.

For low frequencies k_m hardly affects the real part of $\zeta \cdot h$. The flow resistance σ_d has a slight effect of a few percent on the imaginary part. This result is in accordance with the low frequency behaviour as discussed for the capillary model.

These conclusions are confirmed by figures 14 and 15 and the results shown in tabel 4-1.

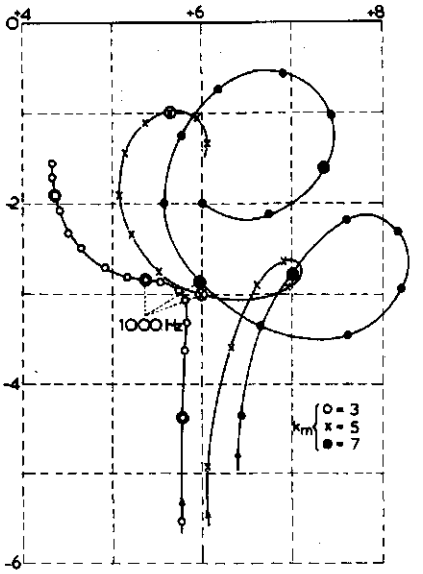

Figure 38 Calculated values of $\zeta \cdot h$ for the Zwikker - Kosten model (σ_s = 36800 Nsm^{-4}; l = 0.080 m; k_m = 3, 5, 7 resp.)

Table 4-1

Effects on the variations of k_m and $\zeta \cdot h$ from the Zwikker Kosten model

(σ_d = 600 Nsm^{-4}; layer thickness 40 mm)

frequency	400 Hz	1000 Hz	1600 Hz
(k_m)			
1	0.01-3.22j	0.02-1.07j	0.02-0.40j
4	0.02-2.92j	0.02-0.18j	0.07+1.98j

The effect of layer thickness is very marked too as is illustrated by table 4-2.

Table 4-2

Effects of layer thickness on $\zeta \cdot h$ from the Zwikker Kosten model

(σ_d = 600 Nsm^{-4}; k_m = 2.0)

frequency	400 Hz	1000 Hz	1600 Hz
(1)			
40 mm	0.02-3.12j	0.02-0.80j	0.03+0.12j
72 mm	0.03-1.48j	0.06+0.44j	2.75+9.44j

From table 4-3 it can be concluded that at higher frequencies and high specific flow resistance the sensitivity of $\zeta \cdot h$ to change in layer thickness decreases rapidly. In such cases the layer approaches what amounts to infinite thickness.

Table 4-3

Effects of layer thickness on $\zeta \cdot h$ from the Zwikker Kosten model

(σ_d = 100.000 Nsm^{-4}; k_m = 2.0)

	k_m frequency	400 Hz	1000 Hz	1600 Hz
(1)				
40 mm	1	3.05-3.80j	3.68-2.33j	2.16-1.84j
	4	3.15-3.54j	3.00-1.90j	2.64-1.61j
72 mm	1	4.10-3.77j	2.61-2.43j	2.11-1.87j
	4	4.33-3.57j	2.90-2.18j	2.51-1.56j

The examples quoted above were selected because the locus for $\zeta.h$ has not completed its first loop for the highest frequency. Only in this case is it pos-

sible to gain insight into the form of the locus for the three frequencies given.
In figure 38 the shift of the apex is shown for the Zwikker Kosten model. It occurs at high values of k_m and at relatively high air flow resistances. These figures show an analogous behaviour to those in figure 31, although the change in the size of the loops and in their position are different for the two models. This difference is presumably due to the fact that in the channel-type models, σ_m and k_m are frequency-dependent.

It is apparent from the calculated curls for $\zeta \cdot h$ (cf. figures 27 ... 38) that the comparatively simple mathematical models used can produce quite complicated contours, incorporating loops, multiple loops and similar features which one would not expect at first sight.
The Zwikker Kosten model and the two channel-type models differ in this respect that, whereas in the former the two adjustable parameters introduced cannot be correlated directly with the pore geometry, in the latter the parameters are geometrically significant and may render at least some assistance in comprehending the acoustical behaviour of the sample.

The channel-type models are but crude approximations of the real pore geometry, as has been stated previously. They are thus incapable of rendering a comprehensive description of the samples, Further refinement is required if the desired end is to be obtained. This might, but neet not, lead to an increase in the number of adjustable parameters.
The problem of the number of significant parameters is complicated considerably by not only the relatively low experimental accuracy, but also by the wide variations in sensitivity to parameter variation occurring along a curl and from curl to curl.

4.4 Discussion of the results of measurements

In tables 4-4 to 4-9 the results for $\zeta \cdot h$ of some series of measurements are compared with calculated curves. The tables have been divided into two sections, except table 4-5. The upper section is subdivided into two parts, corresponding to the two sample thicknesses. The first two rows of each of these subsections give, respectively: the layer thickness and the column indications, under I the measured values of σ_s and h, under II the numerical values of the parameters for the Zwikker Kosten model, under III those for the capillary model and under IV

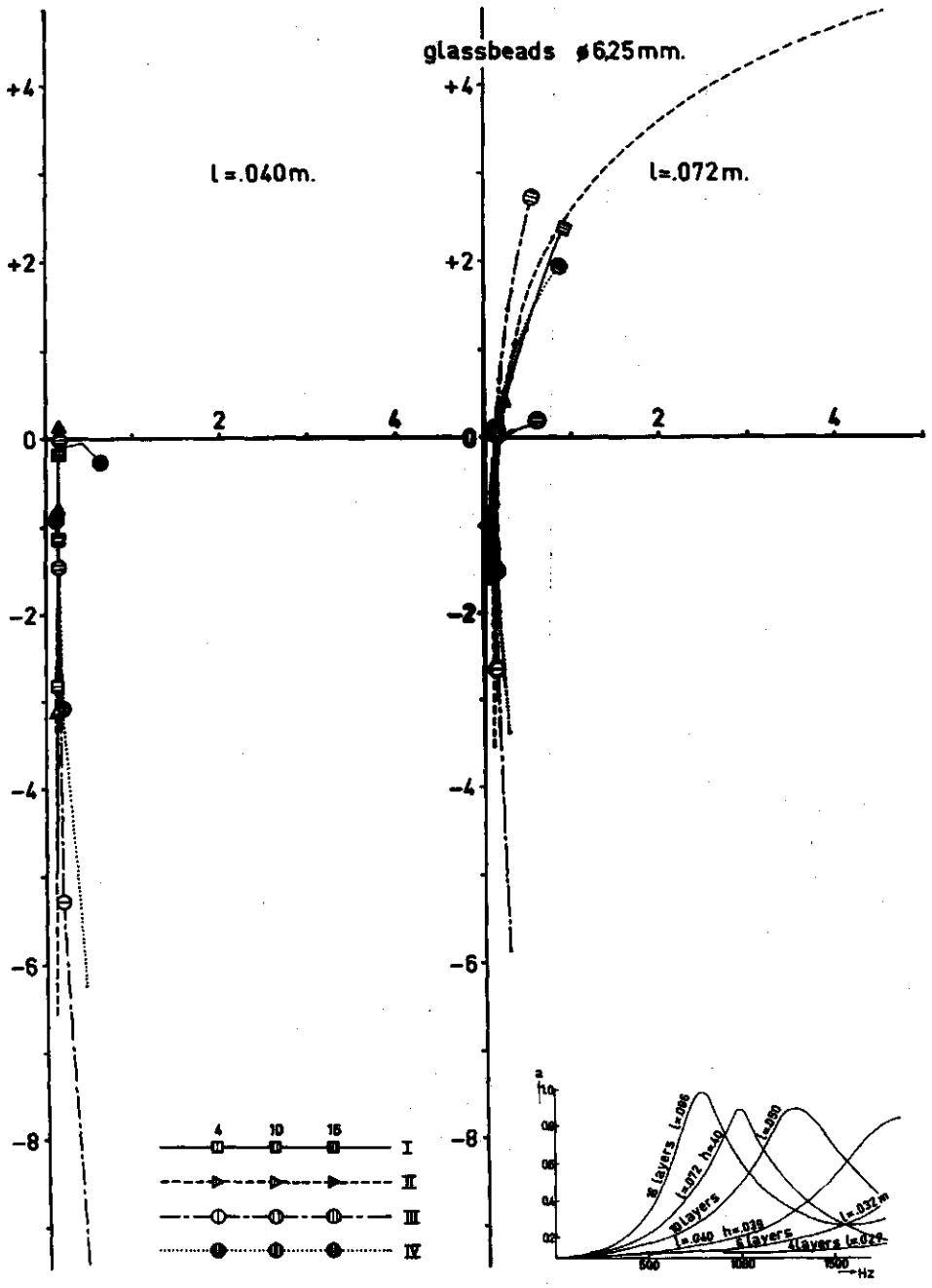

Figure 39 Comparison of measured to calculated values of $\zeta \cdot h$ for glass beads of 6.25 mm diameter

Table 4-4 Values of $\zeta \cdot h$ for glass beads of ϕ 6.25 mm

		I	II	III	IV
l = 40 mm		(h = 0.41)	σ_d = 3500	r = 6.00	D_a = 6.8 mm q_a = 2.0
Hz	a	σ_s = 650	k_m = 2	cos θ = 0.80	cos θ = 0.95
200	0.02	0.12-4.96j	0.11-6.54j	0.51-19.78j	0.47-6.21j
400	0.04	0.12-2.80j	0.11-3.12j	0.21- 5.24j	0.20-3.07j
600	0.06	0.13-2.07j	0.12-1.91j	0.14- 3.25j	0.13-1.94j
800	0.10	0.13-1.47j	0.12-1.25j	0.12- 2.17j	0.11-1.32j
1000	0.16	0.13-1.12j	0.13-0.81j	0.11- 1.44j	0.10-0.92j
1200	0.29	0.13-0.83j	0.14-0.64j	0.11- 0.88j	0.10-0.61j
1400	0.47	0.13-0.41j	0.14-0.15j	0.11- 0.41j	0.10-0.36j
1600	0.69	0.14-0.15j	0.17+0.12j	0.12+ 0.02j	0.11-0.13j
l = 72 mm		(h = 0.39)	σ_d = 2000	r = 6.30	D_a = 6.8 mm q_a = 2.0
Hz	a	σ_s = 880	k_m = 2	cos θ = 0.90	cos θ =0.95
200	0.03	0.08-1.62j	0.11-3.51j	0.29-5.86j	0.30-3.35j
400	0.08	0.08-1.24j	0.12-1.48j	0.14-2.63j	0.16-1.50j
600	0.22	0.08-0.62j	0.13-0.66j	0.12-1.38j	0.14-0.76j
800	0.51	0.11-0.24j	0.16-0.09j	0.12-0.59j	0.14-0.29j
1000	0.78	0.13+0.02j	0.21+0.42j	0.14+0.04j	0.17+0.11j
1200	0.47	0.28+0.69j	0.34+1.09j	0.18+0.68j	0.24+0.53j
1400	0.29	0.48+1.25j	0.79+2.30j	0.28+1.48j	0.39+1.07j
1600	0.20	0.92+2.40j	5.49+5.32j	0.56+2.76j	0.87+1.96j

Hz/100	q_a(-)	l = 40 mm D_a(mm)	cos θ (-)	q_a	l = 72 mm D_a(mm)	cos θ
	(2.0/2.3)	(5.6/8.2)	(0.90/1.00)	(1.8/2.0)	(5.6/8.2)	(0.90/1.00)
4	0.21-3.05j	0.25-3.03j	0.21-3.05j	0.15-1.52j	0.21-1.48j	0.17-1.53j
	0.22-3.06j	0.20-3.07j	0.20-3.09j	0.19-1.48j	0.16-1.50j	0.16-1.53j
		0.17-3.11j			0.13-1.53j	
10	0.11-0.87j	0.12-0.90j	0.11-0.87j	0.14+0.10j	0.22+0.13j	0.20+0.24j
	0.11-0.88j	0.10-0.92j	0.09-0.96j	0.22+0.20j	0.17+0.11j	0.15+0.01j
		0.08-0.93j			0.14+0.10j	
16	0.12-0.03j	0.14-0.11j	0.12-0.03j	0.66+1.71j	1.13+1.93j	1.62+2.71j
	0.13-0.06j	0.11-0.13j	0.10-0.21j	1.44+2.35j	0.87+1.96j	0.55+1.45j
		0.09-0.14j			0.67+1.94j	

those for the fissure model. The values for the parameters given are those for the best fitting calculated curls.

Sometimes interpolated values for the parameters were introduced; now and then these values could only be found by graphical interpolation from the curls with adjacent values of the parameters.

The lower section is confined to the three principal spot frequencies given in the first column. It also gives values for $\zeta \cdot h$ and illustrates the selection of the best fitting curl for the fissure model. In each case two values for q_a, three for D_a and one or two for cos θ are considered. The values of these parameters are given in the heads of the sections for the two layer thicknesses. The resulting combination corresponding to the best fit is underlined. Note that the corresponding values of the parameters for these cases are identical with those given in column IV in the upper section. This procedure justifies the choice made, it also provides some information about the influences of the steps in the parameters.

Figures 39 to 43 present, in graphical form, the curves obtained from both measurement and calculation, the latter for all three models. The marks for the main spot frequencies are enlarged as in the former figures. The marks for these main frequencies are provided with a special indication, shown in the legend of figure 39. The numbers in the legend indicate the frequency divided by 100. At the same time the frequency marks along the lines correspond to the values for $\zeta \cdot h$ in the column I, II, III and IV. The numbers I, II, III and IV in the legend of figure 39 correspond to the numbers of the columns in the tables 4-5 to 4-9.

Table 4-4

Values of $\zeta \cdot h$ for glass beads ϕ 6.25 mm for distinct layer thicknesses

	l = 16 mm (3 layers)		l = 27 mm (h = 0.50) (4 layers)		l = 35 mm (h = 0.39) (6 layers)	
Hz	a	$(\xi+j\eta)h$	a	$(\xi+j\eta)h$	a	$(\xi+j\eta)h$
200	0.022		0.003		0.005	
400	0.004	0.006-j2.00	0.006	0.018-j2.59	0.012	0.02-j1.71
600	0.009	0.012-j1.48	0.012	0.018-j1.70	0.021	0.03-j1.38
800	0.014	0.012-j1.17	0.019	0.017-j1.25	0.033	0.03-j1.03
1000	0.019	0.012-j0.90	0.026	0.017-j1.10	0.049	0.03-j0.74
1200	0.023	0.012-j0.74	0.033	0.016-j0.89	0.075	0.03-j0.54
1400	0.027	0.009-j0.63	0.044	0.016-j0.75	0.122	0.03-j0.44
1600	0.030	0.006-j0.55	0.062	0.016-j0.58	0.200	0.03-j0.31

	l = 56 mm (h = 0.39) (10 layers)		l = 86 mm (h = 0.39) (16 layers)	
Hz	a	$(\xi+j\eta)h$	a	$(\xi+j\eta)h$
200	0.04	0.07-j2.34	0.08	0.07-j1.23
400	0.08	0.07-j1.59	0.13	0.08-j0.90
600	0.10	0.06-j0.87	0.44	0.11-j0.40
800	0.20	0.07-j0.54	0.88	0.19+j0.07
1000	0.40	0.07-j0.33	0.52	0.81+j 1.00
1200	0.74	0.13+j0.04	0.29	2.53-j 2.32
1400	0.71	0.30+j0.42	0.22	0.77-j2.03
1600	0.47	1.22+j1.24	0.19^5	0.23-j1.28

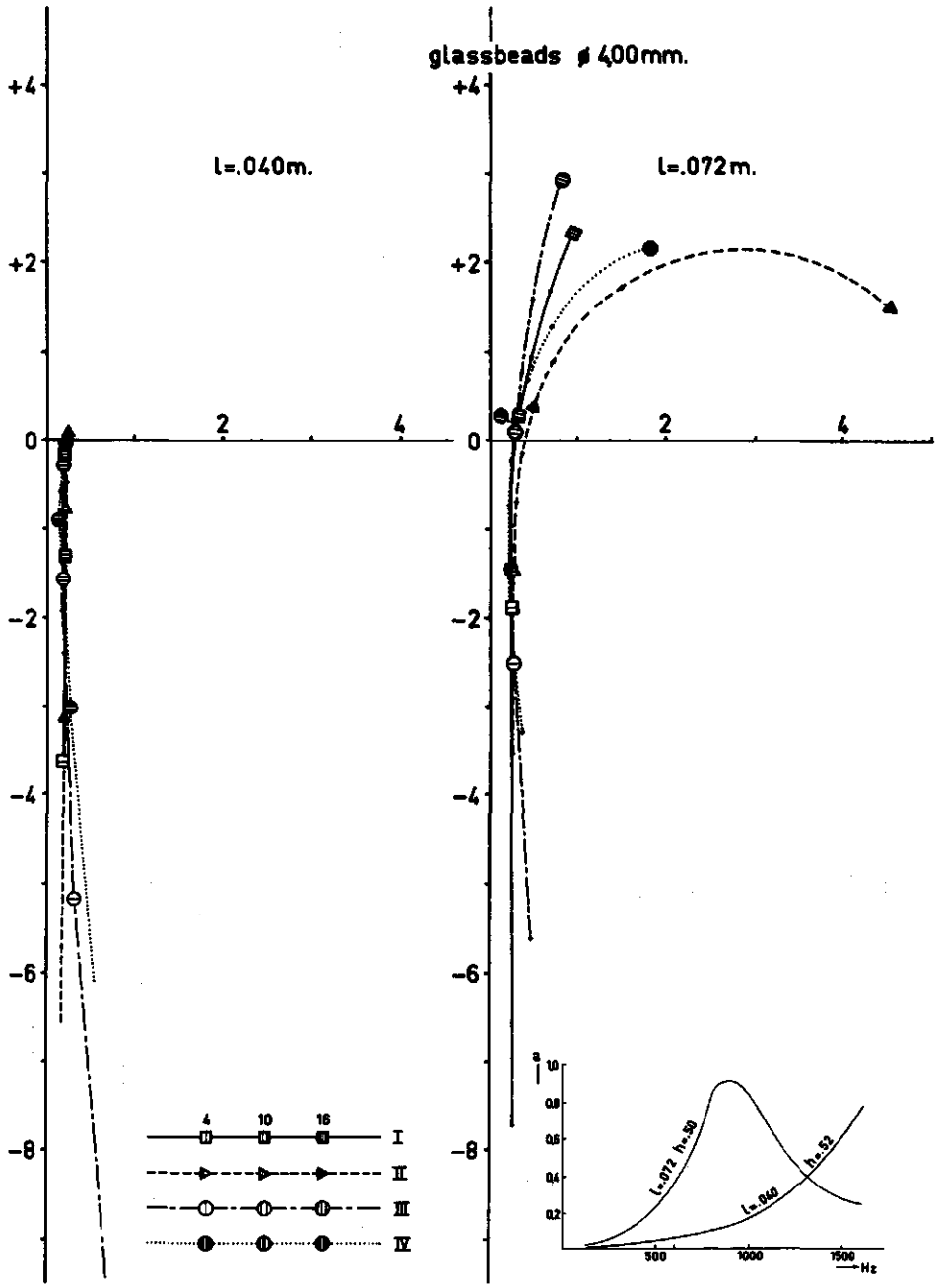

Figure 40 Comparison of measured to calculated values of $\zeta \cdot h$ for glass beads of 4.00 mm diameter

Table 4-6 Values of $\zeta \cdot h$ for glass beads of ϕ 4.00 mm

		I	II	II$_t$	IV
l = 40 mm		σ_s = 4000	σ_d = 5000	r = 3.80	D_a= 5.6 mm q_a = 2.2
Hz	a	h = 0.52	k_m = 2	cos θ = 0.90	cos θ = 0.95
200	0.01		0.16-6.54j	0.73-10.46j	0.54-6.08j
400	0.03	0.17-3.59j	0.16-3.12j	0.31- 5.16j	0.26-3.01j
600	0.06	0.17-2.37j	0.16-1.91j	0.22- 3.27j	0.19-1.89j
800	0.10	0.17-1.73j	0.17-1.25j	0.18- 2.23j	0.16-1.28j
1000	0.17	0.18-1.29j	0.18-0.81j	0.17- 1.56j	0.15-0.87j
1200	0.30	0.18-0.87j	0.20-0.46j	0.17- 1.05j	0.15-0.55j
1400	0.50	0.18-0.49j	0.22-0.16j	0.17- 0.63j	0.15-0.29j
1600	0.76	0.19-0.14j	0.25+0.12j	0.17- 0.26j	0.17-0.05j
l = 72 mm		σ_s = 4400	σ_d = 4500	r = 3.80	D_a= 5.6 mm q_a = 2.2
Hz	a	h = 0.50	k_m = 2	cos θ = 0.90	cos θ = 0.95
200	0.03	0.29-7.70j	0.26-3.52j	0.49-5.59j	0.38-3.27j
400	0.15	0.27-1.85j	0.27-1.49j	0.27-2.51j	0.24-1.45j
600	0.35	0.26-0.92j	0.30-0.67j	0.21-1.28j	0.22-0.71j
800	0.83	0.26-0.22j	0.35-0.12j	0.24-0.50j	0.23-0.22j
1000	0.83	0.32+0.32j	0.47+0.37j	0.34+0.12j	0.29+0.21j
1200	0.52	0.48+0.49j	0.72+0.96j	0.37+0.78j	0.41+0.68j
1400	0.33	0.69+1.70j	1.50+1.73j	0.48+1.61j	0.72+1.29j
1600	0.25	0.95+2.34j	4.51+1.50j	0.98+2.94j	1.83+2.17j

Hz/100	l = 40 mm q_a (2.0/2.4)	l = 40 mm D_a(cm) (0.47/0.68)	l = 40 mm cos θ (0.90/--)	l = 72 mm q_a (2.0/2,3)	l = 72 mm D_a(cm) (0.47/0.68)	l = 72 mm cos θ (0.90/--)
4	0.25-3.03j 0.27-3.00j	0.31-2.96j 0.26-3.01j 0.22-3.06j	0.27-2.99j -	0.21-1.48j 0.26-1.44j	0.30+1.43j 0.24-1.45j 0.19-1.48j	0.25-1.42j -
10	0.12-0.90j 0.16-0.85j	0.18-0.85j 0.15-0.87j 0.11-0.88j	0.16-0.81j -	0.22+0.13j 0.33+0.25j	0.37+0.22j 0.29+0.21j 0.22+0.20j	0.34+0.35j -
16	0.14-0.11j 0.19-0.01j	0.21-0.03j 0.17-0.05j 0.13-0.06j	0.19+0.06j -	1.13+1.93j 2.30+2.17j	2.15+1.82j 1.83+2.17j 1.44+2.35j	3.35+2.32j -

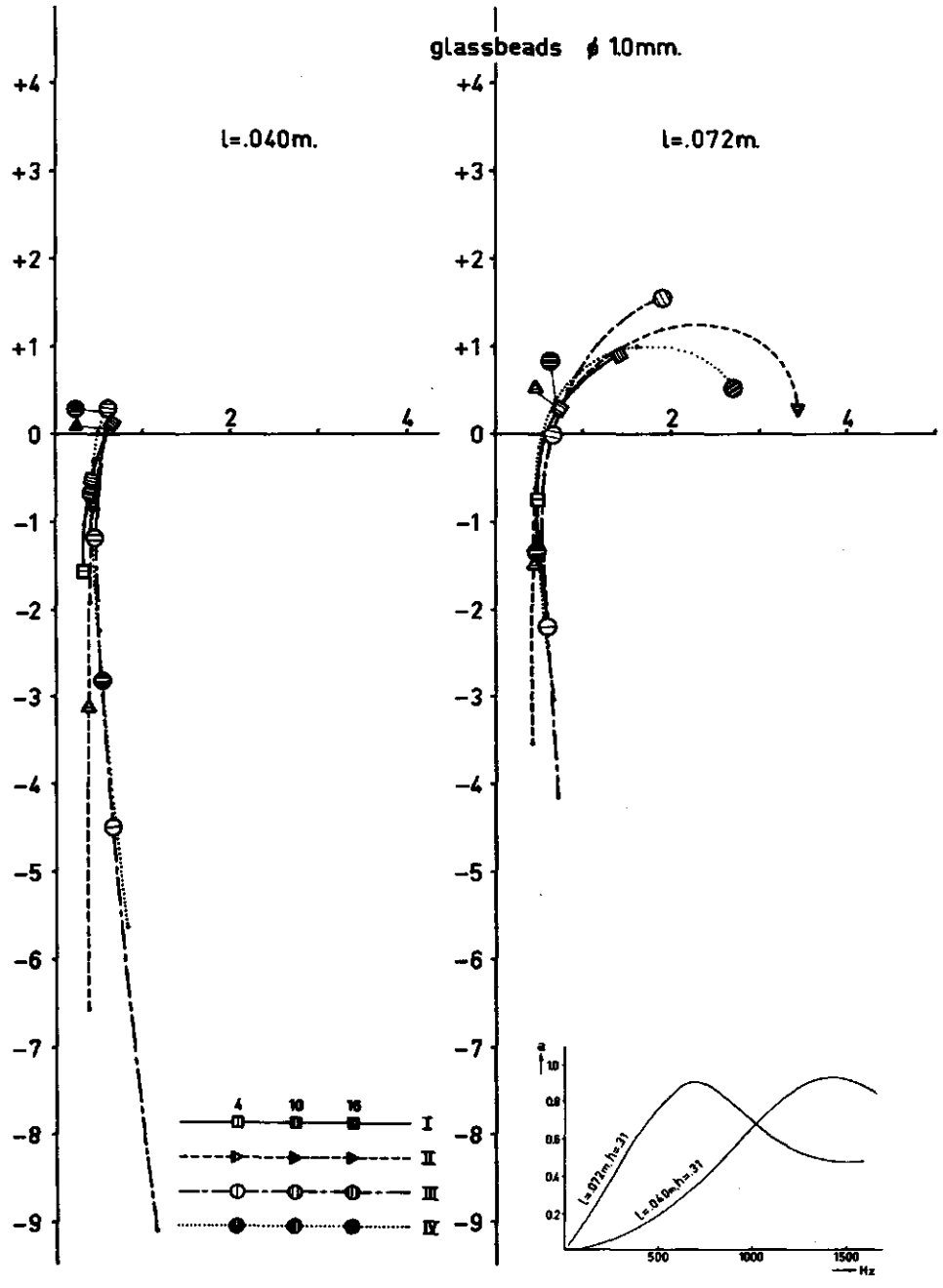

Figure 41 Comparison of measured to calculated values of $\zeta \cdot h$ for glass beads of 1.00 mm diameter

Table 4-7 Values of $\zeta \cdot h$ for glass beads ϕ 1.00 mm

l = 40 mm		σ_s= 19000	σ_d= 12000	r = 1.60	D_a = 3.3 mm
Hz	a	h = 0.31	k_m= 2	cosθ = 0.80	q_a = 2.3, cosθ = 0.85
200	0.05		0.38-6.55j	1.16-9.08j	0.83-5.63j
400	0.13	0.33-1.56j	0.39-3.13j	0.65-4.47j	0.53-2.80j
600	0.28	0.35-1.03j	0.40-1.93j	0.51-2.76j	0.44-1.72j
800	0.47	0.38-0.72j	0.41-1.27j	0.47-1.88j	0.42-1.11j
1000	0.66	0.42-0.51j	0.44-0.83j	0.46-1.18j	0.42-0.68j
1200	0.83	0.49-0.27j	0.47-0.49j	0.48-0.62j	0.44-0.33j
1400	0.92	0.52-0.02j	0.52-0.21j	0.53-0.15j	0.49-0.03j
1600	0.85	0.64+0.12j	0.59+0.05j	0.60+0.30j	0.57+0.26j

l = 72 mm		σ_s = 19000	σ_d = 7000	r = 1.40	D_a = 3.3 mm
Hz	a	h = 0.31	k_m = 2	cosθ = 1.0	q_a = 2.1, cosθ = 0.90
200	0.19	0.59-2.08j	0.40-3.52j	0.70-4.13j	0.64-3.02j
400	0.49	0.47-0.76j	0.44-1.50j	0.58-2.22j	0.49-1.34j
600	0.77	0.49-0.38j	0.48-0.69j	0.53-1.16j	0.48-0.62j
800	0.91	0.59+0.02j	0.56-0.16j	0.56-0.48j	0.53-0.14j
1000	0.77	0.72+0.28j	0.71+0.29j	0.65+0.00j	0.67-0.28j
1200	0.62	0.97+0.58j	1.06+0.74j	0.83+0.52j	0.96+0.69j
1400	0.52	1.18+0.75j	1.87+1.19j	1.17+1.04j	1.62+1.00j
1600	0.47	1.43+0.92j	3.41+0.29j	1.88+1.55j	2.73+0.52j

	l = 40 mm			l = 72 mm		
Hz/100	q_a (2.2/2.4)	D_a (2.7/3.9)	cos θ (0.80/0.90)	q_a (2.0/2.2)	D_a (2.7/3.9)	cos θ (0.90/1.00)
4	0.50-2.80j 0.58-2.80j	0.68-2.72j 0.53-2.80j 0.44-2.86j	0.57-2.77j 0.50-2.82j	0.44-1.35j 0.54-1.33j	0.66-1.31j 0.49-1.34j 0.38-1.37j	0.53-1.30j 0.47-1.37j
10	0.37-0.70j 0.47-0.66j	0.58-0.67j 0.42-0.68j 0.32-0.69j	0.47-0.60j 0.38-0.75j	0.57+0.26j 0.77+0.29j	0.91+0.19j 0.67-0.28j 0.51+0.31j	0.81+0.41j 0.56+0.17j
16	0.49+0.23j 0.66+0.29j	0.78+0.22j 0.57+0.26j 0.44+0.27j	0.70+0.43j 0.48+0.13j	2.68+0.91j 2.77+0.13j	2.32+0.02j 2.73+0.52j 2.94+1.87j	3.00-0.30j 2.14+0.94j

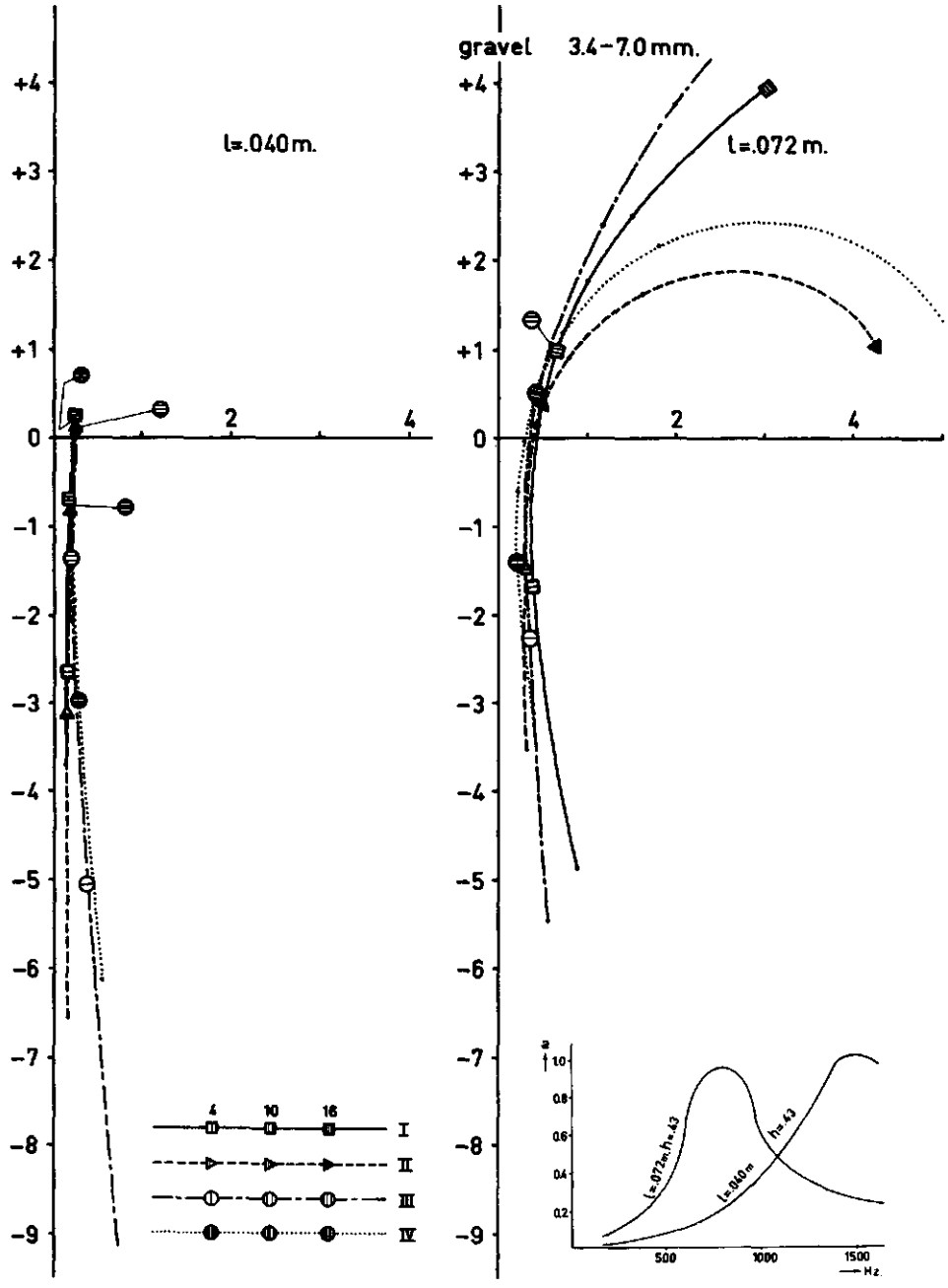

Figure 42 Comparison of measured to calculated values of $\zeta \cdot h$ for gravel (sieve fraction 3.4–7.0 mm)

Table 4-8 Values of $\zeta \cdot h$ for coarse gravel, 3.4-7.0 mm

		I	II	III	IV
l = 40 mm		σ_s = 550	σ_d = 5000	r = 3.20	D_a = 5.6 mm q_a = 2.2
Hz	a	h = 0.43	k_m = 2	cos θ = 0.50	cos θ = 0.85
200	0.02	0.15-3.70j	0.16-6.54j	0.84-10.28j	0.56-6.06j
400	0.04	0.16-2.65j	0.16-3.12j	0.38- 5.04j	0.28-2.97j
600	0.11	0.18-1.55j	0.17-1.91j	0.26- 3.13j	0.21-1.83j
800	0.20	0.18-1.06j	0.17-1.25j	0.22- 2.07j	0.18-1.19j
1000	0.39	0.19-0.68j	0.18-0.81j	0.21- 1.35j	0.17-0.75j
1200	0.65	0.21-0.38j	0.20-0.46j	0.21- 0.80j	0.18-0.40j
1400	0.99	0.23-0.04j	0.22-0.16j	0.23- 0.32j	0.20-0.09j
1600	0.86	0.25+0.19j	0.25+0.12j	0.26+0.12j	0.23+0.20j
l = 72 mm		σ_s = 450	σ_a = 5000	r = 3.20	D_a = 5.6 mm q_a = 2.2
Hz	a	h = 0.43	k_m = 2	cos θ = 0.75	cos θ = 0.85
200	0.08	0.89-4.87j	0.29-3.52j	0.56-5.47j	0.41-3.23j
400	0.21	0.35-1.67j	0.30-1.49j	0.35-2.26j	0.27-1.37j
600	0.62	0.36-0.66j	0.34-0.67j	0.34-0.07j	0.26-0.57j
800	0.96	0.46+0.16j	0.40+0.13j	0.40+0.16j	0.31-0.01j
1000	0.59	0.64+1.01j	0.53+0.36j	0.59+1.09j	0.42+0.53j
1200	0.38	0.97+1.83j	0.81+0.93j	1.17+2.42j	0.72+1.21j
1400	0.28	1.52+2.53j	1.62+1.64j	1.94+3.80j	1.79+2.18j
1600	0.24	3.02+3.98j	4.23+1.06j	11.20.0,20j	5.31+0.47j

Hz/100	l = 40 mm q_a (2.0/2.3)	l = 40 mm D_a (4.7/6.8)	l = 40 mm cos θ (0.80/0.90)	l = 72 mm q_a (2.0/2.3)	l = 72 mm D_a (4.7/6.8)	l = 72 mm cos θ (0.80/0.90)
4	0.20-2.99j 0.29-2.96j	0.34-2.93j 0.28-2.97j 0.23-3.01j	0.29-2.94j 0.27-2.99j	0.23-1.40j 0.30-1.36j	0.50-3.16j 0.27-1.37j 0.21-1.40j	0.30-1.32j 0.25-1.42j
10	0.15-0.79j 0.19-0.73j	0.22-0.72j 0.17-0.75j 0.14-0.77j	0.19-0.67j 0.16-0.81j	0.32+0.42j 0.49+0.59j	0.54+0.53j 0.42+0.53j 0.32+0.52j	0.53+0.77j 0.34+0.35j
16	0.18+0.11j 0.26+0.25j	0.30+0.22j 0.23+0.20j 0.19+0.18j	0.28+0.38j 0.19+0.06j	4.25+2.50j 5.05-0.63j	4.40-0.20j 5.31+0.47j 6.06+1.75j	4.14-2.34j 3.35+2.32j

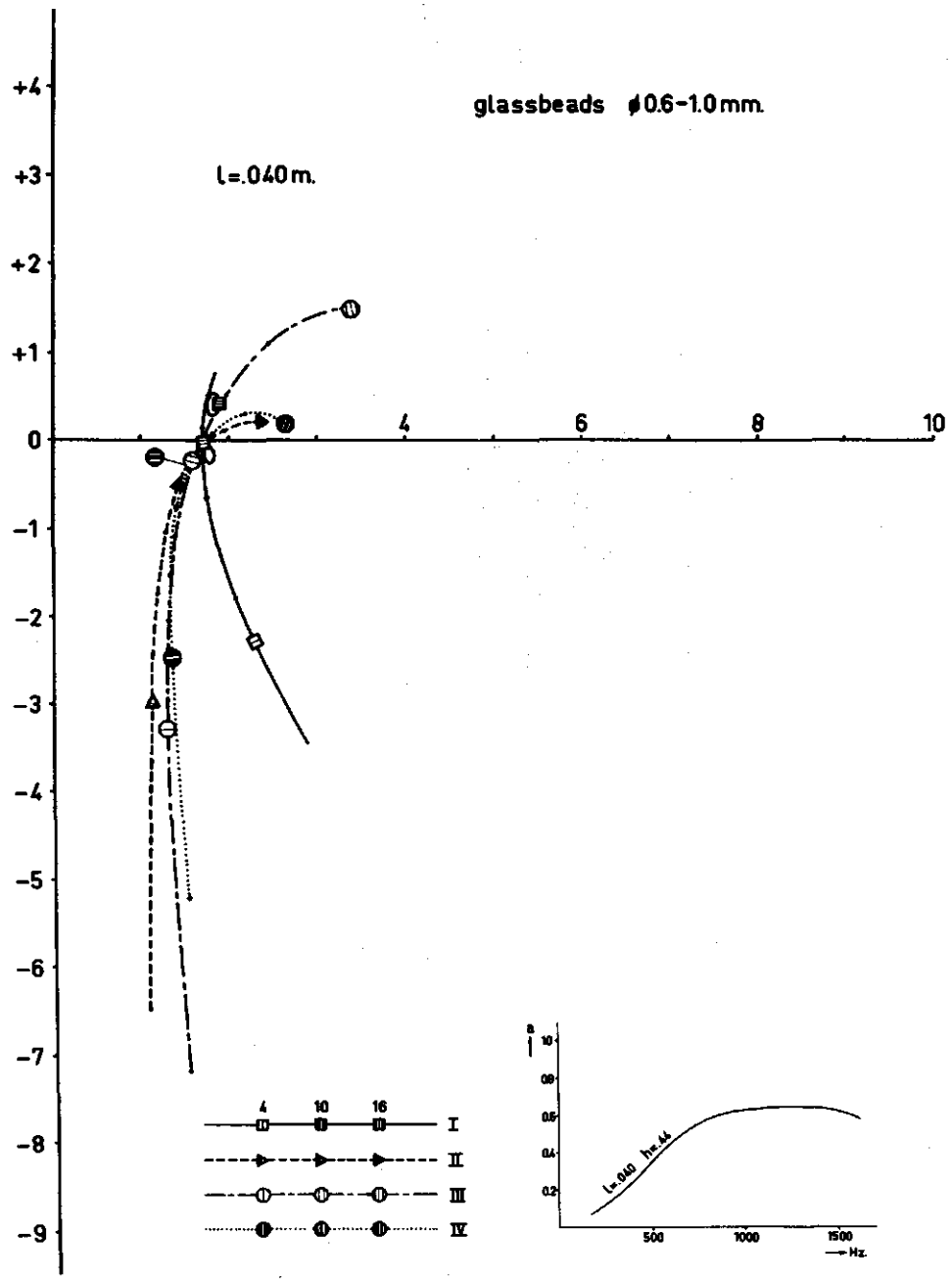

Figure 43 Comparison of measured to calculated values of $\zeta \cdot h$ for a sieve fraction of fine gravel 0.6 - 1.0 mm

Table 4-9 Values of $\zeta \cdot h$ for small glass beads, 0.6 - 1.0 mm

		I	II	III	IV
l = 40 mm		h = 0.44	σ_d = 34000	r = 1.10	D_a = 0.22 mm, q_a = 2.2
Hz		σ_s = 34000	k_m = 4	cos θ = 0.60	cos θ = 0.60
200	0.09	2.30-5.73j	1.09-6.48j	1.56-7.19j	1.53-5.23j
400	0.24	2.30-2.30j	1.12-3.00j	1.30-3.28j	1.34-2.47j
600	0.44	2.06-1.80j	1.18-1.73j	1.34-2.15j	1.32-1.40j
800	0.57	1.75-0.61j	1.28-1.01j	1.40-1.06j	1.39-0.75j
1000	0.62	1.71-0.03j	1.43-0.51j	1.57-0.23j	1.55-0.28j
1200	0.63	1.70-0.15j	1.64-0.13j	1.91+0.46j	1.81+0.06j
1400	0.63	1.73+0.50j	1.96+0.13j	2.44+1.10j	2.19+0.25j
1600	0.59	1.89+0.43j	2.39+0.22j	3.38+1.49j	2.66+0.18j

Hz/100	q_a (2.0/2.4)	D_a (1.8/2.7)	cos θ (0.50/0.70)
4	1.06-2.45j / 1.72-2.5j	1.82-2.49j / **1.35-2.47j** / 0.99+1.27j	1.82-2.36j / 1.05-2.56j
10	1.17-0.21j / 2.00-0.47j	2.05-0.60j / **1.55-0.28j** / 1.12-0.12j	2.41-0.16 / 1.08-0.47
16	2.31+0.71j / 2.79-0.40j	2.61-0.50j / **2.66+0.18j** / 2.50+0.95j	3.28-0.87j / 1.70+0.38j

Table 4-10 recapitulates the values of the parameters for the fissure model, chosen after an examination of the measured results for isodiametrical spheres. The first three columns give, respectively, the diameters of the spheres, the sample thichnesses and the measured values of the porosity h. The remainder of the table has been sectioned solely to reduce its length. In each of the sections the first three columns (numbers 4, 5, and 6; or 9, 10 and 11) give values for the parameters, each combination yielding a reasonable fit with the measured curl. One may conclude that sometimes a number of combinations of values of the parameters prove to be similar and can all be seen as acceptable selections. The underlined combinations correspond to the fit finally estimated to be the best. The nature and magnitude of the discrepancies between the measured and calculated curls is indicated to the right of the values for the parameters by two vertical bars, the first corresponding to the real and the second to the imaginary part of $\zeta \cdot h$. These vertical bars carry side bars whose meaning is explained below in table 4-10. Side bars, when present at the low end of a vertical bar indicate the magnitude of the discrepancies between a calculated curl and a measured one at 200 Hz. The side bars at the upper end correspond to 1600 Hz. Absence of a side bar implies an excellent fit.

On comparing measured and calculated values of $\zeta \cdot h$ it should be considered that accuracy is low when it departs appreciably from + 1. This situation occurs fairly frequently for 200 Hz and thus relatively large discrepancies here may well be rather unimportant.

Table 4-11 gives a general survey of the results for dry materials. for all three models. The first column gives the size of the spheres or of the sieve fractions, the second column the layer thickness and the third column the measured value of the porosity. In the fourth column the mesured values for the air flow resistance σ_s are presented. The next three groups of columns evaluate the results for the Zwikker Kosten, the capillary and the fissure models, respectively. The first two or three columns of each group list the values of the appropriate parameters for the best fit. The quality of the fit is indicated in the same way as in table 4-10.

In some case interpolated values of the parameters from table 4-10 have been introduced. For a number of samples some of the models failes to produce an acceptable curl. These cases have been marked.

Table 4-10 Survey of best fitting parameters for layers of isodiametric spheres

size (mm)	l (mm)	h (-)	D_a (mm)	q_a (-)	cos θ	Re	Im	D_a (mm)	q_a (-)	cos θ	Re	Im
Ø 6.25	.40	.41	6.8	1.6	0.90	⤵	↑	5.6	2.2	1.00	↕	↑
			6.8	1.8	0.95	↑	↑	5.6	1.6	0.90	⤵	↥
			6.8	2.0	0.90	↑	⤵					
			6.8	2.0	0.95	↓	↕					
			6.8	2.2	1.00	↑	↑					
			6.8	2.4	1.00	↑	↑					
	.72	.39	6.8	1.8	0.90	↑	↑	5.6	2.4	1.00	↕	↑
			6.8	2.2	1.00	↑	⤵					
			6.8	2.4	1.00	↕	↑					
Ø 4.00	.40	.50	5.6	2.0	1.00	↘	↘	5.3	1.6	0.90	⤵	⤵
			5.6	2.2	0.95	↘	↕	4.7	1.6	0.95	↕	↥
			5.6	1.6	0.90	↕	↓					
	.72	.52	5.6	2.0	1.00	↕	↑	5.6	1.6	0.95	↑	↥
Ø 2.00	.40	.37	3.3	1.8	0.90	⤵	↑	2.7	1.6	0.90	⤵	↑
			3.3	1.8	1.00	⤵	↕	2.2	1.6	1.00	↘	↘
			3.3	1.6	0.90	↕	↕					
	.72	.37	3.3	1.6	0.90	⤵	↕	2.7	1.6	0.90	⤵	↕
			3.3	1.8	1.00	⤵	⤵					
Ø 1.66	.40	.31	3.3	2.0	0.90	↑	↥					
			3.9	2.2	0.90	↑	↑					
			3.9	2.3	0.95	↑	↥					
Ø 1.37	.40	.30	3.9	2.2	0.90	↑	↥					
			3.9	2.0	0.80	↑	↥					
			3.9	2.4	0.90	↑	↥					
Ø 1.00	.40	.31	3.3	2.3	0.85	↑	↥	2.7	2.0	0.90	⤵	↥
	.72	.31	3.3	2.0	0.90	⤵	↥					
			3.3	2.2	0.90	↘	↥	2.7	2.0	0.95	⤵	↥

Legend

↕ ↑ The calculated value fits with measured value within a few %.

↘ ↑ The calculated value exceeds the measured one with less than 50%

↘ ↑ The calculated value exceeds the measured one with more than 100%

⤵ ↘ The measured value exceeds the calculated one with less than 50%

Table 4-11 General survey of the dry material

2 R (mm)	l (mm)	k (-)	σ_s (Nsm^{-4})	σ_d (Nsm^{-4})	k_m (-)	Re	Im	2 R (mm)	cosθ (-)	Re	Im	D_a (mm)	q_a (-)	cosθ	Re	Im
6.25	40	0.41	650	3500	2			6.2	0.80			6.8	2.0	0.95		
	72	0.39	880	2000	2			6.3	0.90			6.8	2.0	0.95		
4.00	40	0.38	2000	5000	2			3.8	0.90			5.6	1.6	0.95		
	72	0.38	2400	4500	2			3.8	0.90			5.6	1.6	0.95		
2.00	40	0.37	4500	4500	2			2.2	0.95			2.7	1.6	0.95		
1.66	40	0.31	8400	8000	2			1.5	1.00			2.7	1.6	0.95		
1.00	40	0.35	10400	12000	2			1.6	0.80			3.3	2.3	0.85		
	72	0.31	18500	7000	2			1.4	1.00			3.3	2.1	0.90		
3.4-7.0		0.41	550	5000	2			3.2	0.80			5.6	2.2	0.85		
		0.43	450	5000	2			3.2	0.75			5.6	2.2	0.85		
1.0-2.0	40	0.45	7800	16000	3			*				3.3	2.4	0.75		
	72	0.42	8100	*				*				3.9	2.4	0.75		
0.6-1.0		0.43	22000	34000	4			1.1	0.60			2.2	2.2	0.65		
0.3-0.6		0.41	88000	*				*				1.5	2.2	0.60		

* no fitting curl

Evaluation of the models (cf. table 4-11)

In general the fissure model yields the best fitting curls, expecially for sieve fractions, which most closely resemble soils. In the complicated cases, as that presented in figure 45, it is the only model capable of producing a reasonable correspondence between measurements and theory. The performance of the capillary model is usually poorer than the fissure types, although it corresponds reasonably with the experiment, at least in some cases. The simple Zwikker Kosten model leads to the greatest divergence and can be considered inadequate. The mayor disadvantage of this model is the difficulty of introducing a relationship with pore geometry. Another fundamental disadvantage is that it does not incorporate the frequency dependence of the parameters. The fact that measurements on samples of isodiametrical spheres often yield poor results, when compared with the models need not cause undue concern. Plausible reasons for the discrepancies have been advanced and a good fit for sieve fractions is of greater importance as such samples show more resemblance to soils.

Coarse materials are characterized by low losses and, as mentioned previously,by a number of pores wider than to be expected from the particle size. For samples of such materials the best fit is often ambiguous at the lower frequencies. At the higher frequencies very large values for $|\zeta \cdot h|$ occur thus accuracy of measurement is very low there. So the information derived from such curls does not contribute much to the selection of the values of the parameters for the best fit.

For coarse materials the frequency for maximum absorption is practically inversely proportional to layer thickness. This effect is very marked for large spheres, e.q. diam. 6.25 mm. Finer materials show better fitting curls. In such cases q_a is usually higher than the value for the hexagonal packing of spheres and the best fitting curl possesses a cos θ which is usually above the nominal value (0.7303). The fact that the fissure width does not vary in proportion with the diameter of the spheres implies that the fissure model is still too simple.

The samples prepared from sieve fractions often yield better fits than those composed of isodiametrical spheres. One of the reasons may be that the theoretical porosity is more closely approached by samples of the former kind and another related one is that stacked spheres in a cylindrical holder do not give a perfect arrangement. The sample may well contain comparatively wide channels, especially along the walls of the holder which are not incorporated in the model. This effect will be more pronounced for the large spheres. One would expect the presence of such channels to lead to high values for cos θ and low values for q_a. This trend can indeed be detected from table 4-10.

Some special cases will be treated now. Figure 44 shows three impedance curls, for very small spheres. In this special case, the layer thickness was varied. The air flow resistance is high and presumably leads to high losses even for small sample thickness. The absorption coefficient is relatively high for a layer only 3 cm thick. The impedance crul has the same general form as in figure 33. Further increase in layer thickness does not lead to a marked increase in absorption. So a layer 3 to 4 cm thick of the very fine material can be considered infinitely thick. Even at high frequencies the absorption coefficient remains fairly low due to the large mismatch in the wave impedances of the sample material and the air column (see figure 6D).

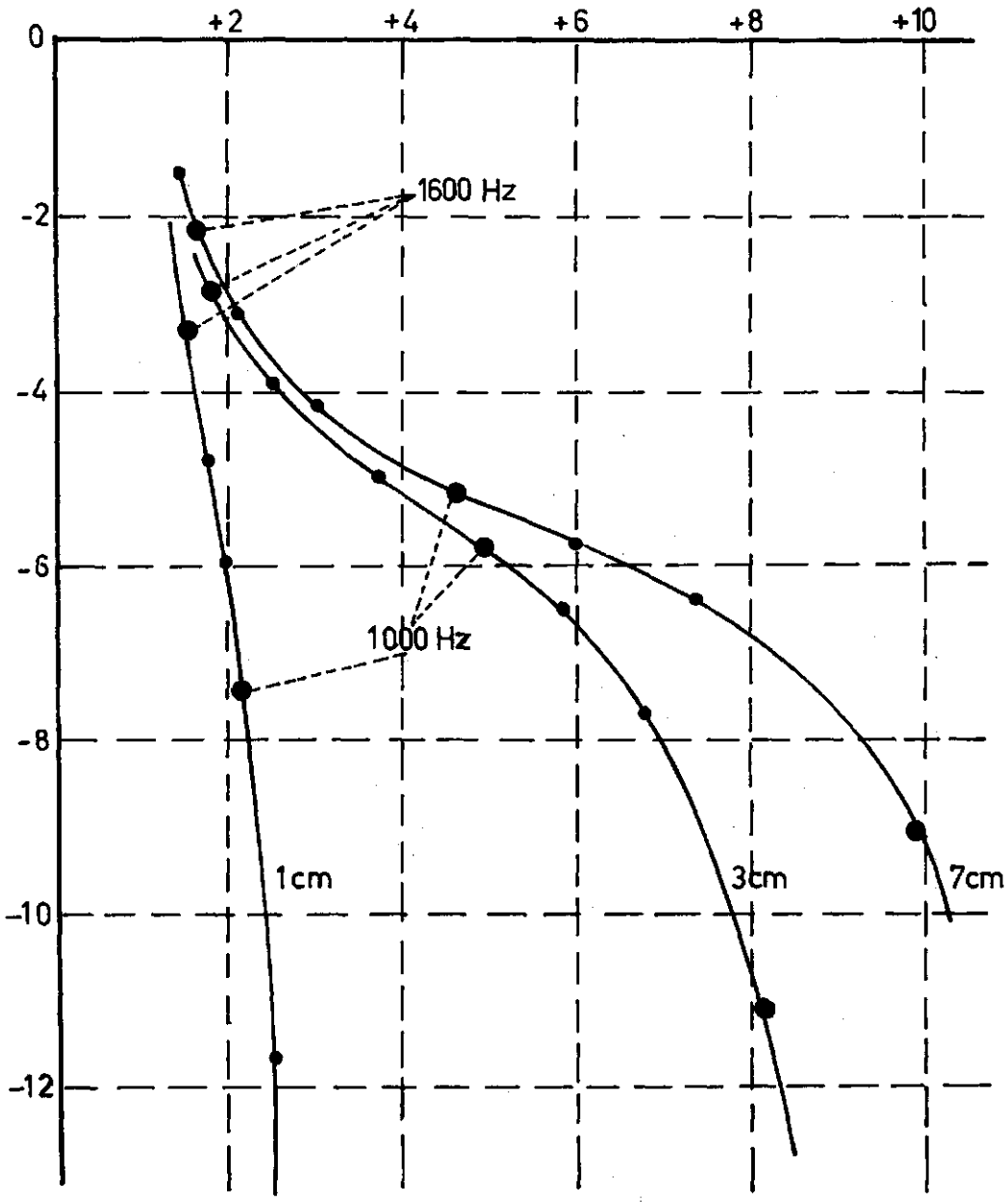

Figure 44 Measured values of $\zeta \cdot h$ for three layers of very small glass spheres

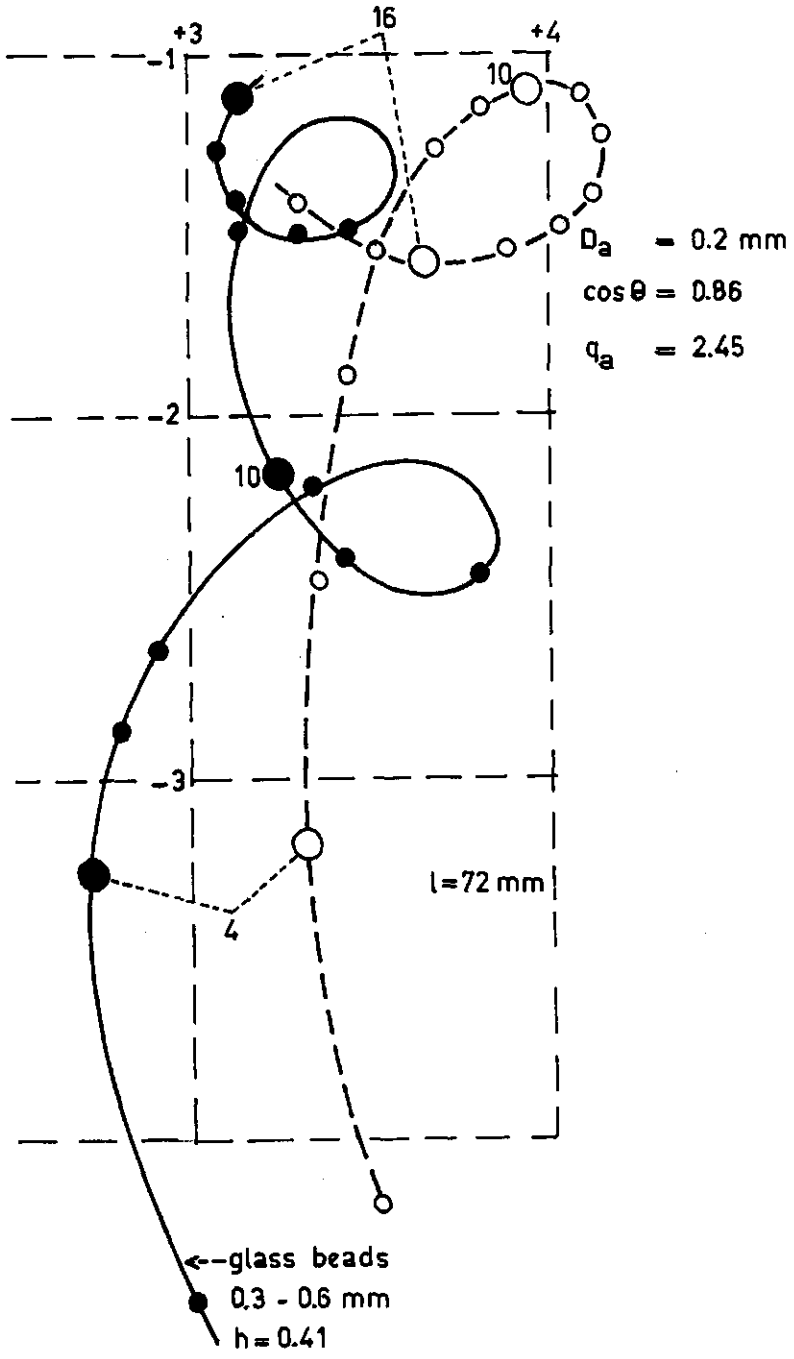

Figure 45 Measured curve for $\zeta \cdot h$ for a fine sieve fraction of gravel compared to a calculated curl with similar contour

In table 4-12 some interesting data are presented. They were determined on six samples of two sieve fractions 1.0 - 2.0 mm and 2.0 - 3.4 mm of the same layer thickness, consisting of gravel. Smooth gravel of large size (7-20 mm) was crushed and sieved to obtain sharp edged material. For this sieve fraction the values of column A were found. Next bricks were crushed and sieved, and curl B was measured. Then the crushed bricks were thoroughly saturated with water by repeated wetting and evacuation. The wet material was dried externally with blotting paper and then column C was found.

The particles composing the crushed brick sample are themselves porous, containing open pores which can be considered as belonging to the dead-end type. Porous of this kind, which are much smaller than the inter-aggregate pores, increase compressibility, more so at the lower frequencies than at the higher. An increase in compressibility reduces the velocity of propagation and thus the fact that the first anti-resonance frequency for sample B is lower than that for sample A is in accordance with expectations. If the intra-aggregate pores are still operative in the anti-resonance, the decrease in resonance frequency is a measure for the volume of these pores in relation to the inter-aggregate or principal pores.

When the intra-aggregate pores in sample B have been filled with water, thus forming sample C, one would expect the results for the latter sample to agree with those for sample A. And generally speaking this proves so. There are,however, some discrepancies, which are expecially pronounced for the higher frequencies. These latter may well be due to residual water at the points of contact of the particles in sample C, no such water being present in sample A.

There are further complications, however. On repeated cycling of the frequency through the measuring range, sample C shows a lack of reproducibility. Various causes of this effect may be surmised. Thus menisci may collapse under the impact of the sound waves. Thus conjecture gains in plausibility on considering, after cycling the frequency, the propagation velocity at the lower frequencies tends to decrease. A further indication is that when reproducibility is low, there is some loss of water from the sample. This loss might be attributed to increased evaporation from the broken menisci.

In figure 45 an example is given of a very complicated curl found sometimes by measurement. This type of curl shows that refinement of the mathematical approach is needed to produce a perfect fit.

Table 4-12 Values of $\zeta \cdot h$ for gravel, dry crushed bricks and crushed bricks, partly filled with water

l = 40 mm, h = 0.44 — 1.0–2.0 mm

	A		B		C *	
Hz	a	$(\xi+j\eta)h$	a	$(\xi+j\eta)h$	a	$(\xi+j\eta)h$
200	0.06	0.62–4.14j	0.25	0.86–3.85j	0.07	0.58–4.36
400	0.14	0.54–2.21j	0.75	0.66–2.25j	0.19	0.59–2.27j
600	0.30	0.56–1.45j	0.79	0.59–1.36j	0.37	0.61–1.49j
800	0.58	0.60–0.97j	0.69	0.62–0.87j	0.61	0.67–0.94j
1000	0.79	0.65–0.57j	0.62	0.77–0.43j	0.84	0.73–
1200	0.92	0.73–0.18j	0.53	0.80–0.10j	0.96	0.78–0.04j
1400	0.91	0.77+0.05j	0.60	0.86+0.22j	0.93	0.83+0.22j
1600	0.81	0.92+0.49j	0.71	0.91+0.48j	0.84	0.92+0.48j

* (= + 10.5% H_2O)

l = 40 mm, h = 0.64 — 2.0–3.4 mm

	A		B		C *	
Hz	a	$(\xi+j\eta)h$	a	$(\xi+j\eta)h$	a	$(\xi+j\eta)h$
200	0.08	0.62–4.52j	0.08	0.77–4.06j	0.05	0.64–4.96j
400	0.17	0.50–2.50j	0.17	0.85–3.24j	0.14	0.42–2.67j
600	0.32	0.50–1.62j	0.27	0.61–2.32j	0.37	0.38–1.79j
800	0.57	0.94–1.15j	0.46	0.56–1.28j	0.62	0.37–1.19j
1000	0.77	0.56–0.65j	0.68	0.56–0.75j	0.90	0.40–0.71j
1200	0.97	0.60–0.20j	0.93	0.59–0.32j	0.99	0.43–0.29j
1400	0.98	0.60+0.17j	0.99	0.61–0.03j	0.97	0.47+0.02j
1600	0.88	0.67+0.47j	0.81	0.62+0.35j	0.92	0.34+0.88j

* (= + 12% H_2O)

4.5 Considerations on the improvement of mathematical models

Of the three models considered, that of Zwikker Kosten is the simplest. Excluding h, it contains only two parameters, which however are purely formal in nature: even for a sample of precise and simple geometry, σ_d and k_m cannot be predicted. Essentially, of course, the quantities corresponding to σ_m and k_m are frequency-dependent.

The two channel-typemodels offer a geometry that bears at least some resemblance to that of the sample material. Thus the parameters r and D_a determine the absolute size of the pores and ought to correlate with the size of the particles of the sample. This correlation however is still of a formal nature, only for extremely simple materials would prediction of r and D_a present any hope of success. The same applies for cos θ and q_a which do depend on sample geometry but the precise form of this dependence is obscure.

The geometrical simplifications introduced into the channel-type models are so far-reaching that perfect matches between measured and calculated curls cannot be expected. To name a few of the imperfections:

a. The arbitrary cross-sections of the pores in the models will differ from those actually obtaining in the samples and thus both the flow and temperature profiles in the samples pores will deviate from those in the models. As an example one might consider flow in a tube of an equilateral triangular cross-section and one having a circular one. For the former, at least at higher frequencies, the viscous boundary layer will have a larger effect than for the latter. Here the free area of the sample material surface per unit volume of material obviously affects the results. Between the fissure and the circular cross-section the differences will be even larger than in the previous case. Note that flow was always laminar under the measuring conditions, Reynolds number* being very low and that contraction coefficients thus do not apply.

b. In actual samples the pore system consists of interconnected channels. Only a fraction, albeit a large one, of these pores will carry the flow of air. The remaining pores are limited to the function of acoustic compliance. Thus the assumption of identical distribution functions for flow and compression in the channel-type models is manifestly incorrect. It was introduced solely for simplicitys sake. For the samples considered here, the pores acting only as compliances are presumably accessible over the entire frequency range; side holes

* $(\frac{\rho v R}{\eta}) << 1000)$

of the type represented in figure 14 showing a series impedance at the entrance are probably either absent or unimportant. Summarizing, the porosity, as determined statically, is probably too high when flow is being considered.

c. The assumption that θ is equal for all channels is also a simplification of dubious validity. It is probably not far from the mark if channels of any selected cross-section occur for the same distribution of the values of θ, the latter then taking on the nature of an average. Should channel cross-section and values of θ be correlated the assumption should not be retained. Whether this correlation does in fact exist is not yet known, (Marshall, 1958)

Although the present models show some promise for the description of the pore geometries of the materials considered, there are still discrepancies and the mind turns to the possibilities of improvement. There appear to be various lines of approach. For instance, the introduction of two porosities, for flow and resistance respectively, correlated by a_priori geometrical considerations, might improve the correspondence between theory and experiment. The general form of the distribution function should be identical in the two cases. Similar considerations hold for the introduction of a correlation between channel cross-section and θ. Neither of the variations proposed above requires the introduction of an extra adjustable parameter. Note that no account has been taken of the probability distribution of two pores of given, different cross-sections adjoining each other. This is not necessary in the present case where the wavelength is very large in relation to pore dimensions.

Should refinement of the models yield inadequate improvement, the introduction of a further adjustable parameter may be considered, e.g. the introduction of different distribution functions for the cross-sections of the pores carrying the flow and those confined to compression. In the simplest case, only the ratio of the porosities for the two kinds of pores could be introduced.

As stated above, the performance of the present models is not too bad. Thus it is practically impossible to predict which and how many of the methods of improvement suggested above are required to render the correspondence between theory and experiment completely acceptable. Even from the material now available, the necessity for introducing one further parameter cannot be deduced. The possibility that more than one extra parameter is required seems remote.

To elucidate the behaviour of the models as descriptive for the sample material, further information is required. For all practical purposes this information must be derived by increasing the frequency range of the measurements as the possibilities for increasing the accuracy of interferometer measurements are indeed limited. Except for some peculiar cases, increasing the number of measuring

frequencies, in the range considered here, yields only a limited improvement in accuracy.
The extension of the frequency range of an acoustical interferometer beyond the customary value of 1:10 is, however, not primarily the concern of the soil scientist but of the acoustician.

Prospects

The experimental results on crushed bricks with variable water content open a way to distinguish between inter-aggregate and intra-aggregate pores (section 4-4). An improved model is presumably devisable as the intra-aggregate pores correspond to something resembling the side fissures in the prismatic soil structure, see section 3.8. Retention to identical pore distribution functions for flow and compression is obviously impossible. In this case the reasonable results from the present crude models especially for sieve fractions, justifies some confidence for future sophistication.

The selection of variants of the pore distribution functions for the models from experimental data still constitutes an obstacle. One could suggest three principal lines for further research.

1. A detailed analysis of the pF curve, together with a theoretical and practical investigation of hydraulic conductivities. The pF curve has however two main disadvantages; the curve shows hysteresis and the results are thus ambiguous and the determination of the curve may introduce shrinkage or swelling of the soil sample. This may lead to a rearrangement or deformation of the pore geometry originally present in the undisturbed sample. Application of the customary type of pF curve may well require adaptation or refinement for the fissure model.
2. An analysis of the fluid flow resistances combined with the determination of aggregate size distribution. This method at present yields information mainly about aggregate geometry and very limited insight into pore geometry, which is of greater interest here.
3. Micromorphological analysis, the optical study of very thin slices of impregnated sample material may lead to a useful description of the pore geometry. This method appears promising when considered fundamentally, but its technical achievement and an adequate mathematical expression of the data is still difficult in most cases.

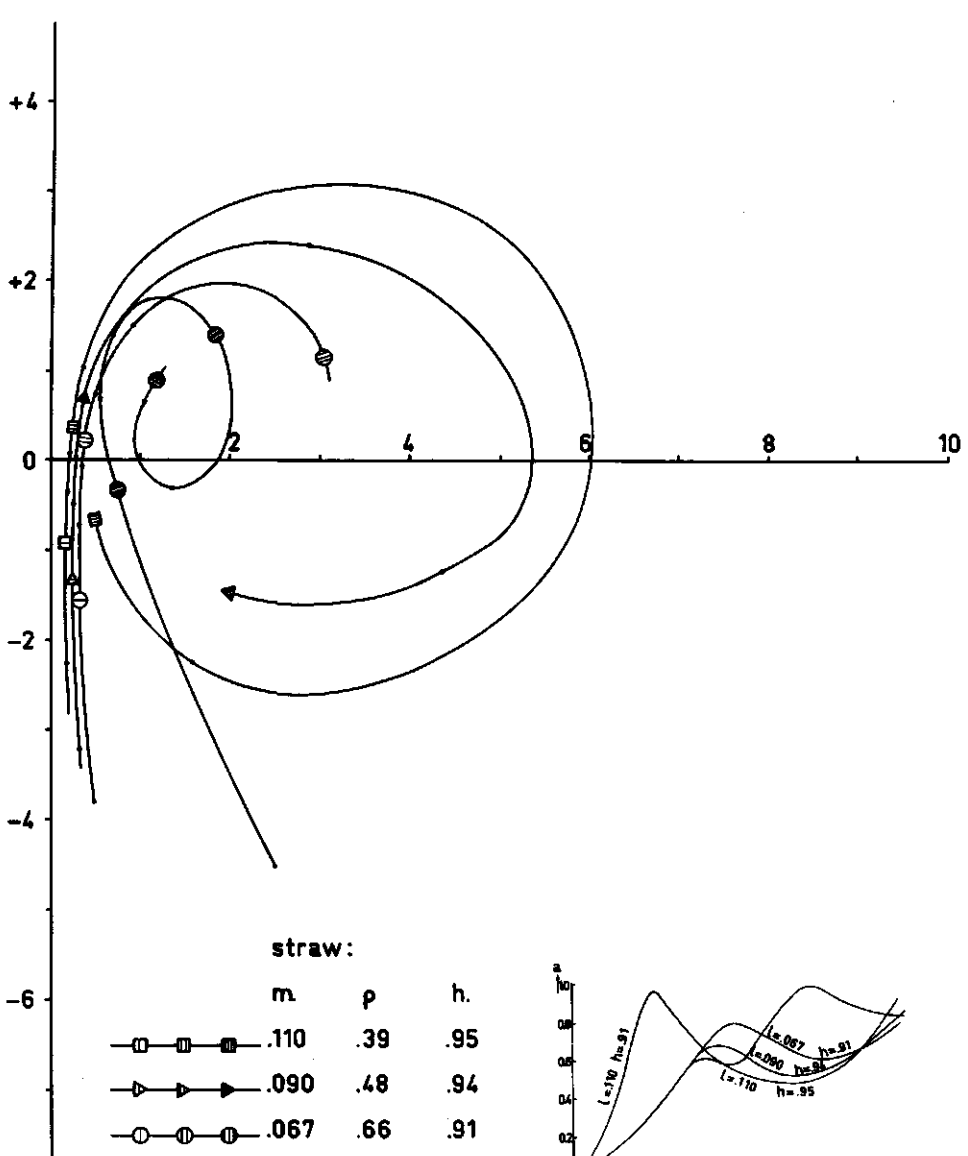

Figure 46 Values of $\zeta \cdot h$ for some layers of straw with variation in layer thickness and packing densities

Table 4-13

Values of a and $\zeta \cdot h$ for some layers of straw at various layer thicknesses and packing densities

	l = 67 mm h = 0.91		l = 90 mm h = 0.94	
Hz	a	$(\xi + j\eta)h$	a	$(\xi + j\eta)h$
200	0.12	0.37 - j 2.76	0.12	0.44 - j 3.80
400	0.30	0.25 - j 1.33	0.30	0.15 - j 1.07
600	0.55	0.26 - j 0.61	0.55	0.20 - j 0.25
800	0.77	0.31 - j 0.08	0.67	0.28 + j 0.38
1000	0.73	0.50 + j 1.05	0.63	0.50 + j 0.92
1200	0.64	0.93 + j 1.33	0.52	2.87 + j 2.37
1400	0.61	3.46 + j 1.16	0.57	2.22 - j 2.17
1600	0.70	1.49 - j 1.41	0.72	1.06 - j 1.26

	l = 110 mm h = 0.91		l = 110 mm h = 0.95	
Hz	a	$(\xi + j\eta)h$	a	$(\xi + j\eta)h$
200	0.31	0.32 - j 1.23	0.12	0.15 - j 2.15
400	0.93	0.41 - j 0.09	0.30	0.12 - j 0.63
600	0.78	0.64 + j 0.74	0.55	0.11 + j 0.10
800	0.58	3.50 + j 2.87	0.57	0.29 + j 0.66
1000	0.73	2.97 - j 1.09	0.53	0.57 + j 1.31
1200	0.97	0.94 - j 0.49	0.49	5.67 + j 0.55
1400	0.92	0.85 + j 0.50	0.54	1.06 - j 1.80
1600	0.85	1.03 + j 0.79	0.75	0.38 - j 0.40

4.6 Measurements on layers of straw

So far now all layer measured, could be considered acoustically rigid. That means that only the air vibrated. As an example of a complete different material some measurements were taken on straw. (See figure 46 and table 4-14). Air-dry straw was cut in 3 cm lengths and packed into the sample holders. Measurements were performed in both interometers.

Several conclusions can be drawn from these data. The impedance curls do not form a logarithmic spiral. At higher frequencies absorbtion increases, because of vibrations of the straw tubes. This effect originates partly from the resonance properties of the straw tubes, which are open at one or both ends. The problem of the resilient frame is discussed extensively by Zwikker and Kosten (1949). In the general case their results are extremely complicated but they may be simplified by the introduction of certain assumptions, e.q. porosity approaching unity. Loosely packed straw satisfies this assumption.

Some theoretical attempts were made to introduce their model with reasonable values for the parameters. The calculated curves for $\zeta \cdot h$ departed significantly from the measured ones and extension of the theory did not improve matters. Interpretation of the results is thus perforce postponed. One article was found dealing with this problem. It discusses measurements on the acoustic behaviour of steelwool (Bies, 1963). There an acceptable agreement was found with a simplified model of Zwikker and Kosten. Steelwool does not however contain resonating tubes.

4.7 Conclusions

1. The introduction of a geometrical model, characterized by a few parameters that are considered to be representative for the material under study, has lead to an acceptable relationship between calculated and measured impedance curls. In some cases, especially for fine grained materials, more of parameters are needed.
2. Layers of straw cannot be considered rigid in an acoustical sense. The frame moves in the sound field. A more complex model is needed to describe their behaviour properly.
3. The method of Ferrero and Sacerdote offers no acceptable results in the determination of the material constants by an extrapolating technique.
4. The introduction of a logarithmic impedance plane for separating the factors W_m and γ_m may help sometimes.
5. Use of scale rules to limit theoretical problems, and more especially the number of measurements to be made, cannot help in the acoustical study of porous materials.
6. The acoustic behaviour of prismatic soil structures can be studied with the aid of formulae given. The size and number of the small horizontal fissures influences the results considerably.
7. The help of an electro-acoustical analogous network for understanding the acoustical behaviour of an porous material is very limited.

Summary

The properties of a soil structure may be examined in various manners. As well as a study of the stability, a knowledge of the geometry of the volume of air-filled pores is often needed. The most common measurements, like those of porosity and flow resistance to gases do not permit a detailed description of this pore volume. Since wave phenomena are characterized by three independent variables, viz. frequency, amplitude and phase, with frequency chosen freely, the measurement of acoustical characteristics of the air in the soil offers new opportunities. Also a determination of the acoustical properties of a porous material is non-destructive.

In chapter 1, a description is given of an interferometric method of measurement following the derivation of the wave equation. The propagation velocity of sound in air and the specific mass of air are the important physical quantities. The change in these quantities is studied from variations in the experimental conditions, such as temperature and humidity. Next the principles of the propagation of sound in porous materials are presented. For a sample of thickness l and having a rigid backing, the specific acoustic impedance Z at the free surface is given by $Z = W_m \coth(\gamma_m l)$, where γ_m is the propagation constant for acoustical waves in the sample and W_m is the specific acoustic wave impedance. Z, W_m and γ_m are complex quantities. Z may be measured in an interferometer and W_m and γ_m characterize the sample material. γ_m and W_m considered as functions of frequency give more information on pore geometry than may be obtained from static measurements. The loci of the function in two types of a complex plane is studied. Finally the behaviour of this function in the complex planes is shown with some examples.

Chapter 2 contains a discussion of the measuring equipment used and of the calibration of the measuring set-up. After a discussion of the measuring techniques, the sources of error are evaluated.

Chapter 3 deals with the propagation of waves in porous materials. Independent determination of W_m and γ_m proves impossible for soil samples. A method for this, described in the literature, is rejected on the grounds of inadequate accuracy. An alternative approach is followed: the material is described by a mathematical model and the parameters in the model are considered as the characteristic quantities for pore geometry. The models assume comparatively

simple geometries and may be considered an extension of the work of previous authors. In addition a new projection plane for the determination of γ_m and W_m by a graphical method is discussed. Use of the plane is confined to cases where the sample thickness may be varied. Also, formulas are derived with which the acoustical properties of prismatic of structures soils can be studied. Finally, the applicability of scale rules and the possibility of an electric-acoustical equivalent network are examined for the sample material. Neither approach seems promising.

Chapter 4 starts with a discussion of the problems to be expected on the comparison of calculated and measured curves for Z. Somes series of measurements are discussed. The mathematical models selected yield a reasonably good relationship between the theoretical and measured values. A short critical discussion is given on the feasibility of an extension of the mathematical model.

In conclusion a brief discussion is devoted to measurements on layers whose solid phases can no longer be considered as rigid, such as layers of mulch and straw. Some results obtained with straw are dealt with.

Samenvatting

Het onderzoek naar de opbouw van een bodemstruktuur kan op uiteenlopende wijzen plaatsvinden. Dikwijls wordt naast een onderzoek naar de stabiliteit een uitzicht verlangd in de geometrie van het met lucht gevulde porievolume. De meest voorkomende metingen, zoals die van de porositeit en de stromingsweerstand voor gassen laten geen gedetailleerde beschrijving van dit porievolume toe. Omdat golfverschijnselen gekenmerkt kunnen worden door drie van elkaar onafhankelijke parameters, nl. de frequentie, de amplitude en de fase, waarbij eerstgenoemde vrij kan worden gekozen, biedt het meten van de akoestische eigenschappen van de lucht in de bodem meer mogelijkheden. Daarenboven is een onderzoek van de akoestische eigenschappen van een poreus materiaal non-destruktief.

In hoofdstuk 1 wordt een beschrijving van een interferometrische meetmethode gegeven, nadat eerst de golfvergelijking is afgeleid. De voortplantingssnelheid van geluid in lucht en de specifieke massa van lucht zijn de belangrijkste fysische grootheden. De wijzigingen in de waarde van deze grootheden onder variaties van de meetomstandigheden, zoals de temperatuur en de vochtigheid worden nader beschouwd. Vervolgens worden de beginselen van de voortplanting van geluid in poreuze materialen gegeven. Van een monster met een laagdikte 1, dat aan de achterzijde hard is afgesloten kan de specifieke akoestische impedantie Z aan het vrij oppervlak van dit materiaal worden weergegeven door de betrekking $Z = W_m \coth \gamma_m 1$, waarin γ_m de voortplantingsconstante voor geluidgolven in het materiaal en W_m de specifieke akoestische golfimpedantie van dit materiaal voorstellen. Z, W_m en γ_m zijn complexe grootheden. Z kan worden gemeten in een interferometer; W_m en γ_m kenmerken het onderzochte materiaal. γ_m en W_m, als funktie van de frequentie geven meer inlichtingen over de opbouw van het porievolume dan de resultaten van statische metingen.

Beschreven wordt vervolgens hoe de funktiewaarden in twee typen van een complex vlak kunnen worden weergegeven. Tenslotte wordt met behulp van enkele voorbeelden het gedrag van deze funktie in het komplexe vlak toegelicht.

Hoofdstuk 2 bevat een bespreking van de gebruikte meetapparatuur en de ijking van de meetopstelling. Nadat de wijze van meten in detail is besproken, volgt een analyse van de foutenbronnen.

In hoofdstuk 3 wordt op de voortplanting van geluidgolven in poreuze materialen uitvoerig ingegaan. Een onafhankelijke bepaling van W_m en γ_m blijkt voor bodem-

monsters niet uitvoerbaar. Een methode die in de literatuur voorkomt en voor dit doel werd ontworpen wordt verworpen om redenen van ontoereikende nauwkeurigheid. Daarom wordt een andere wijze van benaderen gevolgd. Het model wordt beschreven met behulp van een mathematisch model en de parameters, die het model bezit worden gedacht de karakteristieke grootheden van de opbouw van het porievolume te vertegenwoordigen. De modellen bezitten een betrekkelijk eenvoudige opbouw en kunnen beschouwd worden als een voortgezette studie van het werk van eerdere schrijvers. Ook wordt een nieuw type projektievlak voor een grafische bepaling van γ_m en W_m besproken. Het blijkt dat dit vlak slechts hulp kan bieden, als de dikte van de monsterlaag kan worden gevarieerd. Er worden vervolgens vergelijkingen afgeleid waarmede de akoestische eigenschappen van een prismatische bodemstruktuur bestudeerd kunnen worden. Tenslotte wordt onderzocht of schaalregels, respektievelijk een elektro-akoestisch analogon van nut kunnen zijn. Beide benaderingswijzen blijken geen perspektief te bieden.

In hoofdstuk 4 wordt eerst ingegaan op de problemen, die er rijzen wanneer gemeten en berekende waarden van Z met elkaar moeten worden vergeleken. Enkele series meetresultaten worden nader beschouwd. De berekende waarden blijken een redelijke overeenkomst te bezitten met de gemeten waarden. Aan een verdere uitbreiding van het gekozen model wordt een korte beschouwing gewijd.

Ook worden in het kort enkele meetresultaten besproken, die werden verkregen aan een materiaal waarvan gezegd kan worden dat het skelet bij de meting niet meer stijf is, zoals een mulchlaag of een laag stro. Enkele resultaten die bij metingen aan strolagen werden verkregen, worden gegeven.

Literature

van Bavel, C.H.M.	1951	Soil Aeration theory based on diffusion. Soil Science 72, 33-46
Beranek, L.L.	1942	Acoustic impedance of porous materials. J.Ac.Soc.Amer. 13, 248-260.
Beranek, L.L.	1949	Acoustic measurements. Wiley, New York.
Bies, D.A.	1963	Acoustic properties of steel wool. J.Ac.Soc.Amer. 35,4, 495-499
Brown, R.L. and Bolt, R.H.	1942	Measurement of flow resistance of porouw materials. J.Ac.Soc.Amer. 13, 337
Bruel Per	1951	Sound insulation and room acoustics. Chapman and Hall, London.
Bruel Per	1954	Introduction and applications: standing wave apparatus, type 4002 Bruel-Kjaer, Kopenhagen.
Carman, P.C.	1956	Flow of gases through porous media. Butterwordth, London.
Chisnell, R.E.	1960	Vibrating Systems. Routledge-Kegan Paul, London.
Crandall, I.B. (refers to Helmholtz)	1927	Theory of Vibrating System and Sound. MacMillan ltd. 229-241.
Dallavalle, J.Mc	1943	Micromeritics The Technology of Fine Particles. Pitman Publ. New York.
Ernsthausen, W. und Witters, W.v.	1939	Eine Methode zur Bestimmung der Akustischen Reflexionsvermögen von Bodenflächen. Akustischen Zeitung. 4, 353-357.
Eyk, J.v.d.	1941	Absorption of sound by porous materials I. Physica VIII, 149-158.
Eyk, J.v.d., Zwikker, C. and Kosten, C.W.	1941	Absorption of Sound by porous materials II. Physica VIII, 469-476.

Ferrero, M.A., Sacerdote, G.G.	1960	The acoustic impedance of thin layers of porous materials. Akustica 10, 336-339.
Gonnagle, Mc, W.J.	1962	Non-destructive testing. McGrow Hill (chapter 9, 279-301)
Hardy, H.C., Telfair,D., Pielemeier, W.H.	1942	The velocity of sound in air. J.Ac.Soc.Amer. 13, 226-233.
Heaps, H.S.	1956	Reflection of a plane acoustic wave from a surface of non-uniform impedance. J.Ac.Soc.Amer. 28, 4, 666-671.
Jahnke, E. and Emde, F.	1945	Tables of functions. Dover S 133.
Janse, A.R.P. and Bolt, G.H.	1960	The determination of the air permeability of soils. Neth.Journ.of Agr.Sci. 8, 124-131.
Kawasina, Y.	1960	Sound propagation in a fibre block. Akustica 10, 208-217.
Kirchhoff, G.	1868	Ueber den Einfluss der Wärmeleitung in einen Gase auf die Schallbewegung. Ann.Physik, 134, 177-193.
Korringa, J., Kronig, R. and A. Smit	1945	On the theory of the reflection of sound by porous media. XI Physica, 4, 209-230.
Kosten, C.W., Zwikker,C.	1941	Theory of the absorption of sound by compressible walls with a non-porous surface-layer. Physica VIII, 251-272.
Kosten, C.W., Zwikker,C.	1941	Measurements of the absorption of sound by porous rubber wall covering layers I. Physica VIII, 933-946.
Idem	1941	Idem II. Physica VIII, 947-956.
Idem	1941	Physica II. Physica VIII, 957-967.
Kosten, C.W., Janssen, J.H.	1957	Acoustic properties of flexible and porous materials. Akustica 7, 6, 372-378.

Kosten, C.W., Zwikker,C. 1941 Extended theory of the absorption of sound by compressible wall-coverings. Physica VIII, 9, 968-978.

McLacklan, N.W. 1951 Theory of vibrations. Dover S. 190, 1-153.

Marshall, T.J. 1958 A relation between permeability and size distribution of pores. J. of Soil Science 9, 1-8.

Lamb, H. 1960 The dynamical theory of sound. Dover, S 655, 1-307.

Lippert, W.K.R. 1953 The practical representation of standing waves. Akustica, 3, 154-160.

Loebell, R. 1953 Barometerfreie Luftpyknometer. Zeitschr. Bodenk. und Pflanzenern. 60, 2, 172.

Mawardi, O.K. 1956 Some notes on the measurement of acoustic impedance. J.Ac.Soc.Amer. 28, 3, 351-356.

Morse, P.M. 1948 Vibration and Sound. McGraw Hill, 1-458.

Muskat, M. 1946 The flow of homogeneous fluids through porous media. J.W. Edwards, Ann.Arbor. Michigan.

Nederveen, C.J. 1962 Resonance frequency of a gas in a tube with a
Wulfften Palthe, D.W. van short closed side-tube. Akustica, 13, 2, 65-70.

Nicols, R.H. 1947 Flow-resistance characteristics of fibrous acoustical materials. J.Ac.Soc.Amer. 19, 866-871.

Parker, J.C. 1956 Reflection of plane sound waves from an irregular surface. J.Ac.Soc.Amer. 28, 4, 672-680.

Penman, H.L., 1933 The absorption by porous materials at normal
Richardson, E.G. incidence - a comparison of theory and experiment. J.Ac.Soc.Amer. 4, 322-330.

Rayleigh, J.W. 1945 The theory of sound, vol.I and II. Dover S 292, S 293.

Richardson, E.G.	1953	Technical aspects of sound.Vol.I. Elseviers Publ. Company Esp.Introduction and Chapter 4.
Rybner, J.	1947	Nomograms of complex hyperbolic functions Copenhagen, 1-36.
van Santen, G.W.	1950	Inleiding tot het gebied der mechanische trillingen. Ahrend, Amsterdam.
Scheidegger, A.E.	1957	The physics of flow through porous media. University of Toronto press.
Schuster, K., Hohlberg, A.	1933	Die Beeinflussung einer Telephonmembran durch ein Luftpolster mit absorbierender Abschlusswand. Ann.Phys. 5 Folge, Band 16. 203-216.
Schuylenborgh, J.v.	1947	A study on soil structure. Thesis Wageningen.
Scott, R.A.	1946	An apparatus for accurate measurement of the acoustic impedance of sound absorbing materials. Proc.Phys.Soc. 58, 253-264.
Sharman, R.v.	1963	Vibrations and waves. Butterworths, 1-253.
Shea, T.E.	1929	Transmission networks and wave filters. Chapman, Hall, Chapter IV,100-123.
Skudrzyk, E.	1954	Die Grundlagen der Akustik. Springer, München. 1-1084.
Visser, W.C., Stakman, W.G., a.o.	1962	Conception and methods in relation to the descriptions of soil structures by physically significant parameters. Rapport I.C.W. Wageningen 1-37.
Wenke, W.	1939	Theoretische Bemerkungen zur Schalldämpfungs-messung and Rohren und Schläuchen. Akustische Zeitschrift, 4, 1 1-9.
Waetzmann, E., Wenke, W.	1939	Schalldämpfun in Rohren und Schläuchen. Akustische Zeitschrift, 4, 1, 10-12.
Wigan, E.R.	1963	Transmission parameters of porous sound absorbers with particular reference to the flow resistance. Nature 6, 59-71.

Wiggs, P.K.C.	1958	The relation between gas permeability and pore structure of solids. 10th Colston Symposium, Butterworth, 183-188.
Zwikker, C.	1941	Absorption of sound by porous materials IV. Physica VIII, 1102-1106.
Zwikker, C. and Kosten, C.W.	1948	Sound absorbing materials. Elsevier, 1-174.
Zwikker, C., Eyk, J.v.d. and C.W. Kosten	1941	Absorption of sound by porous materials III. Physica VIII, 1094-1101.
	1951	Ontwerp electro akoestiek V 1097 Ned. Electro Comité
	1942	Ontwerp akoestische begrippen en grootheden V 1029 Publ. Geluidstichting, Delft.

Appendices

Appendix A. Basic formulae from the theory of vibrations

For a spring which behaves in accordance with Hooke's law, the displacement x is proportional to the applied force f. Thus,

$$f = -x/C, \tag{A-1}$$

where the proportionality factor C is called the compliance of the spring. For a mass m, subject to a force f the displacement x is determined by the following relationship

$$f = m\, d^2x/dt^2. \tag{A-2}$$

If a mass is attached to one end of a spring whose other end is anchored, in the absence of an external force acting on the system, and if the mass of the spring is neglected the sum of the forces acting on the connecting point of the spring and mass must vanish, or

$$m\, d^2x/dt^2 + x/C = 0. \tag{A-3}$$

A general solution of this equation is

$$x(t) = \hat{x} \cos(\omega t + \phi), \tag{A-4}$$

where $\hat{x}$ and ϕ are the integration constants and where the angular frequency ω, corresponds to

$$\omega = 1/\sqrt{(mC)}. \tag{A-5}$$

In complex notation,

$x = \hat{x} = \frac{1}{\sqrt{2}} \hat{x} \exp(j\phi)$, see section 1-3.

The total energy W of the vibrating system is constant here and equal to the

sum of the potential and kinetic energies.

In the real representation,

$$W = \tfrac{1}{2}m\left(\frac{dx}{dt}\right)^2 + \tfrac{1}{2}\frac{x^2}{C}$$

$$= \tfrac{1}{2}\omega^2 m\,\hat{x}^2\sin^2(\omega t + \phi) + \tfrac{1}{2}\frac{\hat{x}}{C}\cos^2(\omega t + \phi)$$

$$= \hat{x}^2/C = 2|\tilde{x}|^2/C. \qquad \text{(A-6)}$$

In the presence of a damping force which is considered to vary linearly with the velocity of the moving mass the above differential eq.(A-3) changes to

$$m\frac{d^2x}{dt^2} + r\frac{dx}{dt} + \frac{x}{C} = 0, \qquad \text{(A-7)}$$

where r is the proportionality factor between the velocity and the damping force. Sometimes r is called the resistance of the system. The general solution of this equation in the real representation is

$$x = \hat{x}\exp(-t/\tau)\cos(\omega t + \phi), \qquad \text{(A-8)}$$

where the angular frequency is given by

$$\omega = \sqrt{\left(\frac{1}{mC} - \frac{r^2}{4m}\right)} \qquad \text{(A-9)}$$

and the relaxation time by

$$\tau = 2m/r. \qquad \text{(A-10)}$$

Eq.(A-8) represents a solution for non-steady state of the modified differential equation. Although the introduction of the complex representation for transient phenomena such as that under consideration is perfectly feasible, this matter will not be pursued here as being beyond the scope of this book.

The behaviour of a damped mass spring system subject to a sinusoidal external force is described by the differential equation

$$m\frac{d^2x}{dt^2} + r\frac{dx}{dt} + \frac{x}{C} = f, \qquad \text{(A-7a)}$$

where, in complex notation (c.f. section 1-3),

$$f = \tilde{f}\exp(j\omega t), \qquad \text{(A-11)}$$

where the factor $\exp(j\omega t)$ has been introduced explicitly in order to indicate that the angular frequency ω is a given quantity.

This equation is analogous to the differential equation describing the electrical behaviour of a series circuit of self-inductance L, resistance R and capacitance C, driven by a harmonic alternating voltage

$$L\frac{d^2Q}{dt^2} + R\frac{dQ}{dt} + \frac{Q}{C} = \hat{V}\exp(j\omega t.) \qquad \text{(A-12)}$$

When the steady state has been reached the following particular solution of eq. (A-7a) is found

$$x = \frac{\hat{f}\cos(\omega t - \phi)}{\omega\sqrt{(r^2+(\omega m-1/\omega C)^2)}}, \qquad \text{(A-13)}$$

or in complex notation,

$$\tilde{x} = \frac{\tilde{f}}{1/C - \omega^2 m + j\omega r}, \qquad \text{(A-14)}$$

from which the dependence of $\hat{x}$ on the frequency is evident. Utilizing the complex notation the concept of mechanical impedance was used in this book. This quantity Z_M is defined as the ratio of the complex force exerted on a point divided by the complex velocity of that point.

$$Z_M = \frac{\tilde{f}}{\tilde{u}}, \qquad \text{(A-15)}$$

with $u = dx/dt$.
The unit for Z_M in S I-units is Nsm^{-1}.
The mechanical impedance of the mass spring system is given by

$$Z_M = \frac{\tilde{f}}{j\omega\tilde{x}} = r + j\omega m + \frac{1}{j\omega C}. \qquad \text{(A-16)}$$

It thus follows that

$$|Z_M| = \sqrt{(r^2 + (\omega m - \frac{1}{\omega C})^2)}.$$

Note from eq.(A-17) that in resonance, when $\omega = 1/\sqrt{(mC)}$, $|Z_M|$ is minimal and equals r. Introductory textbooks on the theory of vibrations are: van Santen (1950), Jones (1951), Mc Lachlan (1951), Sharman (1963). An introduction on sound vibration is given by: Lamb (1960). Further details on the theory of sound can be found in: Rayleigh (1945), Morse (1948), Beranek (1949), Skudrzyk (1949), Wood (1966).

Appendix B. Derivation of the perturbation factors for homogeneous channels

The viscosity and the thermal conductivity inherent in gaseous media cause damping of acoustic waves propagating in channels. This damping may be ascribed to two effects.

1. Wall absorption, comprising the losses in the viscous and thermal boundary layers at the walls of the channel.
2. Volume absorption, which takes place in the body of the medium and corresponds to the residual losses in free waves.

These two forms of absorption differ in that the first is caused by diffusion of momentum and kinetic energy in directions normal to the direction of propagation and the second by the diffusion of these same quantities in the direction of propagation.

For the range of temperatures, barometric pressures, frequencies and channel cross-sections encountered in the acoustical investigation of porous materials the second effect is negligible in relation to the first and need not be further considered.

In a homogeneous channel, i.e. one having a constant cross-section, the concept of a plane wave, perturbed only near the channel walls by the boundary layers, is appropriate only if the transverse dimensions of the channel are comparatively large with respect to boundary layer thickness. As these transverse dimensions diminish, the boundary layers tend to cover the entire cross-sectional area, resulting in Poiseuille flow and isothermal changes of state in the limiting case of very small dimensions. Although, in this latter case, the dissipation of acoustic energy is distributed over the entire volume of the channel, the dissipative mechanism is still that of wall absorption.

Taking into account that momentum and kinetic energy are carried by the same molecules, one would expect the viscous and thermal boundary layers to have thicknesses of the same order of magnitude. That such is indeed the case will be shown later in this section.

Kirchhoff solved the problem for the cylindrical tube in the high frequency approximation and found formulae for the velocity of sound and the attenuation of waves. In this case the ratio of the thickness of the boundary layers and the

tube diameter is very small. Rayleigh (1927, p.319-327) studied the low frequency approximation; the above ratio is then large. Kosten (1949) extended this derivation, giving formulae that can be used to higher frequencies. Crandall (1927, p.229-241) studied the influence of viscosity for all frequencies, neglecting heat conduction. This led to a correction of the equation of motion which corresponds to the introduction of a complex density for the gaseous medium. The theory comprises both the high and the low frequency approximations. Kosten (1949, SAM, p.30-40) solved the complementary problem, i.e. the influence of heat conduction for all frequencies by neglecting viscosity. The result was a corrected equation of continuity in which the compression modulus of the medium takes a complex form. The solution comprises the high and low frequency approximations.

The solutions of Crandall and Kosten cover the problem of the propagation of waves in cylindrical tubes, provided the tube diameters are not excessively large, and that does not occur in porous materials. The reductions required by this approach are brief, an advantage over the more cumbersome treatment which introduces viscosity and thermal conductivity simultaneously. The results are both the same (D.W.van Wulfften Palthe private communication). To demonstrate the abbreviated method, it will be used to find the viscous and thermal perturbation factors for homogeneous fissures ξ_f' and η_f' respectively.

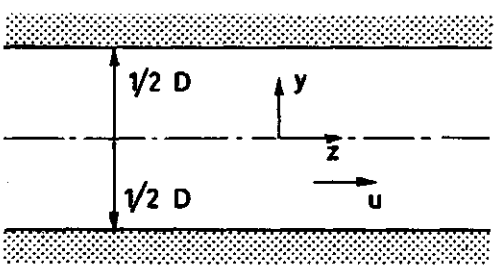

Figure B-1 Section through a fissure

Figure B-1 represents a section through a fissure, the waves propagating in the z-direction and y being the transverse coordinate. The particle velocity component in the direction of propagation is u.

The derivation of ξ_f' departs from the equation of motion for an infinitesimal element of the medium. This equation may be brought into the form:

$$- \partial p/\partial z + \eta \, \partial^2 u/\partial y^2 = \rho_s \partial u/\partial t, \qquad \text{(B-1)}$$

where η is the dynamic coefficient of viscosity and p is assumed to be independent of y. Solution of eq.(B-1) for harmonic time dependence and symmetry in y yields:

$$u = -\frac{1}{j\omega\rho_s}\frac{\partial p}{\partial z}\{1 + A\cos((1-j)y/l_v)\}, \tag{B-2}$$

where the viscous boundary layer thickness l_v is given by

$$l_v = \sqrt{(2\eta/\omega\rho_s)}. \tag{B-3}$$

The integration constant A is eliminated from eq.(B-2) with the boundary condition for a rigid frame: $u = 0$ for $y = \pm \frac{1}{2}D$:

$$u = -\frac{1}{j\omega\rho_s}\frac{\partial p}{\partial z}\left\{1 - \frac{\cos((1-j)y/l_v)}{\cos(\frac{1}{2}(1-j)D/l_v)}\right\}, \tag{B-4}$$

Integrating eq.(B-4) over the interval $-\frac{1}{2}D<y<\frac{1}{2}D$, yields

$$U = \int_{-\frac{1}{2}D}^{\frac{1}{2}D} u\,dy = -\frac{D}{j\omega\rho_s}\frac{\partial p}{\partial z}\frac{1}{\xi_f}, \tag{B-5}$$

$$\text{where } \xi_f' = 1/\left\{1 - \frac{\tan(\frac{1}{2}(1-j)D/l_v}{\frac{1}{2}(1-j)D/l_v}\right\}. \tag{B-6}$$

ξ_f' is the perturbation factor sought.

The derivation of η_f' is based on the following fundamental equations.

1. The law of Boyle - Gay Lussac $p_s = \rho_s R_g T_s$, which reads in differential form

$$\frac{dp}{p_s} = \frac{d\rho}{\rho_s} + \frac{dT}{T_s}. \tag{B-7}$$

The differentials dp, dρ, dt are the variables in the given case. They will be indicated further on by p, ρ and θ. So one can write $\frac{p}{p_s} = \frac{\rho}{\rho_s} + \frac{\theta}{T}$

ρ is the incremental density due to the sound field, T_s is the static absolute temperature,

Θ is the incremental temperature due to the sound field,
R_g is the gas constant per unit mass.

As p, ρ and Θ are small quantities, a first order approximation of eq.(B-7) is:

$$\rho = p/(R_g T_s) - \rho_s \Theta / T_s . \tag{B-8}$$

2. The equation of continuity. This expresses the fact that a gradient in particle displacement results in an incremental density. The appropriate form for harmonic phenomena is

$$- \rho_s \partial u/\partial z = j\omega\rho . \tag{B-9}$$

3. The equation of heat transport: Assuming heat to be transported transversely only, the net flow of heat per unit mass (having a volume $1/\rho_s$) is given by:

$$\frac{\partial Q}{\partial t} = \frac{\lambda}{\rho_s} \frac{\partial^2 \Theta}{\partial y^2} , \tag{B-10}$$

where λ is the thermal conductivity of the medium. The appearance of the derivative of the second order on the right side of eq.(B-10) may be understood by considering that heat flow density is proportional to temperature gradient and that it is thus the variation in gradient which determines whether and how much a net flow of heat into a given volume will result.
4. The First Law of Thermodynamics for an ideal gas. For harmonic phenomena this equation, applied to the unit of mass for the flow of heat is given by

$$\partial Q/\partial t = j\omega c_p \Theta - j\omega p/\rho_s , \tag{B-11}$$

where c_p is the specific heat per unit mass at constant pressure for the gaseous medium.

Elimination of the term $\partial\phi/\partial t$ from the eqs(B-10) and (B-11) yields

$$\frac{j\lambda}{\omega \rho_s c_p} \cdot \frac{\partial^2 \Theta}{\partial y^2} + \Theta = \frac{p}{\rho_s c_p} . \tag{B-12}$$

Assuming p to be independent of y, a solution, symmetrical in y, is sought for eq.(B-12):

$$\Theta = p\{1 + A\cos((1-j)y/l_h)\}/\rho_s c_p, \qquad \text{(B-13)}$$

where the thermal boundary layer thickness l_h has been introduced:

$$l_h = \sqrt{(2\lambda/\omega\rho_s c_p)}. \qquad \text{(B-14)}$$

The integration constant A in eq.(B-13) is eliminated with the boundary condition for a frame of constant temperature:
$\Theta = 0$ for $y = \pm \frac{1}{2}D$ so that

$$\Theta = \frac{p}{\rho_s c_p}\left\{1 - \frac{\cos((1-j)y/l_h}{\cos(\frac{1}{2}(1-j)D/l_h}\right\}. \qquad \text{(B-15)}$$

ρ is eliminated from eqs(B-8) and (B-9) which yields

$$-\partial u/\partial z = j\omega p/p_s - j\omega\Theta/T_s. \qquad \text{(B-16)}$$

where θ is given by eq.(B-15). Elimination of θ and integration over the interval $-\frac{1}{2}D<y<\frac{1}{2}D$ yields

$$-\partial U/\partial z = -\int_{-\frac{1}{2}D}^{\frac{1}{2}D}\frac{\partial u}{\partial z}\,dy = j\omega pD n_f'/\kappa p_s, \qquad \text{(B-17)}$$

where

$$n_f' = 1 + (\kappa-1)\frac{\tan(\frac{1}{2}(1-j)D/l_h)}{\frac{1}{2}(1-j)D/l_h}. \qquad \text{(B-18)}$$

Comparison of eqs(B-17) and (3-46) shows that n_f' from eq.(B-18) is indeed the perturbation factor sought.

Rayleigh (1927, II, p.327-328) considered a homogeneous fissure, confining the results to the low and the high frequency approximations.

Discussion of the results

The quantities l_v and l_h prove to be measures for the thicknesses of the boundary layers, e.g., if $\frac{1}{2}D/l_h >> 1$, in the range where $\frac{1}{2}D-y << \frac{1}{2}D$:

$$\Theta \approx p\{1 - \exp((1+j)(y-\tfrac{1}{2}D)/l_h)\}/\rho_s c_p\ . \qquad \text{(B-19)}$$

The right of eq.(B-19) shows that, on decreasing y from the value $\frac{1}{2}D$ (where Θ = 0), Θ rises to the value $p/\rho_s c_p$ with a rapidity determined by l_h. Thus, for $y = \frac{1}{2}D - l_h$, $|\Theta| = 0.859 \frac{p}{\rho_s c_p}$.

A relation for ideal gases, due to Eucken (Physik.Z., 14, 324-332,1913).

$\lambda/\eta c_p = (9\kappa-5)/4\kappa$.

Using this equation together with eqs.(B-13) and (B-14), the ratio of the thermal and viscous boundary layers is found to be:

$$l_h/l_v = \sqrt{(4\kappa/(9\kappa-5))}. \qquad \text{(B-20)}$$

As the gaseous medium is composed of gases ranging from monatomic to triatomic, $7/5<\kappa<5/3$ and thus, from eq.(B-20):

$$0.82<l_h/l_v<0.87 \ . \qquad \text{(B-20a)}$$

Roughly, the two boundary layers prove to be equally thick.

The viscous and thermal perturbation factors for the homogeneous cylindrical tube, ξ_c' and η_c', respectively, may be read directly from Crandall's and Kosten's results as presented by Zwikker & Kosten (1949, SAM, p.25-40). It thus follows from their eq.(2.06) that, on introducing the present notation:

$$\xi_c' = 1/\{1- \frac{2}{(1-j)R/l_v} \frac{J_1}{J_0}((1-j)R/l_v)\}, \qquad \text{(B-21)}$$

and from their eq.(2.13) that:

$$\eta_c' = 1+ (\kappa-1) \frac{2}{(1-j)R/l_h} \frac{J_1}{J_0}((1-j)R/l_h), \qquad \text{(B-22)}$$

where R is the radius of the tube.

Note: Zwikker & Kosten's quantity ν, defined on p.30, should be taken to equal $\lambda_h/\rho_o c_v$ in their notation or $\lambda/\rho_s c_v$ in the notation used in this book.

Appendix C Calculation of the function H(x) and its associated functions

There are three ranges for the arguments, the first is that where the function is best described by its asymptotic behaviour for small values of the argument, then there is a transition range and finally the range where the function is best described by its asymptotic behaviour for large values of the argument. In the present instance, the limits for the three ranges, respectively

$$0 \leq x \leq 1.0 \; ; \; 1 \leq x \leq 3.2 \; ; \; 3.2 \leq x$$

appear to be the most practical with the computation of the numerical values of H(x) in view (see eq.(3-70).

Approximations valid for one of the ranges only are indicated by the subscripts 1, 2 and 3 to H(x), F(x), M(x), G(x) and L(x), defined by eqs(3-71), (3-72), (3-81) and (3-82) respectively are also approximated and receive the same subscript as H(x), indicating the range of validity for the argument.

Calculation of the function H(x) from series expansions of the Bessel functions.

As the polynomial series representing Bessel functions are convergent, an algorithm for the generation of H(x) and suitable for computer processing may be formulated. The result is the Bessel subroutine described below. It should be noted that the argument of the Bessel function, $z = x\sqrt{-j}$ is assumed to lie in the fourth quadrant, the angle being $-\pi/4$;

x is the modulus of the argument. As H(z) is a symmetrical function in z with respect to zero, the arbitrary selection of the fourth quadrant for z does not restrict the generality of the results.

Rewriting a series expansion as given by Jahnke and Embde, (p.128) gives:

$$J_0(z) = \sum_{k=0}^{\infty} \frac{(\frac{1}{2}z)^{2k}}{(k!)^2} (-1)^k.$$

$$= \sum_{k=0,1,2,3}^{\infty} \frac{(\frac{x}{2})^{2k} \cdot j^k}{(k!)^2} =$$

$$= \sum_{k=0,2,4}^{\infty} \frac{(\frac{x}{2})^{2k} \; (-1)^{k/2}}{(k!)^2} + j \sum_{k=1.3.5}^{\infty} \frac{(\frac{x}{2})^{2k} \; (-1)^{(k-1)/2}}{(k!)^2} =$$

$$= \sum_{k=0,1,2}^{\infty} \frac{(\frac{x}{2})^{4k}\ (-1)^k}{\{(2k)!\}^2} + j\frac{x^2}{4} \sum_{k=0,1,2}^{\infty} \frac{(\frac{x}{2})^{4k}\ (-1)^k}{\{(1+2k)!\}^2} \ .$$

Furthermore:

$$J_1(z) = \sum_{k=0}^{\infty} \frac{(\frac{1}{2}z)^{2k+1}\ (-1)^k}{k!\ (k+1)!} = \sqrt{-j} \sum_{k=0}^{\infty} \frac{(\frac{1}{2}x)^{2k+1}\ j^k}{(k!)^2\ (k+1)} =$$

$$= \tfrac{1}{2}x \cdot \sqrt{-j} \left[\sum_{k=0,2,4}^{\infty} \frac{(\frac{1}{2}x)^{2k}\ (-1)^{k/2}}{(k!)^2\ (k+1)} + j \sum_{k=1,3,5}^{\infty} \frac{(\frac{1}{2}k)^{2k}\ (-1)^{(k-1)/2}}{(k!)^2\ (k+1)} \right] .$$

$$J_1(z) = \tfrac{1}{2}z \left[\sum_{k=0,1,2}^{\infty} \frac{(\frac{1}{2}x)^{4k}\ (-1)^k}{\{(2k)!\}^2\ (2k+1)} + j\frac{x^2}{4} \sum_{k=0,1,2}^{\infty} \frac{(\frac{1}{2}x)^{4k}\ (-1)^k}{\{(2k+1)!\}^2\ (2k+2)} \right] .$$

The terms required for the calculation of J_0 and J_1 can easily be derived consecutively. The following quantities are introduced:

$$P_k = \frac{(x/2)^{4k}\ (-1)^k}{\{(2k)!\}^2} \ ; \ Q_k = \frac{(x/2)^{4k}\ (-1)^k}{\{(2k+1)!\}^2} .$$

$$R_k = \frac{(x/2)^{4k}\ (-1)^k}{\{(2k)^2!\}(2k+1)} \ ; \ S_k = \frac{(x/2)^{4k}\ (-1)^k}{\{(2k+1)!\}^2\ (2k+2)} .$$

The quantities are interrelated by:

$$Q_k = \frac{P_k}{(2k+1)^2} \ ; \ R_k = \frac{P_k}{2k+1} \quad \text{and} \quad S_k = \frac{Q_k}{2k+2} \ ;$$

$$P_{k+1} = P_k \frac{-(x/2)^4}{(2k+1)^2\ (2k+2)^2} = \frac{-(x/2)^4\ S_k}{(2k+2)} .$$

The function H(x) can now be written as follows:

$$H(x) = \frac{2J_1(z)}{z\ J_0(z)} = \frac{\Sigma_k R_k + j(x/2)^2\ \Sigma_k S_k}{\Sigma_k P_k + j(x/2)^2\ \Sigma_k Q_k} . \qquad \text{(C-1)}$$

As P_k is the largest of the quantities with the same subscript, $\Sigma_k P_k$ can best serve as criterion for the required degree of accuracy. Eq.(C-1) has been programmed and is referred to as the Bessel subroutine. In table C-1 some numerical values of H(x) are given.

table C-1

Numerical values of H(x) obtained from the Bessel subroutine

x	H(x)	x	H(x)
0.2	0.999966-0.004999 j	2.2	0.711598-0.366031 j
0.4	0.999466-0.019986 j	2.4	0.650648-0.376057 j
0.6	0.997310-0.044833 j	2.6	0.593947-0.376765 j
0.8	0.991570-0.079073 j	2.8	0.543214-0.370598 j
1.0	0.979772-0.121525 j	3.0	0.499010-0.359962 j
1.2	0.959304-0.169931 j	3.2	0.461086-0.346849 j
1.4	0.928155-0.220811 j	3.4	0.428761-0.332719 j
1.6	0.885683-0.269752 j	3.6	0.401190-0.318544 j
1.8	0.833178-0.312268 j	3.8	0.377534-0.304900 j
2.0	0.773776-0.344894 j	4.0	0.357038-0.292089 j

In practice, the calculation turned out to be time consuming. For this reason, another method of calculation was developed. Eventually this last method produced results with sufficient accuracy. The method described above was used as a check only.

Calculation of the function H(x) and its associated functions (0<x<1)

The converging series for the Bessel functions were rewritten; a procedure which is especially appropriate if the argument of the Bessel function is relatively small.

$$J_0(z) = 1 - \frac{z^2}{4} + \frac{z^4}{64} - \frac{z^6}{64.36} + \ldots , \quad \ldots ,$$

and

$$J_1(z) = \tfrac{1}{2}z\left(1 - \frac{1}{8}z^2 + \frac{1}{192}z^4 - \frac{1}{64\cdot 144}z^6 + \ldots\right).$$

Making use of eq.(3-70) where H(x) has been defined, substitution and further reduction leads to:

$$H_1(z) = \frac{2J_1(z)}{zJ_0(z)} \approx 1 + \frac{1}{8}z^2 + \frac{1}{48}z^4 + \frac{33}{64\cdot 144}z^6 + \ldots ,$$

where $z = x\sqrt{-j} = ((1-j)/\sqrt{2})x$.

Separating the real and imaginary parts of the argument by:

$z = x\sqrt{-j} = (\frac{1-j}{\sqrt{2}})x$ gives

$$H_1(x) = 1 - \frac{x^4}{48} \ldots + j(-\frac{x^2}{8} + \frac{33x^6}{64.144} \ldots) \qquad (C\text{-}2)$$

The last term of eq.(C-2) influences the result of the calculated value of $H_1(x)$ but slightly, the contribution of this term can therefore be neglected. From this series the calculation of the values for $F_1(x)$ and $G_1(x)$ as defined in eqs(3-72) and (3-82) can be done readily. The calculation of the integrals in $L_1(x)$ and $M_1(x)$ merits further attention.

The integral $L_1(x)$.

Introduction of the above series expansion from eq.(C-1) into eq.(3-81) and (3-82) results in:

$$L_1(x) = \int \{1 + 0.4(1 - \frac{jx^2}{8} - \frac{1}{48}x^4)\}x^2 dx =$$

$$= \frac{1.4}{3}x^3 - \frac{jx^5}{100} - \frac{x^7}{120 \cdot 7}. \qquad (C\text{-}3)$$

Confining x to the interval $0 \leq x \leq 1$ limits the error at the upper bound within 1%.

The calculation of the integral $M_1(x)$.

Introducing the series expansion from eq.(C-2) into eq.(3-72) leads to:

$$M_1(x) = \int \frac{dx}{x^2(\frac{jx^2}{8} + \frac{x^4}{48})} = \int \frac{dx}{\frac{x^4}{48}(x^2 + 6j)} = 48 \int \frac{(x^2 - 6j)}{x^4(x^4 + 36)} dx .$$

The solution of this integral can be obtained by separating the integrand:

$$\frac{1}{48}M_1(x) = \int \frac{dx}{36x^2} - \int \frac{j\,dx}{6x^4} + \int \frac{-x^2/36 + j/6}{x^4 + 36} dx. \qquad (C\text{-}4)$$

The integral

$\int \frac{x^2}{x^4+36} dx$, is solved by substituting $x = \sqrt{6} \tan y$, resulting in:

$$\int \frac{6\sqrt{6}\tan^2 y}{36(1+\tan^4 y)\cos^2 y} dy = \frac{1}{\sqrt{6}} \int \frac{\sin^2 y}{\cos^4 y + \sin^4 y + 2\sin^2 y \cos^2 y - 2\sin^2 y \cos^2 y} dy =$$

$$= \frac{1}{4\sqrt{3}} \arctan(\frac{2x\sqrt{3}}{6-x^2}) - \frac{1}{8\sqrt{3}} \ln\left\{\frac{x^2+2x\sqrt{3}+6}{x^2-2x\sqrt{3}+6}\right\}. \qquad (C\text{-}5)$$

In an analogous way the solution of the following integral is found:

$$\int \frac{dx}{x^4+36} = \frac{1}{24\sqrt{3}} \arctan\left\{\frac{2x\sqrt{3}}{6-x^2}\right\} + \frac{1}{48\sqrt{3}} \ln\left\{\frac{x^2+2x\sqrt{3}+6}{x^2-2x\sqrt{3}+6}\right\}.$$

The last term of the right hand side of eq.(C-3) can be written as:

$$-\frac{1}{36}\int \frac{x^2}{x^4+36}\,dx + \frac{j}{6}\int \frac{1}{x^4+36}\,dx =$$

$$= -\frac{1}{144\sqrt{3}}(1-j)\arctan\frac{2x\sqrt{3}}{6-x^2} + \frac{1}{288\sqrt{3}}(1+j)\ln\frac{x^2+2x\sqrt{3}+6}{x^2-2x\sqrt{3}+6}\,.$$

The integration of the two other terms presents no problems. Thus

$$M_1(x) = -\frac{4}{3x} + \frac{8j}{3x^3} - \frac{(1-j)}{3\sqrt{3}} \arctan\left\{\frac{2x\sqrt{3}}{6-x^2}\right\} + \frac{1+j}{6\sqrt{3}}\ln\left\{\frac{x^2+2x\sqrt{3}+6}{x^2-2x\sqrt{3}+6}\right\}. \qquad (C\text{-}6)$$

The last two terms of the right side of eq.(C-6) can themselves be developed into series for small values of the argument: ($x \ll 1$).

$$\frac{-1}{3\sqrt{3}}\left[(1-j)\arctan\left(\frac{2x\sqrt{3}}{6-x^2}\right) - \tfrac{1}{2}(1+j)\ln\left\{\frac{1+\frac{2x\sqrt{3}}{6+x^2}}{1-\frac{2x\sqrt{3}}{6+x^2}}\right\}\right] \approx$$

$$\approx -\frac{(1-j)}{3\sqrt{3}}\left[\frac{2x\sqrt{3}}{6-x^2} - \frac{x^3}{3\sqrt{3}}\right] + \frac{(1+j)}{3\sqrt{3}}\left[\frac{2x\sqrt{3}}{6+x^2} + \frac{x^3}{3\sqrt{3}}\right].$$

$$\approx -\frac{(1-j)}{3\sqrt{3}}\cdot\frac{x}{\sqrt{3}}\left[1+\frac{x^2}{18}\right] + \frac{(1+j)}{3\sqrt{3}}\cdot\frac{x}{\sqrt{3}}\left[1-\frac{x^2}{18}\right] \approx -\frac{2jx}{9} - \frac{x^3}{81}$$

Thus an analytic approximation is found:

$$M_1(x) = -\frac{4}{3x} - \frac{x^3}{81} - \frac{2}{9}jx + \frac{8}{3x^3}j. \qquad (C\text{-}7)$$

For a more accurate calculation of M_1, more terms than in eq.(C-6) have to be included in the integration. From a practical standpoint this is feasible by numerical integration only. The influence of the number of steps per unit of x was examined. The approximation directly from the program for the Bessel sub-

routine (to be discussed later) is compared in table C-2 with the chosen approximation with 20 and 30 steps, respectively, and with a series expansion of 4 terms.

table C-2

$-(x_1-x_2)$ Integr.lim.	Bessel subroutine	Numerical integration °)	Numerical integration *)
0.2-0.4	3.3190-287.2903 j	3.3034-282.0960 j	3.3260-289.1789 j
0.4-0.6	1.1097- 29.1976 j	1.1081- 29.0438 j	1.1103- 29.2520 j
0.6-0.8	0.5552- 7.1242 j	0.5548- 7.1002 j	0.5553- 7.1306 j
0.8-1.0	0.3332- 2.5400 j	0.3331- 2.5362 j	0.3332- 2.5413 j
1.0-1.2	0.2221- 1.1243 j	0.2220- 1.1123 j	0.2221- 1.1243 j

°) From numerical integration with 20 steps per unit of x

*) From numerical integration with 30 steps per unit of x

Disregarding the smallest values of the arguments the differences between the results for the various methods remain below 1%.

An approximation for H(x) and its associated functions in the transition range

Values for $H_2(x)$ in the range $1.0<x<3.2$ can be obtained from the tables from Jahnke and Emde; the complex conjugates of the function required being listed on pages 246 to 249. The following relations held:
$J_0(x\sqrt{-j}) = J_0^*(x\sqrt{j})$, and $\sqrt{-j}\ J_1(x\sqrt{-j}) = \{\sqrt{j}\ J_1(x\sqrt{j})\}^*$
where $\sqrt{j}$ is taken to lie in the first quadrant. After substitution, H(x) follows from:

$$H(x) = \frac{2j\left[\sqrt{j}J_1(x\sqrt{j})\right]^*}{x\left[J_0(x\sqrt{j})\right]^*} .$$

An example of the determination of H(x) is given as an illustration. For x = 1.8, the real and imaginary components of $\sqrt{j}\ J_1(x\sqrt{j})$ are: + 0.3612 and + 0.8509 j,

respectively. The real and imaginary terms of $J_0(x\sqrt{j})$ are: + 0.8367 and - 0.7953 j, respectively. Using eq.(C-8) it follows that:

$$H(x) = \frac{2j}{1.8} \frac{(0.3612 - 0.8509j)(0.8367 - 0.7953\ j)}{(0.7953^2 + 0.8367^2)} = 0.832 - 0.312\ j.$$

In this manner the second column of table C-3 was composed.

Table C-3

Numerical values of H(x) and those of an approximate function $H(x)'$

x	H(x)	$H(x)'$
1.0	0.980-0.122 j	0.980-0.122 j
1.2	0.958-0.172 j	0.958-0.172 j
1.4	0.925-0.221 j	0.925-0.221 j
1.6	0.882-0.269 j	0.882-0.269 j
1.8	0.832-0.311 j	0.832-0.311 j
2.0	0.776-0.344 j	0.776-0.344 j
2.2	0.715-0.366 j	0.716-0.366 j
2.4	0.654-0.376 j	0.654-0.376 j
2.6	0.595-0.377 j	0.595-0.377 j
2.8	0.543-0.371 j	0.543-0.371 j
3.0	0.503-0.360 j	0.503-0.360 j
3.2	0.461-0.347 j	0.448-0.347 j
3.4	0.429-0.333 j	0.353-0.333 j

In the transition range an analytic approximation for $H_2(x)$ is introduced: eqs. (C-8), (C-9). Table C-3 shows that this approximation, $H_2(x)$, is acceptable in the range $1<x<3.2$.

The somewhat complicatad course, especially of the real part means that for practical purposes an approximate formula must be used in which higher powers of x are included. Through adjustment to numerical factors appearing in eq. (C-8) and (C-9) reasonable agreement with the values in the second column of table C-3 may be achieved.

$$\text{Re } H_2(x) = 1 - \frac{(x-0.4)^3}{(x-0.4)^3+8.60+3.75(x-0.4)-0.052(x-0.4)^5+0.052^2(x-0.4)^8} \qquad (C-8),$$

$$- \text{Im } H_2(x) = 0.122+0.249(x-1)-\frac{(x-1)^5}{0.514(x-1)^5+10(x-1)^3+26.66} . \qquad (C-9)$$

With the use of eqs(C-8) and (C-9) the function $F_2(x)$ and $G_2(x)$ can be written. A polynomial through the calculated values of $F_2(x)$ and $G_2(x)$ will be given in the survey at the end of appendix C.

The derivation of $M_2(x)$ and $L_2(x)$ is more difficult.

The integral $L_2(x)$

$$\text{Re } L_2(x) = \frac{x^3}{3} + 0.4 \int x^2 \cdot \left[1- \frac{(x-0.4)^3}{(x-0.4)^3+8.60+3.75(x-0.4)-0.052(x-0.4)^5+0.052^2(x-0.4)^8}\right] dx$$

$$\text{Re } L_2(x) = + \frac{1.4}{3} x^3 - 0.4\ I_1 . \qquad (C-10)$$

After the introduction of $\frac{x-0.4}{5} = u$, u lying between 0.12 and 0.52, the integral I_1 can be transformed into

$$I_1 = \int \frac{(5^5u^5 + 0.8\cdot5^4u^4 + 0.16\cdot5^3u^3)d\ 5u}{5^3u^3 + 8.60 + 3.75\cdot5\ u - 0.052\cdot5^5u^5 + 0.052^2\cdot5^8\cdot u^8} =$$

$$= 14.793 \int \frac{(u^5 + 0.16\cdot u^4 + 0.0064\ u^3)du}{u^8 - 0.15383\ u^5 + 0.11834\ u^3 + 0.017751\ u + 0.008142} = 14.793\ I_2 \qquad (C-11)$$

Splitting of the denominator into the above integrand involves a search for a number of complex or real roots of a polynomial. Kunz (1939) presents a solution through use of the Lin-Bairstow method. A Fortran program was made for this technique.

The real roots of the denominator turn out to be:

$u_1 = - 0.30145825$

$u_2 = - 0.59601104$

while the products of the pairs of conjugated complex roots can be written as:

$(u-u_3)\cdot(u-u_4) = u^2 - 1.22857214\ u + 0.47065730$

$(u-u_5)\cdot(u-u_6) = u^2 - 0.24548668\ u + 0.18610927$

$(u-u_7)\cdot(u-u_8) = u^2 + 0.57658953\ u + 0.51734090$

As a result of this, the integral I_2 can be split up

$$I_2 = \int \left[\frac{AA}{u-u_1} + \frac{B}{u-u_2} + \frac{Cu+D}{(u-u_3)\cdot(u-u_4)} + \frac{Eu+F}{(u-u_5)\cdot(u-u_6)} + \frac{Gu+H}{(u-u_7)\cdot(u-u_8)} \right] du.$$

Solution of a matrix will lead to the coefficients of the numerators. This involved more difficulties than anticipated and was possible only after repreated programming, for which use was made of the well-known Crout-reduction method. Substitution of the coefficients of the denominators leads to:

$$I_2 = \int \left[\frac{-0.032103222}{u-u_1} + \frac{0.33772185}{u-u_2} + \frac{0.38647294u + 0.01060727}{(u-u_3)\cdot(u-u_4)} + \right.$$

$$\left. + \frac{-0.288872957u + 0.11556302}{(u-u_7)\cdot(u-u_6)} - \frac{0.40321186u + 0.57094917}{(u-u_7)\cdot(u-u_8)} \right] du \qquad (C\text{-}12)$$

Integration of these partial subintegrals leads to further subdivision, since

$$\int \frac{Cu+D}{u^2+pu+q}\, du = \left[\frac{C}{2} \ln(u^2+pu+q) + \frac{D-C\cdot p/2}{\sqrt{(q-p^2/4)}} \arctan \frac{u+p/2}{\sqrt{(q-p^2/4)}} \right], \qquad (C\text{-}13)$$

where the limits for u are derived from $u = 0.2x-0.08$.
After integration of all the subintegrals, the function for the real part of $L_2(x)$ can be written as:
$\mathrm{Re}\ L_2(x) = \frac{1.4}{3} x^3 - 5.9172\ I_2$.

The imaginary component of $L_2(x)$ can be treated as follows:

$$-\mathrm{Im}\ L_2(x) = 0.4 \int x^2 \left[0.122 + 0.249(x-1) - \frac{(x-1)^5}{0.514(x-1)^5+10(x-1)^3+26.66} \right] dx,$$

$$= 0.4 \left[-(0.127 + \frac{1}{0.514}) \frac{x^3}{3} + 0.249 \frac{x^4}{4} + \frac{1}{0.514^2} \int \frac{x^2(10(x-1)^3+26.66)}{(x-1)^5 + \frac{10}{0.514}(x-1)^3 + \frac{26.66}{0.514}} \right] dx. \qquad (C\text{-}14)$$

The last term of eq.(C-14) is defined as I_3. This leads to

$$I_3 = \frac{10}{0.514^2}\int\left[\frac{(x-1)^5+2(x-1)^4+(x-1)^3+2.666(x-1)^2+5.332(x-1)+2.666}{(x-1)^5+\frac{10}{0.514}(x-1)^3+\frac{26.66}{0.514}}\right]d(x-1).$$

On introducing $v = \frac{x-1}{10}$ and $I_3 = \frac{10}{0.514^2}(x+I_4)$ it follows that

$$I_4 = \int\left[\frac{2v^4-1.8455v^3+0.02666v^2+0.005332\,v-0.0049292}{v^5+0.1946v^3+51.87\cdot10^{-5}}\right]dv.$$

When the denominator is split according to the method applied previously the real root of the denominator is given by:

$v_1 = -0.1345979023$,

while the coefficients of the pairs of conjugate complex roots meet the conditions:

$(v-v_2)\cdot(v-v_3) = v^2 - 0.1482298637\,v + 0.0197654211$

$(v-v_4)\cdot(v-v_5) = v^2 + 0.0136319614\,v + 0.1949718380$

Substitution of the calculated coefficients in the numerators of the integrands now yields:

$$I_4 = \int\left[\frac{0.0001395136164}{v+0.1345979023} + \frac{0.013801585v + 0.0032919790}{v^2-0.1482298637v+0.0197654211} + \right.$$

$$\left. + \frac{1.98605890v - 1.81716117}{v^2+0.0136319614v+0.1949718380}\right]dv,$$

where the limits for v follow from $v = (x-1)/10$.

Integration can now be carried out immediately.

The high accuracy of the numerical factors in the above equations takes the possibility into account that two numbers with a small difference will be subtracted in the course of the calculations. It is not worthwhile analysing whether this contingency is realized or not as a reduction in accuracy does not increase the speed of the calculations.

It now follows that

$$+\ \mathrm{Im}\ L_2(x) = -0.0249\,x^4 + 0.27632\,x^3 - 15.1403\,x - 15.1403\,I_4. \qquad \text{(C-15)}$$

In the following table (C-4) are listed the results obtained from the expansions of $L_2(x)$. The values, as obtained by numerical integration of H(x) are

given in column I. The results of the considerably less time consuming procedure of approximation through root splitting and the introduction of sub-integrals are listed in column II.

Column III presents the results obtained from a polynomial approximation which was fitted to the numerical values of L(x) as given in column I. This polynomial is given by:

$$\text{Re } L_2(x) = 0.44133\, x^3 + 0.0456\, x^4 - 0.027\, x^5 + 0.00333\, x^6 + 0.00000267\, x^2(x-1)^7, \tag{C-16}$$

$$\text{Im } L_2(x) = (0.016\, x^3 - 0.04201\, x^4 + 0.05202\, x^5 - 0.015887\, x^6 + 0.001587\, x^7)\,j \tag{C-17}$$

and this simple approximation deviates less than 1% from the values of column I.

Table C-4

Integr.lim.		Numerical values of $L_2(x)$		
x_2	x_1	I	II	III
1.2	1.0	0.3372-0.0144 j	0.3367-0.0145 j	0.3367-0.0145 j
1.4	1.2	0.4669-0.0268 j	0.4661-0.0270 j	0.4661-0.0268 j
1.6	1.4	0.6145-0.0446 j	0.6134-0.0446 j	0.6135-0.0447 j
1.8	1.6	0.7778-0.0678 j	0.7769-0.0677 j	0.7768-0.0677 j
2.0	1.8	0.9550-0.0955 j	0.9547-0.0954 j	0.9544-0.0955 j
2.2	2.0	1.1448-0.1260 j	1.1455-0.1263 j	1.1451-0.1257 j
2.4	2.2	1.3467-0.1575 j	1.3481-0.1580 j	1.3481-0.1574 j
2.6	2.4	1.5617-0.1886 j	1.5623-0.1893 j	1.5619-0.1889 j
2.8	2.6	1.7900-0.2182 j	1.7896-0.2190 j	1.7914-0.2185 j
3.0	2.8	2.0330-0.2459 j	2.0334-0.2468 j	2.0317-0.2455 j
3.2	3.0	2.2915-0.2717 j		

The integral $M_2(x)$:

$$M_2(x) = \int \frac{dx}{x^2(1-H(x))} = \int \frac{\Sigma P_k + j(x/2)^2 \Sigma Q_k\, dx}{x^2\, \Sigma(P_k - R_k) + j(x/2)^2 \Sigma(Q_k - S_k)}.$$

Restricting the series to three terms and temporary replacement of $(x/2)^2$ by z yields:

$$M_2(x) = -2\int \frac{(1-v^2/4+v^4/242)+jv(1-v^2/36)-v^4/120^2)}{x^2v\left\{v(1-v^2/120+v^4/140\cdot720)/(3-j\ (1-v^2/24+v^4/720\cdot120)\right\}}\,dx.$$

A simple check makes clear that terms with higher values of the exponent than six can be neglected, the range being limited to $x<3.2$

$$M_2(x) = \int \frac{4\ x^2/3\left\{1+(v^2/10)+(v^4/630)\right\}-8j\left\{(1+(v^2/6)+v^4\right\}}{x^4\left\{1+(v^2/9)+(v^4/540)\right\}}. \qquad (C-18)$$

Root splitting to prepare partial fractions of this integral gives very expanded forms. As computer facilities were available the integration for (C-18) was performed numerically. Extensive testing proved that with 20 steps per unit of x an accuracy of 0.2% could be obtained.

A simpler way for calculating $M_2(x)$ was found by approximating values for M(x) calculated from the values of the Bessel function and numerical integration. The following function was found:

$$M_2(x) = -\frac{4}{3x} - 0.0003x^2 + j\left(\frac{2.658}{x^3} - 0.023\sqrt{x}\right). \qquad (C-18a)$$

Values of the integrand $M_2(x)$ obtained by numerical integration, making use of eq.(3-72) and the Bessel subroutine and those, $M_2'(x)$, from eq.(C-18)

Table C-5

Integrand of $M_x(x)$

x	From series expansion eq.(C-18)	From analytic approximation eq.(C-18a)
1.0	1.333-8.007j	1.333-7.986j
1.2	0.926-3.865j	0.925-3.856j
1.4	0.680-2.089j	0.679-2.085j
1.6	0.520-1.228j	0.520-1.226j
1.8	0.411-0.769j	0.410-0.772j
2.0	0.332-0.5068j	0.332-0.5066j
2.2	0.274-0.3483j	0.274-0.3482j
2.4	0.230-0.2478j	0.230-0.2478j
2.6	0.1958-0.1816j	0.1956-0.1816j
2.8	0.1684-0.1366j	0.1684-0.1366j
3.0	0.1463-0.1051j	0.1467-0.1051j
3.2	0.1281-0.0825j	0.1283-0.0825j

Expansion of H(x) for large argument (x>3)

Jahnke and Emde (1938), page 138, give on the series expansion for large argument of the Bessel functions of the respective orders, together with literature reference:

$$J_0(z) \approx \frac{1}{\sqrt{(\frac{1}{2}\pi z)}}\left[P_0(z)\cos(z - \frac{\pi}{4}) - Q_0(z)\sin(z - \frac{\pi}{4})\right],$$

and

$$J_1(z) \approx \frac{1}{\sqrt{(\frac{1}{2}\pi z)}}\left[Q_1(z)\cos(z - \frac{\pi}{4}) + P_1(z)\sin(z - \frac{\pi}{4})\right].$$

in which the functions $P_0(z)$ etc. can be represented as series:

$$P_0(z) = 1 - \frac{9}{128\ z^2} \ldots ,$$

$$Q_0(z) = -\frac{1}{8z}\ (1 - \frac{75}{128\ z^2} \ldots) ,$$

$$P_1(z) = 1 + \frac{15}{128\ z^2} \ldots ,$$

$$Q_1(z) = \frac{3}{8z}(1 - \frac{35}{128\ z^2} \ldots) .$$

After substitution it follows that

$$H(x) = -\frac{2}{z}\frac{P_1(z)}{P_0(z)}\frac{\tan(z - \pi/4) + Q_1(z)/P_1(z)}{1 - \tan(z - \pi/4)Q_0(z)/P_0(z)} , \qquad \text{(C-19)}$$

where once again $z = x\sqrt{-j}$.
Provided that $|\tan(z-\pi/4)| \not> 1$ and that $\left|(Q_{0,1}(z)/P_{0,1}(z))\right| << 1$, which is the case for large values of z it follows that:

$$H_3(x) \approx \frac{2}{z}\tan(z - \frac{\pi}{4})\left[1 + \frac{24}{128\ z^2} + \frac{1}{64\ z^2}\tan^2(z - \pi/4)\right] \cdot$$

$$\cdot\left|1 + \frac{3}{8z}(1 - \frac{50}{128\ z^2}\left[\cot\tan(z - \pi/4) - \frac{1}{8z}(1 - \frac{66}{128\ z^2})\tan(z - \pi/4) - \frac{3}{64\ z^2}\right]\right| . \qquad \text{(C-20)}$$

where

$$\tan(z-\pi/4) = -j\ \frac{\exp(x\sqrt{2}+jx\sqrt{2}-j\pi/2)-1}{\exp(x\sqrt{2}+jx\sqrt{2}-j\pi/2)+1} .$$

For large values of x the terms $\exp(+x\sqrt{2}) >> 1$; this means that $\tan(z-\pi/4) \approx -j$. Making use of eq.(C-19) one may write

$$H(x) = \frac{-2j}{z} \frac{P_1(z)}{P_0(z)} \cdot \frac{1+jQ_1(z)/P_1(z)}{1+jQ_0(z)/P_0(z)}$$

If, in the series expansion, the terms $1/z^4$ are incorporated, then

$$H(x) = \frac{-2j}{z} \frac{P_1(z)}{P_0(z)} \cdot \frac{1+jQ_1(z)/P_1(z)-jQ_0(z)/P_0(z)+Q_0(z)Q_1(z)/P_0(z)Q_1(z)}{1+Q_0^2(z)/P_0^2(z)} .$$

Introduction of the series developments for P and Q leads to:

$$H_3(x) \approx \frac{-2j}{z} + \frac{1}{z^2} - \frac{j}{4z^3} - \frac{1}{4z^4} . \qquad \text{(C-21)}$$

From eq.(C-21), $F_3(x)$ and $G_3(x)$ can be approximated

$$F_3(x) = 1 + \frac{2j}{z} - \frac{1}{z^2} + \frac{j}{4z^3} + \frac{1}{4z^4} =$$

$$= 1 - \frac{\sqrt{2}}{x} - \frac{1}{4\sqrt{2}\,x^3} - \frac{1}{4x^4} + j\left(\frac{\sqrt{2}}{x} - \frac{1}{x^2} - \frac{1}{4\sqrt{2}\,x^3}\right), \qquad \text{(C-22)}$$

and

$$G_3(x) = 1 + 0.4\left(\frac{\sqrt{2}}{x} + \frac{1}{4\sqrt{2}\,x^3} + \frac{1}{4x^4}\right) - j\,0.4\left(\frac{\sqrt{2}}{x} - \frac{1}{x^2} - \frac{1}{4\sqrt{2}\,x^3}\right). \qquad \text{(C-23)}$$

In table C-6 the results are shown for the calculation of F(x). This table indicates that the selection of $x<1$ and $x<3.2$ as range-limits yields acceptable results for the approximations.

Table C-6

	F(x)		$F_1(x)$		$F_2(x)$		$F_3(x)$	
0.2	0.000033	0.0050	0.00033	0.00048				
0.4	0.00054	0.0200	0.00054	0.00198				
0.6	0.00269	0.0448	0.0027	0.0450				
0.8	0.0084	0.0791	0.0085	0.0798				
1.0	0.020	0.122	0.0208	0.1245	0.0195	0.122		
1.2	0.042	0.170	0.0432	0.1800	0.0423	0.172		
1.4	0.075	0.222	0.0800	0.2448	0.0752	0.221		
1.6	0.117	0.270	0.1356	0.3198	0.1175	0.269		
1.8	0.167	0.312	0.2187	0.4050	0.1678	0.310		
2.0	0.222	0.345			0.2243	0.344		
2.2	0.288	0.366			0.2845	0.366		
2.4	0.349	0.376			0.3453	0.372		
2.6	0.406	0.377			0.4048	0.377	0.441	0.385
2.8	0.457	0.371			0.4568	0.371	0.483	0.369
3.0	0.501	0.360			0.4966	0.360	0.519	0.354
3.2	0.539	0.347			0.5567	0.346	0.550	0.339
3.4	0.571	0.333			0.6467	0.333	0.5778	0.325
3.6	0.599	0.319			0.7976	0.318	0.5896	0.311
3.8	0.622	0.305					0.6129	0.300

Calculation of $M_3(x)$

Introduction of $F_3(x)$ from eq.(C-22) yields $1/x^2F_3(x) = -j/z^2((z+j)^2+j(1-j/z)4z)$ The second term in the denominator of the right side of the equation is comparatively small. Therefore, in first order-approximation:

$$\frac{1}{x^2\,F(x)} = \frac{-j}{(z+j)^2}\left[1 - \frac{j}{4z(z+j)^2}\left(1-\frac{j}{z}\right)\right].$$

Temporary introduction of $\gamma = z+j$ leads to

$$\frac{1}{z} = \frac{1}{\gamma-j} = \frac{\gamma+j}{\gamma^2+1} = \frac{\gamma^3+j\gamma^2-\gamma-j}{\gamma^4-1} = \frac{\gamma^3+j\gamma^2-\gamma-j}{\gamma^4},$$

while

$$\frac{1}{z^2} = \frac{\gamma^6+2j\gamma^5-3\gamma^4-4j\gamma^3+3\gamma^2+2j\gamma-1}{\gamma^8},$$

so that

$$\frac{1}{x^2\,F(x)} \approx -\frac{j}{\gamma^2} - \frac{1}{4\gamma^5} - \frac{1}{4\gamma^7} - \frac{1}{2\gamma^8} + \frac{1}{\gamma^9} \ldots .$$

Using $dx = \sqrt{j}\,d\gamma$, it follows that

$$M_3(x) = \int \frac{dx}{x^2\,F dx} = \sqrt{j}\left[-\frac{j}{\gamma^2} - \frac{1}{4\gamma^5} - \frac{1}{4\gamma^7} - \frac{j}{2\gamma^8} \ldots\right] d\gamma =$$

$$= -\frac{\sqrt{-j}}{\gamma} + \frac{\sqrt{j}}{16\gamma^4} + \frac{\sqrt{j}}{24\gamma^6} - \frac{\sqrt{-j}}{14\gamma^7} \ldots .$$

As appears from a simple check, it makes little sense in practice to retain more than two terms of the expansion on the right side of the equation. Thus, as an approximation with acceptable accuracy, it is found that

$$M_3(x) = \frac{-\sqrt{-j}}{\gamma} + \frac{\sqrt{j}}{16\gamma^4} = \frac{-1}{x-\sqrt{-j}} - \frac{\sqrt{j}}{16(x-\sqrt{-j})^4} ,$$

in which

$$\frac{1}{x-\sqrt{-j}} = \frac{x-\sqrt{j}}{x^2-x\sqrt{2}+1} ,$$

so that

$$M_3(x) = \frac{-(x-\sqrt{j})}{x^2-x\sqrt{2}+1} - \frac{\sqrt{j}(x-\sqrt{j})^4}{16(x^2-x\sqrt{2}+1)^4} ,$$

$$M_3(x) = \frac{-(x-1/\sqrt{2}}{x^2-x\sqrt{2}+1} - \left[\frac{x^4/\sqrt{2}-6x^2/\sqrt{2}+4x-1/\sqrt{2}}{16(x^2-x\sqrt{2}+1)^4}\right] + j\left[\frac{1}{\sqrt{2}(x^2-x\sqrt{2}+1)} - \frac{-1+6x^2-4\sqrt{2}x^3+x^4}{16\sqrt{2}(x^2-x\sqrt{2}+1)^4}\right],$$

$$M_3(x) = \frac{-(x-1/\sqrt{2})}{x^2-x\sqrt{2}+1} - \frac{x^4-6x^2+4x\sqrt{2}-1}{16(x^2-x\sqrt{2}+1)^4\sqrt{2}} +$$

$$+ j\left[\frac{1}{(x^2-x\sqrt{2}+1)\sqrt{2}} - \frac{x^4-4x^3\sqrt{2}+6x^2-1}{16\ (x^2-x\sqrt{2}+1)^4\sqrt{2}}\right]. \qquad \text{(C-24)}$$

For an accurate calculation with large arguments it appears that an additional term of the series development has to be included, namely

$\frac{1}{4}j(x-\sqrt{j})^6/24(x^2-x\sqrt{2}+1)^6$.

This extension is included in the computer program.

The integral $L_3(x)$

$$I_3(x) = \int x^2\{1+0.4\ H_3(x)\}dx = \frac{x^3}{3} + 0.4\ j\sqrt{j} \int H_3\ z^2 dz =$$

$$= \frac{x^3}{3} + 0.4\sqrt{-j}\ \left[jz^2 - z + \frac{j\ \ln\ z}{4} - \frac{1}{4z}\right].$$

Neglecting the constant term gives

$$L_3(x) = \frac{x^3}{3} + 0.4\left[x^2\sqrt{-j} + jx + \frac{\sqrt{j}\ \ln\ x}{4} - \frac{1}{4x}\right]. \qquad \text{(C-25)}$$

Some remarks about accuracy should be made. The error in $H_3(x)$, due to the approximation of $\tan(z - \pi/4)$, is in the order of 1% when x equals 3. This means that terms with $1/x^3$ should be incorporated and that terms with $1/x^4$ or higher order may be dismissed.

A comparison was made between the results obtained with the approximative method and the method to be referred as the expansion of the Bessel subroutine. The calculations were performed on the IBM 1620 computer. The following table gives examples of the results for ζh obtained with the two procedures.

Table C-7

$\zeta \cdot h$ for the capillary model calculated according two procedures.

frequency (Hz)	Bessel subroutine	Approximative method
200	12.44-11.56j°	12.32-11.60j°
400	9.88- 8.55j	9.90- 8.46j
600	8.21- 7.04j	7.88- 6.80j
800	7.21- 5.99j	6.86- 5.72j
1000	6.58- 5.23j	6.21- 4.95j
1200	6.14- 4.67j	5.76- 4.39j
1400	5.82- 4.23j	5.35- 3.88j
1600	5.57- 3.88j	5.23- 3.64j

° layer thickness 0.040 m; sphere radius 3 mm; cos θ = 0.500.

200	0.70- 5.26j*	0.66- 5.08j*
400	0.41- 2.44j	0.40- 2.34j
600	0.35- 1.31j	0.35- 1.31j
800	0.36- 0.61j	0.36- 0.61j
1000	0.41- 0.05j	0.41- 0.05j
1200	0.51+ 0.47j	0.51+ 0.46j
1400	0.72+ 1.05j	0.72+ 1.04j
1600	1.18+ 1.76j	1.18+ 1.76j

* layer thickness 0.072 m; sphere radius 2 mm; cos θ = 1.00.

The results given show that the accuracy with the approximative method is adequate.

Calculations were made for values of r between 0.0003 and 0.0063 m. The values of cos θ were chosen to lie between 0.50 and 1.00.

Appendix D Some remarks on the calculation of the locus of the sample surface impedance in the complex plane

In section 3-10 one of the principal problems in constructing a locus for the normalized specific acoustic impedance at the sample surface was referred to briefly: the unequal distribution of calculated points along the locus if the steps in frequency are constant. A reasonable distribution of the points facilitates the construction of the locus and a procedure to that end is considered below. A reasonable distribution is considered to have been realized if:
a) The distance along the locus between two adjacent calculated points exceeds a given value $\delta\hat{s}$,
b) the angle between the tangents in two adjacent calculated points does not exceed a given value $\delta\hat{\phi}$.

As in section 1-11 attention will be focused on the transcendental factor in Z (eq.(1-65)):

$$x + jy = \coth(\gamma_m l), \tag{D-1}$$

for the simple case of constant frequency and variable sample thickness. The variables Δ and q as introduced in section 3-4 will be applied; in the case considered, Δ is a parameter and q a variable. Eqs(3-12a) and (D-1) yield:

$$x = \sinh(\Delta \cdot q)/(\cosh(\Delta \cdot q) - \cos q), \tag{D-2}$$

$$y = -\sin q/(\cosh(\Delta \cdot q) - \cos q). \tag{D-3}$$

For an infinitesimal step dq in q, the distance ds traversed by the locus is given by

$$ds = \left[(dx/dq)^2 + (dy/dq)^2\right]^{\frac{1}{2}} dq$$
$$= \left[\sqrt{(1+\Delta^2)}/(\cosh(\Delta \cdot q) - \cos q)\right] dq \tag{D-4}$$

and the radius of curvature, R, is given by

$$R = \left| \frac{\left[1+(dy/dx)^2\right]^{3/2} (dx/dq)}{d(dy/dx)/dq} \right|$$

$$= \sqrt{(1+\Delta^2)}/(\sinh(\Delta \cdot q) - \Delta \cdot \sin q). \qquad (D\text{-}5)$$

The angle $d\phi$ between the tangents in two points of the locus separated by a spacing ds is given by:

$$d\phi = ds/R. \qquad (D\text{-}6)$$

As high accuracy is unnecessary, the differential eqs(D-4) and (D-6) will be assumed to retain their validity when accorded the form of difference equations and thus:

$$\delta q = (\cosh(\Delta \cdot q) - \cos q)\delta s/\sqrt{(1+\Delta^2)}, \qquad (D\text{-}7)$$

$$\delta\phi = \delta s/R, \qquad (D\text{-}8)$$

$$\delta q = (\cosh(\Delta \cdot q) - \cos q)\delta\phi/(\sinh(\Delta \cdot q) - \Delta \cdot \sin q), \qquad (D\text{-}9)$$

where use has been made of eq.(D-5).

If $\delta s = \delta\hat{s}$ is introduced in eq.(D-7), the largest permissable step δq in q follows. Increasing q from a low value, a complication arises from the fact that 1/R increases monotonically with q (eq.(D-5)). Thus, keeping δs at $\delta\hat{s}$, $\delta\phi$ will exceed $\delta\hat{\phi}$ if q exceeds a critical value q_o (eq.(D-8)). In the range $q>q_o$, the largest permissible step δq follows from eq.(D-9) with $\delta\phi = \delta\hat{\phi}$. For $q = q_o$, $R = R_o$ and eq.(D-8) yields

$$R_o = \delta\hat{s}/\delta\hat{\phi}. \qquad (D\text{-}10)$$

R_o is thus easily determined. This is not true for q_o itself, because of the transcendental nature of eq.(D-5).

For vanishing q, x and y tend to $+\infty$ and $-\infty$, respectively. It is thus necessary to select a finite initial value for q, q_1, when calculating the locus and here $q_1 = \pi$, corresponding to the first anti-resonance, has the advantage of yielding a point certainly falling within the limits of a finite diagram. For the initial value q_1, R_1 is derived from eq.(D-5) and now two cases must be distinguished, differing in the manner in which further values for q are generated. In case I, $R_1>R_0$ and in case II, $R_1<R_0$, corresponding to $q_1<q_0$ and $q_1>q_0$, respectively. As the various values for q are generated, the corresponding points

of the locus follow from eqs(D-2) and (D-3). For the sake of clarity, the procedures for the two cases will be described separately, although this involves some duplication.

Case I, $q_1 < q_0$.

1. Departing from q_1, q diminishes by steps following from eq.(D-7) with $\delta s = \delta \hat{s}$.
2. The above process is terminated when x or y exceed predetermined limits, usually dictated by the finite dimensions of the diagram.
3. Departing from q_1, q is increased by steps following from eq.(D-7). For each step, R is determined from eq.(D-5) and compared to R_o. If $R > R_0$, the process is continued.
4. If $R < R_0$, q is increased by steps following from eq.(D-9), with $\delta\phi = \delta\hat{\phi}$.
5. The procedure is terminated if q exceeds a given maximal value. Note that this value determines the number of antiresonances and resonances in the calculated section of the locus.

Case II, $q_1 > q_0$.

1. Departing from q_1, q diminishes by steps following from eq.(D-9) with $\delta\phi = \delta\hat{\phi}$. For each step, R is calculated and compared to R_0. Provided $R < R_0$ the process is continued.
2. If $R > R_\wedge$, q diminishes by steps following from eq.(D-7), with $\delta s = \delta \hat{s}$.
3. The process is terminated if x or y exceeds a predetermined limit.
4. Departing from q_1, q_0 is increased by steps following from eq.(D-9).
5. The procedure is terminated if q exceeds a set maximum.

In the simple case of constant frequency and variable sample thickness, the computation procedures are thus complicated appreciable if a reasonable distribution of the calculated points of the locus is deemed essential. In this simple case, $\delta\hat{s}$ and the limits for x and y may be selected, allowing for the complex specific wave impedance of the sample material.

If, however, sample thickness is held constant and frequency is varied, computation becomes even more complicated, as variations in W_m and Δ should be taken into account too, thus requiring adjustment of $\delta\hat{s}$ and $\delta\hat{\phi}$, and q is also a complicated function of frequency. As most of the measurements were carried out under the above conditions, the simple case considered previously can only illustrate the nature of the problem. Its solution, under the present conditions, seems to require excessively complicated procedures of computation.

Acknowledgments

The present work was carried out at the Agricultural University of Wageningen, The Netherlands. The author is greatly indebted to Ir. D.W. van Wulfften Palthe, lecturer at the Delft University of Technology, under whose direction the theories were developed and the experiments carried out.